An Investigation of the Last Interglacial's Climate Characteristics

Insights from a Stable Water Isotope Equipped Climate Model

By

PAUL JOHANNES GIERZ

Department of Physics
UNIVERSITY OF BREMEN

A dissertation submitted to the University of Bremen
in accordance with the requirements of the degree of
DOCTOR OF NATURAL SCIENCES.

JULY 2016

Abstract

The Last Interglacial (LIG), spanning from approximately 130,000 to 115,000 years ago, is the warm period immediately preceding the last ice age, and represents one of the most recent intervals in Earth‚Äôs history that was significantly warmer than the pre-industrial. As such, it is an excellent test bed for understanding the controlling dynamics of warm climate periods.

By performing simulations of this period using a fully coupled, stable water isotope enhanced climate model (COSMOS-WISO), new insights into the strength of stable water isotopes as temperature proxies could be uncovered. The utility of the isotopic composition of rainfall, $\delta^{18}O_P$, as a paleothermometer is examined. It was found that the changes in $\delta^{18}O_P$ do not always correspond to changes in temperature, particularly when only small magnitude temperature changes are considered.

A second set of studies examined the match between simulated responses to LIG climate boundary conditions to measurements from various different paleoclimate archives. Of particular interest is the ability to reconstruct the North Atlantic temperature changes during the LIG, as these are closely tied to changes in the Atlantic Meridional Overturning Circulation (AMOC), which in turn redistributes large amounts of heat from the equatorial latitudes to the mid and high latitudes. Proxy evidence points to a cooling in this region during the early LIG, which may be indicative of a relatively weaker overturning circulation. However, the extent of this weakening is difficult to gauge based solely on temperature differences. When compared to model simulations, feasible temperature differences could be simulated with AMOC possibilities ranging from only a slightly weaker overturning circulation, to a stronger collapse possibly triggered by ice sheet melting. In order to eliminate one of these possibilities, additional comparisons with simulated isotopic signature in calcite were performed. When comparing to measurements from planktic foraminifera, a strong AMOC collapse triggered by ice melting could be ruled out, as the resulting simulated $\delta^{18}O_C$ values do not match with the observations.

Comparing against Italian speleothem records allowed for the discovery of possible rapid climate change events during the LIG. Simultaneous excursions of $\delta^{18}O_C$ enrichment and $\delta^{13}C$ enrichment indicate rapid drying and cooling, a typical response of an AMOC collapse. When comparing against model simulations of a hypothetical freshwater perturbation due to ice sheet melting, it was found that COSMOS-WISO was able to qualitatively reproduce the cooling and drying signals, yet quantitative comparisons of the $\delta^{18}O_C$ failed to produce the response seen in the records, and instead of an enrichment,

a depletion is simulated. This led to several hypotheses; either the triggering mechanism used in the simulation is incorrect, and that the AMOC collapse is caused in a different way. Alternatively, the model and real-world have different dominant effects acting on the speleothem record. While in the real-world, the isotopic signature is dominated by the precipitation amount effect, in the model, changes to the source region play a more important role. Should this source region change also occur in the real world, this would indicate that the drying needed to achieve the $\delta^{18}O_C$ enrichment might be larger than previously thought.

Finally, when examining possible triggering mechanisms for this overturning collapse, instabilities in the West Antarctic Ice Sheet (WAIS) were found. With the aid of a dynamic Ice Sheet Model, it could be determined that the WAIS collapses if ocean temperatures increase above a certain threshold, between 2 °C to 3 °C. Applications to the future also demonstrated that Greenland Ice sheet melting plays an important role on the AMOC strength in the next several hundred years. Coupled climate-ice sheet modeling revealed that if Greenland melting is not included in the simulations, the AMOC strength is overestimated by as much as 2 Sv, which consequently also leads to an overestimation of the amount of future warming.

Collectively, it could be found that the AMOC is a key player in the climate system, as changes to the overturning circulation induce feedbacks in other subcomponents of the climate as well. The isotopic signature of precipitation, $\delta^{18}O$ is a useful simulation addition that allows for more direct model data comparisons, but it is still prone to the same limitations of model resolution as is also seen in the more traditional simulation/proxy comparisons.

Dedication and Acknowledgements

I would like to thank my advisors, Gerrit Lohmann, Martin Werner, Thomas Felis, Russell Drysdale for their support throughout my PhD project. Furthermore, I would like to thank my colleagues in the paleoclimate dynamics working group, in particular Christian Stepanek, Michael Stärz, Xu Zhang, Chris Danek, Uta Krebs-Kanzow, and many others for the numerous coffee breaks and lunches. POLMAR, my graduate school, assisted in funding my research visit to the University of Melbourne, which helped tremendously in putting together a significant part of this project. Finally, I would like to thank my family, without whose support I probably wouldn't have gotten this far.

Author's declaration

I hereby affirm that: (1) I wrote the thesis without the help of others, (2) I used only those sources and aids cited in the text, and (3) All passages taken from the sources used, whether quoted literally or in context, have been indicated as such.

SIGNED: ..... DATE: .....

Table of Contents

List of Tables

Table **Page**

List of Figures

Figure **Page**

AMOC Atlantic Meridional Overturning Circulation

AIS Antarctic Ice Sheet

AICC2012 Antarctic Ice Core Chronology 2012

AO-GCM Atmosphere-Ocean General Circulation Model

ACC Antarctic Circumpolar Current

AWP Atlantic Warm Pool

AMO Atlantic Multidecadal Oscillation

ARC Arctic Seas

CAPE Circum-Arctic PaleoEnvironments

DF Dome F

EBM Energy Balance Model

EMIC Earth System Model of Intermediate Complexity

EPICA European Project for Ice Coring in Antarctica

EDC EPICA Dome C

EDML EPICA Dronning Maud Land

ENSO El Niño/Southern Oscillation

ECMWF European Centre for Medium-Range Weather Forecasting

ETOPO5 Earth Topography Five Minute Grid

ESM Earth System Model

GCM General Circulation Model

GrIS Greenland Ice Sheet

GHG greenhouse gas

GIN Greenland, Iceland, and Norwegian Seas

IPCC Intergovernmental Panel on Climate Change

ISM Ice Sheet Model

IRD Ice Rafted Debris

IKM Imbrie and Kipp transfer function method

ka B.P. kiloanni before present

LIG Last Interglacial

LGM Last Glacial Maximum

LAB Labrador Sea

MAT Modern Analogue Technique

MIS Marine Isotope Stage

MISI Marine Ice Sheet Instability

NADW North Atlantic Deep Water

NAO North Atlantic Oscillation

PI Pre-Industrial

PFT Plant Functional Group

PMIP Paleoclimate Model Intercomparison Project

PGM Penultimate Glacial Maximum

RCP4.5 Representative Concentration Pathway 4.5

RCP6 Representative Concentration Pathway 6

ST Surface Temperature

SST sea surface temperature

SSST summer sea surface temperature

THC Thermohaline Circulation

VK Vostok Ice Core

VSMOW Vienna Standard Mean Ocean Water

WMO World Meterological Association

WSI Winter Sea Ice

WAIS West Antarctic Ice Sheet

CHAPTER 1

INTRODUCTION

Earth is an incredibly complex system. It is composed of a large number of subsystems that form the foundation of every process that takes place on our planet, from the tectonics governing earthquakes and volcanism, the genetics responsible for biology and life, to the fluid dynamics controlling weather and climate. While it can be argued that the planet's various subsystems are intimately interconnected, the following examinations contained within this thesis will specifically focus on climate.

Currently, the Earth's climate is changing in ways that generate fundamental questions regarding the basic functionality of the climate system,why these changes are occurring, and how exactly the system will act in the future. Any number of interesting topics could be listed here, among them atmospheric and oceanic warming, sea ice area decline, ice-sheet and ice-shelf collapse, extreme rainfall events, and ocean acidification. These changes also lead to the question regarding natural variability. Have such changes occurred in the past? If so, did they happen at a similar pace? What caused climate changes to end? Will these same mechanisms be active in the future?

1.1 What is Climate?

Given this focus, a precise definition of climate is required. Several definitions have already been formulated:

- "The climate can ... be defined as a set of averaged quantities completed with higher moment statistics (such as variances, covariances, correlations, etc.) that characterize the structure and behavior of the atmosphere, hydrosphere, and cryosphere over a period of time" [Peixoto and Oort, 1992]

- "The climate system is made up of building blocks, which in themselves are based on elementary physical principles, but which have surprising and profound collective behavior when allowed to interact on the planetary scale." [Pierrehumbert, 2010]

- "Climate in a narrow sense is usually defined as the *average weather* or more rigorously, as the statistical description in terms of the mean and variability of relevant quantities over a period of time ranging from months to thousands or millions of years. These quantities are most often surface variables such as temperature, precipitation, and wind. Climate in a wider sense is the state, including a statistical description, of the climate system." Intergovernmental Panel on Climate Change (IPCC)

While these definitions vary slightly from one another, a few common elements can be extracted.

1. Any study of climate will inevitably focus on the **physical dynamics** of the various subsystems, answering questions regarding mass and energy flow.

2. Climate is a **statistical average** of weather conditions over a period of time. Generally, 30 years are considered to be required to make statements about a

region's climate, which is the time frame defined by the World Meterological Association (WMO)

3. Climate is an **interdisciplinary** study of the physical interaction of various subsystems. The IPCC divides the climate into 5 subsystems, namely the atmosphere, hydrosphere, cryosphere, lithosphere, and biosphere.

4. Climate is both **spatially and temporally** hetereogenous, and is subject to variability.

1.2 Paleoclimatology and Climate Proxies

Paleoclimatology is the study of the Earth's past climate prior to the widespread availability of instrumental observations. An excellent analogy to paleoclimatology can be found in the field of archaeology; where the fossilized and cultural remains of a society are utilized to make deductions about its nature and organization. Paleoclimatology works in a very similar manner, using indirect environmental records of the past to make deductions about the climate at that time. The study of paleoclimatology also fits in excellently with the definition of climate given above. Paleoclimatology investigates the *statistical average* of the *dynamics* of the climate system. These records are *variable* in both time and space, and the nature of these records requisites *interdisciplinary* approaches in order to make useful statements about our planet's past climate.

What exactly are these records of the past climate? These so-called *paleoclimate archives* come in a variety of forms. These archives are natural features of the Earth, and preserve the climate conditions under which they were formed. Examples include tree rings, skeletons of tropical coral reefs, ice cores, laminated sediments from lakes and the ocean floor, and cave stalactites (speleothems), among others. Each of these archives

have unique time scales at which they are applicable, and record climate features with varying degrees of temporal resolution.

Before useful information may be attained from these climate archives, information regarding their age must first be obtained. Chronology involves the assigning of these records into the geological time record, using a variety of tools from long term radioactive markers, or stratigraphic features to date the archive and assign it a context within Earth's history. Constructing such a geochronology can be challenging [as discussed in e.g. Govin et al., 2015], as there are only few absolute age markers, and the remainder of the chronology is then based upon stratigraphic alignment to reference chronologies, such as European Project for Ice Coring in Antarctica (EPICA) Dome C EDC3 chronology [Parrenin et al., 2007], or the Antarctic Ice Core Chronology 2012 (AICC2012), originally published by Bazin et al. [2013].

Paleoclimate proxies are geochemical, physical, geological, or biological measurements that enable the transfer of the information regarding the paleoclimate's behavior from the recorded archive itself into a physically meaningful value. A more detailed examination of how some proxies[1] work is given in Chapter 4, an examination and test of some information gained from speleothems is given in Chapter 5, and in the following section, one particular proxy, namely the isotopic composition of water within the Earth's hydrological cycle, is presented in greater detailed.

1.3 Stable Water Isotopes as a Climate Proxy

One example of a geochemical climate proxy may be found in the various stable isotopes of water, H_2O, $H_2^{18}O$, and $^1H^2HO$ (also referred to as HDO). These stable water isotopes, and the mechanisms by which they fractionate (i.e. separate based upon physical properties)

[1]The following proxies shall be examined in detail: ice cores, fossilized corals, benthic and planktic foraminifera, fanaul assemblages, and multi-proxy reconstructions for sea surface temperature

and distribute themselves throughout the various hydrological reservoirs of the climate system, have provided a powerful tool for reconstructing past climate situations [2]. In particular, these stable water isotopes – hereafter referred to via the usual relative δ-notation with respect to the Vienna Standard Mean Ocean Water (VSMOW) – have been used to make inferences about past temperatures and precipitation. The δ notation is defined as:

$$\delta X = \frac{R_{sample} - R_{standard}}{R_{standard}} \cdot 1000‰ \tag{1.1}$$

where X can any stable isotope ratio of a compound, in the case of water, either δ^{18}O or δD is utilized. R refers to the absolute amount of each compound.

δ^{18}O and δD trapped in polar ice cores have been used for past temperature reconstructions over interglacial-glacial cycles [EPICA community members, 2004], and sub-tropical isotope archives, such as speleothems, have been employed to provide an indication of the amount of precipitation via the water isotope concentration [Drysdale et al., 2004, 2005, 2007, 2009]. While it is possible to measure the isotopic concentration of water in some archives directly as with ice cores, others necessitate a transfer function from the water in the environment to the ultimately preserved climate archive, as is the case with marine species such as foraminifera as well as with the calcite in speleothem formations [Kim et al., 2006].

Regardless if the stable water isotope signal is recorded directly in the climate archive or not, in order determine a physically meaningful climate variable, a transfer must be made between the stable water isotope concentration and the reconstructed climate variable. Due to the requirement of this transfer function, a necessary assumption must be made *a priori*, namely, that the physical variability of the climate state, both temporally and spatially, maintains a constant relationship to the variability of the

[2] The exact fractionation processes, as well as how they are numerically simulated, are described in Chapter 2

recorded isotopic signal. The processes responsible for the signature of oxygen both in precipitation as well as in calcite are now briefly summarized in the following sections.

1.3.1 Stable Water Isotopes in Precipitation

The processes that control the isotopic signature of precipitation are described in detail during the model description in Chapter 2, yet it should be noted that fractionation occurs during phase changes of water, namely during evaporation and precipitation, with lighter (heavier) isotopes of oxygen evaporating (precipitating) more readily before the other isotope. This occurs due to the relatively higher volatility of $H_2^{16}O$. A schematic of the hydrological cycle and isotopic components therein is shown in Figure 1.1. Primary influencing factors here are the local temperature as well as the humidity, and a $\delta^{18}O$/T relationship has been formulated.

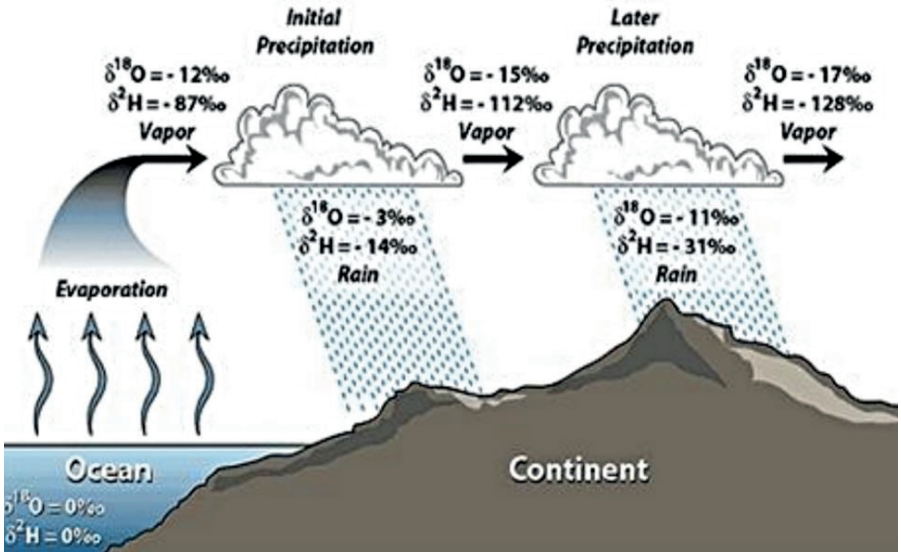

Figure 1.1: A schematic representation of the hydrological cycle, demonstrating how the isotopic signature in precipitation becomes increasingly depleted. Figure is reproduced from Hoefs [1997]

The $\delta^{18}O/T$ relationship was first discovered by Dansgaard [1964], and describes the changes in the precipitation signal of δ^{18}O as being a linearly dependent function of the

surface temperature (as t_a below) on a global scale:

$$\delta^{18}O = 0.69 t_a - 13.6‰ \tag{1.2}$$

The linear factor of 0.69 was empirically derived from global, modern-day observations. Therefore, it is of key importance to determine if in fact these relationships remain stable regardless of the background climate state, and is has been suggested that this relationship may in fact not be temporally stable for glacial periods [Werner et al., 2016]. If one of the general aims of paleoclimatology is to better understand the possible future warmer-than-present climate scenarios by examining past warm periods, an excellent first step would be to test if the temperature/isotope relationships change between the Pre-Industrial (PI) climate and past warm interglacials have stayed constant in time and space, as this is the primary tool by which paleoclimatologists are able to infer information about the climate's structure in the past.

In addition to this temperature effect, a negative correlation between the amount of precipitation and the isotopic signature of precipitation has also been found. This "amount effect" suggests that low (relatively depleted) δ values during very rainy months, and high (enriched) δ values during months with relatively little precipitation. While the exact reasons for the amount effect are quite complex (as discussed in e.g. Dansgaard [1964]), Rozanski et al. [1992] summarize that the "amount effect" can be attributed to several factors: (1) The isotopic value of condensation in a cloud decreases as cooling and rainout proceeds; (2) relatively smaller raindrops equilibrate to larger degree with the water vapor and temperature conditions below the cloud, and (3) small raindrops evaporate more readily than large ones on their way to the surface, leading to an increased enrichment; since lighter isotopes evaporate more readily than heavy ones.

1.3.2 Stable Water Isotopes in Calcite

While ice cores are able to record the $\delta^{18}O$ (as well as δD) in precipitation directly, other climate proxies that utilize stable oxygen isotopes examine the oxygen concentration in calcite ($CaCO_3$). This calcite can come from the skeletons of plankton, which are extracted from ocean sediment cores, or the calcite in speleothems.

While the isotopic composition of water in ice cores is relative straightforward to understand, with fractionation processes only being dependent on phase changes, the isotopic composition of oxygen in speleothems is more complicated, relying not only on the composition of precipitation, but also on the underlying geology, soil water, CO_2 degassing processes during speleothem formation, and drip water rates. A summary of the relevant processes is provided by Dreybrodt and Scholz [2011].

Similar complications also exist in understanding the isotopic composition of calcite in planktic and benthic foraminifera; as the biological activity of these species also directly influences the fractionation of oxygen. The δ^{18}O of both the global ocean, and of the local seawater may change due to ice sheet volume changes [Shackleton, 1967], as well as temperature-dependent isotopic exchange with the isotopic crust [Gregory and Taylor, 1981, Muehlenbachs and Clayton, 1976], yet these geologic changes occur on the order of hundreds of millions of years, and therefore typically the ice volume is considered to be the only dominant factor in controlling global isotopic signatures of oceanic water. Evaporative effects as well as changes to the incoming precipitation may influence the δ^{18}O composition of local seawater. Additionally, changes to the ocean circulation may have an impact on the local signature of δ^{18}O

In the foraminifera itself, changes in $\delta^{18}O$ is primarily dependent on the ocean temperature. A common paleothermometer equation utilized to reconstruct temperature from $\delta^{18}O$ in calcite is formulated by Kim and O'Neil [1997], which is based earlier work by Shackleton [1974]:

$$T = a - b \cdot (\delta^{18}O_c - \delta^{18}O_{sw}) + c \cdot (\delta^{18}O_c - \delta^{18}O_{sw})^2 \tag{1.3}$$

where a (16.9), b, (4.2) and c (0.13) are all empirical factors derived from laboratory experiments.

While it might be a common assumption to apply the oxygen isotope paleotemperature equation shown in (1.3), there are indications that foraminifera sometimes do not calcify in oxygen isotopic thermodynamic equilibrium with seawater due to biological "vital" effects, as discussed by Duplessy et al. [1970]. Primarily, ocean pH values and carbon chemistry may plan an important role here, yet the exact extent of this role is still under debate [Zeebe, 1999, Deines, 2005, Zeebe, 2005]. In these studies, such "vital effects" are not considered.

1.4 The Last Interglacial

Since the onset of the Pleistocene 2.58 million years ago, the Earth's climate has oscillated between relatively long, cold ice ages known as glacials, and relatively short, warm interglacials. While the exact mechanism behind the cycle of glacials and interglacials is not proven, one theory by Hays et al. [1976], suggests changes in the configuration of the Earth's orbit around the Sun may be responsible, at least in part.

The Serbian geophysicist Milutin Milankovic theorized that orbital variations of *eccentricity*, *axial tilt*, and *precession* may be responsible for climatic patterns in the 1940's [Milankovic, 1941]. The basis of this theory is that changes in the Earth's orbital configuration redistribute the amount of incoming solar radiation that is available at any given location.

Eccentricity describes the shape of Earth's orbit, which is an ellipse, as is given by Keppler's Laws of orbital mechanics. For our planet, the eccentricity varies from being

nearly circular to slightly elliptical [3]. The eccentricity of Earth's orbit varies due to gravitational influence from other bodies in the solar system, particularly the large gas giants Jupiter and Saturn in the outer solar system. There are a number of components to eccentricity variation, which loosely combine to a peridiocity of 100,000 years, spanning variations in the eccentricity of 0.05.

Obliquity determines the tilt of the Earth's rotation axis. Since this tilt affects the zonal distribution of incoming solar radiation, obliquity is the primary cause for the variation in the seasons. On Earth, the axial tilt varies from 22.1° to 24.5 °, with a periodicity of 41,000 years.

Precession is a gravity induced change of the orientation of the Earth's rotational axis relative to the orbital plane, with a period of approximately 22,000 years. This gyroscopic motion occurs due to tidal forces exerted on the Earth by both the Sun and the Moon. When the Earth's rotational axis points toward the sun in perihelion (the point in Earth's orbit with least distance between the planet and the Sun), the northern hemisphere has a larger difference between the seasons, and simultaneously, the southern hemisphere has a relatively reduced seasonal amplitude. The opposite is true when the axis points away from the Sun in perihelion.

A schematic diagram of these orbital change is presented in Figure 1.2 (adapted from the IPCC report), and a time series of the orbital changes over the past 800,000 years is shown in Figure 1.3.

The Last Interglacial (LIG)[4], spanning from approximately 130,000 to 115,000 years, is the interglacial immediately preceding the last Last Glacial Maximum (LGM). The LIG was relatively stable, and is believed to have been warmer than present day [CAPE Last Interglacial Project members, 2006]. Further evidence from corals [Felis et al., 2004] suggest that the LIG's hydrological cycle and temperature had an enhanced seasonal

[3] a minimum value 0.000055 and maximum value of 0.0679 [Laskar et al., 2011]. Eccentricity is a measurement of the ratio of the major and minor axes of an ellipse, and thus has no units.

[4] also sometimes referred to as the Eemian or Marine Isotope Stage (MIS) 5.5e

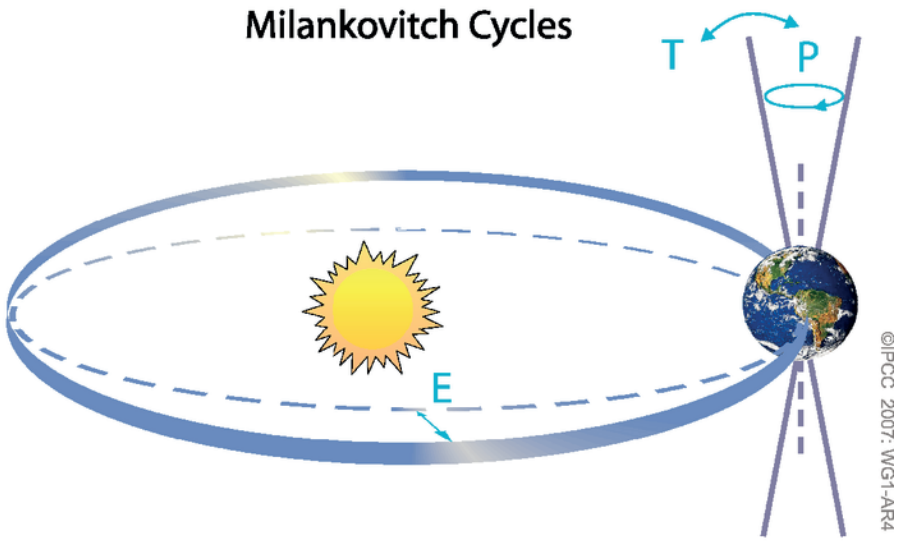

Figure 1.2: : A schematic representation of the orbital variations described by Milankovic [1941], adapted from the IPCC 2007 Report.

amplitude in the sub-tropics. Sea level may have been between 7 and 9 meters higher than during the PI, which suggests that the ice sheet geometry and rheology may have been different, both from the Greenland Ice Sheet (GrIS), as well as the Antarctic Ice Sheet (AIS) [O 'Leary et al., 2013, Dutton et al., 2015b].

As such, the LIG has gained interest from the paleoclimate community as a case study in understanding the governing dynamics of warm climate states. Some of these changes shall now be elaborated upon in greater detail, with particular focus on proxy based studies; as the modeling results of both the studies presented in this thesis as well as comparison of these results to other simulation efforts are reserved for later sections.

1.4.1 Temperature Changes during the LIG

The Circum-Arctic PaleoEnvironments (CAPE) project has examined temperature changes during the LIG, constructing a compilation of various terrestrial and marine proxies which reconstruct LIG warmth. The CAPE Last Interglacial Project members [2006] conclude that the summer temperatures in the Arctic were increased by as much as 5 °C

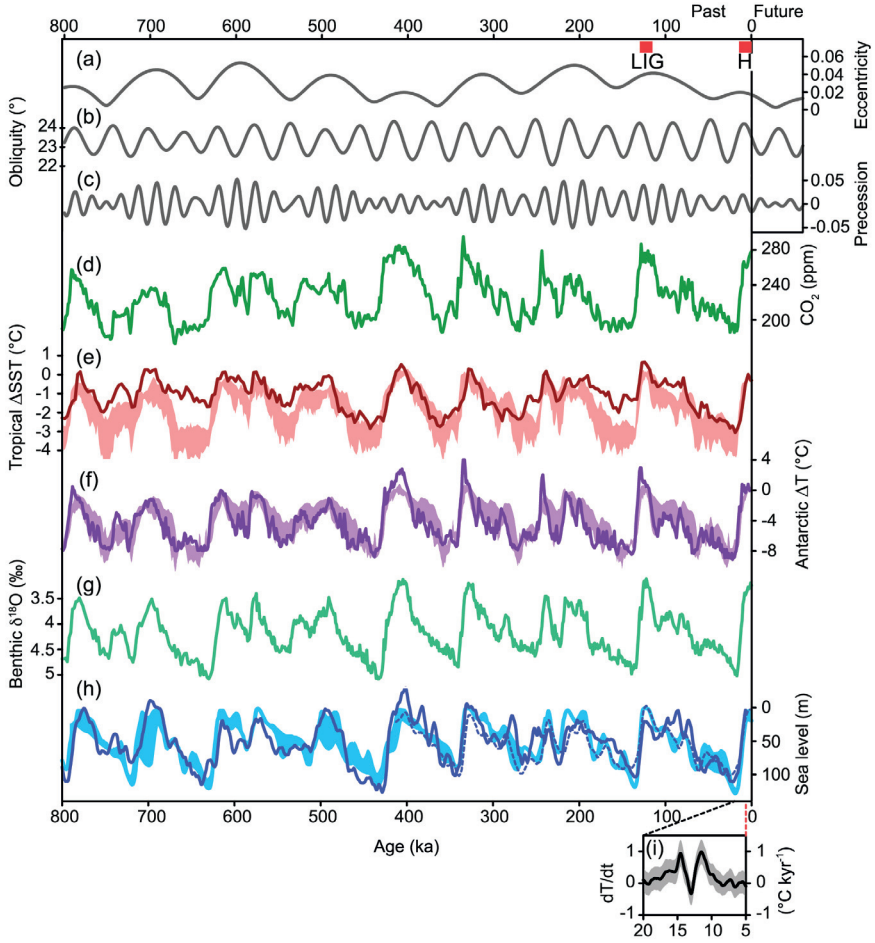

Figure 1.3: : Time series of multiple climate indicators over the past 800,000 years, adapted from the IPCC Report. (a), (b), and (c) show the eccentrcity, obliquity, and precession as described int he text, whereas the other sub plots show GHG concentration (d), temperature changes in both the tropics (e) and from Antarctic ice (f), as well as variations in key climate proxy, benthic $\delta^{18}I$ (g). Glacial/interglacial ice volume can be deduced from global sea level, shown in (h).

relative to PI. It is argued that a sea ice area reduction is the primary explanation for this warmth, caused by the changes in solar insolation during the LIG. The CAPE Last Interglacial Project members [2006] also break down this analysis regionally, showing changes between 1 °C to 4 °C over Europe, between 4 °C and 8 °C over Greenland, and between 2 °C and 8 °C over Siberia.

Additional multi-proxy compilations have attempted to reconstruct boreal summer sea surface temperature (SSST) in the North Atlantic [Capron et al., 2014]. In this study, while some areas of warmth are discovered in the northern sectors of the North Atlantic as well as in the Arctic, an interesting area of localized cooling is found in the North Atlantic. This same area demonstrates sensitivity to deep ocean circulation changes (i.e. Atlantic Meridional Overturning Circulation (AMOC) changes), as has been shown by Rahmstorf et al. [2015]. An examination of these particular temperature changes, as well as how well climate simulations may be able to reproduce them, will be given in Chapter 4.

Furthermore, some work has gone into understanding the seasonal amplitude of temperature during the LIG. Felis et al. [2004] utilized fossilized coral reef beds to make determinations about the seasonal amplitude of temperature based upon Mg/Ca paleothermometry, which is possible due to the subannual resolution within coral proxies, with specific focus on the Red Sea. It was discovered that the LIG had a generally enhanced temperature seasonal amplitude. A similar study was performed for the Carribbean, and an enhanced seasonal amplitude in temperature was also discovered [Felis et al., 2015]. Comparisons to these studies will also presented in Chapter 4.

1.4.2 Sea Level and Ice Sheet Geometry during the LIG

One of the primary concerns regarding possible future anthropogenically induced climate warming is the fate of the continental ice sheets, and, correspondingly, the evolution of

the global sea level over the next several decades and centuries. To properly understand the possible changes to the global sea level, potential instabilities in the cryosphere must be examined in order to understand what configuration the ice sheets may have in slightly warmer than present day climates.

The relative sea level is influenced by a number of factors:

- **Global ice sheet volume** directly controls how much liquid water is available to fill the global oceans. Inland mountain glaciers also effect the availability of liquid water to the ocean, yet the overall amount is much smaller compared to ice sheets.
- **Thermal expansion** of the ocean also contributes to global sea level change.
- **Isostatic adjustment** of the Earth's crust influences the ocean's bathymetry, and due to the depression and uplift of the crust into the mantle with increasing and decreasing ice sheet mass, the global sea level can be influenced.

The LIG is generally thought to have had elevated sea levels compared to the PI. Estimates place the relative sea level at 4.0 m to 6.0 m above PI levels [Stirling et al., 1998]. These estimates are based upon the presence of fossilized coral reef beds in the Pacific and Indian oceans, which were dated to the LIG using Th^{230}/U^{238}, a common geochronology method for obtaining the age of certain proxies. Newer estimates by Kopp et al. [2009], suggest that the sea level increase may have been as high as 8 m, although this was considered to be an unlikely highest estimate. Dutton and Lambeck [2012] however, suggest that this estimate of 8 m – or even higher sea level rise – may have been likely. While the earlier estimates can possibly be explained by thermal expansion of seawater, loss of mountain glaciers, and partial loss of the GrIS, the latter estimate would necessitate an inclusion of contributions from the AIS [Dutton et al., 2015b].

Changes to the GrIS's geometry during the LIG have been investigated, both Koerner [1989] as well as Cuffey and Marshall [2000] utilize ice core evidence to suggest that

the GrIS was smaller than at present. Pfeiffer and Lohmann [2015] have examined the climatic effect of such a reduction in model studies, concluding that changing the geometry would lead to a seasonal warming in boreal winter of several degrees Celsius. Pfeiffer and Lohmann [2015] also compare their results to proxy records, and discover that the simulated results fit well with the reconstructions when a reduction in the GrIS is considered.

A large scale melting of the AIS would also have severe climatic impacts [Otto-Bliesner et al., 2013]. In particular the West Antarctic Ice Sheet (WAIS), which is for a large part grounded below sea level, plays an important role in buttressing the AIS, and is sensitive to ocean circulation and temperature changes. Should the WAIS disintegrate, a large localized warming of 10 °C could occur [Otto-Bliesner et al., 2013], although this estimate is the result of only a single model study. Mechanistically, such a disintegration might be triggered by the so-called Marine Ice Sheet Instability (MISI). Sutter et al. [2016] investigated such an instability using an Ice Sheet Model (ISM) forced by both simulation output as well as hypothetical warming amounts, and discovered that threshold of 2 °C to 3 °C warming must be crossed before the WAIS begins to collapse. Some collaborative results from that study, as well as some implications for future climate change scenarios and the role of ice sheets in the climate system will be given in Chapter 6.

1.5 Scientific Questions Addressed

Having examined the current knowledge surrounding the LIG, it is possible to formulate some scientific questions that will be addressed in the course of this work:

- What are the general characteristics of the LIG climate that are produced using a stable water isotope equipped climate model? In how far are the physical and

isotopic representations of the climate consistent with one another?

- Are there cases do stable water isotopes fail to accurately reproduce the physical climate?
- To what extent can this climate model reproduce isotopic signals that are acquired from paleoclimate archives? Are any paleoclimate archives particularly difficult to reproduce?
- Is the climate of the LIG stable, or is it sensitive to rapid non-linear changes induced by small perturbations?
- Are the ice sheets stable during the LIG?
- Can any of the findings from these questions find application to future climate scenarios?

1.6 Outlook

In an attempt to answer some of these questions, this thesis shall be divided into the following parts. In Chapter 2, the climate model used for the studies is presented. Thereafter, a first examination of the climate of the LIG as simulated by this model is presented, and several large scale features are discussed in Chapter 3. Next, an examination of the model's ability to reproduce climate proxies is shown in Chapter 4. In Chapter 5, the stability of the LIG's climate under freshwater perturbation is discussed. A brief discussion of collaborative results about ice sheet instabilities during the LIG along with implications of ice sheet dynamics for future climate change scenarios is given in Chapter 6. Chapter 7 shows a synthesis of these results and some common lessons learned, and conclusions are presented in Chapter 8

CHAPTER 2

THE CLIMATE MODEL COSMOS-WISO

In the following chapter, the primary tool used for the experiments in this thesis shall be presented. All studies that are discussed used simulations produced with the General Circulation Model (GCM) COSMOS-WISO, a stable water isotope equipped variant of the GCM COSMOS. Before examining model specifics, it may be of benefit to place this model in context regarding computational ability and skill in representing a standard Pre-Industrial (PI) climate.

2.1 Types of Models

Goosse et al. [2010] provide a comprehensive overview of the current state-of-the-art for climate modeling. Climate models can be divided into three categories. (1) Energy Balance Models (EBMs) are on the lower end of the complexity spectrum, providing information solely about the changes the climate system may exhibit in terms of the planet's energy budget, as shown in e.g. Chen et al. [1995]. However, valuable information may still be obtained from an EBM [Lohmann et al., 1996]. (2) Earth System Models

of Intermediate Complexity (EMICs) also involve some simplifications, but generally include some representation of the planet's geography, yet due to limitations of scale, many processes in EMICs are still parameterized rather than explicitly solved [Claussen et al., 2002]. (3) GCMs, on the other hand, represent a more sophisticated view of a planet's climate, including many more processes, and treating many more physical concepts directly rather than via parameterizations. This is not to say that GCMs are without limitations – most notably, these models are computationally rather expensive – and some processes are still not resolved.

More recently, the scientific community has been moving towards a next generation of models, namely Earth System Models (ESMs). These models additionally have started to incorporate processes that have traditionally been viewed as more relevant for geology, such as isostatic adjustment and changes in ice sheet dynamics. While these processes play a critical role in paleoclimate over glacial-interglacial cycles, technical limitations forced the use of a GCM, although the implications of the neglected processes shall be discussed later on.[1]

2.2 The General Circulation Model COSMOS

Before examining the specialized version of COSMOS that can simulate stable water isotopes, a description of the physical components of the model is presented. While each model component has been separately published, an excellent summary is provided in Stepanek and Lohmann [2012], and the following description is adapted from that publication, as well as from the technical manuals published for each model within COSMOS.

The most relevant physical equations are presented for each model. For the atmo-

[1] Indeed, many ESMs are still under development are at not yet at a stage where paleoclimate modeling on the scale of the studies undertaken here would be feasible.

sphere; the continuity equation and the hydrostatic equation are shown, and a brief summary of the processes which much be parameterized is given. For the ocean; the primitive momentum equation, as well as sea ice motion and sea ice formation processes. The description of the land surface model contains information regarding the Plant Functional Groups (PFTs) available to the model, as well as the hydrology scheme employed within COSMOS.

2.2.1 ECHAM5

The atmospheric component of COSMOS is called ECHAM5. ECHAM5 is primarily developed by the Max Planck Institute for Metereology in Hamburg, Germany. The model has been published by Roeckner et al. [2006].

ECHAM5 was adapted for climate research by modifying the weather forecasting model of the European Centre for Medium-Range Weather Forecasting (ECMWF). The model is based upon a spectral dynamical core which simulates the troposphere and lower stratosphere to a vertical height of 10 hPa. Vertically, the model is organized on a hybrid sigma/pressure coordinate system, which closely follows the Earth's orography for lower levels and the orographic effect tapers off at higher levels. In the model setup used in these studies, a resolution of T31/L19[2] was employed. The approximate lateral resolution is $3.75° \times 3.75°$. Temporally, the model uses a time step of 2400 s.

The most relevant equations for atmospheric dynamics are shown below. Atmospheric processes are of course far more complicated than the dynamics summarized here, and many other phenomena[3] as well as the numerical representations thereof are presented in Roeckner [2003]. The continuity equation can be expressed as:

[2] i.e. there are 19 total vertical levels, and truncation of the series of spherical harmonics is performed at wave number 31

[3] e.g. radiative balance, cumulative and convective cloud processes, stratiform cloud schemes, just to name a few

$$\frac{\partial}{\partial \eta}\left(\frac{\partial p}{\partial t}\right) + \nabla \cdot \left(\vec{v}_h \frac{\partial p}{\partial \eta}\right) + \frac{\partial}{\partial \eta}\left(\dot{\eta}\frac{\partial p}{\partial \eta}\right) = 0 \tag{2.1}$$

Where η = general, pressure-based vertical coordinate

p = pressure

$\vec{v}_h$ = horizontal velocity

The hydrostatic equation can take the form:

$$\frac{\partial \phi}{\partial \eta} = -\frac{R_d T_v}{p}\frac{\partial p}{\partial \eta} \tag{2.2}$$

Where ϕ = geopotential height

R_D = Ideal Gas Constant

T_V = Virtual Temperature

A semi-implicit time scheme for solving the equations of temperature, divergence, and surface pressure is employed in ECHAM5. Passive tracer transport is treated in a semi-Lagrangian scheme, as described in Lin and Rood [1996]. Orography is used for the lower boundary conditions of atmospheric circulation, and is defined via the surface geopotential in the spectral domain. Subgrid-scale orographic effects are considered using a parameterization scheme as is described in Lott [1999]. This parameterization depends on several orographic parameters such as the mean and standard deviation of elevation, as well as the slope, orientation, and height of orographic peaks and valleys. A full scientific model description and validation is provided by Roeckner [2003].

2.2.2 JSBACH

The vegetation module employed by COSMOS is JSBACH. It is described by Raddatz et al. [2007], and uses the same horizontal resolution as the atmospheric component. Many of the atmospheric boundary conditions are also applied to land surface scheme. JSBACH is able to simulate the exchange of energy, water, and momentum between the land surface and the atmosphere. In principle, the model divides each grid cell into 8 tiles, which then represent the fraction covered by one of the PFTs. These PFT are able to distinguish between tropical, nontropical, deciduous, and evergreen trees, as well as deciduous and evergreen curbs, C3 and C4 grasses, and lastly seasonally as well as permanently bare soil. The simulated vegetation is based on temporal change of growing, natural mortality, and disturbance mortality by natural disasters (e.g. fire). The vegetation and resulting dynamics are described in detail by Brovkin et al. [2009].

The model's hydrology comprises of three surface reservoirs, a snow layer, water at the skin layer of the canopy, and a soil water layer. Each of these layers can be filled or drained in a so-called bucket model. The snow layer may be filled by snowfall and is emptied by snowmelt or sublimation. The canopy layer may be filled by either rainfall or snowmelt until its water storage capacity is reached, and thereafter the soil water reservoir is filled. This canopy reservoir may only be emptied by evaporation, whereas the soil water reservoir can only be emptied by evapotranspiration. Once the soil water is saturated, surface runoff occurs.

2.2.3 MPIOM

The last component in the COSMOS GCM is MPIOM, which is a hydrostatic, Boussinesq, primitive equation ocean and sea ice model, described by Marsland et al. [2003]. In principle, MPIOM must solve the horizontal momentum balance for a hydrostatic Boussinesq fluid:

$$\frac{d\vec{v}_o}{dt} + f(\vec{k} \times \vec{v}_o) = -\frac{1}{\rho_w}\left[\vec{\nabla}_H(p + \rho_w g\zeta)\right] + \vec{F}_H + \vec{F}_V \tag{2.3}$$

Where $\vec{v}_o$ = oceanic horizontal velocity

t = time

f = Coriolis parameter

$\vec{k}$ = unit vector normal to the Earth's center

ρ_w = constant reference density

$\vec{\nabla}_H$ = horizontal gradient operator

p = internal pressure of the ocean

g = gravitational acceleration

ζ = sea surface elevation

$\vec{F}_H$ and $\vec{F}_V$ are parameterized formulations of the horizontal and vertical eddy viscosity, respectively. They are defined as:

$$\vec{F}_H = -\vec{\nabla}_H \cdot \left(B_H \vec{\nabla}_H \Delta_H \vec{v}_o\right) \tag{2.4}$$

B_H is a coefficient proportional to the fourth power of the grid spacing.

$$\vec{F}_V = \frac{\partial}{\partial z}\left(A_V \frac{\partial}{\partial z}\vec{v}_o\right) \tag{2.5}$$

A_V is the eddy coefficient, which is allowed to partially relax relative to the value at the previous time step.

MPIOM also includes a module which is able to calculate sea ice dynamics, which plays an important role in climate feedback processes as well as the salinity budget of the ocean. Sea ice motion is defined via the two-dimensional momentum balance equation:

$$\frac{d\vec{v}_i}{dt} + f(\vec{k} \times \vec{v}_i) = -g\vec{\nabla}\zeta + \frac{\vec{\tau}_i}{\rho_i h_i} + \frac{\vec{\tau}_O}{\rho_i h_i} + \vec{\nabla} \cdot \sigma_{mn} \tag{2.6}$$

Where $f, \vec{k}, \zeta, g, t$ = as in equation 2.3

h_i = Sea ice thickness

ρ_i = Sea ice density

$\vec{v}_i$ = Sea ice velocity

$\vec{\tau}_a$ = Wind Stress

$\vec{\tau}_o$ = Ocean Current Stress

σ_{mn} = Stress tensor

The thermodynamics of sea ice resolve processes responsible for local growth and melting of sea ice, both at the base of the sea ice as well as at the surface. The most important process here is the consideration of salt and freshwater exchange with the ocean during sea ice growth and melting. The ocean salinity in the topmost layer, S_1 is changed by an amount ΔS by:

$$(S_1 + \Delta S)\Delta z'^{old} + \frac{\rho_i h_i^{old}}{\rho_w} S_{ice} = S_1 \Delta z'^{new} + \frac{\rho_i h_i^{new}}{\rho_w} S_{ice} \tag{2.7}$$

Here, $\Delta z'^{old}$ is the upper ocean layer thickness accounting for sea surface elevation and sea ice draft, $\Delta z'^{new}$ is the change resulting from sea ice melt or growth, while $hi^{new} - h_i^{old}$ is the amount of sea ice growth or melt.

These model dynamics are solved on an Arakawa C-grid [Arakawa and Lamb, 1977], and this grid is formulated on a bipolar, orthogonal, curvilinear GR30/L40 grid, with poles over Greenland and Antarctica, shown in Figure 2.1.

This setup provides an advantage, as the resolution is relative high at many of the deep water formation sites, which allows for a more realistic simulation of the physical

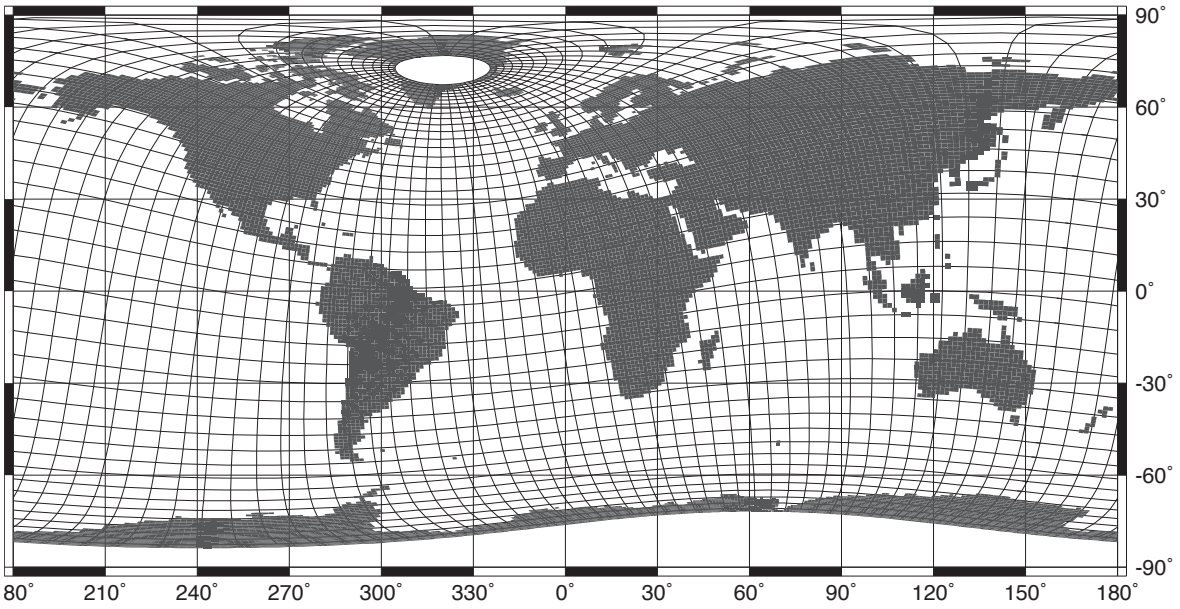

Figure 2.1: Standard MPIOM orthogonal curvilinear grid used for these studies.

processes at work in these regions, although several sub-grid scale processes are still parameterized[4].

Laterally, the resolution is $3.0° \times 1.8°$, with the vertical dimension split into 40 unevenly spaced depth layers. Bathymetry is resolved on partial grid cells, and defined via a global data set of ocean bottom depth[5]. Due to the coarse resolution of the model grid, several processes must be parameterized, such as slope convection, horizontal and vertical viscosity, vertical and isopycnal diffusivity, eddy-induced mixing, as well as convection. A full description of how these parameterizations are implemented is documented in Marsland et al. [2003]. Motion at the bottom of the ocean is parameterized by a boundary layer scheme in a similar way as described by Beckmann and Döscher [1997]. Eddy-induced mixing follows a parameterization designed by Gent et al. [2010], McWilliams [1995]. Finally, an isopycnal diffusion scheme for subscale mixing is applied, as in Jungclaus et al. [2002].

[4] e.g. Eddy motion

[5] The ocean's bathymetery input is generated from Earth Topography Five Minute Grid (ETOPO5)

The ocean model is run at a time step of 8640 seconds, and therefore no flux adjustments need to be applied. The system consisting of ECHAM5, JSBACH, and MPIOM is coupled with the OASIS3 coupler, which is responsible for exchanging all fluxes of energy, momentum, and mass between the various model domains [Valcke, 2013].

2.3 Inclusion of Stable Water Isotopes in COSMOS

Beyond the implementation of climate physics presented via these three components, stable water isotopes are additionally included within the entire hydrological cycle. Here, each model domain was again independently tested and validated for various paleoclimate settings, and a brief summary of the relevant processes and their numerical implementations is included below.

In this process, fractionation of stable water isotopes in the hydrological cycle is also explained, along with the relevant physical mechanisms that control these processes.

2.3.1 ECHAM5-WISO

The atmospheric model ECHAM5-WISO extends the simulation by explicitly including two stable water isotopologues HDO and $H_2^{18}O$ in the hydrological cycle [see Werner et al., 2011]. Fractionation is occurs during the phase changes of liquid water to water vapor or snow, due to differences in vapor pressures and diffusivities. In general, two types of fractionation processes are considered, equilibrium and non-equilibrium processes. Equilibrium fractionation takes place if the corresponding phase occurs slowly enough to allow full isotopic equilibrium. Non-equilibrium processes depend on the velocity of the phase change, thereby necessetiating information regarding the molecular diffusivity of the different water isotopologues.

For the fractionation process during evaporation from oceanic surfaces, the bulk formula in Hoffmann et al. [1998] is used:

$$E_x = \rho C_v |\vec{v}_h| (1-k)(x_{vap} - \underbrace{\alpha(T_s)^{-1} \beta R_{Oc} q_{sat}}_{x_{sat}}) \tag{2.8}$$

Where E_x = evaporative flux

ρ = density of air

C_v = drag coefficient

$|\vec{v}_h|$ = horizontal wind speed

x_{vap} = mixing ratio of water isotopes in the first layer

α = equilibrium fractionation factor

T_s = Surface temperature

β = factor of slight isotopic enrichment in the oceanic surface

R_{Oc} = isotope mass relation of the ocean

q_{sat} = saturation mixing ratio

The factor α is defined by Majoube [1971], and is the equilibrium fractionation factor for the water liquid-vapor phase transition. The values of α are 1.0098 and 1.084 at 20 °C and 1.0117 and 1.111 at 0 °C for ^{18}O and ^{2}H, respectively. The factor β is set to be 0.5 ‰ for ^{18}O and 4 ‰ for deuterium. If equation 2.8 is divided by the vapor flux, which is

$$E = \rho C_v |\vec{v}_h| (q_{vap} - q_{sat}) \tag{2.9}$$

the following relationship is then obtained, which describes the isotopic composition of the evaporative flux:

$$\delta_E + 1 = \frac{1-k}{1-h} [\alpha(T_s)^{-1} (\delta_{Oc} + 1) - (\delta_{vap} + 1) \cdot h] \tag{2.10}$$

Evaporation from land surfaces is handled by JSBACH-WISO, and described in section 2.3.3. Isotopic fractionation taking place during stratiform cloud processes, such as

autoconversion, accretion, or aggregation, are considered as temperature dependent equilibrium fractionation processes. For processes acting on liquid cloud water, it is assumed that the condensate remains in isotopic equilibrium with the surroundings during condensation, whereas during ice crystal formation, an instantaneous condensate is considered. This latter choice is based on the fact that frozen condensate is not able to exhchange with the surrounding vapor because of the low diffusivities in ice.

One additional fractionation is applied when a raindrop falls through the undersaturated air below the cloud. It is assumed that convective showers produce primarily large raindrops, equilibrating isotopically to only 45% with the surrounding vapor, while large scale clouds produce smaller drops equilibrating almost completely to 95%.

A summary of the fractionation processes handled by ECHAM5-WISO is presented in Figure 2.2

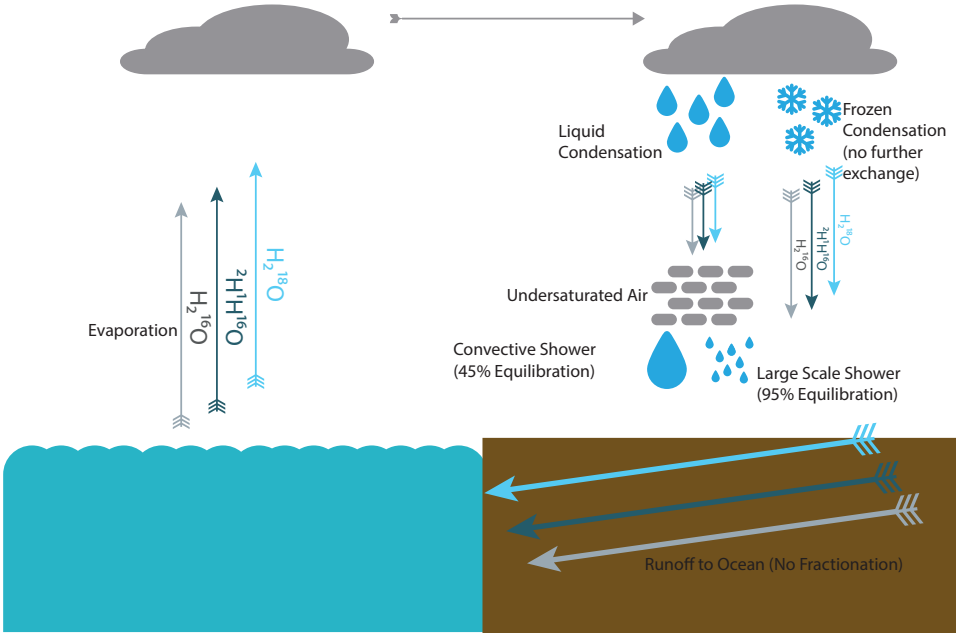

Figure 2.2: Isotopic fractionation processes simulated by ECHAM5-WISO.

2.3.2 MPIOM-WISO

Just as the simulation of the atmospheric water cycle can benefit from including stable water isotopes, the ocean's freshwater fluxes have unique and distinctive isotopic signatures, allowing the isotopic signature of a water mass to act as a tracer, in a similar way as salinity can be considered a passive tracer [Craig and Gordon, 1965]. The stable water isotopes $H_2^{18}O$ and HDO are included as conservative tracers in MPIOM-WISO, and as these traces are passive, the ocean model must only recieve boundary conditions provided by the atmospheric model, namely river runoff and precipitation. River runoff is determined by the bucket model already described above, which drains the continental freshwater fluxes (net P-E) – including the isotopic composition of these fluxes – which are simulated by ECHAM5-WISO.

One phase transition is handled by MPIOM, namely the formation and melting of sea-ice. However, no fractionation in $\delta^{18}O$ or δD are assumed by MPIOM-WISO, as the fractionation between liquid water and sea ice is small compared to other processes, such as evaporation [Xu et al., 2012].

2.3.3 JSBACH-WISO

The biosphere simulation of COSMOS has also been expanded to include stable water isotopes, resulting in the stable water isotope equiped vegetation model JSBACH-WISO, documented in detail in Haese et al. [2013]. The following description is adapted from that publication.

The water isotopes are treated passively for almost all processes described by JSBACH, with the exception of evapotranspiration, which consists of two processes, evaporation and transpiration.

2.3.3.1 Fractionation during Evaporation

Evaporation can occur from the three reservoirs described above: the snow layer sn, the canopy skin wl, or the soil layer ws. Water sublimates from snow at a potential evaporation rate, given by:

$$E_{sn} = \rho C_V |\vec{v}_h| (q_{vap} - q_{sat}) \tag{2.11}$$

Where E_{sn} = Potential Evaporation Rate: Snow Layer

ρ = density of air

C_V = drag coefficient for water flux

$|\vec{v}_h|$ = horizontal wind speed

q_{vap} = humidity of the air

q_{sat} = saturation-specific humidity

It is assumed that no fractionation occurs during sublimiation, as the diffusion rate in the ice crystal structure is very low. These leads to the assumption that the evaporative flux from snow has the same isotopic composition as the snow itself. Analogously to equation 2.11, evaporation rates from the canopy layer wl and from bare soil bs can be constructed:

$$E_{wl} = \rho C_V |\vec{v}_h| (q_{vap} - q_{sat}) \tag{2.12}$$

$$E_{bs} = \rho C_V |\vec{v}_h| (q_{vap} - h_{ws} q_{sat}) \tag{2.13}$$

The term h_{ws} in equation 2.13 of the relative humity of the soil surface. Fractionation during evaporation is calculated in the same way as done by Hoffmann et al. [1998], as

described above. During evaporation from the skin layer E_{wl}, no fractionation is assumed. For evaporation from the bare soil layer E_{bs}. As before, an equilibrium fractionation factor $\alpha^x(T)$ is obtained after Majoube. This results in the temperature dependency of the isotopic composition of evaporation. Additionally, kinetic fractionation α_k must be considered, as well as the mixing ratio of the water isotopes in the layer above the surface. After all processes are accounted for, evaporation from the land surface enhanced with fractionation may be described by the follow:

$$E^x_{bs} = \rho C_v |\vec{v}_h| \alpha_k \left(q^x_{vap} - \frac{R^x_{ws}}{\alpha^x(T)} h_{ws} q_{sat} \right) \tag{2.14}$$

The term α_k describes the kinetic fractionation may be defined after Merlivat and Jouzel [1979]:

$$a_k = 1 - \lambda k \tag{2.15}$$

$$\text{with } k = \begin{cases} 0.006, & \text{if } |\vec{v}_h| \leq 7\,\mathrm{m\,s^{-1}} \\ 0.000285 \times \vec{v}_h + 0.00082 & \text{if } |\vec{v}_h| > 7\,\mathrm{m\,s^{-1}} \end{cases} \tag{2.16}$$

$$\lambda = \begin{cases} 1 & \text{for } {}^{18}\mathrm{O} \\ 0.88 & \text{for D} \end{cases} \tag{2.17}$$

In this formulation, λ describes the ratio of the isotope molecular diffusivity in air. Here, α_k is dependent on the molecular and turbulent resistance of water vapor. Typical values for H^{18}_2O range between 0.994 and 0.998 when using equation 2.15, and are slightly larger for HDO.

2.3.3.2 Fractionation during Transpiration

The hydrology of JSBACH does not describe processes within the plants themselves, and transpired water is simulated as a potential transpiration flux, given by:

$$T = \rho C_V |\vec{v}_h| S^{-1} (q_{vap} - q_{sat}) \tag{2.18}$$

The factor S^{-1} describes the transpiration efficiency. It has been shown by Gat [1996] that no fractionation occurs as roots take up water. This leads to the assumption that the isotopic composition inside the plants is the same as the isotopic composition of the soil water. Therefore, no transpiration is assumed to occur during plant transpiration.

2.4 Application of COSMOS-WISO

In the following studies, the climate model described above has been utilized to generate simulations of the Last Interglacial (LIG), both for time-slice snapshot realizations of the climate state, as well as a transient simulation spanning the entire interglacial period. In the next chapter, large scale features of the LIG climate as simulated by COSMOS-WISO will be presented.

CHAPTER 3

LARGE SCALE FEATURES OF THE LAST INTERGLACIAL CLIMATE

This chapter describes the large scale features of the Last Interglacial (LIG) climate as simulated by COSMOS-WISO. Both physical and isotopic responses are examined, as well as the relationships between δ^{18}O in precipitation (hereafter noted as $\delta^{18}O_P$) and temperature T in order to examine to what extent the δ^{18}O proxy maintains its viability during the LIG.

3.1 Experiments in this Study

In the following two subsections, the orbital configuration, the resulting incoming solar radiation distribution, and the greenhouse gas (GHG) concentrations used in this study are described.

3.1.1 Forcings

To perform this study, three time slices during the LIG were simulated, corresponding to 120 ka B.P.[1], 125 ka B.P., and 130 ka B.P., utilizing both GHG and orbital forcings prescribed by the Paleoclimate Model Intercomparison Project (PMIP) protocol [Crucifix et al., 2012]. These are referred to as LIG-120, LIG-125, and LIG-130, respectively. Additionally, a control simulation is generated using Pre-Industrial (PI) forcing. The values for the orbital parameters were derived based upon the Berger and Loutre [1991] solution, and the PMIP GHG forcings were extracted from Antarctic ice cores. The values are set according to Lüthi et al. [2008] for CO_2, Loulergue et al. [2008] for CH_4, and Spahni et al. [2005] for NO_2. Dynamic vegetation was started with PI values and allowed to adapt to the climate state for each time slice. The global $\delta^{18}O$ and δD budget for the water isotopes are not modified, as a PI ice-sheet configuration is assumed in all experiments. Correspondingly, the global sea level is not modified. All time slices underwent long-term spinups of 2000 years, followed by an evaluation period of 100 years used for analysis. The simulations are summarized in Table 3.1.

Table 3.1: Description of the simulations described in this study and the relevant forcings applied to each. Ice sheets are fixed to pre-industrial geometry, while vegetation is initialized from pre-industrial and allowed to evolve as the model equilibrates.

Experiment	CO_2 (ppm)	CH_4 (ppb)	NO_2 (ppb)	Eccentricity (-)	Obliquity (°)	Precession (-)
PI	280	760	270	0.016724	23.446	282.04
LIG-120	268	572	261	0.041090	22.998	209.04
LIG-125	276	640	263	0.040000	23.790	127.14
LIG-130	257	512	238	0.038209	24.246	48.320

To ensure that the simulations were in equilibrium after the spinup period, the trends in the global deep ocean salinity are examined. For these simulations, the globally averaged deep ocean salinity changed by less than 0.01% over 100 years, corresponding

[1]The timescale kiloanni before present (ka B.P.), from the Latin word *annus* for year, denotes thousands of years before present.

to salinity changes that were less than 0.002 practical salinity units (psu) in magnitude. To confirm that the passive isotopic tracers are also in equilibrium, the deep ocean $\delta^{18}O$ concentration is examined. It was found that the globally averaged $\delta^{18}O$ signature of the deep ocean changed by less than 0.002‰ over the 100 years used for evaluation.

3.1.2 Solar Insolation

The LIG is forced by changes in the orbital configuration, changes in GHG concentrations, and the climatic feedbacks that result from these changes. The prescribed changes to the incoming solar radiation distribution throughout the year are shown in Figure 3.1. An increase in incoming solar radiation in boreal summers for LIG-130 and LIG-125 over the Northern Hemisphere can be seen, and a slight decrease in radiation in autumn. Over the Southern Hemisphere, the insolation increase happens later in the year, between September and November. LIG-120 presents a very different pattern, with a decrease in insolation during the first half of the year, and an increase in the second half.

3.2 Mean Climate State during the Last Interglacial

In the following, the yearly mean climate state of the LIG is examined for each of the simulated time slices, followed by an examination of the seasonal changes in boreal summer and boreal winter (Section 3.4). This examination is divided into several parts: First, an analysis of Surface Temperature (ST) changes and changes in precipitation to describe the state of the atmosphere state is shown. Furthermore, a description of the precipitation-weighted $\delta^{18}O$ signals is presented, and the analysis is concluded by presenting the simulated $\delta^{18}O$ signatures in ocean seawater.

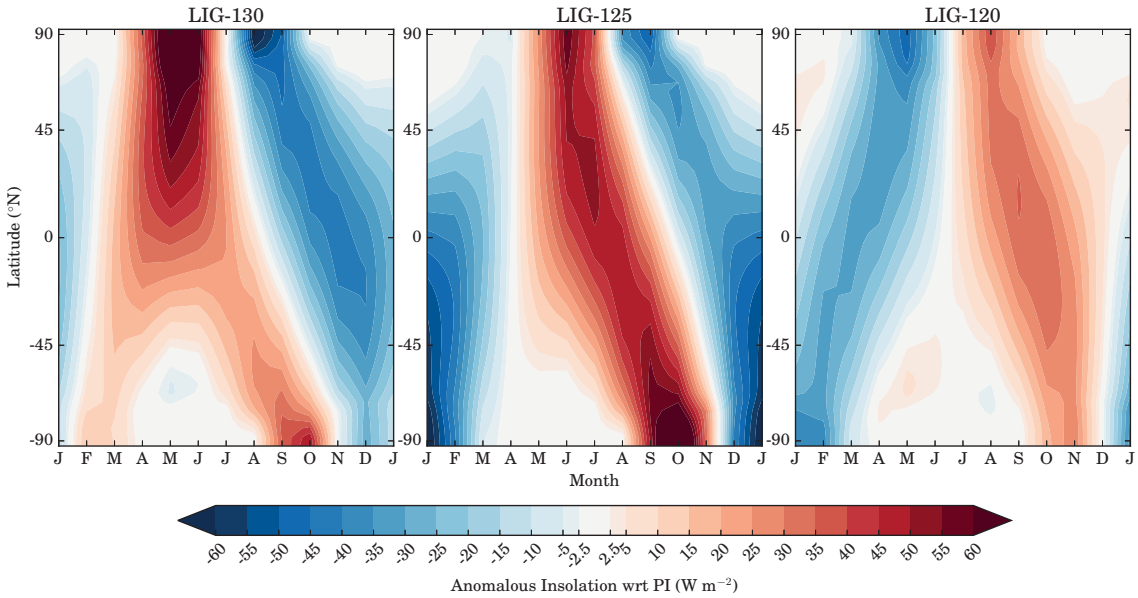

Figure 3.1: Anomalous Incoming Solar Radiation at the top of the atmosphere relative to PI. A strong increase in boreal summer incoming radiation can be seen in both LIG-130 and LIG-125, with a decrease during Autumn and Winter. During LIG-120, the climate receives less energy in Spring, and more in Autumn.

3.2.1 Surface Temperature Response

The first examination shows changes in ST relative to PI. The yearly mean ST in LIG-130, shown in Figure 3.2-A, is generally cooler than PI. Particularly over the Sahara, temperature decreases by more than −3.0 °C, and an equally strong cooling is seen over the Indian subcontinent. Slight localized warming, with a magnitude ranging from 1.5 °C to 2.0 °C is simulated in the Arctic and the Sea of Okhotsk. Another slight warming is simulated in the mid latitudes of the Pacific off the California coast, with temperature anomalies between 0.25 °C and 0.5 °C. The remainder of the global oceans demonstrate cooling signals ranging from −0.5 °C to −2.0 °C.

During LIG-125 the results differ greatly, as shown in Figure 3.2-B. Large scale warming is simulated, particularly in the high latitudes, with Arctic climatologically averaged temperature increases of beyond 2.0 °C. Just as in LIG-130 there is again a cooling simulated over the Sahara and the Indian Subcontinent. A vast majority of the

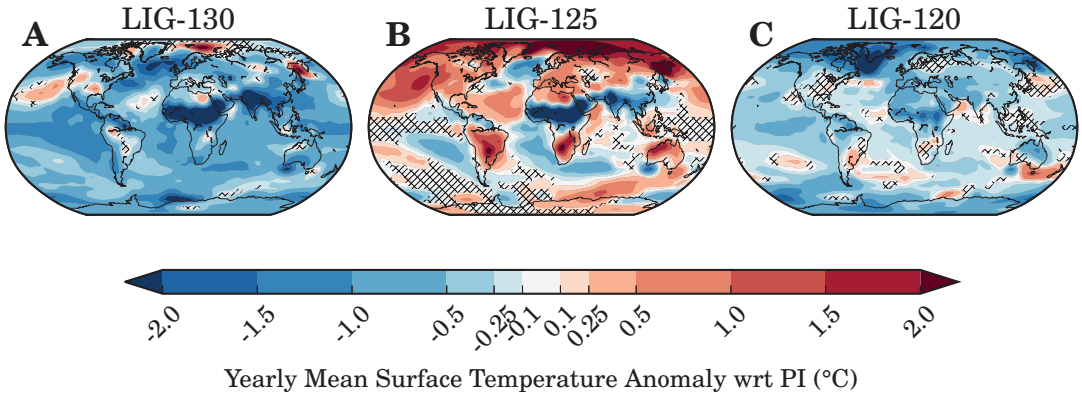

Figure 3.2: Changes in ST relative to PI for the three simulated timeslices during the LIG. These anomalies are constructed from 100 year means. While cooling is seen for much of LIG-130 (panel A), LIG-125 demonstrates pronounced warming, especially over the Northern Hemisphere. LIG-120 is slightly cooler than PI, due to relatively reduced GHG concentrations.

tropical ocean temperatures changes are insignificantly different from PI (based upon a 95% Students T-Test), with the exception of a slight cooling of up to −1.0 °C in the South Pacific, west of South America. A similar magnitude of cooling can be seen in the Agulhas region surround both the Atlantic and Indian ocean Basins around South Africa, while the southern North Atlantic displays anomalous warming of up to 1.0 °C. In the northern North Atlantic COSMOS-WISO simulates a cooling of up to −1.5 °C, whereas over the continents of Europe, Asia, and North America, as well as over the North Pacific, the model produces a warming with anomalous temperature responses between 0.5 °C to beyond 2.0 °C.

In LIG-120, shown in Figure 3.2-C; ST is generally cooler than PI in the climatological mean, similar as was demonstrated for the simulation of LIG-130. In particular, the northern high latitudes over Greenland are up to −2.0 °C cooler, whereas the response over the Arctic and the high latitudes over Asia is less pronounced, with temperature decreases of up to −1.0 °C. A slight cooling over the tropical latitudes, with temperature responses ranging from −0.1 °C to −0.5 °C. Unlike the other two time slices of the LIG,

the Sahara cooling is less pronounced (with changes of only −1.5 °C, whereas the other time slices exceeded −2.0 °C), and there is no localized warming in the Arctic.

3.2.2 Sea Ice Response

When examining the sea ice extent, shown in Figure 3.3, it can be seen that the maximum sea ice remains very close to the PI case for all three simulations. Given the changes in prescribed insolation during the three simulations, this is not surprising, as boreal winter incoming radiation anomalies are close to zero. However, a very strong changes in maximum sea ice extent is simulated, with drastically reduced sea ice cover for the early (-46% decrease by area) and mid (-56%) LIG simulations. The reduction is most severe in the mid LIG simulation, were sea ice cover is constricted solely to the central Arctic Ocean. The late LIG simulation maintains a similar maximum sea ice extent as in the PI case.

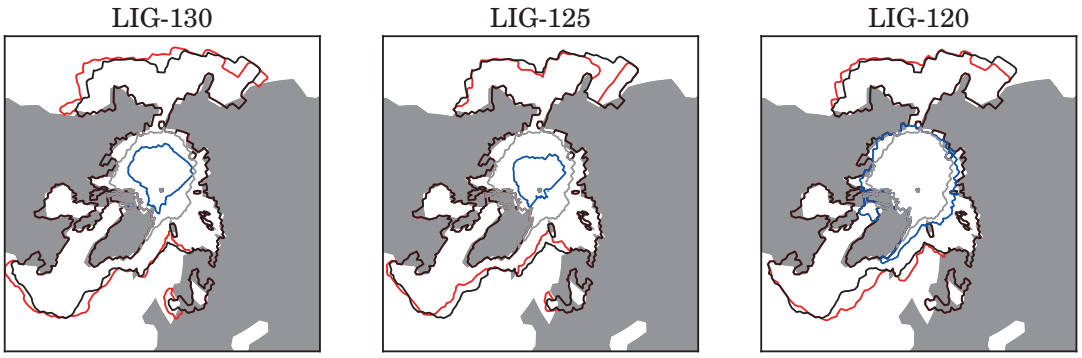

Figure 3.3: Changes in sea ice area coverage relative to PI for the three simulated timeslices during the LIG. The red (black) and blue (gray) contour lines demonstrate maximum and minimum yearly sea ice extent for each individual examined LIG (PI control) simulation.

3.2.3 Precipitation Changes

Next, changes to the amount of precipitation throughout the LIG are examined. During LIG-130, shown in Figure 3.4-A, a mean climatology is simulated that is in general wetter than the PI, particularly over the equatorial Atlantic, Africa, and the Indian Ocean and Indian Subcontinent. There, precipitation amounts increase by up to 50 mm month^{-1}. A drying occurs with a similar magnitude over Indonesia and the equatorial Pacific. A very slight drying signal is simulated over South America, with values up to -20 mm month^{-1} less than in the PI case, and a slight drying is also simulated along the Gulf Stream, Europe, and North Atlantic, with values between -2.5 mm month^{-1} and -10 mm month^{-1} less than in the PI simulation. Also, an increase in precipitation over southern part of the North Pacific is simulated, with anomalous precipitation values of up to 20 mm month^{-1}.

These anomalous precipitation patterns are largely repeated in the LIG-125 simulation (Figure 3.4-B), with an increase in precipitation over the equatorial Atlantic, the Sahara, and the Indian Ocean, where rainfall values increase by up to 50 mm month^{-1}. Drying again occurs just south of the equatorial Pacific, over South America, and over South Africa, with anomalous values of up to -30 mm month^{-1}. A drying signal over Indonesia is also simulated, with up locally up to 50 mm month^{-1} less rainfall than in the PI case. Contrary to the LIG-130 simulation, the increase in precipitation over the Pacific is not confined to the ocean basin, but also extends to the western coast of North America. Finally, a slight increase in rainfall over Europe and Asia can be seen, although this increase is only very slight, with anomalous precipitation values of only up to 10 mm month^{-1} relative to the PI simulation.

Finally, during the LIG-120 simulation (Figure 3.4-C), only minimal changes relative to the PI simulation can be seen. The large scale increase in precipitation over the Atlantic, Sahara, and Indian subcontinent is either weaker or absent, and a slight drying throughout the North Atlantic and equatorial Pacific is simulated, with values of

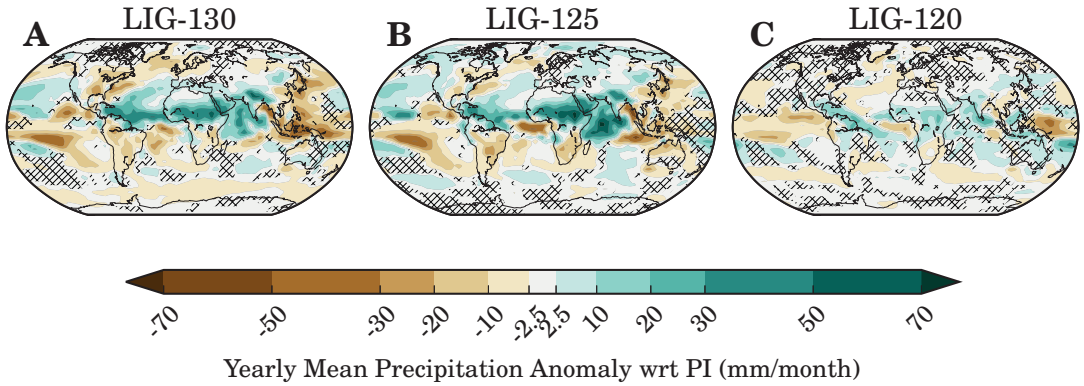

Figure 3.4: Changes in precipitation relative to PI for the three simulated timeslices during the LIG

$-20\,\mathrm{mm\,month^{-1}}$ less precipitation than in the PI simulation. A majority of the precipitation patterns that are simulated do not vary significantly compared to the control case, based upon a 95% Student T-Test.

3.3 Isotopic Representation of Mean LIG Climate

Next, the isotopic signatures produced by these physical responses is examined. First, the isotopic $\delta^{18}O$ of precipitation is presented (denoted as $\delta^{18}O_P$), followed by the signature of $\delta^{18}O$ in surface sea water ($\delta^{18}O_{sw}$). Finally, a cross section of the $\delta^{18}O_{sw}$ in the Atlantic basin is shown.

3.3.1 Isotopic Signal in Precipitation

Examining the LIG-130 simulation of the yearly mean isotopic signature in precipitation, a large-scale $\delta^{18}O_P$ depletion of up $-2.5\,‰$ over Saharan North Africa can be found, as shown in Figure 3.5-A. Furthermore, the simulation reveals a $\delta^{18}O_P$ depletion with values between $-0.5\,‰$ and $-1.5\,‰$ over the Caribbean and North Atlantic, and this

depletion signal extends over continental Europe and much of Asia. In the equatorial Pacific, the simulation shows a slight $\delta^{18}O_P$ enrichment, with values between 0.5‰ and 1.5‰ above the PI values, and this signal extends over Australia and Indonesia. Over Greenland, a slight $\delta^{18}O_P$ enrichment of 1.0‰ in the north and a slight depletion of −0.5‰ is simulated.

For the LIG-125 simulation (Figure 3.5-B), the changes are similar to LIG-130. A strong $\delta^{18}O_P$ depletion over Africa and the northern Indian Ocean is simulated, with values −1.5‰ to −2.5‰ lower than in the PI case. This depletion pattern extends over North Atlantic and Europe, with values that are between −0.1‰ and −0.5‰ lower than PI. The Arctic Ocean is largely enriched in $\delta^{18}O_P$, with 1.5‰ to 2.5‰ higher than PI. The precipitation over the Greenland Ice Sheet (GrIS) has a uniform signal, and is enriched by between 0.5‰ and 2.0‰.

During the late LIG (Figure 3.5-C), a $\delta^{18}O_P$ depletion over Greenland, with values −1.0‰ to −1.5‰ lower than in the PI can be seen, a feature not seen in the other LIG time slices. Over the Atlantic, precipitation is also enriched in $\delta^{18}O_P$ rather than depleted, although this enrichment is only slight, with changes between 0.0‰ and 0.5‰ higher than the PI values. A slight $\delta^{18}O_P$ depletion in precipitation over Northern Africa is also simulated, yet it is not as strong as in the LIG-130 and LIG-125 simulations. The $\delta^{18}O_P$ enrichment feature seen over the Pacific is also seen in this time slice.

3.3.2 Isotopic Signature of the Surface Ocean

Next, the isotopic signal in the surface ocean waters is shown, results which are presented in Figure 3.6. During LIG-130, a pronounced dipole response in the North Atlantic can be seen, with $\delta^{18}O_{sw}$ depletion in the isotopic signature by up to −0.6‰ in the Northern Atlantic, and a slight $\delta^{18}O_{sw}$ enrichment around the tropical Atlantic, with values enriched by 0.2‰ and up to 0.4‰ in the South Atlantic. The Pacific Ocean is much more

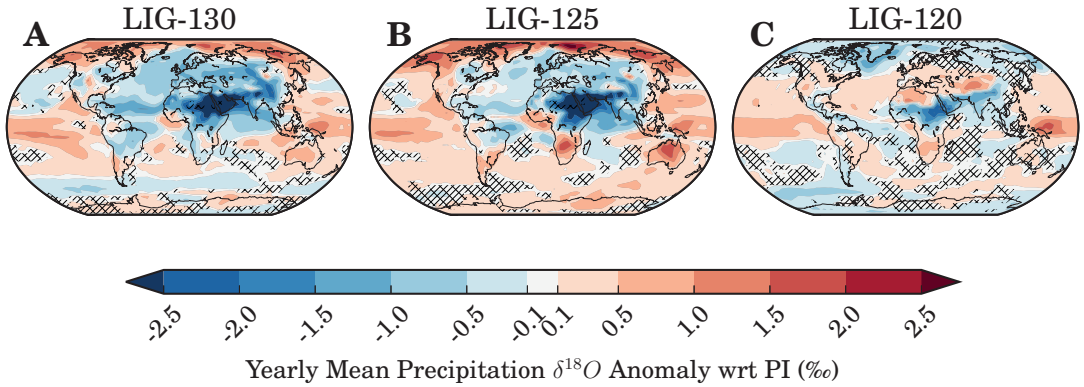

Figure 3.5: Changes in the isotopic signature of precipitation $\delta^{18}O_P$ relative to PI for the three simulated timeslices during the LIG

enriched than the Atlantic, with values of 0.4 ‰. The Arctic Ocean shows the strongest $\delta^{18}O_{sw}$ enrichment, with values exceeding 0.8 ‰.

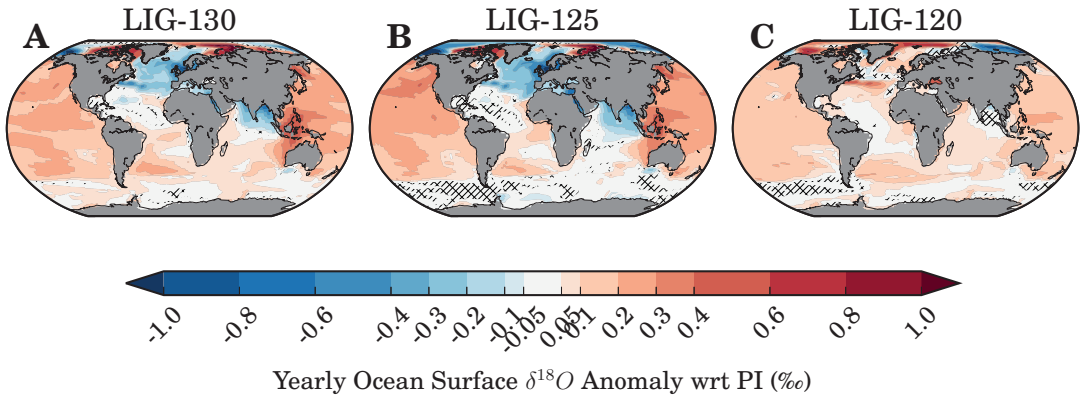

Figure 3.6: Changes in $\delta^{18}O_{sw}$ relative to PI for the three simulated timeslices during the LIG

During LIG-125 (Figure 3.6-B), the patterns remain very similar to LIG-130, although the Arctic is slightly less enriched in $\delta^{18}O_{sw}$ and even demonstrates localized depletion with values of -0.8 ‰ prevailing around the western Arctic basin, with slight protrusions of this signal into the North Pacific.

In the simulation for LIG-120 (Figure 3.6-C), there is a weakening of the isotopic changes, with the anomalies approaching PI values. There are still anomalous $\delta^{18}O_{sw}$ depletions in the eastern Arctic Ocean, with values demonstration depletion of $-1.0\,‰$ or more relative to the PI.

3.3.3 Isotopic Signature of Water Masses in the Atlantic Basin

Next, the response of the modeled isotope values within the ocean are examined, in order to see if there are any interesting signatures that may not appear at the surface. To do so, the δ^{18}O signal of the Atlantic Basin as a zonal mean is investigated. During LIG-130, surface depletion is seen in the North Atlantic, which extends down into the ocean's depth, with water masses with depleted $\delta^{18}O_{sw}$ signatures of between $-0.45\,‰$ at the surface, to $-0.20\,‰$ at a depth of between 2000 m to 3000 m. This same magnitude of depletion is mirrored in an enrichment at the equatorial latitudes, with slightly weaker enrichment simulated in the southern high latitudes. These results are shown in Figure 3.7-A.

During LIG-125 (Figure 3.7-B), the results are very similar to those of LIG-130. The enrichment that is simulated in the equatorial water masses of the Atlantic Ocean are slightly smaller than in LIG-130, and the depletion of the North Atlantic is still present during this timeslice.

During LIG-120 (Figure 3.7-C), the signature of the Atlantic Basin is slightly different. The North Atlantic depletion seen in LIG-130 and LIG-125 is much weaker, with values of $\delta^{18}O_{sw}$ only between $0.00\,‰$ and $-0.15\,‰$ more depleted than in the PI. The enrichment found in the equatorial latitudes is much stronger, with values of up to $0.30\,‰$ more enriched in $\delta^{18}O_{sw}$ than in the PI.

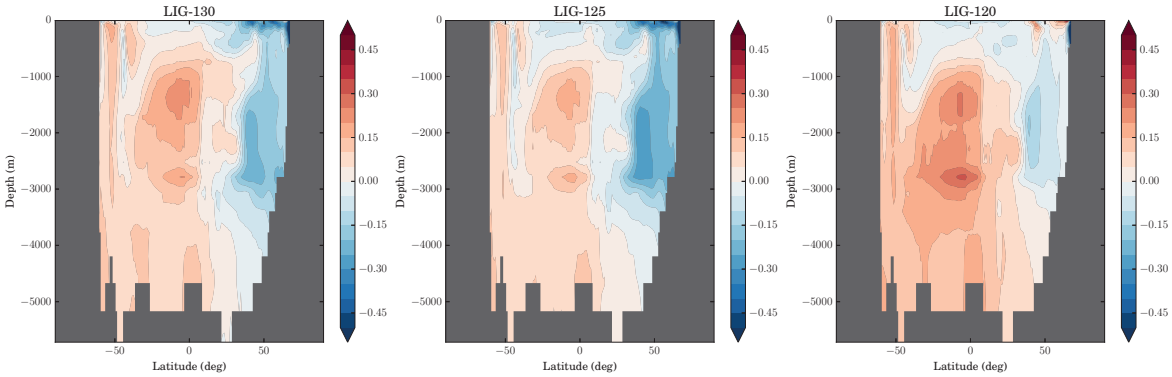

Figure 3.7: Changes in the $\delta^{18}O_{sw}$ signature of water masses in the Atlantic basin relative to PI for the three simulated timeslices during the LIG

3.4 Seasonal Responses

Next, an analysis is presented to see if the responses in ST, precipitation, and isotopic signature of precipitation to LIG forcing are subject to any seasonal changes. To accomplish this, changes in boreal summer (winter) for each simulated time slice during the LIG with respect to the simulation of PI summer (winter) are examine. The standard meteorological definitions of boreal summer and boreal winter (hereafter referred to simply as summer and winter) are used, averaging over June, July and August to create a representative summer mean, and over December, January, and February to construct the winter mean.

3.4.1 Seasonal Changes in Surface Temperature

Examining the seasonal changes in surface temperature, it is found that summers during LIG-130 (Figure 3.8-A) were in general warmer over the Northern Hemisphere, with temperature anomalies ranging from 1.0 °C to beyond 2.0 °C, with the exception of a small cooling area in the North Atlantic, where summers were between −0.5 °C and −1.5 °C cooler than during the PI. Over the Southern Hemisphere, a clear land-sea contrast in the summer response can be seen. Over the oceans, the LIG-130 summers were between

−0.5 °C and −1.5 °C cooler than in the PI, with the exception of the northern Indian Ocean and a slight warming in the mid South Pacific, where the simulation shows a slight temperature increase of between 0.25 °C and 0.5 °C. Over land, temperature increases range between 0.5 °C and 1.5 °C, with the exception of the Sahel region and the Indian subcontinent, where a cooling of between −3.0 °C and −4.0 °C is simulated.

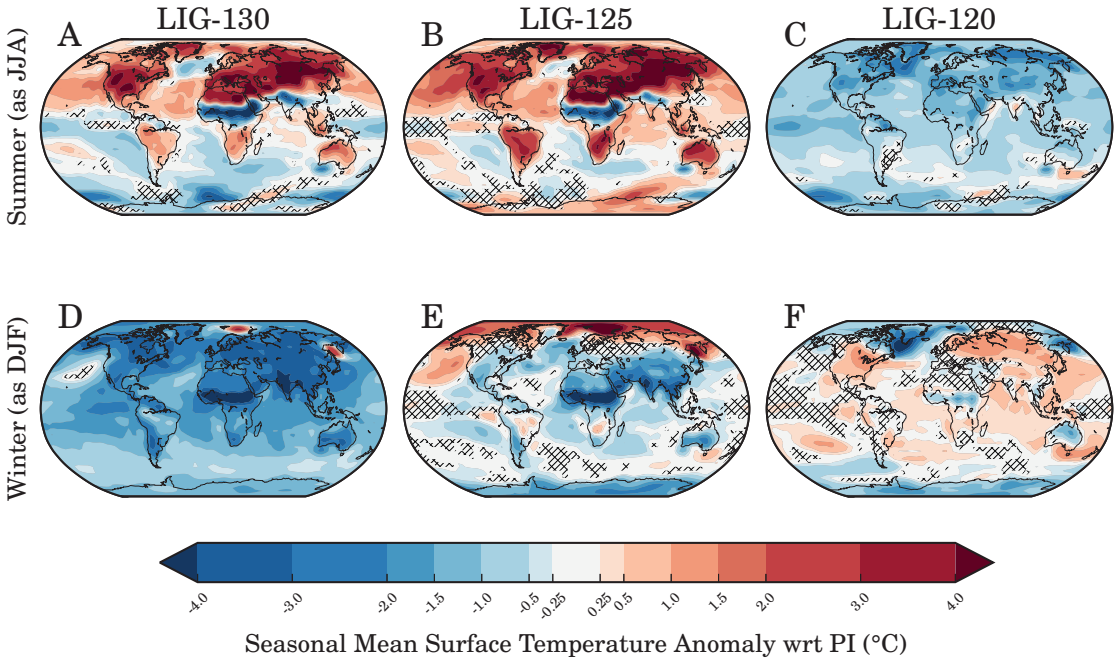

Figure 3.8: Seasonal changes in ST relative to PI for the three simulated timeslices during the LIG

During LIG-125 (Figure 3.8-B), a very similar response as during LIG-130 can be seen, yet the magnitudes are overall stronger. Over the Northern Hemisphere, temperature increases are above 2.0 °C, again with the exception of the small cooling area in the North Atlantic, which is smaller in extent than during LIG-130, and only cools by up to −0.5 °C. The land-sea contrast seen over the Southern Hemisphere is not as pronounced as during LIG-130, with considerably more warming in the Indian Ocean of up to 1.5 °C,

and a greater extent of the warming area in the mid South Pacific. The cooling feature seen over the Sahel is also present, yet the Indian subcontinent displays a heterogeneous temperature response during this timeslice, with the cooling restricted to the Himalaya region.

During LIG-120 (Figure 3.8-C), the summers are nearly uniformly cooler than the PI, with cooling signals ranging from $-0.25\,^{\circ}\mathrm{C}$ to $-1.5\,^{\circ}\mathrm{C}$. The cooling appears to be stronger over the northern high latitudes, in particular over the GrIS and surrounding ocean, with overall less cooling in the southern hemisphere mid latitudes. A few areas of localized warming are simulated, particular in the Pacific Ocean just south of Australia, where temperatures are between $0.5\,^{\circ}\mathrm{C}$ and $1.0\,^{\circ}\mathrm{C}$ warmer than in the PI.

During winters, the responses are rather different. LIG-130 displays globally colder winters than PI, as shown in Figure 3.8-D, with anomalous temperatures ranging from $-1.0\,^{\circ}\mathrm{C}$ to beyond $-2.0\,^{\circ}\mathrm{C}$. Two exceptions can be seen, on in the Arctic Ocean, where the simulation produces a localized area of severe warming with temperatures above $2.0\,^{\circ}\mathrm{C}$ warmer than in PI, and also in the Sea of Okhotsk, where a warming with similar magnitude is produced.

During LIG-125, the model simulates cooler winters than in PI for many regions, with temperature anomalies ranging between $-0.25\,^{\circ}\mathrm{C}$ and over $-2.0\,^{\circ}\mathrm{C}$. These results are shown in Figure 3.8-E. The cooling signal is strongest over the Sahel region of Africa as well as over the Indian subcontinent, and is generally stronger over the continents than over the ocean. An exception to this cooling pattern is the Arctic Ocean, which is $2.0\,^{\circ}\mathrm{C}$ warmer than in the PI winter, as well as the eastern North Pacific, where temperatures are up to $1.5\,^{\circ}\mathrm{C}$ warmer than in PI.

During LIG-120 (Figure 3.8-F), the winters are generally milder, with a majority of the Earth experiencing temperatures that are between $0.25\,^{\circ}\mathrm{C}$ and $1.0\,^{\circ}\mathrm{C}$ warmer than in the PI. Both northern and southern high latitudes are cooler than PI winters, with

temperature anomalies ranging from −0.5 °C to −1.5 °C in the south to beyond −2.0 °C in the north. Additionally, the Sahel region is slightly cooler in LIG-120 winters than in the PI, with anomalous temperatures of −0.5 °C. Australia is also slightly cooler in LIG-120 winters, with values −1.0 °C to −1.5 °C cooler than in the PI.

3.4.2 Seasonal Changes in Precipitation

During LIG-130 summers (Figure 3.9-A), COSMOS-WISO simulates a strong intensification of precipitation over the equatorial latitudes in the Atlantic Ocean, the African Continent, and the Indian Ocean, with values of over 70 mm month^{-1} more than during the PI simulation. Just south of this region in the Atlantic, the simulation generates a reduction in precipitation by a similar magnitude. The equatorial latitudes over the Pacific also get drier, with values between −30 mm month^{-1} and −50 mm month^{-1} less precipitation than in the PI simulation. A majority of the continental landmass in the northern hemisphere come slightly drier, with values between −2.5 mm month^{-1} and −10 mm month^{-1} less rain than in the PI, although there are some exceptions, particularly in the high latitudes, where there is a very slight increase in precipitation.

In the LIG-125 simulation (Figure 3.9-B), this pattern is largely repeated, with an increase in summer precipitation of more than 70 mm month^{-1} over the equatorial latitudes of the Atlantic, African and Indian continents, and a corresponding decrease in precipitation of similar magnitude over the Philippines. A smaller decrease on the order of −20 mm month^{-1} to −30 mm month^{-1} in precipitation is simulated over the equatorial Pacific. As in the LIG-130 simulation, COSMOS-WISO produces a slight increase in precipitation over the northern high latitudes.

During LIG-120 (Figure 3.9-C), the changes in summer precipitation are much smaller than in the other two LIG simulations. A slight increase in precipitation over the equatorial Atlantic is simulated, with values of up to 20 mm month^{-1} higher than in

the PI. Unlike the other two LIG simulations, this increase in precipitation is not nearly as pronounced over Africa and India, where a very slight increase is still simulated, yet values here are only up to 10 mm month^{-1} higher than in the PI. Similarly, the decrease in precipitation over the Pacific is reduced compared to the other two timeslices, and a majority of the mid and high latitudes do not undergo significant changes to the hydrological cycle, as demonstrated by a 95% t-test.

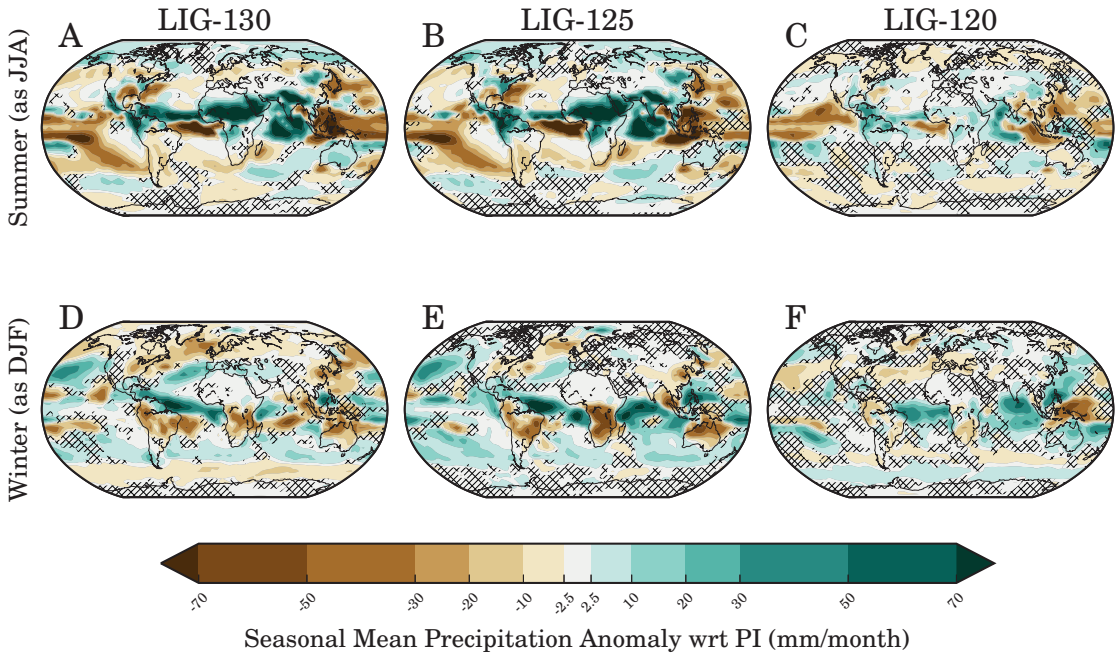

Figure 3.9: Seasonal changes in precipitation relative to PI for the three simulated timeslices during the LIG

In winters, LIG-130 (Figure 3.9-D) demonstrates an increase in precipitation over the tropical Atlantic, with values up to 70 mm month^{-1} higher than in the PI. The Sahel region does not undergo a significant change in precipitation, while the southern part of the African continent gets slightly drier, with values between -30 mm month^{-1} and -50 mm month^{-1} less precipitation than in the PI. The Indian subcontinent, like the

Sahel region, also does not undergo a significant change in the amount of precipitation. Over the oceans, COSMOS-WISO simulates a slight decrease in precipitation amount over the North Atlantic, with values between $-20\,\mathrm{mm\,month^{-1}}$ and $-30\,\mathrm{mm\,month^{-1}}$ less precipitation than in PI, whereas the North Pacific undergoes a heterogeneous response, with an increase in precipitation over the eastern side and a decrease in precipitation over the western side. The Southern Ocean experiences a slight decrease in precipitation, with values of up to $-10\,\mathrm{mm\,month^{-1}}$ less precipitation than in the PI.

During LIG-125 (Figure 3.9-E), these patterns are generally repeated and partly intensified. The model once again simulates a strong increase in precipitation over the tropical Atlantic, and a strong decrease in precipitation over Africa, with a corresponding increase in precipitation over the Indian Ocean. Unlike LIG-130, the decrease in precipitation over the North Atlantic is not as pronounced, nor is the decrease in precipitation over the western part of the North Pacific.

The response during LIG-120 winters is not as strong as in the other two timeslices, as can be seen in Figure 3.9-F. A majority of the Earth does not undergo a significant change in the hydrological cycle, yet the increase of precipitation over the tropical Atlantic is still simulated, with changes of up to $30\,\mathrm{mm\,month^{-1}}$.

3.4.3 Seasonal Response of Isotopic Signatures of Precipitation

During LIG-130 summers, shown in Figure 3.10-A, the isotopic composition of precipitation is depleted in $\delta^{18}O_P$ by between $-2.0\,‰$ and $-2.5\,‰$ over the Sahel region and Indian subcontinent and surrounding ocean. Additionally, the tropical Atlantic is depleted in $\delta^{18}O_P$ by between $-0.5\,‰$ and $-1.5\,‰$. With the exception of a slight area of depletion in the North Atlantic of less than $-0.05\,‰$, the remainder of the globe is enriched in $\delta^{18}O_P$ by between $0.5\,‰$ and more than $2.5\,‰$. Some missing values are generated by the analysis, as a mask is applied to regions where little absolute precipitation occurs.

The criteria used here is to mask out grid cells where less than 0.05 mm month^{-1} of precipitation is simulated.

During LIG-125 (Figure 3.10-B), this pattern is generally repeated, although the depletion over the Caribbean is not as pronounced, with values only −0.5 ‰ below the PI value. Additionally, the area of slight depletion simulated in LIG-130 is absent in this time slice, and the enrichment signals are generally stronger. Over both the Greenland and Antarctic ice sheets, COSMOS-WISO simulates an enrichment of $\delta^{18}O_P$ by over 2.0 ‰ for Greenland and between 0.5 ‰ and 1.5 ‰ for Antarctica.

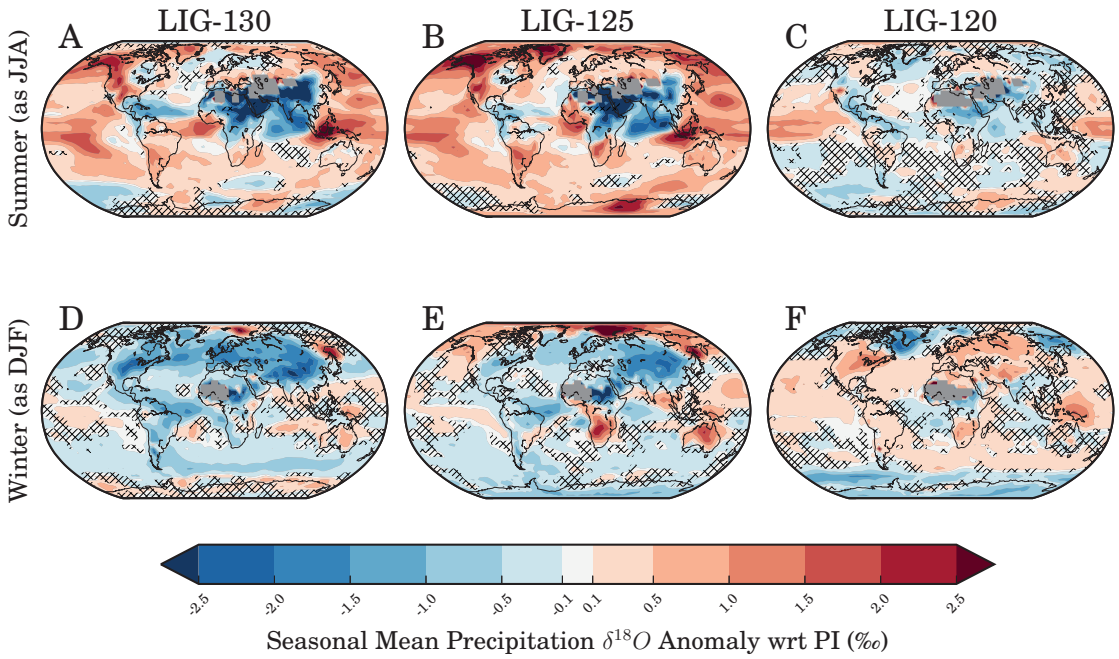

Figure 3.10: Seasonal changes in precipitation isotopic signature relative to PI for the three simulated timeslices during the LIG

In LIG-120 summers (Figure 3.10-C), a majority of the Earth does not experience a significant change in the isotopic signal in precipitation. There is an exception over the Sahel region in Africa, which undergoes a depletion in $\delta^{18}O_P$ by between −0.1 ‰

and −0.5 ‰, as well as over the equatorial Pacific, where a slight enrichment of $\delta^{18}O_P$ is simulated, with anomalous values between 0.1 ‰ and 1.0 ‰ above the PI values.

In winter, the isotopic signature of precipitation during LIG-130 (Figure 3.10-D) is in general depleted in $\delta^{18}O_P$ relative to the PI, with values typically −0.5 ‰ to −1.5 ‰ lower. These depletion patterns are strongest over the continents, with relatively weaker depletion taking place over the ocean. Additionally, some enrichment in $\delta^{18}O_P$ takes place over the equatorial Pacific, yet anomalous values here are rather small, with changes on the order of up to 0.5 ‰. It is also interesting to note that a majority of the precipitation over Antarctic continent does not change its isotopic signature significantly.

During LIG-125 winters (Figure 3.10-E), a more heterogeneous response in the isotopic signature of the precipitation can be seen. Over the North Atlantic and major parts of the Greenland Ice Sheet, the model simulate a depletion of $\delta^{18}O_P$ between −0.5 ‰ and −1.0 ‰. Precipitation over parts of the tropical Atlantic does not change its signature significantly, yet COSMOS-WISO simulates an overall depletion in $\delta^{18}O_P$ of between −0.1 ‰ and −1.0 ‰ over the Atlantic. An even stronger depletion is simulated over the Sahel region of Africa as well as over the Asian continent, where the signature of $\delta^{18}O_P$ in precipitation is between −1.0 ‰ and −2.0 ‰ lower than in the PI. Furthermore, the model simulates a depletion over the Southern Ocean, the South Pacific, and the Antarctic Continent, where values are typically −0.1 ‰ and −1.0 ‰ lower than in the PI. Some areas of enrichment are simulated, in particular over the Arctic Ocean, where an enrichment in $\delta^{18}O_P$ of between 1.5 ‰ and 2.5 ‰ can be seen, with the stronger signals occurring over the eastern Arctic.

Lastly, the changes in the isotopic signature of precipitation in LIG-120 winters are presented in Figure 3.10-F. Contrary to the LIG-130 and LIG-125 simulations, here, the $\delta^{18}O_P$ values are enriched by between 0.1 ‰ and 0.5 ‰ over the North Pacific, North and South Atlantic, European continent as well as over the Americas. COSMOS-WISO

simulates a slight depletion over tropical Atlantic of −0.5‰. Furthermore; a strong depletion over the GrIS is produced, with values typically between −1.5‰ and −2.0‰ lower than in the PI. This depletion is also seen in the precipitation over Antarctica, where the model simulates $\delta^{18}O_P$ values that are between −0.5‰ and −1.0‰ lower than in the PI.

3.5 Discussion

The next section is divided into several parts, first discussing changes in physical responses, possible reasons for these changes, and comparing these physical responses to other simulation attempts of the LIG where possible. Following this, a discussion of the changes in isotopic changes is presented, and the section concludes by examining the stability of the isotopic/temperature relationship to understand the extent to which this relationship may be utilized as a paleothermometer.

3.5.1 Changes in Physical Responses: Surface Temperature

An examination of the solar insolation forcings of LIG-130 and LIG-125 initially shows quite similar responses, with an increase in solar insolation in boreal summer, and a decrease in solar insolation in the winter. Despite this, climatologically averaged temperature responses in these two time slices varies quite drastically, with nearly uniform globally cooler than PI temperatures simulated for LIG-130, whereas LIG-125 shows a more diverse response. Some similarity between the two simulations still exists, the areas of strongest warming in LIG-125 (the North Pacific Ocean, the Caribbean region of the Atlantic Ocean, the central region of the Arctic Ocean, the Sea of Okhotsk, and parts of the amazon forest region in South America), are the same regions of LIG-130 that demonstrate slight warming relative to the PI simulation. Similarly, the regions of greatest cooling in LIG-125 (the Sahel and Sahara regions of Africa, the Indian

subcontinent, the North Atlantic, as well as the equatorial Pacific and a small region southwest of Australia) are also regions of strongest cooling in LIG-130. While the magnitude of the changes in two simulations relative to PI is very different, the spatial distribution of the anomalous responses is similar.

A further break down of the analysis into seasonal changes (as presented in Section 3.4) shows that LIG-130 and LIG-125 are even more similar. Both simulations produce large-scale boreal summer warming over the Northern Hemisphere continents, with cooling in the North Atlantic, and the Sahel region as well as over the Indian subcontinent. The winter responses of the two time slices also show similar distributions (strongest cooling over the Sahel region, Indian subcontinent, slight warming in the North Pacific, and strong warming in the central Arctic and Sea of Okhotsk), yet with different magnitudes.

While the similarities in the distribution of the responses – both seasonally and in the yearly means – might be connected to the similarities in solar insolation (shown in Figure 3.1, and broken down into individual orbital parameters in Table 3.1); the magnitudes are strikingly different. Due to the similarities in the overall insolation, both internal feedbacks and other forcing mechanisms within the climate system could be responsible for these changes in surface temperature. In particular, a strong difference in the chosen GHG forcing may be responsible for the difference in the magnitude of the responses. GHG values between the two simulations varies greatly, and is much lower in LIG-130 (relative to LIG-125: CO_2: -19 ppm, CH_4: -126 ppb NO_2: -25 ppb), and as LIG-130 has GHG values that are considerably lower than the PI simulation, it is not surprising that a global cooling response can be seen.

Lastly, the LIG-120 response is examined in a bit more detail. From the insolation response (Figure 3.1), and the GHG concentrations (Table 3.1), one would expect general cooling, as the GHG concentrations are lower relative to the PI simulation, and

the General Circulation Model (GCM) produces this response; shown in Figure 3.2-C. Seasonally, the insolation would suggest a more heterogeneous response. COSMOS-WISO simulates a globally cooler summer, which is a result of the slightly reduced GHG concentrations as well as a lagged response from the cooler boreal spring, a season in which the insolation is strongly reduced relative to PI. The winter response is varied, producing high latitude cooling over the Arctic and the Greenland Ice Sheet. This may be a result of minimally changed insolation at high latitudes, as well as a sea ice coverage that is very similar to that in the PI. An interesting land-sea contrast is simulated over Russia, however a close examination of the insolation also shows here that incoming radiation values are slightly increased, with values of between $2.5\,\mathrm{W\,m^{-2}}$ and $10\,\mathrm{W\,m^{-2}}$ more energy than in PI. The temperature response to this small positive forcing anomaly may be further enhanced with a lag from the strong warming in late autumn.

3.5.2 Comparing Surface Temperature Responses to other Simulation Efforts

If these results are contrasted to other studies examining the LIG climate, COSMOS-WISO produces some interesting differences when compared to other paleoclimate simulations. One example would be the simulations performed by Otto-Bliesner et al. [2013], who used CCSM3 to generate similar time slices. A striking difference between the COSMOS-WISO realizations of both the LIG-130 and LIG-125 climates and the simulations of that study is a clear cooling signal in the North Atlantic, which is seasonally persistent. Otto-Bliesner et al. [2013] instead simulate a warming in this region, and argue that understanding sea ice is of crucial importance to interpreting modeled polar responses. A second study for comparison of the LIG ST response is presented in Lunt et al. [2013], who show a multi-model ensemble assessment of the LIG. Several models, such as the Hadley Centre model, which has a comparable model resolution

and complexity to the COSMOS-WISO set up also demonstrates a warming signal with a comparable magnitude to that presented by Otto-Bliesner et al. [2013]. However, the multi-model ensemble of all included models show no significant change in this region. A previous study by Pfeiffer and Lohmann [2015], which used the GCM COSMOS[2], also demonstrated a warming in the North Atlantic, however; these signals were in response to a modification of the GrIS orography, and Pfeiffer and Lohmann [2015] did not adapt the GHG values to the LIG as prescribed by PMIP. The differences between the COSMOS-WISO realizations of LIG climate states and those of the other groups mentioned above might stem from a number of reasons. For instance, Otto-Bliesner et al. [2013] utilized higher concentrations of GHG, and it has been well documented that different models react to climate forcings with various sensitivities in various model intercomparison projects (as summarized, e.g. by Knutti et al. [2010], Crucifix et al. [2012])

3.5.3 Changes in Physical Responses: Hydrology

Next the hydrological cycle is examined. Contrary to the strong temperature differences between the simulations, the precipitation responses (Sections 3.2.3 and 3.4.2) are more similar for LIG-130 and LIG-125, both in the climatology mean, and in the seasonal responses. LIG-120, which was different from the other two LIG simulations with respect to the temperature responses, is similar in the precipitation response, although the magnitudes are reduced.

One can attribute the changes seen in the global precipitation patterns as a result of the overall warmer climate characteristics LIG. Such an invigoration has also been demonstrated based upon simple physical mechanisms (as a consequence of the Clausius-Clapeyron relation, warmer air is able to hold more moisture, as summarized by Barron et al. [1989]). This type of response in the hydrology for warmer-than-present day climates

[2]COSMOS is identical to the model utilized in the analysis of this chapter, however, Pfeiffer and Lohmann [2015] did not include stable water isotopes in their study

(e.g. during the Pliocene) has been previously established for COSMOS by Stepanek and Lohmann [2012], and is also seen in other modeling studies [Haywood et al., 2013]. An invigoration of the hydrological cycle is also suggested to be a feature of warmer-than-present day future climate scenarios simulated in many Intergovernmental Panel on Climate Change (IPCC) projections [Wild et al., 2008, Intergovernmental Panel on Climate Change, 2014]

3.5.4 An Examination of the Isotopic Responses

Having described the changes in isotopic distribution in various times during the LIG (Section 3.3), an exploration of what causes these different distributions is now shown. This part is divided into several parts, describing first isotopic signals that can be primarily explained by changes in precipitation, and then showing signals that can be primarily explained by changes in temperature. Thereafter, the utility of the $\delta^{18}O_P$/T relationship as a tool to reconstruct temperature changes in the past is examined, and followed by a short discussion of potential drawbacks that may depend on the chosen forcing scheme and boundary conditions. The chapter is then concluded with an outlook and next steps.

3.5.4.1 Isotopic Signals Caused by Changes in Precipitation

During all of the LIG simulations, a strong anomalous depletion is simulated in $\delta^{18}O_P$ over the Sahara region. This can be attributed to the amount effect (described, e.g. in Lee and Fung [2008]), since the overall amount of precipitation increases in this region in all three LIG simulations. The same effect is seen over the equatorial Pacific as well as over southern Africa; here, COSMOS-WISO simulate overall less precipitation, and correspondingly, an enrichment of $\delta^{18}O_P$.

The connection between changes in precipitation and changes in the isotopic signa-

ture of precipitation can be examine seasonally as well. During LIG-130 and LIG-125, a particularly strong increase in precipitation over the equatorial latitudes is simulated. The same equatorial band over the Atlantic, Saharan Africa, and the Indian Subcontinent undergo a anomalous depletion of $\delta^{18}O_P$. Just south of this region of increased precipitation, the model simulates a drying, which is mirrored in enrichment. While the magnitudes of precipitation increase in LIG-120 are much smaller over this region, the same effect is still seen, with depletion in $\delta^{18}O_P$. In winters, the model simulates an increase in precipitation just south of the equator for LIG-130 and LIG-125, with corresponding depletion in the $\delta^{18}O_P$ signal. During LIG-120 winters, the changes in precipitation and in the isotopic signature of precipitation is not as strong as in the other two time slices, yet here COSMOS-WISO also simulates some areas of increased precipitation (in particular the South Atlantic, and Indian Ocean basin) and corresponding depletion in the $\delta^{18}O_P$ signature of precipitation.

Some previous work has been performed using atmosphere-only stable-water equipped models to investigate the LIG hydrological cycle. Herold and Lohmann [2009] describe changes in the isotopic composition of precipitation using the atmospheric model ECHAM4-WISO, discovering that changes are linked to the amount effect, as the LIG has a stronger hydrological cycle than PI. Additionally, they find some isotopic signatures that can be attributed to the continental effect, as overall moister air masses are transported further inland than in the PI. The results presented in this analysis would confirm these findings still hold true with the newer fully coupled model COSMOS-WISO.

3.5.4.2 Isotopic Signals linked to Changes in Surface Temperature

While the changes in the isotopic signature of precipitation in the equatorial and tropic latitudes can be attributed to changes in the amount of precipitation, changes in mid- to high-latitudinal regions may be stronger linked to changes in the surface temperature [Dansgaard, 1964, Rozanski et al., 1992], and it would be expected that a positive

relationship between changes in temperature and changes in $\delta^{18}O_P$ can be found. For example, the North Atlantic undergoes a fairly significant cooling of between $-0.5\,^{\circ}$C to $-1.5\,^{\circ}$C during LIG-130 and LIG-125. The same region undergoes slight depletion of δ18O in precipitation. Another example can be found during LIG-120, where COSMOS-WISO simulates a yearly average cooling over the Arctic Ocean and the Greenland Ice Sheet, as well as over the Antarctic Ice Sheet (Figure 2-C), and correspondingly, a slight depletion in $\delta^{18}O_P$ (Figure 3.5-C)

Some regions appear to have a strong seasonal dependence. Over North America, Greenland, and Siberia, the yearly averaged signals for surface temperature and isotopic composition of precipitation do not seem to match. This is especially true during LIG-130, where a cooling is simulated, yet the isotopic composition of precipitation is still enriched in $\delta^{18}O$. If instead the seasonal responses are examined, it can be found that seasonal warming is accompanied by seasonal enrichment and vice versa, both in summers and winters of LIG-130 and LIG-125.

There appear to also be some seasonal dependencies in LIG-120. For example, the precipitation over North America is slightly enriched in δ18O, despite the fact that slight cooling is simulated in the yearly average signal. If the seasonal responses are examined instead, the patterns show the same response, with a warming and corresponding enrichment in $\delta^{18}O_P$. It can therefore be concluded that those changes in $\delta^{18}O_P$ caused by variations in surface temperature may indeed have a strong seasonal dependence.

3.5.4.3 Stability of the $\delta^{18}O_P$/T Relationship

The final investigation in this first study seeks to examine if the relationship between the $\delta^{18}O_P$ and temperature remains stable, as it is this relationship that allows the stable water isotope proxy to be useful as a paleothermometer. Classically, paleoclimatologists utilize a relationship between $\delta^{18}O_P$/T, which was initially constructed by Dansgaard [1964] and presented in the introduction (Equation (1.2)).

To test if the model is able to reproduce this empirical global relationship, mean climatologies from the three LIG simulations and constructed, and these are filtered to only show temperatures where the average temperature is below 20 °C. This selection is to ensure that only locations where the temperature effect is dominant are used in the analysis. Next, the slope of the regression line between $\delta^{18}O$ and T is analyzed to see if it remains stable throughout the LIG.

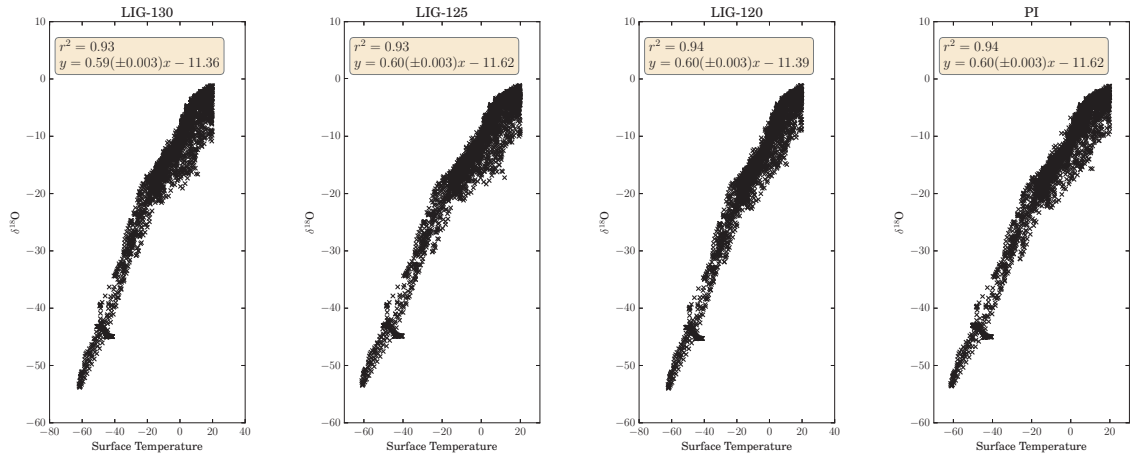

Figure 3.11: The spatial relationship between $\delta^{18}O_P$ and temperature for all three simulated LIG time periods as well as the PI simulation. Only those points are selected where the climatologically averaged annual mean surface temperature is below 20 °C

During the control simulation of the PI, a spatial $\delta^{18}O$/T regression slope of 0.600 ± 0.003 ‰ °C^{-1} is found, whereas a slope of 0.590 ± 0.003 ‰ °C^{-1}, 0.600 ± 0.003 ‰ °C^{-1}, and 0.600 ± 0.003 ‰ °C^{-1} is found for the simulations of LIG-130, LIG-125, and LIG-120 respectively (Figure 3.11). One can therefore conclude that the spatial relationship between temperature and $\delta^{18}O$ does not change significantly in the climatological mean states of the LIG.

Despite the stability of this relationship throughout the simulated LIG, the slopes of the $\delta^{18}O$/T are still approximately 0.09 ‰ °C^{-1} lower than the observed value of Dansgaard [1964]. However, ECHAM5-WISO (as well as other models, e.g. CAM2 [Lee et al., 2007], or LMDZ4 [Risi et al., 2010]) simulate a spatial gradient that is often somewhat too small. Werner et al. [2011] have demonstrated that improving the model's

resolution can partially rectify this. However, increasing the model resolution comes with higher computational costs, and as such, a compromise must be made between the speed required to perform paleoclimate studies and the increased detail of a high resolution model.

Next, it should be determined if this spatial relationship is consistent on the temporal scale investigated in this study. The temporal gradient can be defined as:

$$m = \frac{\delta^{18}O_{\mathrm{LIG}} - \delta^{18}O_{\mathrm{PI}}}{T_{\mathrm{LIG}} - T_{\mathrm{PI}}}$$

This would give an indication of how well a LIG-PI change measured in $\delta^{18}O$ translates into a corresponding change in temperature, as is done when paleoclimate proxies are used to reconstruct LIG temperature changes. To achieve this the temporal $\delta^{18}O$/T relationship between the PI and the three LIG simulations is examined for every grid cell where the following conditions are met:

1. Mean annual temperature of the grid cell is lower than 20 °C for both PI and LIG.
2. The model simulates a significant change in both $\delta^{18}O_P$ as well as temperature between the PI and the LIG climate, with significance determined by a t-test considering a 95% significance interval.
3. Absolute difference between the examined LIG time slice and the PI simulation is at least above a minimum temperature change threshold of $\Delta T \geq 0.5\,^{\circ}\mathrm{C}$

These three criteria are selected in hopes of isolating the temperature effect where fractionation between different phases of water is dominantly controlled by temperature.

The simulated temporal $\delta^{18}O$/T relationships are shown as a frequency distribution in Figure 3.12 (blue portions of the histogram), and the corresponding global maps are shown in the Figure 3.13. Upon initial examination, it appears as if the well-known positive $\delta^{18}O$/T relationship [Dansgaard, 1964] is not only variable in time, but also

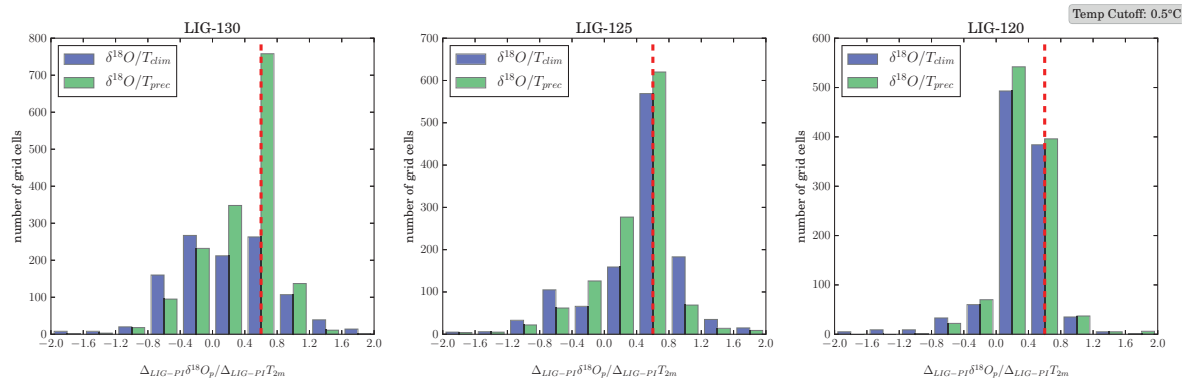

Figure 3.12: Histogram of the change in the δ^{18}O/T relationship for all grid points where the following three conditions are met: i) average mean annual temperature is lower than 20 $°C$. ii) absolute change in temperature between the LIG time slice and the PI control simulation is at least 0:5 $°C$ iii) the change in both temperature and isotopic composition is significant based upon a 95% confidence interval. Blue bars indicate the number of grid cells for each δ^{18}O/T quotient for climatology mean temperatures, whereas green bars indicate the number of grid cells where we utilize precipitation-weighted temperatures rather than climatologically averaged ones.

can have a negative slope rather than a positive one at certain locations for the LIG-PI climate changes.

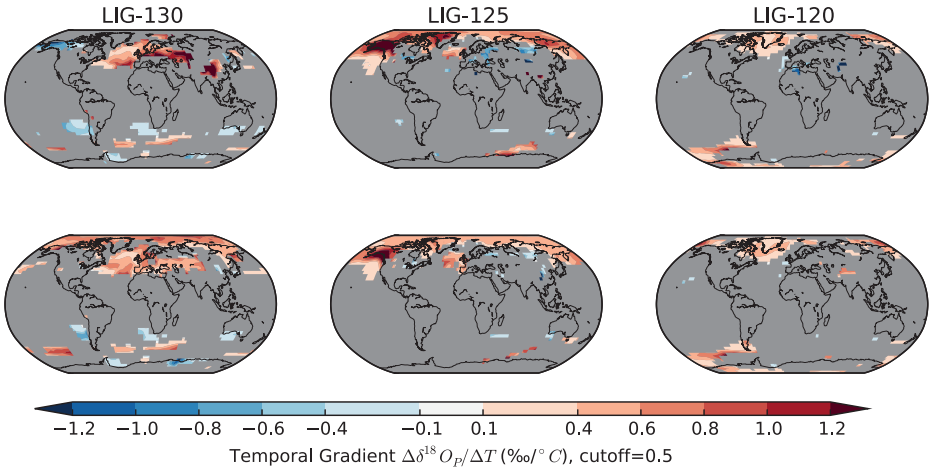

Figure 3.13: Spatial distribution of the $\Delta\delta^{18}O/\Delta T$ quotient. Top panels show the quotient with climatology averaged temperature changes, whereas the bottom panels show the quotient with precipitation weighted averages.

From the fundamental principles of water isotope fractionation physics, a negative $\delta^{18}O$/T-relationship is implausible. Thus, these results indicate a "recorder problem", as the use of $\delta^{18}O_P$ as a temperature proxy is always critically dependent on the precipitation amount at the recording site, too. $\delta^{18}O$ signals in precipitation can only be recorded for times when precipitation occurs. Prior analysis (Section 3.4.3) also suggests that the isotopic response may indeed have a seasonal dependence, and it is next assessed if this "recorder bias" persists when constructing a $\delta^{18}O$/T-relationship that takes into account such seasonal precipitation dependence. To accomplish this, precipitation-weighted temperature anomalies are generated, and the analysis is performed once again. Precipitation weighting is done by using both monthly temperatures as well as precipitation amounts of 100 simulation years to calculated the long-time mean annual precipitation-weighted temperature T_p.

It is found that the $\delta^{18}O_P/T_p$ ratio changes, with a greater number of quotient values (shown in the green portions of the histogram in Figure 3.12) closer to the modern spatial $\delta^{18}O$/T-relationship. Despite this, a large portion of the grid cells still produce a negative quotient. A further test is done to see if the magnitude of the temperature change plays a deciding role in the utility of the $\delta^{18}O$ paleothermometer. When the cutoff is increased to $\Delta T \geq 1.5\,^{\circ}\mathrm{C}$, many of the negative quotients are removed. These results are shown in Figures 3.14 and 3.15.

These findings suggest that great care must be taken when interpreting reconstructed LIG temperatures from $\delta^{18}O$ anomalies. The $\delta^{18}O$/T relationship found in these studies of the LIG is not only spatially variable, but also appears to have a substantial bias resulting from the season in which the recorder system received most input, as already has been found for Greenland ice core data by previous studies [e.g. Krinner and Werner, 2003]. Furthermore, the assumption of a positive temporal $\delta^{18}O_P/T$ relationship appears to only be valid if the magnitude of past temperature change is rather large. The results

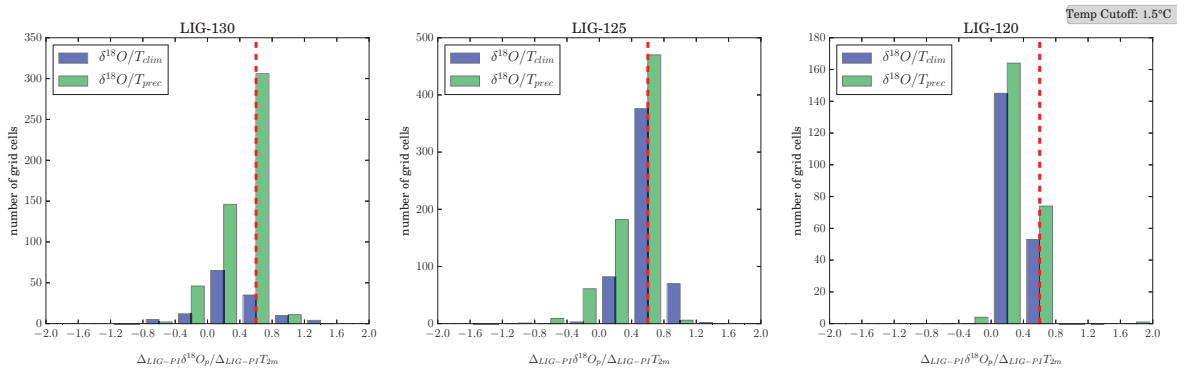

Figure 3.14: As before in Figure 3.12, but with a cutoff value of 1.5°C.

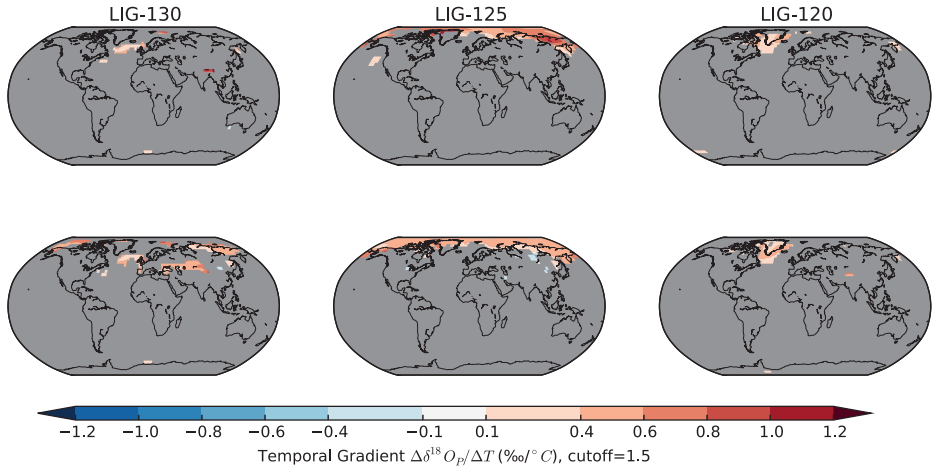

Figure 3.15: As Figure 3.13, but with a 1.5°C cutoff.

indicate that there might exist some critical threshold temperature change ΔT at which the $\delta^{18}O_P/T$ relationship is useful for reconstructing LIG paleotemperatures.

These considerations might not be specific to the LIG; a similar study of the Last Glacial Maximum (LGM) $\delta^{18}O_P/T$ changes performed by Werner et al. [2016] found complications in the $\delta^{18}O$ paleothermometer as well, although since the magnitude of the temperature changes between LGM and PI climate is generally large, far fewer negative slopes were simulated, and the slope discrepancy of $\delta^{18}O_P/T$ is not nearly as large as in the LIG case.

Nevertheless, these results of the LIG climate suggest that the classically applied paleothermometer is not only slightly influenced, as would be the case with a varying positive slope, but would in fact deliver results which do not match the actual simulated changes in temperature for a quite large portion of the grid cells. Therefore, the interpretation of proxy $\delta^{18}O$ might be reconciled over many regions in terms of temperature changes during interglacials.

The results shown in this chapter also support the findings of previous studies with atmosphere-only models, which have mainly focused on a model-data comparison for δ^{18}O signals in polar precipitation under present and warmer climate conditions. Several simulations with the isotope-enhanced model versions of LMDZ, HADAM3, and ECHAM4 under varying interglacial and future warming boundary conditions revealed lower temporal than spatial δ^{18}O-T-slopes for both Greenland [Masson-Delmotte et al., 2011, Sime et al., 2013, Sjolte et al., 2014] and Antarctica [Sime et al., 2008]. Potential past changes in the seasonality of precipitation were also identified as highly important in these studies, especially for Greenland. A recent study with the fully coupled isotope-enabled GCM HADCM3 [Tindall and Haywood, 2015], which is comparable to the COSMOS-WISO coupled model setup, also concluded that the δ^{18}O-T-relationship might have changed in time and space. However, this simulation was performed for the warm climate of the Pliocene, and not the LIG.

3.6 Conclusions

In conclusion, in this study three climate states during the LIG were examined, for 130, 125, and 120 kiloyears before present using a fully coupled general circulation model enhanced with stable water isotopes. Strong seasonal biases in the responses of $\delta^{18}O$ in precipitation were found. While it could be determined that the relationship between $\delta^{18}O$ and temperature remains stable throughout the LIG based upon a globally

averaged spatial relationship, attempts to utilize this spatial relationship to recreate temporal temperature anomalies uncovered inconsistencies, namely that the $\delta^{18}O$/T quotient has a large degree of heterogeneity and deviates from the spatial relationship. If the results are filtered and only strong temperature changes are examined, the amount of variation in the $\delta^{18}O$/T quotient decreases, and the quotient values approach the value of the spatial $\delta^{18}O$/T relationship, yet there are still areas that are inconsistent. This would suggest a "recorder problem" in $\delta^{18}O$ due to the complexity of the signal, and that the classic paleothermometer discovered by Dansgaard [1964], while useful for large magnitude temperature changes, may not be sufficient to understand smaller magnitude changes.

There are several potential improvements that should be considered for future studies. Primarily, the continental ice sheet geometry or extent were not modified during these simulations, although there have been suggestions (e.g. Pfeiffer and Lohmann [2015] and references therein) that the LIG GrIS in particular may have been smaller than at present. Further study [Sutter et al., 2016] suggests that the West Antarctic Ice Sheet (WAIS) may have been partially collapsed during the LIG. The justification for prescribing an identical PI ice sheet in all LIG simulations was to minimize a possible uncertainty in the climate forcing, and to maintain comparability with other studies. While ice sheet geometry and extent both play an important role in for climate feedbacks, examining the effect of ice sheet geometry on isotopic response was beyond the scope of these examinations, yet it remains an important point for futher research.

Furthermore, an important advantage of this new modeling approach has not yet been leveraged. By enabling the climate model COSMOS-WISO to simulate stable water isotopes, it is now possible to produce more direct comparisons between geochemical climate proxies and climate simulations, and allusions to such comparison studies have already been made in several LIG proxy studies, such as Capron et al. [2014]. This

advantage will allow for the potential discovery of climate mechanisms that may have previously been difficult or impossible to analyze due to the inherent challenge in comparing geochemical proxy data with simulations. Thereby minimizing one possible source of misinterpretation regarding climate reconstructions during interglacial climates, a topic which has been becoming increasingly focused upon given the growing concerns about future anthropogenically induced global warming.

3.7 Next Steps

In this first study, performing such a detailed model data comparison was considered to be beyond the scope of the intended investigation. However, the analysis has demonstrated that new questions must be raised regarding the robustness of $\delta^{18}O$-climate reconstructions. In particular, one must ask if $\delta^{18}O$ can be used to reconstruct temperatures during interglacials if the temperature responses are not particularly strong. It has been demonstrated that the typical $\delta^{18}O$/T quotient is subject to a large degree of variability. This variability partially subsides if the examination is restricted to larger magnitude temperature changes. While this is not necessarily a problem during glacial periods when temperature changes are quite large with respect to PI – as discussed in Werner et al. [2016] – during interglacials, this may not be the case.

In order to examine in how far $\delta^{18}O$ based temperature reconstructions are feasible, in the next set of studies, the simulations discussed here are compared against a variety of paleoclimate archives, both with and without $\delta^{18}O$. This is done to test not only the isotopic response in the model with respect to proxies, but also independently verify if the climate simulation matches measurements that were not obtained from $\delta^{18}O$.

CHAPTER 4

COMPARING THE SIMULATED LAST INTERGLACIAL CLIMATE TO RECONSTRUCTIONS

In the following sections, several simulations of the Last Interglacial (LIG) will be compared to available proxy reconstructions of the same period. Each proxy is introduced, in an effort to explain its ability to reconstruct the compared climate feature. Furthermore, the climate feature that is being examined is brought into context with the larger climate system, and how information gained about any particular region or time period may be useful in better understanding the entire LIG.

4.1 Comparison against North Atlantic Multi-proxy Summer Sea Surface Temperature Reconstructions

The first study that shall be compared against is a data compilation generated by Capron et al. [2014], which is targeted at reconstructing the high latitudes beyond 40°N and

40°S. The aim of the project was to uncover both the temporal and spatial structure of temperature changes during the LIG, and produced a compilation of four temperature anomalies at 115 ka B.P., 120 ka B.P., 125 ka B.P., and 130 ka B.P..

4.1.1 Motivation

The North Atlantic region plays a very important role in the overall climate system. Sea ice extent is one of the primary factors leading to polar amplification, as has been found by the CAPE Last Interglacial Project 2006 as well as the Intergovernmental Panel on Climate Change [2014]. Recent examinations have focused on how changes in the North Atlantic may lead to melting of Arctic glaciers as well as the Greenland Ice Sheet (GrIS) [Huybrechts et al., 2002, Robinson et al., 2012]. Such melting would result in a change in the freshwater budget of the North Atlantic, which would activate further feedbacks.

Firstly, freshwater perturbation in the Arctic will influence sea ice formation rates, and thereby influence sea ice extent and planetary albedo. Secondly, freshwater perturbations influence the key formation areas of North Atlantic Deep Water (NADW) off the eastern and southern coasts of Greenland. Changes in this region have the ability to impact the Atlantic Meridional Overturning Circulation (AMOC), which in turn would influence the latitudinal distribution of heat.

The AMOC is a system of deep ocean circulation, characterized by northward flow of warm, salty water in the upper layers of the Atlantic, which becomes colder and denser until forming NADW, which then returns southward through the North and South Atlantic. As air has a much smaller heat capacity than water, the AMOC transports a sizable amount of heat from the tropics and the southern hemisphere into the northern hemisphere. A weakening of the AMOC would therefore result in more heat being trapped at equatorial latitudes and cooling in the North Atlantic. This relative cooling is a typical fingerprint of an anomalously weak AMOC (as discussed in e.g. Dima and

Lohmann [2009], Drijfhout et al. [2012], Rahmstorf et al. [2015]).

The scenario of a weaker AMOC in the future has been examined with a variety of methods, most recently with fully interactive Ice Sheet Models (ISMs) coupled to General Circulation Models (GCMs), as was done by Ridley et al. [2005], Mikolajewicz et al. [2007], Vizcaíno et al. [2014], and Gierz et al. [2015]. While the simulations have produced a broad spectrum of possible AMOC variability, the results generally agree that a weakening of the AMOC results in a reduction of heat transport and a relative cooling of the North Atlantic.

Given this region's significance both in determining planetary abledo via sea ice coverage, as well as latitudinal heat distribution via deep ocean circulation; it is of crucial importance to understand how the North Atlantic may have changed during the LIG. This information would give some insight into the region's vulnerabilities in slightly warmer-than-present day climates.

Some modeling examinations of how the North Atlantic may have been different during the LIG have already been performed. Pfeiffer and Lohmann [2015] examined how changes to the GrIS orography impact temperature changes in the region, finding that reducing the GrIS resulted in a warming of several degrees Celsius in boreal winter. Otto-Bliesner et al. [2006] examined responses in simulated sea ice extent due to LIG forcing, finding that a reduction of sea ice area by up to 50% relative to Pre-Industrial (PI), and both Bakker et al. [2013] and Lunt et al. [2013] looked at how various different models simulate changes in the North Atlantic, discovering differences in the simulations particularly in those regions that have been found to be sensitive to AMOC changes.

Multiple paleoclimate proxy compilations for this region have also been generated [Kaspar et al., 2005, CAPE Last Interglacial Project members, 2006, Turney and Jones, 2010, McKay et al., 2011]. The results were varied and often not comparable to one another, utilizing different assumptions. For example, Turney and Jones [2010] discovered

a warming of up to 2.0 °C, yet they had to average over the entire LIG's time span. McKay et al. [2011] found a sea surface temperature (SST) warming of 0.7 ± 0.6 °C, yet this was relative to the Holocene rather than the PI. The advantage of the data compilation made by Capron et al. [2014] is the ability to divide the proxy reconstructions of the LIG into distinct time periods, and provide estimates of temperature change relative to PI, thus providing a sense of the LIG's transient evolution.

In the following section, a description of this newest North Atlantic LIG reconstruction is shown. The proxies utilized to reconstruct the North Atlantic's sea surface temperature are presented, along with a short description of how each proxy works. Following this, a brief explanation of age models is given, and a description is provided demonstrating how each proxy record is dated, allowing it to be tied to a specific time frame during the LIG. Finally, a comparison of the proxies to the model simulations made with COSMOS-WISO is shown, and implications of the changes to the North Atlantic region during the LIG are discussed.

4.1.2 Proxy Description & Simulations Used

A combination of both ice core records as well as ocean sediment core records was used in order to construct the data compilation. A pre-condition of selecting the data is the availability of measurements at a temporal resolution of at least 2 ka or higher, in order to ensure that each individual record could be synchronized to the common temporal framework. A total of five records of surface air temperature deduced from stable water isotopes measured in polar ice cores as well as 42 SST records from marine sediment cores were used to create the time composite snapshots of the LIG climate..

The ice core records used include 4 from Antarctica: EPICA Dome C (EDC), EPICA Dronning Maud Land (EDML), Vostok Ice Core (VK), and Dome F (DF). One core from Greenland is included; the NEEM ice core [NEEM community members, 2013],

extends into the LIG from 116 ka B.P. to 128 ka B.P.[1]. The sediment cores are located primarily in the North Atlantic. Furthermore, the SST reconstructions are made from a variety of proxies. In total, 3 records are based upon Mg/Ca ratios, 3 on alkenone unsaturation ratios, and 30 on faunal assemblages, and 6 records are based upon the relative abundance of the polar foraminifera species *Neogloboquadrina pachyderma*. As such, a majority of the reconstructions are based upon faunal assemblages, since very few records with geochemical methods have been published.

How does each proxy reconstruct SST?

Mg/Ca Ratios The SST values reconstructed with the aid of Mg/Ca ratios utilized a temperature calibration by Kozdon et al. [2009]. This calibration is commonly used for the species *Neogloboquadrina pachyderma*:

$$\frac{Mg}{Ca} = 0.13(\pm 0.037)T + 0.35(\pm 0.17)$$

where T is the temperature of Calcification. As *N. pachyderma* is a planktic foraminifera species, these temperatures are assumed to correspond to SST.

Alkenone Unsaturation Index Prahl and Wakeham [1987] discovered a physiological response in *Emiliania huxleyi*'s membrane chemical composition. The degree of unsaturation of alkenones is related to temperature changes, and can be expressed as:

$$U_{37}^{K'} = 0.043 + 0.033 \times T$$

Faunal Assemblages Here, a Modern Analogue Technique (MAT) is applied [Hutson, 1980], which relies on the similarity of faunal species distribution to a modern-day core top sample. The modern samples are thought to be analogues of the oceanographic conditions which produced a particular faunal distribution, and

[1] All five of these ice cores are compared against in Section 4.4

therefore, the similarity between the modern and past sample can be used to estimate changes in sea surface temperature.

Foraminifera Abundance The abundance of *N. pachyderma* also relies on MAT estimations (based upon the method described by Prell [1985]) to reconstruct SST. An example of such reconstructions, along with a detailed methodology, can be found in Bauch et al. [2012].

Determining Ages

The LIG presents a further problem, namely that it is beyond the age range that can be directly determined by radiocarbon dating. As ^{14}C has a half life of 5730 ± 40 years [Godwin, 1962], it is an unsuitable tool to determine exact ages of measurements during the LIG, which covered a time period from 115 ka B.P. to 130 ka B.P.. Therefore, other tools must be used.

Chronostratigraphic age scales are constructed to assist in anchoring proxy data – which are measured on relative depths of a sediment or ice core – to ages in the Earth's past. This would allow proxy data points to be tied to specific ages. Constructing such a chronology can be accomplished by a variety of methods. As glacial ice accumulates in a sequence of annual increments, it is possible to generate a chronology based upon the visible banding in the ice; and such a layer counting technique has been employed for dating parts of the the GRIP and NGRIP ice cores [Rasmussen et al., 2006, Svensson et al., 2008].

At deeper levels within the ice sheet, defomation makes the individual layers more difficult to recognize. This problem is further complicated at low accumulation sites, such as over Antarctica, where the seasonal layers are not clearly deposited, and further smoothed during the conversion of snow to ice (known as firnification). While some absolute age markers can be used, such as tying ^{10}Be peaks to magnetic reversals

[Raisbeck et al., 2007], $^{40}Ar/^{39}Ar$ ratios [Dunbar et al., 2008], or U/Th ratios [Aciego et al., 2011], such absolute dating markers are sparse, necessitating additional methods. One such approach of dating relies on the fact that certain atmospheric trace gases concentratations (such as methane) vary in correlation to variations in the earth's orbital parameters, which can be independently dated based upon astronomical calculations [Ruddiman and Raymo, 2003]. Other measurements of air content properties trapped in the ice cores are also useful. Long records of $\delta^{18}O_{atm}$ [Bender et al., 1994, Petit et al., 1999], $\delta O_2/N_2$ [Bender, 2002, Kawamura et al., 2007], and total air content [Raynaud et al., 2007] have been found to be highly correlated with the insolation variations in Earth's orbit, thereby providing additional constraints on ice core chronologies.

All of these orbital tuning constraints rest upon the principle that variations in the Earth's orbit can be precisely calculated. The basis for this theory was shown earlier in Chapter 1.2, and calculations for the various oscillations of Earth's orbit have been performed by Berger [1978] as well as by Laskar et al. [2011].

Synchronizing Proxy Records

The age scale chosen was the Antarctic Ice Core Chronology 2012 (AICC2012) chronology, initially published by Bazin et al. [2013] and Veres et al. [2013]. This time scale is the first of its kind, integrated over the LIG based upon multiple locations, and provides age/depth relationships both for Greenland (NGRIP) as well as Antarctic ice cores (EDC, EDML, TALDICE, Vostok).

Capron et al. [2014] transferred the records onto the AICC2012 age scale utilizing a method outlined by Govin et al. [2012]. This synchronization bases upon the assumption that surface water temperature changes in the North Atlantic occurred simultaneously with air temperature variations over Greenland. A detailed description of this methodology is presented in Capron et al. [2014], along with a summary of which events are considered to be synchronous between the NGRIP ice core and the sediment cores. In

principle, age models are built based upon linear interpolation operates under the assumption that the sedimentation rate remains constant. The resulting synchronized records include errors based upon Monte-Carlo analysis to propagate the errors associated with both the uncertainty linked to the SST reconstruction as well as the age uncertainties of the AICC2012 chronology. The Monte-Carlo analysis utilizes 1000 age model simulations, adding random noise to the SST reconstruction values within the space of the method's error, and randomly perturbing the age of each tie-point within the age uncertainty. This method resulted in a combined uncertainty for both reconstruction method and age. The data compilation claims to reconstruct boreal summer sea surface temperature, as is given by the respective authors of each of the individual records

Model Runs Employed for Comparison

These proxy compilations are compared to simulations of the early and mid LIG, LIG-130 and LIG-125, as already described in Chapter 3. Additionally, as the records are available as time series as well as time composites, some of the records are compared against a transient comparison of the LIG. This simulation was created using the greenhouse gas (GHG) concentrations described in the Paleoclimate Model Intercomparison Project (PMIP) project as well as orbital parameters calculated using the Berger and Loutre [1991] routine. Both of these forcings were accelerated by a factor of 10, following a method initially documented by Lorenz and Lohmann [2004]. This simulation is hereafter referred to as LIG-T.

4.1.3 Early LIG Spatial Comparison

The results comparing the spatial patterns simulated for LIG-130 against the proxy data for 130 ka B.P. are presented in Figure 4.1-A. The multi-proxy dataset of North Atlantic SSST anomalies shows a cooling of up to $-7.5 \pm 3.0\,^{\circ}\mathrm{C}$. The simulation of the early LIG

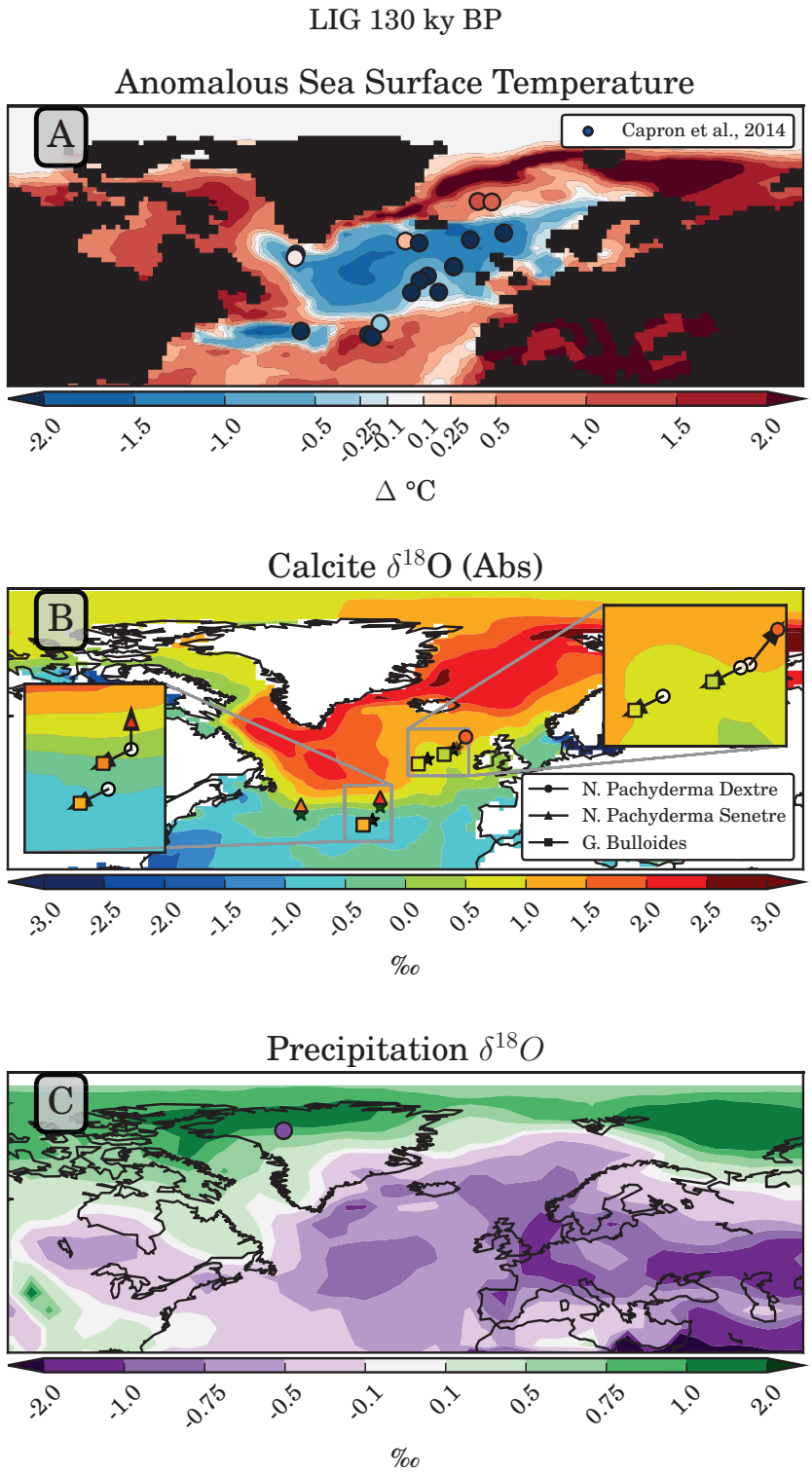

Figure 4.1: A) Spatial comparison of SSST changes relative to PI. B) Comparison of available $\delta^{18}O_C$ cores. C) Comparison of the NEEM ice core. Sea surface temperatures are constructed with the average of the upper 10 meters of water.

realized by COSMOS-WISO matches the distribution of this cooling signature quite well, capturing the cooling area itself as well as the fronts and locations of warming slightly further north. Solely the southern extent of the cooling is not well represented. However, this may be a difficulty caused by the course model resolution.

While the dataset's SSST reconstruction is a combination of multiple proxy types; some of the cores also offer calcite measurements of planktic $\delta^{18}O_C$. These measurements can be used as an independent test of the proxy/model comparison, thereby providing a separate benchmark. Unfortunately, only a preliminary analysis of these cores is possible, as Monte Carlo simulations have not yet been performed. Thus, an estimation of both measurement as well as age error is not yet available (Emilie Capron, *personal communication*).

While direct surface values were used to compare SSSTs in order maintain comparability with other modeling studies, the $\delta^{18}O_C$ values are treated slightly differently. As calcifying foraminifera live in the surface layers of the ocean, and not strictly at the direct surface, an average of the upper 150 m is generated from the simulated values in order to compare against the $\delta^{18}O_C$ of the sediment cores.

The comparison between the available $\delta^{18}O_C$ in the cores and in the model is shown in Figure 4.1-B. The model calcite was calculated from simulated $\delta^{18}O_{sw}$ and T_{sw} based upon the Shackleton [1974] paleothermometry equation, shown below:

$$T = 16.9 - 4.38 \cdot (\delta^{18}O_C - \delta^{18}O_{sw}) + 0.1 \cdot (\delta^{18}O_C - \delta^{18}O_{sw})^2 \tag{4.1}$$

where both $\delta^{18}O_C$ and $\delta^{18}O_{sw}$ are measured on the Pee Dee Belemnite (PDB) standard. Following a conversion by Hut [1987], this can be expressed relative to the SMOW standard via:

$$\delta^{18}O_{sw(PDB)} = \delta^{18}O_{sw(VSMOW)} - 0.27 \tag{4.2}$$

As several different species are used when measuring $\delta^{18}O_C$, each is presented as a separate symbol in Figure 4.1-B; however, the model only reconstructs a general calcite value. The match between the model $\delta^{18}O_C$ and data is also fairly close, solely the southern extent is once again not captured. As before, this may be due to the coarse model resolution.

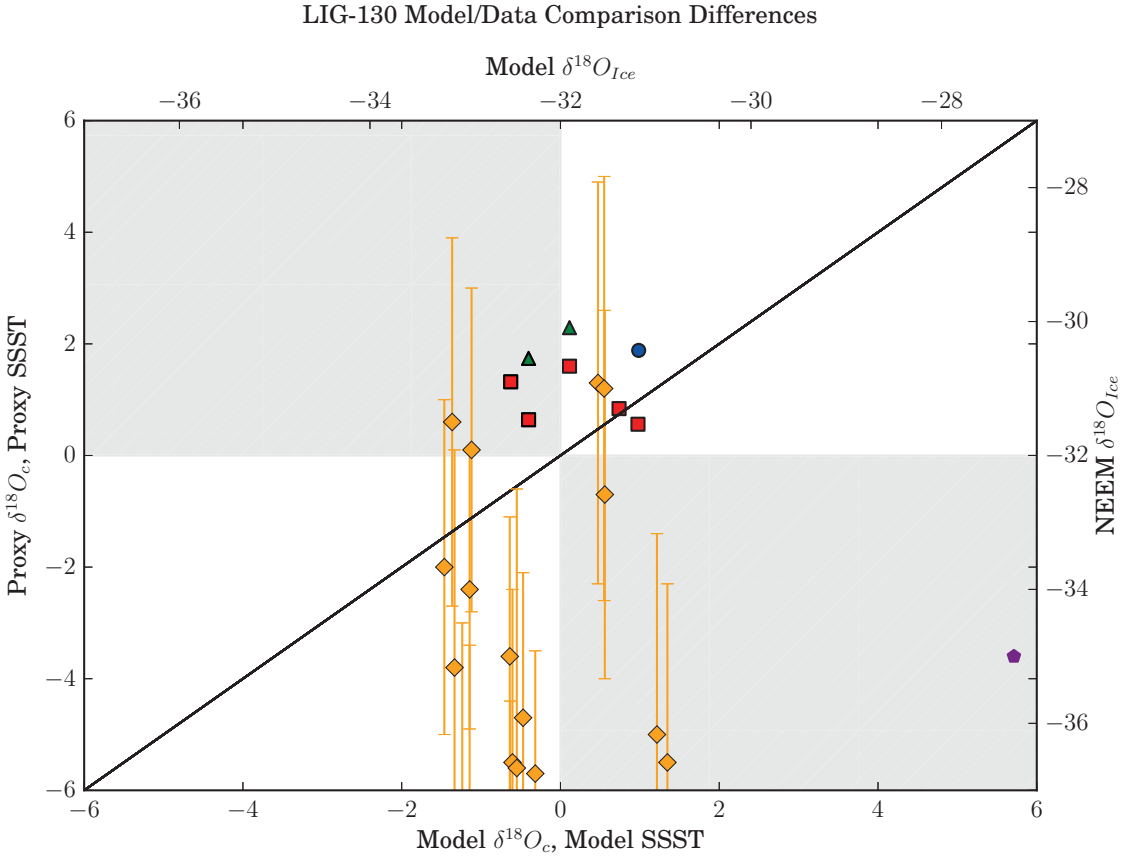

Figure 4.2: Errors of the model/data comparison for LIG-130. Orange diamonds show anomalous temperature reconstructions, red, green, and blue symbols show calcite values, and the purple hexagon shows the NEEM ice core. The Y axis represents the measured SSST, $\delta^{18}O_C$ and $\delta^{18}O_{ice}$ values, X shows the simulated values.

Figure 4.2 shows the deviations of the simulation from the data. The SSST changes, shown with the orange diamonds, are underestimated by the simulation, and most of the points fall below the 1-1 fit line, which would indicate the position of a perfect model/data match. While this might at first appear as if the simulation does not reproduce the

measured SSSTs very well, the uncertainties in the data would suggest that the fit could be improved if the error range is utilized; a point which will be expanded upon in the discussion. Furthermore, it should be noted that the reconstructions rely heavily on faunal assemblages, which in turn must make the assumption that transfer functions or modern analogs are useful for interpretations of the past environment. Other methods, such as Mg/Ca or Sr/Ca reconstructions, would instead rely on geochemical principles which can be extensively tested via laboratory studies, and as such might be considered to be more reliable.

When examining the difference in calcite reconstructions, it can be seen that the simulation and the data have a much smaller disagreement, and as the $\delta^{18}O_C$ signal is a combination of both sea temperature as well as $\delta^{18}O_{sw}$, the match between simulation and data could be used to validate two different variables in the model. The largest differences in $\delta^{18}O_C$ occur solely in the southern extent of the available data, where the model and data have opposite signs. Here, as with the spatial distribution of temperatures shown in Figure 4.1, it could be argued that the model resolution is insufficient to adequately show boundaries and fronts of ocean features as they may occur in the real world.

4.1.4 Mid LIG Spatial Comparison

Next, the comparison is repeated for LIG-125. The spatial comparison is shown in Figure 4.3. The SSST comparison does not fit as well as during LIG-130; while the cooling area of between $-0.1\,°C$ to $-0.5\,°C$ in the North Atlantic is still simulated by COSMOS-WISO, the multi-proxy compilation records a warming in this region, with values ranging from $0.5\,°C$ to beyond $2.0\,°C$. Interestingly, some areas of cooling still appear in the proxy records, which are matched by the simulation in location, yet with weaker magnitudes. The northern and southern extent of the anomalous cooling simulated in the model is

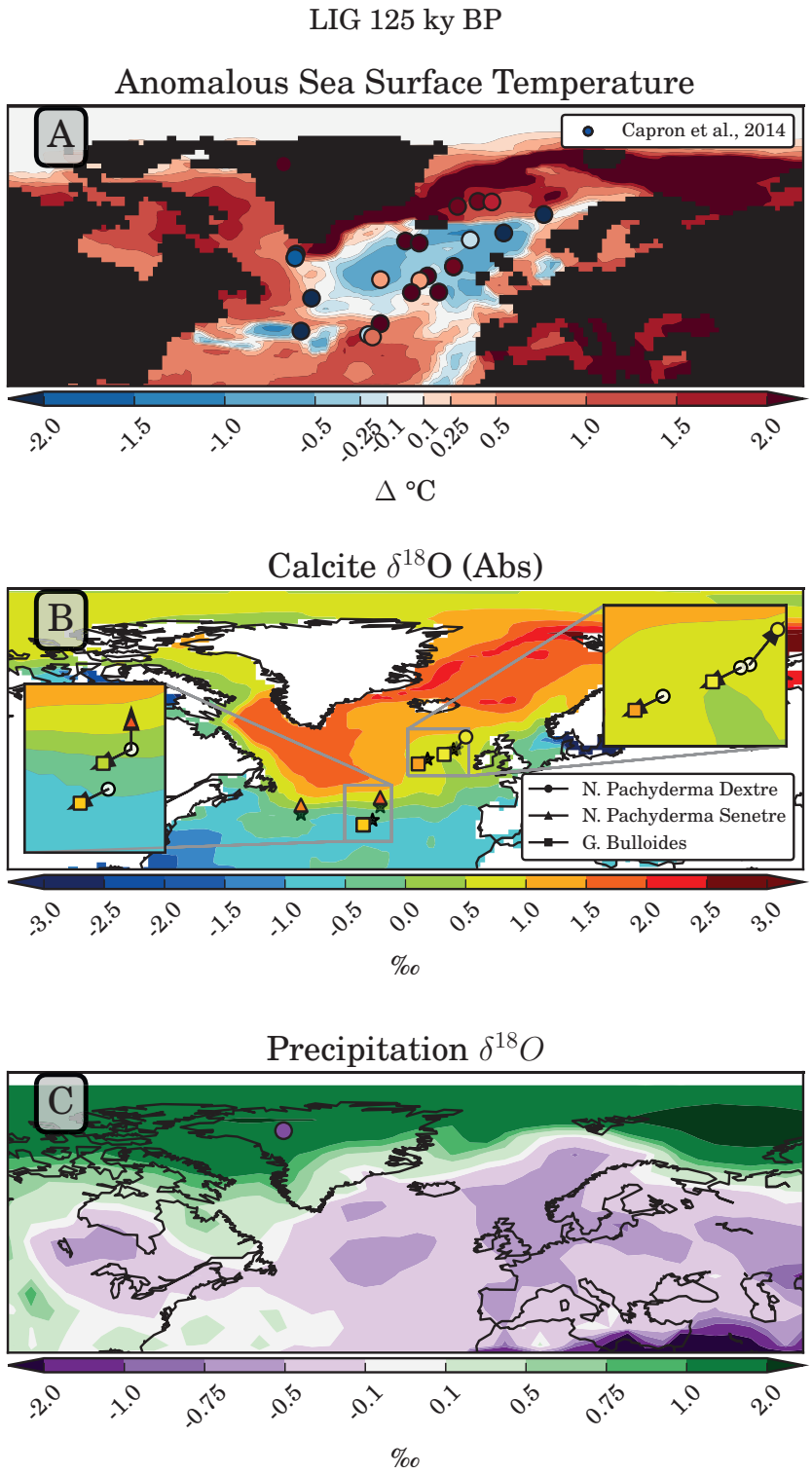

Figure 4.3: A) Spatial comparison of SSST changes relative to PI. B) Comparison of available $\delta^{18}O_C$ cores. C) Comparison of the NEEM ice core. Vertical averages of sea surface temperature are used as before.

bounded by warming (0.5 °C to 2.0 °C) just north of Iceland, which is also seen in the proxy record. A slight area of cooling (−0.25 °C to −1.0 °C) is simulated off the eastern coast of Canada, which the proxy record also captures.

The calcite records and simulations for LIG-125 also fit quite well, with calcite values of between 0.5 ‰ to 1.0 ‰ simulated off the western coast of Ireland, values which are also captured by the proxy records. The cores in the central North Atlantic appear to match the values slightly higher north, where the model produces values of between 1.5 ‰ to 2.0 ‰. This mismatch in location again may be indicative of a limitation stemming from the model's coarse resolution. The ice core values are offset, as they were in LIG-130, and the simulated values are unable to match the measured values of the NEEM ice core.

Quantifying these differences, as done in Figure 4.4, reveals that the model does indeed underestimate the change in SSST, with many of the points producing contradictory signs. However, when including the uncertainty of the reconstructions, the model and data comparison could in fact be largely rectified. As in LIG-130, the calcite values also fit rather well between the values measured in the sediment cores and those simulated by COSMOS-WISO. Solely the NEEM ice core $\delta^{18}O$ value is offset by nearly 5 ‰; the simulation value is more depleted than what is measured in the actual ice core. This difference may be due to the coarse orography that is included at the T31L19 model resolution. Werner et al. [2011] have shown that increasing the model resolution can partially rectify $\delta^{18}O$ mismatches that may stem from coarsely resolved orography.

Before comparing to the transient simulation, these time slice results are summarized in Table 4.1. The RMSE between the model and the data is presented, demonstrating that calcite values are offset by approximately 1.5 ‰, the SSST values are offset by between 3.0 °C to 4.3 °C, and the NEEM ice core value is off by 4.9 ‰ to 7.8 ‰.

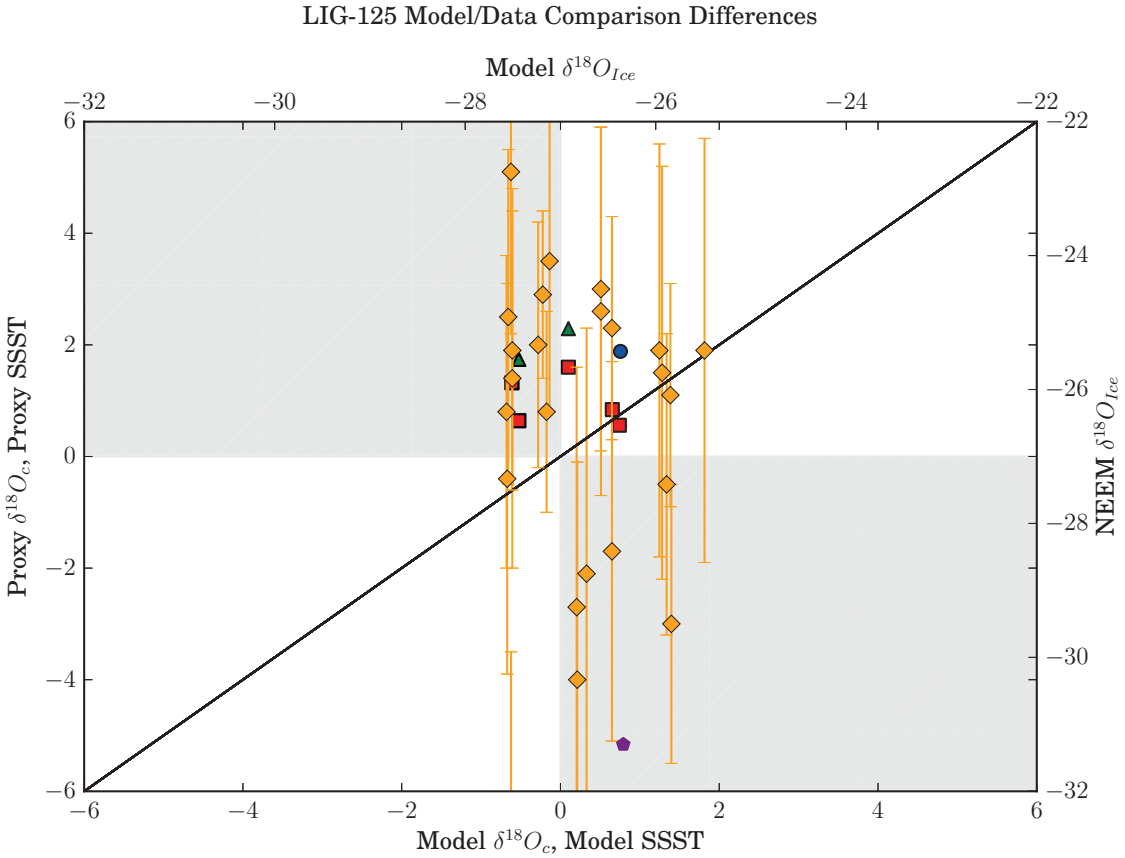

Figure 4.4: Errors of the model/data comparison for LIG-125. Orange diamonds show anomalous temperature reconstructions, red, green, and blue symbols show calcite values, and the purple hexagon shows the NEEM ice core. Axes are in units as in Figure 4.2.

Table 4.1: RMSE of the multi-proxy compilation created by Capron et al. [2014] for SSSTs, along with calcite reconstructions available for select sites, and the $\delta^{18}O_{ice}$ values of the NEEM ice core.

RMSE	LIG-130	LIG-125
SSST (°C)	4.24	3.0
$\delta^{18}O_C$ (‰)	1.47	1.52
$\delta^{18}O_{Ice}$ (‰)	7.76	4.96

4.1.5 Transient Comparison

Next, the transient simulation is used to examine how well the model is able to reproduce the evolution of the LIG, as would be measured by stable water isotopes. In order to see how well the stable water isotope enabled model performs, $\delta^{18}O_C$ is utilized as a benchmark, and the comparison is performed against those cores of the Capron et al. [2014] dataset which have this measurement preliminarily available.

A total of six marine sediment cores also provide measurements of $\delta^{18}O_C$, shown in Figure 4.5. Based upon these 6 cores, it appears as if COSMOS-WISO captures several features of the LIG as they are recorded in $\delta^{18}O_C$ quite well. Many of the cores demonstrate a slow decrease in temperature (and a corresponding increase in enrichment of $\delta^{18}O_C$) as the LIG progresses, which is also simulated by the model. The core SU9003 displays a rather large mismatch between simulation and model, however the location of this core at the southern extent of the anomalous cooling pool seen in LIG-130 and LIG-125 might place it in a zone where the real climate is at the edge of a front which cannot be captured by the coarse resolution, an issue which was already the case in the equilibrium simulations of the early and mid LIG. However, given the strong similarities with the other cores, it appears as if the transient realization of the LIG is consistent with reconstructions, at least in the North Atlantic region.

Unfortunately, the sediment cores do not offer a very high temporal resolution, and as such, it is difficult to judge in how far COSMOS-WISO correctly simulates climate variability on submillenial time scales. Furthermore, none of the sediment cores that also have $\delta^{18}O_C$ measures lie in the area where the faunal assemblage reconstructions show anomalous cooling during LIG-130 and warming during LIG-125, thus making it difficult to tell if uncertainty seen in these proxies (as shown in Figures 4.2 and 4.4) is truly indicative of an early LIG cooling and a mid LIG warming.

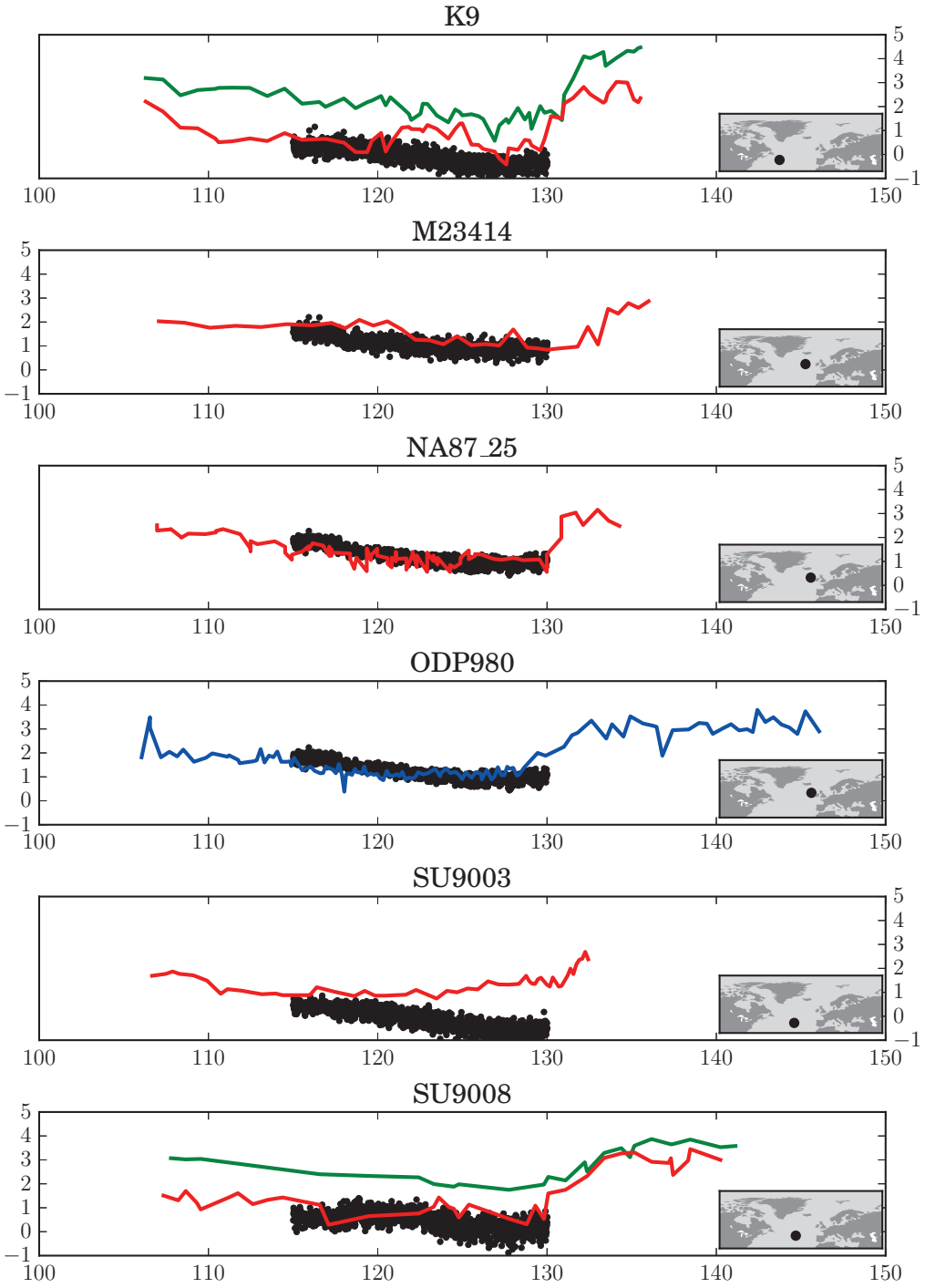

Figure 4.5: Transient comparison of the $\delta^{18}O_C$ values simulated by COSMOS-WISO against ocean sediment cores during the LIG. Red curves show *G. Bullodies*, blue curves show *N. Pachyderma Dextre*, and green curves show *N. Pachyderma Senetre*

4.1.6 Discussion

The Capron et al. [2014] reconstruction of the North Atlantic provides an important insight into the temperature evolution of the region during the LIG. Not only does the North Atlantic play an important role in polar amplification [Intergovernmental Panel on Climate Change, 2014], but the region also plays a fundamental role in deep water mass formation, and therefore is a component of the AMOC, as discussed in the motivation for this study (See Section 4.1.1)

Temperature changes in the North Atlantic have been shown to be a response of AMOC changes, as was previously mentioned. As such, the cooling seen in the multi-proxy reconstruction of LIG-130 is one of the typical fingerprints of a weaker AMOC, and may be indicative of a reduction in overturning strength during the early LIG, relative to the PI climate. Indeed, upon examination it is discovered that the AMOC simulated by COSMOS-WISO is between -2 Sv to -4 Sv weaker during LIG-130 compared to PI (Shown in Figure 4.6)

Capron et al. [2014] compared their reconstructions to two different modeling attempts in the publication, as was already discussed in section 3.5.2. A more recent study by Stone et al. [2016] also attempted to match the North Atlantic reconstructions, and determined that a freshwater perturbation assists in rectifying the previous mismatch simulated by HADCM3 for the LIG-130 time slice, with the justification that an AMOC weakening, which results in a cooling of the North Atlantic, may be needed to match the proxy results. However, since COSMOS-WISO is able to also match the reconstructions qualitatively without freshwater perturbation, multiple possibilities for the North Atlantic climate during the early LIG exist.

The North Atlantic cooling may either be indicative of a slightly reduced AMOC, which is solely a result of the orbital and greenhouse gas forcing, or, the North Atlantic cooling may be a result of a strongly weakened AMOC, due to freshwater perturbations

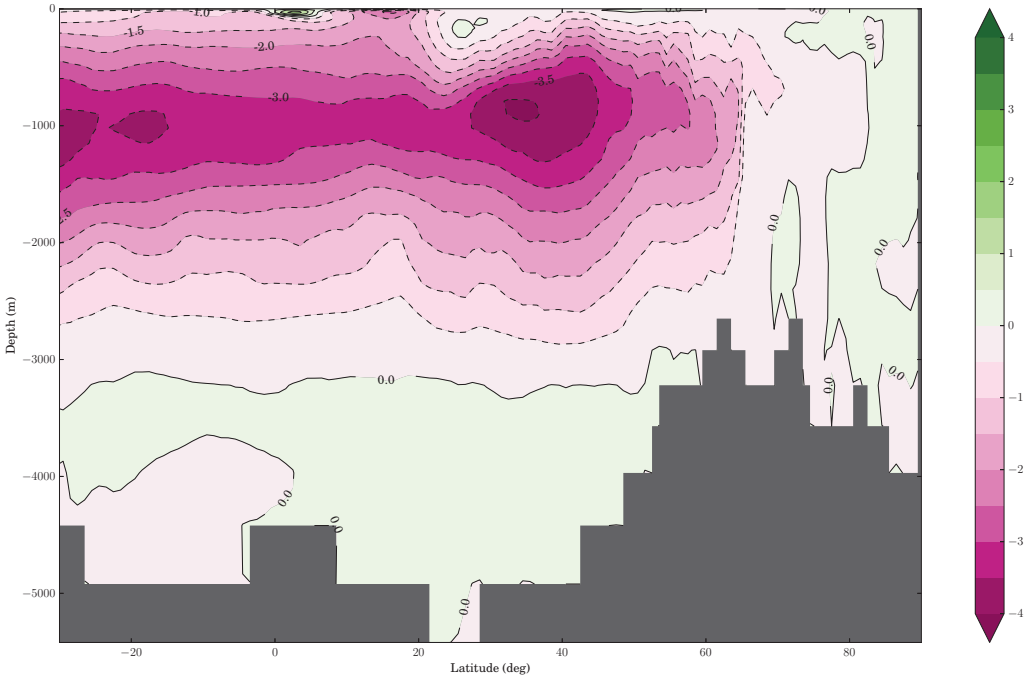

Figure 4.6: Anomalous AMOC strength during LIG-130, represented as a stream function. Positive values indicate stronger clockwise circulation, negative values indicate weaker circulation. Units are in Sverdrup (Sv).

in the North Atlantic. The examinations by Bakker et al. [2013] and Lunt et al. [2013] both demonstrated that this North Atlantic is a region with very large model biases, with each model responding differently to LIG climate forcing. Varying simulations of the AMOC were one of the underlying causes, and it can be deduced that an adequate simulation of the AMOC is of critical importance to correctly capture North Atlantic climate.

Since the two different models (the simulation from HADCM3 by Stone et al. [2016], and the simulation from COSMOS-WISO respond with different sensitivities to both an unperturbed and a freshwater perturbed realization of LIG-130, to better constrain the climate characteristics a further basis of comparison is required beyond the SSST reconstructions. The modeling approach discussed here provides the distinct advantage of additionally being able to compare $\delta^{18}O_C$, thereby providing an independent test to

examine the response of the climate system to the early LIG.

In order to test if the cooling signal seen by the proxies is indeed indicative of an freshwater-perturbed AMOC weakening during the early LIG, it is necessary to compare the responses of SST as well as $\delta^{18}O$ in calcite to the reconstructions in both a perturbed and an unperturbed state. To do so, a simulation is created with an identical freshwater perturbation in the North Atlantic as was done by Stone et al. [2016]; and a freshwater injection of 0.2 Sv in the North Atlantic is performed. Furthermore, as COSMOS-WISO is able to simulate stable water isotopes, an isotopic signature must be attached to this melt water. A value of −30 ‰ was assigned to the perturbation, with the justification that if indeed the North Atlantic underwent a freshwater perturbation (in this case, analogous to a Heinrich Event) during the early LIG, this water would stem from remnant ice of the penultimate glacial maximum. Other studies with stable water isotope equipped models examining freshwater perturbations have used similar isotopic signatures, as done in e.g. Lewis et al. [2010] and Hemming [2004]. This simulation is referred to as LIG-130-H1

Before investigating how the results of the SSST and Calcite change from the freshwater perturbation experiment, the responses of COSMOS-WISO and HADCM-3 are compared. Both COSMOS-WISO (results from this study, shown in Figure 4.7) and HADCM-3 (results from Stone et al. [2016], shown in Figure 4.8 which is reproduced from that publication, the relevant simulation is highlighted in yellow) simulate an AMOC strength of between 5 Sv to 6 Sv resulting from the freshwater perturbation. Consequently, both models also demonstrate a cooling in the North Atlantic in the simulations including freshwater perturbation. Stone et al. [2016] show a cooling of between −1 °C to −4 °C, whereas COSMOS-WISO shows a cooling of −3 °C to −6 °C. The results for SSST from COSMOS-WISO are shown in Figure 4.9, with the same proxy overlay as done in Figure 4.1.

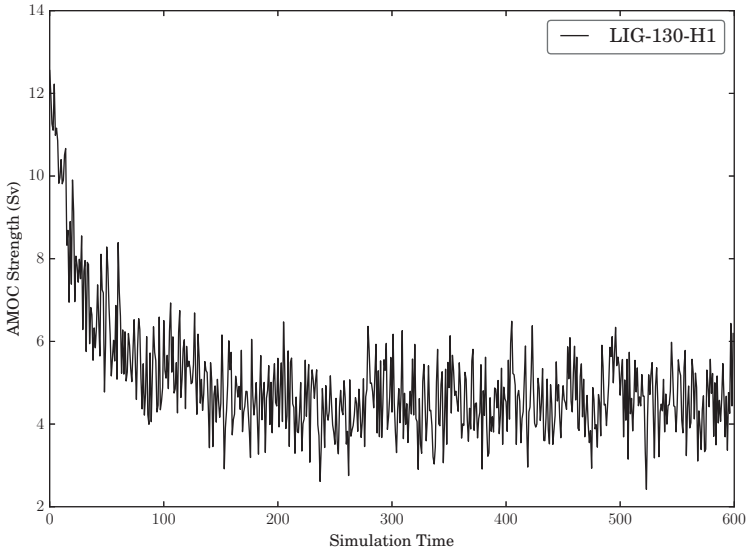

Figure 4.7: Evolution of the AMOC strength during experiment LIG-130-H1. The final 100 years are used for evaluation, and it can be seen that the AMOC strength reaches about 5 Sv

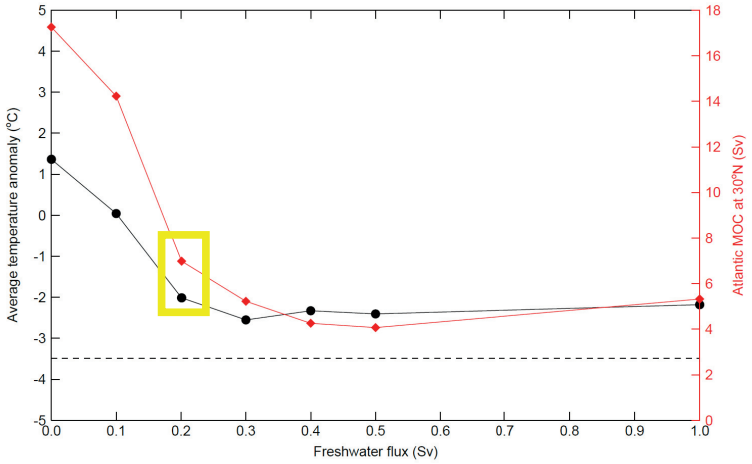

Figure 4.8: Reproduction of Figure 9 from Stone et al. [2016], showing AMOC strength in HADCM-3 resulting from various freshwater perturbation experiments. Temperature averages of all marine cores in the Capron et al. [2014] dataset are also shown. The relevant simulation is highlighted in yellow.

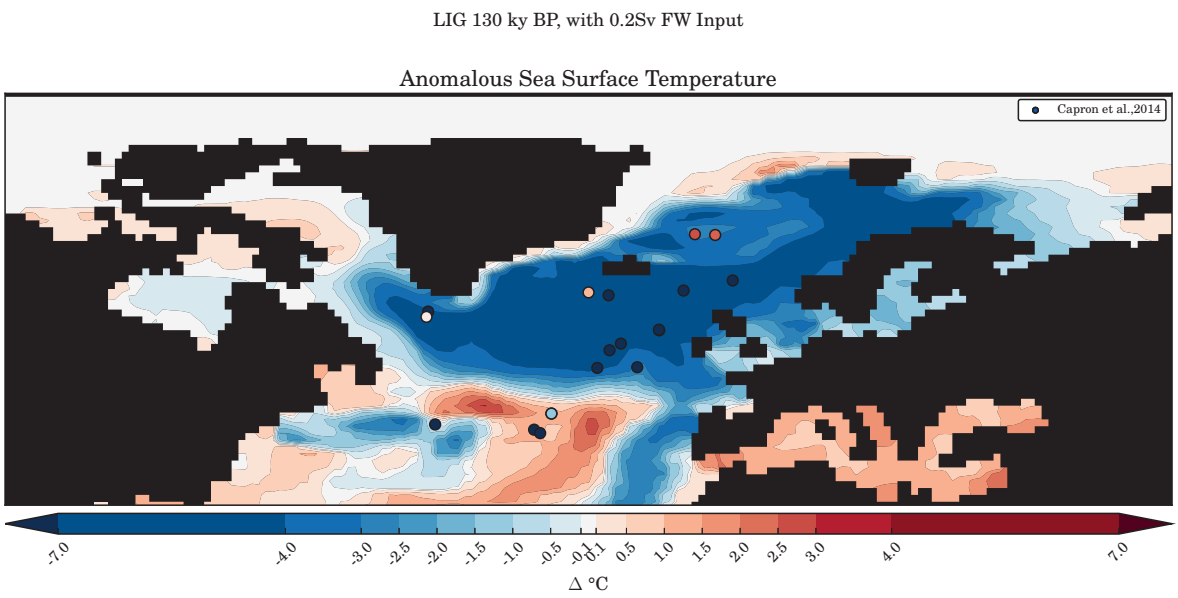

Figure 4.9: SSST anomaly during LIG-130, when perturbed by 0.2 Sv of freshwater in the North Atlantic. A marked cooling can be seen, which results from the weaker AMOC strength.

Using LIG-130-H1 to calculate the RMSE of the cooling shown by the Capron et al. [2014] dataset and the simulation, it can be seen that the deviation between the model and the simulation does indeed decrease compared to the LIG-130 simulation, from 4.24 °C without the freshwater perturbation to 3.82 °C, a change of Δ_{RMSE} =0.42 °C. Stone et al. [2016] report a much larger decrease in RMSE for their simulations, from 5.9 °C to 3.3 °C, Δ_{RMSE}=2.6 °C.

It was shown in Figure 4.2 that the SSST reconstructions had relatively large errors, ranging from 1.3 °C to 5 °C, and the next analysis makes use of these uncertainties. The aim is to understand the extent of the model/data mismatch and to see if the simulation with freshwater perturbation realized in LIG-130-H1 is truly an improvement over LIG-130. The mismatch between COSMOS-WISO and the Capron et al. [2014] dataset is minimized by allowing both the simulation as well as the proxy reconstruction to move along the respective errorbars. The proxy points are allowed to move up and down

the Y axis in the error range for each proxy point, and the model points are allowed to move left and right along the X axis in a range of 2 standard deviations (2σ) based upon 100 years of simulated SSSTs. These "adjusted errors" are shown in Figure 4.10; blue symbols represent LIG-130-H1, red symbols LIG-130.

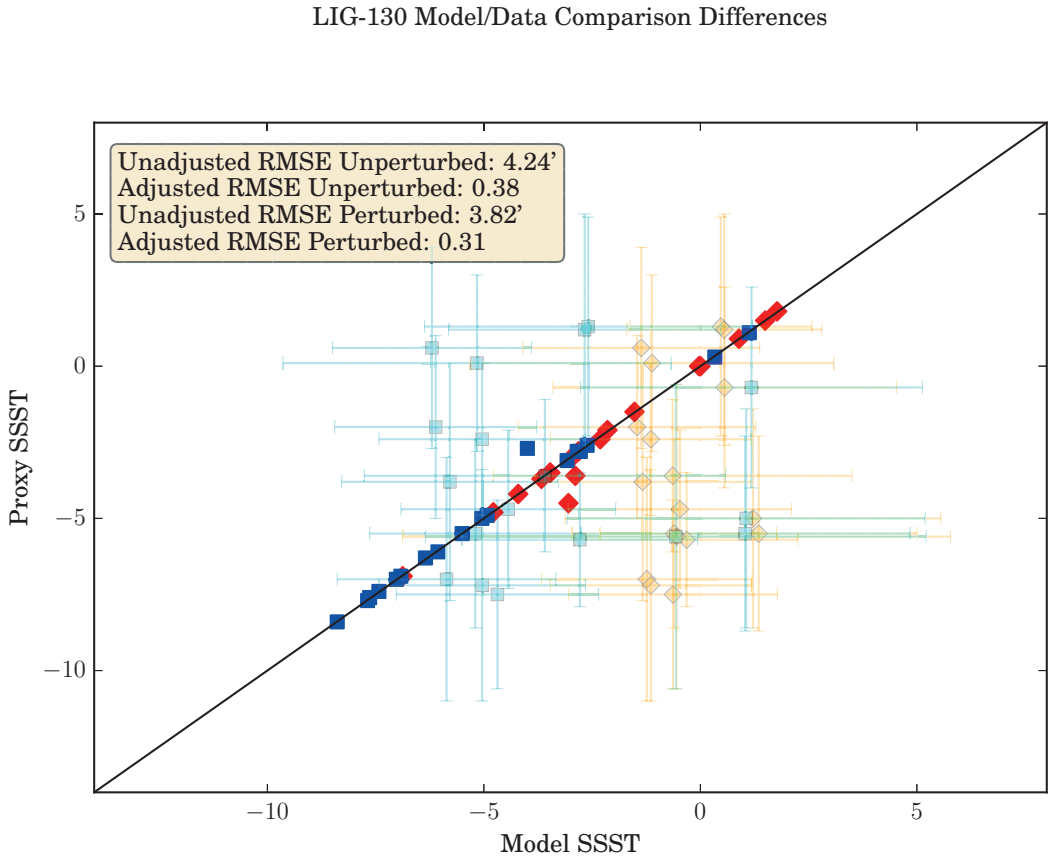

Figure 4.10: Reduction of model/data mismatch when error range is exploited for LIG-130 and LIG-130-H1 compared against the reconstruction of the early LIG SSST from Capron et al. [2014].

It can be seen that while the unadjusted RMSE may improve slightly, if one allows for the error range; the change in RMSE between the two simulations is minimal and both the perturbed simulation LIG-130-H1 (RMSE=0.31 °C) as well as the unperturbed simulation LIG-130 (RMSE=0.38 °C) are able to reproduce the proxy reconstruction. Therefore, a further constraint on the climate state is required to determine which of

the AMOC states is more feasible, either a strongly reduced AMOC due to freshwater perturbation in addition to climate forcing, or a slightly reduced AMOC solely due to climate forcing.

As COSMOS-WISO can reproduce the $\delta^{18}O_C$ signal that would be measured in planktic foraminifera, this signal could be used as another basis for comparison, hopefully eliminating one of the two possibilities. Figure 4.11 shows the $\delta^{18}O$ signal in calcite, generated from seawater temperature as well as seawater $\delta^{18}O$, as described above[2]

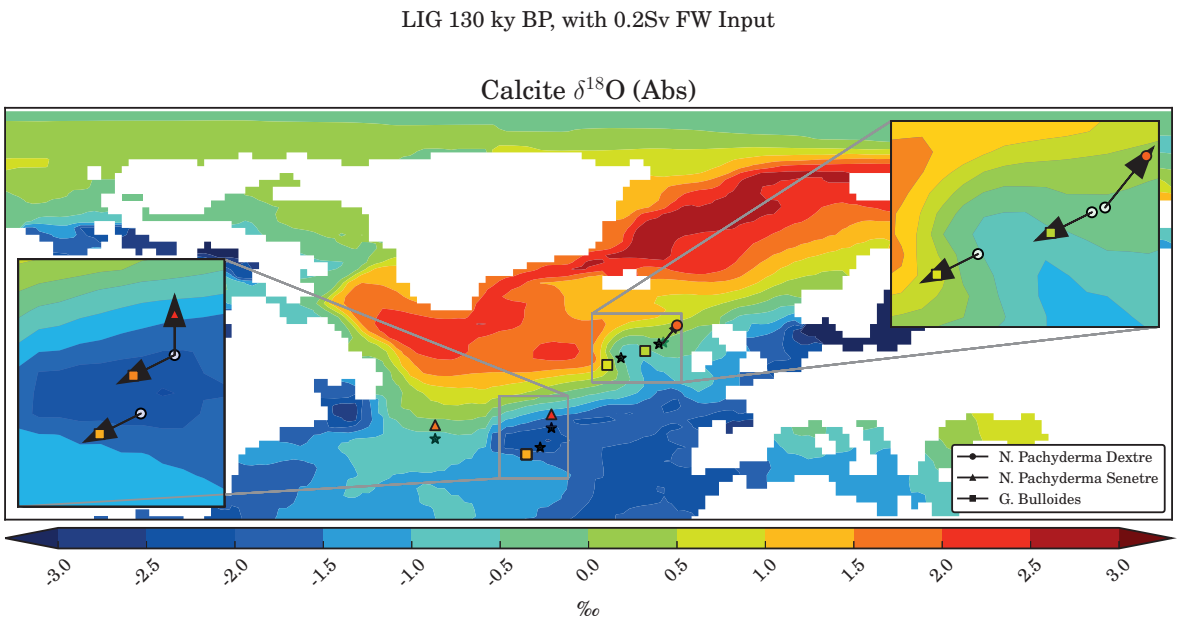

Figure 4.11: $\delta^{18}O_C$ as simulated by COSMOS-WISO in LIG-130-H1. An average is shown for the months June, July, and August, as well as for the upper 150 meters.

It can be seen that the values are strongly depleted, which is a result of the strong depletion of the incoming freshwater from the ice sheet. Since the values reported by the proxies are not this strongly depleted, it is unlikely that a strong freshwater perturbation is responsible for the cooling signal in the North Atlantic.

[2]An examination of how well this proxy is generally reproduced by MPIOM-WISO is presented by Xu et al. [2012], and in the coupled COSMOS-WISO model by Werner et al. [2016].

The possibility remains that the isotopic signature of the incoming freshwater was less depleted than what is assumed during this experiment. However, better estimates for the signal of $\delta^{18}O_{ice}$ are not available, and the values suggested by Lewis et al. [2010] and Hemming [2004] remain the best estimation for the signature of ice during a Heinrich Event.

The model/data comparison of LIG-125 also shows a mismatch in the sign of the SSST reconstructions. Other modeling efforts, such as Otto-Bliesner et al. [2013] have had more success at this comparison, however, the GHG concentrations used by that study were considerably higher than the values chosen here. As the uncertainties of the SSST reconstruction are again rather large, combined with the fact that the $\delta^{18}O_C$ comparison of the transient simulation fits with very small deviations, gives some pause to the claim that the mid LIG North Atlantic was warmer than during the PI.

Figure 4.12 shows the possibility of minimizing the misfit between the simulation and the proxy, given the uncertainty in the reconstructions and the model's standard deviation. 2σ are used to show the spread of SSST differences that COSMOS-WISO could simulate over a 100 year time span. It can be seen that nearly all proxy points can be reconciled, and the RMSE reduces to 0.23 °C

In conclusion, the proxy compilation made available by Capron et al. [2014] reveals some interesting features of the North Atlantic during the LIG. An anomalous cooling of the North Atlantic region during LIG-130 may indicate a relatively weaker AMOC during this time, a feature which is also present in the simulation. By utilizing multiple comparisons, it can be demonstrated that this cooling is possibly solely the result of COSMOS-WISO's simulation of the early LIG responding to climate, and that a freshwater perturbation may not be required to rectify any model/data discrepancies. COSMOS-WISO also able to reproduce the features found in the proxies during the mid LIG, yet the fit must rely on the relatively large uncertainties in the reconstruction and additionally the

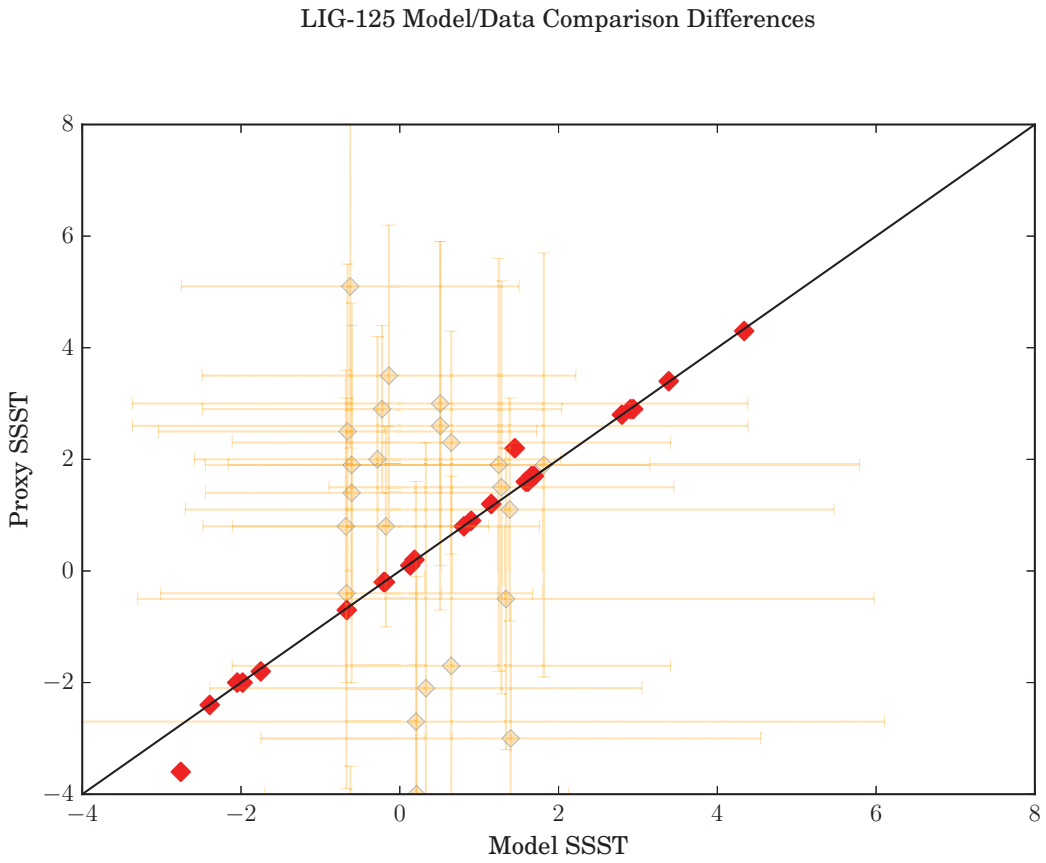

Figure 4.12: Deviations in SSST in the North Atlantic during LIG-125, utilizing the uncertainty in the proxy reconstructions as well as the model standard deviation to minimize differences.

large variability of the simulation in this region.

In the next section, proxy reconstructions of the Southern Ocean are examined and compared against the LIG realization produced by COSMOS-WISO.

4.2 Southern Ocean SSST Reconstructions

The Southern Ocean represents another key component in the climate system, as ocean/ice interactions with the Antarctic ice sheet can play an important role not only in ice sheet geometry, but also in global ocean circulation due to potential changes to Antarctic Bottom Water formation, which plays an important role in the Earth's carbon

budget as well as the heat distributions of the planet.

4.2.1 Proxy Description & Simulations Used

Utilizing paleoenvironmental information derived from micropaleonotological data sets has been an important tool assisting in paleoceanographic reconstruction since the initial development of the Imbrie and Kipp transfer function [Imbrie and Kipp, 1971] and Modern Analog Techniques developed by Hutson [1980]. More recently, Esper and Gersonde [2014a] developed a new diatom transfer function, enabling such techniques to be used for reconstructions of the Southern Ocean. A dataset consisting of 26 marine sediment cores has been obtained, and using the techniques described by Esper and Gersonde [2014a], these cores have been utilized to create reconstructions of Southern Ocean SSST, noting that summer here refers to austral summer; December, January, and February. A detailed description of the proxy follows.

Diatom Counts

Quantiative reconstructions of SSST and Winter Sea Ice (WSI) concentrations are based on the statistical analysis of diatom counts. In the Southern Ocean, diatom assemblages are useful tools for the reconstruction of the past environment, as diatoms are widely distributed. They are phototrophic algae living in the euphotic zone of the ocean, thus representing environmental conditions in the upper water column, and their biogeographic distribution patterns are closely related to SSST and WSI distribution, as has been shown by Esper et al. [2010], Esper and Gersonde [2014a], and 2014b. The counts on diatom species were carried out on permanent mounted slides of acid-cleaned materials. Following the taxonomy described by Zielinski and Gersonde [1997], the diatom taxa were counted at the magnification of x1000 with a Zeiss Axioplan II microscope with apochromatic optics. The counting procedure and definition of counting units followed

those of Schrader and Gersonde [1978]. A minimum of 400 specimens were counted in each sample.

Summer Sea Surface Temperature

The SSSTs were estimated using the Imbrie and Kipp transfer function method (IKM). The IKM is an application of principle component regression to generate a single calibration formula between diatom counts and the environmental variables [Imbrie and Kipp, 1971]. IKM is an effective method for diatom based SSST reconstruction in the Southern Ocean due to the strong relationship between diatom assemblage and SSST, analyzed by statistic methods of Detrended Correspondance Analysis and Canonical Correspondence Analysis, as discussed in Esper and Gersonde [2014a]

The reference data set (D336/29/3q) applied with IKM includes diatom assemblage data obtained from 336 sites from the Southern Ocean, considering the abundance pattern of 29 diatom taxa or taxa groups, and using 3 factor mode analysis. This data set deals well with high assemblage variability in SSST estimation [Esper and Gersonde, 2014a]. The referenced hydrographic dataset for SSST calibration represents values measured at 10 m water depth as presented by Olbers et al. [1992], a dataset not strongly affected by Southern Ocean warming during the last decades. The estimation of past surface ocean temperature is restricted to summer. This considers the results from sediment trap experiments, which showed significant diatom flux to the sea floor is restricted to austral summer in the Southern Ocean [Abelmann and Gersonde, 1991, Fischer et al., 2002]. Log transformation of the diatom abundance data was applied in order to reduce the dominance of *Fragilariopsis kerguelensis* and enhance the weight of less abundant taxa in calculation. The standard error of the estimates is 0.83 °C.

Winter Sea Ice Concentrations

The past WSI concentration was calculated by the MAT transfer function [Hutson, 1980]. This method searches for the best analogs based on similarity indexes between the surface sediment reference and the down-core assemblage, and uses the average for the modern conditions observed at these best analog sites as an estimate for past environmental conditions, dealing best with the non-linear distribution of sea ice. The MAT calculation is based on a 274 surface sediment sample diatom data set from the Atlantic, Pacific and Western Indian sectors of the Southern Ocean (D274/28/4an), considering the abundance pattern of 28 diatom taxa or taxa groups and calculated with 4 analogs, and showing high fidelity (Root Mean Square Error of Prediction 5.5%) in estimating the non-linear distributed Southern Ocean WSI concentration [Esper and Gersonde, 2014b]. The WSI estimates refer to September sea-ice concentrations averaged over a time period from 1981-2010 at each surface sediment site [Reynolds et al., 2002, 2007]

Establishing Chronologies

The timescales for the Southern Ocean are established following a so-called multi-proxy approach (Oliver Esper *personal communication*). Similar techniques have been documented by Xiao et al. [2016]. This multi-proxy approach allows to place the cores in a relative chronology, although exact dating (as would be done with a radioactive decay series) is not always possible. To begin, Termination II (T-II) is determined, signaling the end of the Penultimate Glacial Maximum (PGM). This is accomplished with a fossil index. The diatom species *Rouxia leventerae* and *Hemidiscus karstenii* become extinct at respecitvely the middle of T-II (approximately 130 ka B.P.) and the end of Marine Isotope Stage (MIS)-7 (approximately 191 ka B.P.). In conjunction with this measurement of diatom abundance, biogenic Opal has been shown to vary from low

values in glacial periods to high values during interglacials. This mass percentage gives a second indication of the termination.

Furthermore, XRD scanning of the sediment core can be used to determine the elemental composition. The abundance of calcium (Ca) reflects the calcifying biogenic components within the sediment core, which are high during warm periods. Iron (Fe) can be used as an indication of aeolian dust influence, which is higher during glacial periods. Finally, the ratio of silicon (Si) to titanium (Ti) shows the relationship between biogenic and terrestrial influence in the sediment core, which also follows a glacial/interglacial curve.

Lastly, the abundance and frequency of three diatoms can be used as glacial/interglacial indications: *Fragilariopsis kerguelensis* occurs frequently during warm periods, the genus *Chaetoceros* are frequent during the termination, and *Eucampia antarctica* is frequent during cold periods.

Using all of these multiple indicators in combination assists in generating a relative sequence of events throughout the LIG for the Southern Ocean sediment cores.

Model Simulations

In order to compare against these proxies, several simulations of both the penultimate glaciation, MIS6, as well as simulations of various time periods throughout the LIG are used. The used simulations are summarized below in Table 4.2. Each time-slice underwent a spinup as described in Section 3.1.

4.2.2 Temperature Comparison

In Figure 4.13, SSST values for the Southern Ocean are compared against model output for the three time slices described in Table 4.2. All values are displayed as anomalies against PI.

Table 4.2: Description of the simulations described in the study comparing COSMOS-WISO with southern ocean sediment cores. GHG and orbital forcings applied to each. Ice sheets are fixed to pre-industrial geometry for LIG simulations, whereas an LGM geometry is assumed during MIS6. Vegetation is initialized from pre-industrial and allowed to evolve as the model equilibrates.

Experiment (Age ka B.P.)	CO_2 (ppm)	CH_4 (ppb)	NO_2 (ppb)	Eccentricity (-)	Obliquity (°)	Precession (-)
PI (0)	280	760	270	0.016724	23.446	282.04
MIS-5.5 (120.0)	268	572	261	0.041090	22.998	209.04
Late T-II (128.0)	276	709	266	0.039017	24.133	79.70
MIS 6 (140.0)	185	350	200	0.032796	23.414	253.244

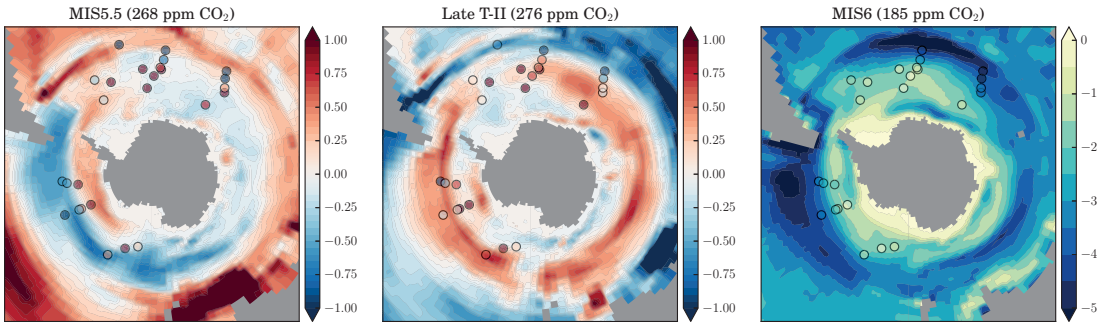

Figure 4.13: Deviations in SSST in the Southern Ocean during MIS-6, T-II, and MIS-5.5.

The simulation of MIS-6 can capture the cooling around the Antarctic continent. The proxies display some spatial hetereogenity, with slightly less cooling closer to the continent. COSMOS-WISO appears to be able to capture this quite well, and the fronts are well represented. The simulations of both T-II and MIS-5.5 also display a good spatial match with the proxy reconstructions; a warming of between 0.25 °C to 0.5 °C is simulated around the entire Southern Ocean during T-II, with cooling of between −0.5 °C to −1.0 °C slightly further north, signals which are mirrored in the proxy reconstructions. The simulation of MIS-5.5 displays an anomalous cooling of between −0.25 °C to −0.75 °C in the Pacific sector of the Southern Ocean, a pattern which is also seen in the proxy measurements. Some mismatch can be seen in the Atlantic sector during this time period, with COSMOS-WISO simulating slightly cooler values despite the proxies indicating

rather pronounced warming of between 0.5 °C to 1.0 °C.

4.2.3 Sea Ice Extent Comparison

Next, Figure 4.14 shows the comparison of the WSI reconstructions, which are based upon a MAT, with the simulations.

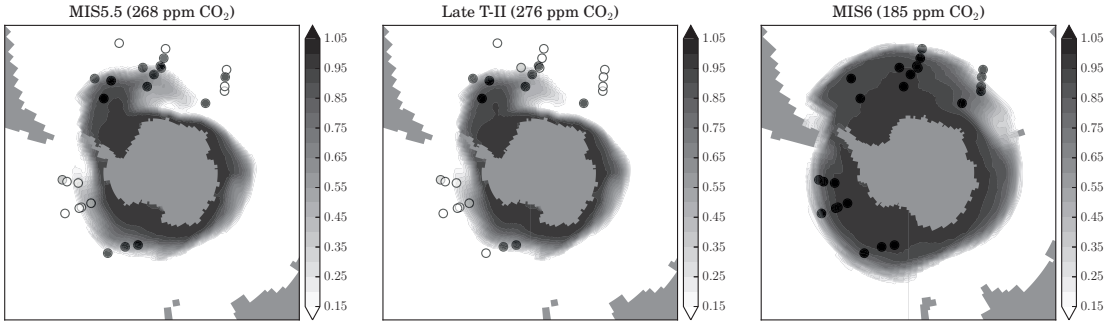

Figure 4.14: Spatial comparison of winter sea ice concentration as recorded by proxies and simulated by COSMOS-WISO for MIS-6, T-II, and MIS-5.5

Contrary to the reconstructions of SSST, the sea ice reconstructions and simulations by COSMOS-WISO differ greatly, especially for the 2 stages of the LIG. The sea ice extent during MIS-6 roughly matches the area simulated by the model, however, the model appears to grossly underestimate the sea ice extent recorded by the proxy during both T-II and MIS-5.5. Despite this, the model and the data generally agree qualitatively. While the magnitude of sea ice concentration in the proxy is much higher than what is simulated by COSMOS-WISO both the simulation and the reconstruction show an expanded sea ice area during the glacial, and a reduction of the area during the interglacial.

This mismatch is not necessarily surprising, as simulating sea ice extent and variability remains one of the principle challenges for GCMs, as has been documented by e.g. DeWeaver et al. [2008], Winton [2011], and Notz [2012], and it is possible that improving the simulation resolution may partially assist in rectifying the mismatch. Furthermore,

the proxy reconstructions are based upon paleoecological rather than geochemically or physically robust measurements, and it has been discussed that the techniques used in this field to reconstruct quantitative results from ecological information is not without limitations [Juggins, 2013]. Indeed, reconstructing sea ice has, just as in modeling, been a key challenge for the paleoclimate proxy community as well [Armand and Leventer, 2010].

4.2.4 Quantifying Model/Data Differences

Finally a quantitative comparison of the temperature differences simulated by COSMOS-WISO and measured in MAT reconstructed SSST is presented in Figure 4.15.

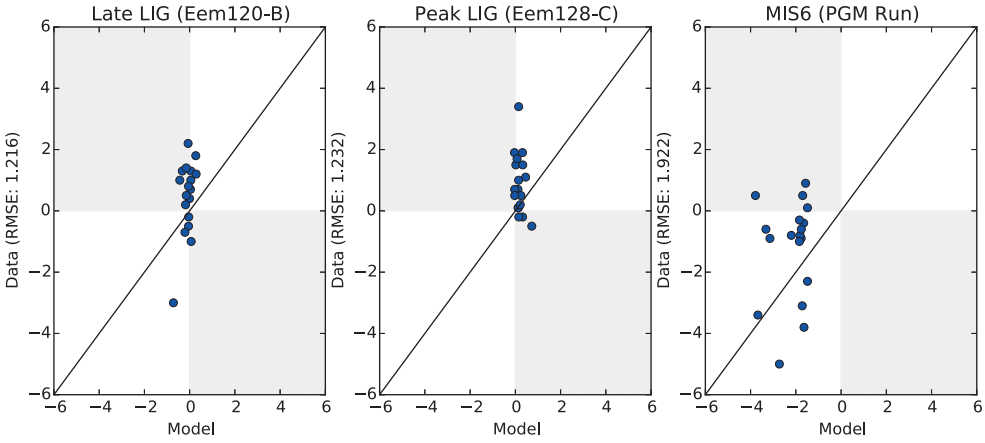

Figure 4.15: Quantitative comparison of simulated vs. measured SSST in the southern ocean during the penultimate glaciation, termination, and last interglacial.

It can be seen that COSMOS-WISO is unable to reproduce the same variability during the LIG as is measured by the proxies. Furthermore, while the model correctly captures the sign of the anomalous temperature change, the magnitude is also generally underestimated, both during the simulation of MIS-5.5 and during T-II, and slightly overestimated during the simulation of MIS-6, demonstrating that the model might not be sensitive enough in the Southern Ocean. Despite this, the overall errors between

the simulation and the data are still smaller compared to the reconstruction/simulation differences seen for the North Atlantic. This is in part because the fronts are better captured in the Southern Ocean, and very few points show opposite signs between the simulation and reconstruction anomalies. As was the case for the North Atlantic, the model/data discrepancies may also reduce if the simulation were repeated with a higher resolution.

4.2.5 Discussion

It is not surprising that both the simulation as well as the proxy reconstructions show a cold climate during MIS-6, as this is a result of the glacial climate forcing, due to the large ice sheets modifying the planetary albedo, the decreased GHG concentrations, and the orbital forcing. Examining the two time periods during the LIG reveals some interesting differences. The simulation of T-II demonstrates a fairly uniform warming of the Antarctic Circumpolar Current (ACC), which persists throughout the entire year. Both the proxies and the simulation capture an abrupt spatial gradient further toward the north, with SSST values between $-0.25\,°C$ to $-1.0\,°C$ lower than in the PI, as can be seen in Figure 4.13-B. An examination of the insolation anomaly (Shown in Figure 4.16) reveals that austral summers receive between $-20\,W\,m^{-2}$ to $-50\,W\,m^{-2}$ less radiation during T-II than during PI, possibly explaining the cooling north of the ACC.

The warming of the ACC itself may be a result of the bipolar interhemispheric seesaw mechanism, initially discussed by Crowley [1992], later modified in a conceptual model by Stocker and Johnsen [2003], and more recently by Barker et al. [2009]. In essence, the bipolar seesaw couples the heat reservoir in the ocean to the Thermohaline Circulation (THC) system; the density driven meridional overturning circulation shown in pioneering work by Stommel [1961]. As the THC transports a substantial amount of heat northward, a weakening of this circulation results in cooling in the North Atlantic,

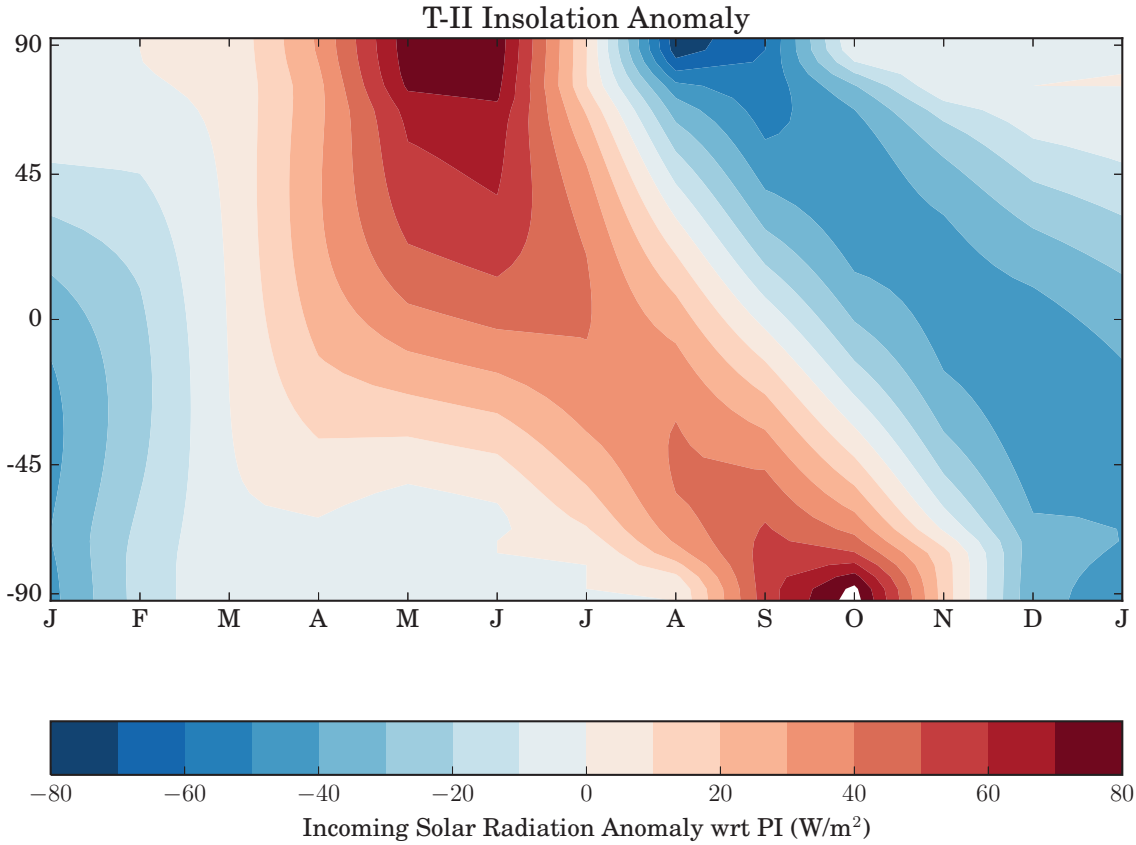

Figure 4.16: Insolation anomaly relative to PI for the simulation of T-II.

and a corresponding warming in the Southern Ocean, as the heat is no longer exported northwards.

As such, the warming seen in the ACC may be indicative of a weaker AMOC at this time. While the latter study by Barker et al. [2009] discussing the bipolar seesaw during deglaciations focused on the most recent deglaciation (Termination I, also T-I), it has been suggested that a similar mechanism may occur during T-II [Landais et al., 2013]. As was the case for the comparison of LIG-130 in the North Atlantic, where the AMOC was slightly weaker, during T-II, this is also the case, as is shown in Figure 4.17.

During the simulation of MIS-5.5, the response of the Southern Ocean is more varied. The Pacific sector cools by between $-0.5\,°C$ to $-1.0\,°C$ in both the simulation and the

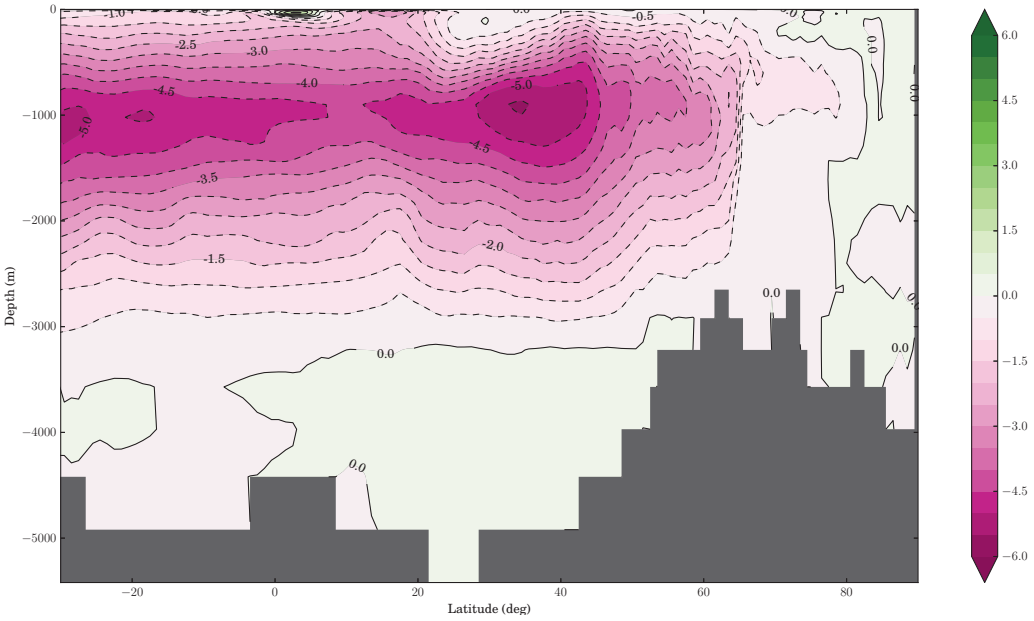

Figure 4.17: Anomalous AMOC strength relative to PI during the simulation of T-II.

proxy reconstructions, whereas the Atlantic sector is reconstructed to be slightly warmer than PI, although the simulation is not able to match the proxy reconstruction's warming magnitude, nor is it able to simulate a cooling front found in the proxy data. This spatial hetereogenity may be a result of both changes in the insolation as well as transport into the Southern Ocean from other ocean basins. The MIS-5.5 simulation has overall less incoming solar radiation during the austral winter (as shown in Figure 3.1), potential explaining the cooling in the Pacific Ocean, and water coming in from the Atlantic via the South Atlantic gyre is slightly warmer than in PI (shown in Figure 3.8), possibly explaining the warming in the Atlantic sector of the Southern Ocean.

In the next section, an example of a highly temporally resolved proxy taken from fossilized coral records is examined in order to determine changes to the seasonal amplitude of Atlantic tropical temperature during the LIG

4.3 Using Corals to Examine Seasonal Amplitude

A further aspect of the climate system that is important to understand is seasonal temperature amplitude in the tropical ocean, as this area plays an important role in seasonal climate extremes, such as hurricanes, floods, and droughts. The variability of the tropical Atlantic climate plays a significant role in larger scale climate patterns and although a fairly comprehensive picture of the modern variability of this region is know, the implications of past changes to this system have not been fully explored. In the Caribbean basin, SST variability is the result of variations in several factors, most importantly variations in the North Atlantic sea level pressure that modulates the surface winds, inducing fluctuations to the Atlantic Warm Pool (AWP). The AWP is characterized by modern surface water temperatures of approximately 28.5 °C, and experiences flucations on seasonal, interannual, and multidecadal time scales, as has been discussed by Wang et al. [2008]. On the longer time scales, both El Niño/Southern Oscillation (ENSO) as well as Atlantic Multidecadal Oscillation (AMO) perturb the AWP, thereby modifying the climate of the tropical Atlantic. This can cause changes in hurricane activity, and furthermore, precipitation in the Sahel region originates here.

Unfortunately, very few paleoclimate proxies are able to reconstruct temperature seasonality due to constraints of temporal resolution. One archive that does have this ability is fossilized coral reefs, and these records have been used to make deductions about temperature seasonality of the Carribbean during the Holocene [Giry et al., 2012] and late LIG [Felis et al., 2015], and have been also useful in examining climate changes in the Red Sea during the LIG [Felis et al., 2004], where increased SST seasonality has been attributed to a more positive state of the North Atlantic Oscillation (NAO). Coral records have additionally been employed to study ENSO variability in the Pacific [see Hughen et al., 1999, Tudhope et al., 2001], Termination II [McCulloch et al., 1999], and modulations in the Kurshio Current [Suzuki et al., 2001]. Both McCulloch et al. [1999]

and Suzuki et al. [2001] report increased western Pacific SST seasonal amplitude during the LIG.

In the following study, tropical Atlantic SST variability is assessed as recorded by fossilized corals. COSMOS-WISO simulations were used to further examine possible seasonality changes in the Carribbean, and a model/data comparison of seasonal amplitude variations in SST is presented.

4.3.1 Study Area and Coral Material

The island of Bonaire ($12°10'N, 68°18'W$) is located approximately 100 km from the north coast of Venezuela. Modern day observations characterize the climate of Bonaire as semi-arid, with less than 550 mm per year of precipiatation and dominant easterly trade winds. Seasonal SST varies between a mean winter minimum of 25.8 ± 0.6 °C, and a mean maximum of 28.3 ± 0.5 °C throughout the measurement period made available from 1910-2000 by the ERSSTv3b Dataset [see Smith et al., 2008].

Cores from 32 fossil *Diploria strigosa* coral colonies were drilled during expeditions in 2006 and 2009 from the top of an elevated reef terrance along the north-eastern and eastern coast of the island of Bonaire. This material was obtained between 1.5 m to 5.5 m above present sea level. Thin cross sections of 6 mm to 7 mm were extracted, and microsampling extracted material directly parallel to the direction of coral growth. 7 of these 32 colonies were then utilized for further analysis, based upon their suitability to produce long and reliable geochemical records.

4.3.2 Sr/Ca Paleothermometry and Coral ^{230}Th/U Dating

Annual growth rates based upon annual density bands seen in X-radiographs of the corals were estimated using techniques described in Giry et al. [2010], Giry et al. [2012], and Felis et al. [2015]. Based upon these growth rates, the corals were microsampled in

such a way as to ensure that twelve samples per growth year were obtained. Seasonal amplitude was determined by subtracting the maximum Sr/Ca value from the minimum, and the average of all years recorded for a coral colony was used to determine the mean Sr/Ca seasonlity value. This seasonality was converted to a SST seasonality following the Sr/Ca-SST relationship of $-0.042\,\mathrm{mmol\,mol^{-1}\,°C^{-1}}$. This relationship was initially described for *D. strigosa* by Hetzinger et al. [2006]. This calibration closely replicates the instrumental SST record for Bonaire, as was demonstrated by Giry et al. [2012], who used three modern coral colonies. The comparison against modern measurements is shown in Figure 4.18, adapted from Brocas et al. [2016].

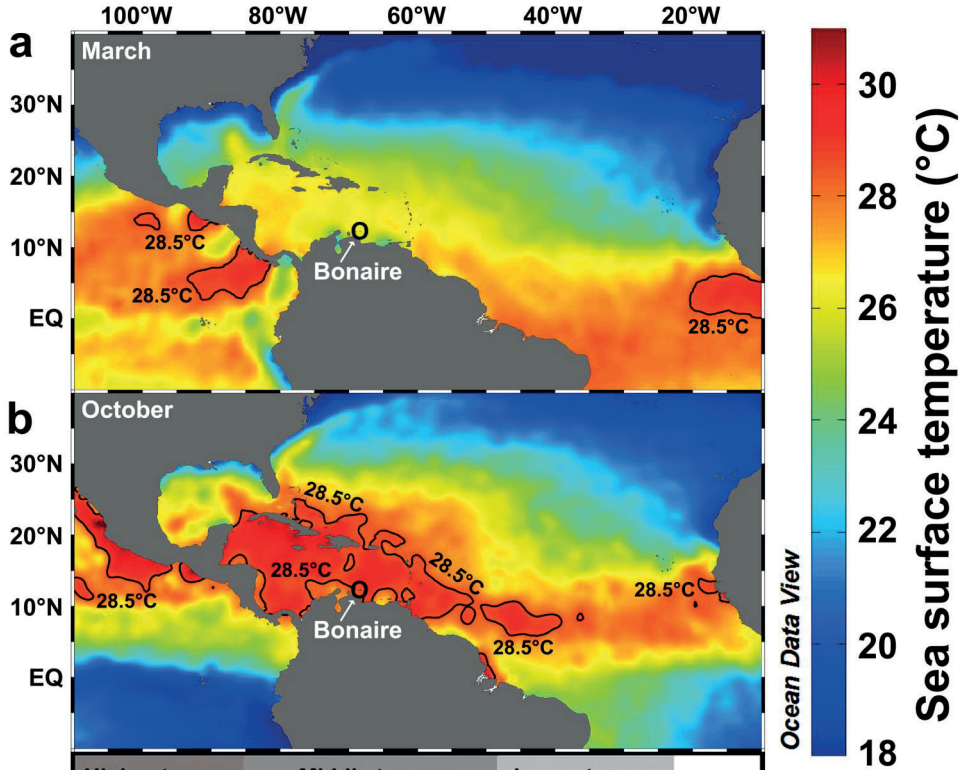

Figure 4.18: Adapted from Brocas et al. [2016], demonstrating SST as measured by the EESSTv3b dataset in comparison with the modern coral Sr/Ca measurements. The top panel A shows the minimum temperature in winter (March), while the bottom panel B shows the maximum temperature in summer (October)

In order to assign precise dates to each of these samples, ^{230}Th/U was employed, as described by Obert et al. [2016]. The ages, lengths and seasonal amplitudes of each coral

Table 4.3: Details of the coral Sr/Ca records employed for the investigation of Carribbean SST seasonal amplitude changes during the LIG

Sample ID	Age (ka)	Standard Error (ka)	Record Length (yr)	Sr/Ca Seasonality (mmol/mol)	SST Seasonality (°C)
BON-5-D	117.7	0.8	20	0.109 (0.003)	2.6 (0.1)
BON-5-A	120.5	1.1	14	0.129 (0.011)	3.1 (0.3)
BON-28-AI	12.3	3.1	6	0.128 (0.013)	3.0 (0.3)
BON-12-A	123.9	1.3	37	0.172 (0.008)	4.1 (0.2)
BON-26-A	124.9	1.9	3	0.139 (0.016)	3.3 (0.4)
BON-24-AII2	125.5	2.4	5	0.139 (0.019)	3.3 (0.5)
BON-13-AI.1	125.8	1.6	10	0.205 (0.023)	4.9 (0.5)
BON-33-BI.2	129.7	1.7	10	0.124 (0.017)	2.9 (0.4)

record are summarized in Table 4.3.

These coral based SST amplitudes are compared to the Carribbean SST amplitudes produced by the simulations described in Chapter 3, representing time slices for LIG-130, LIG-125, and LIG-120. The forcings for these simulations are summarized in Table 3.1, on page 34.

4.3.3 Comparing Temperature Seasonality

The seasonal amplitude as recorded by the corals is presented in Figure 4.19. A distinct increase in seasonal amplitude to 4.5 °C can be seen during the mid LIG, which declines back to modern levels towards the end of the LIG, where seasonal amplitudes are approximately 3.0 °C.

Comparing these results to the model simulations, a similar pattern can be found, with an increase in seasonal amplitude during the mid LIG simulation (seasonal amplitude of approximately 5.5 °C), and a decrease towards the end of the LIG (seasonal amplitude of 4.2 °C. This comparison is shown in Figure 4.20. Both the relative increase during the mid LIG and the return to close to PI conditions are well captured in both the

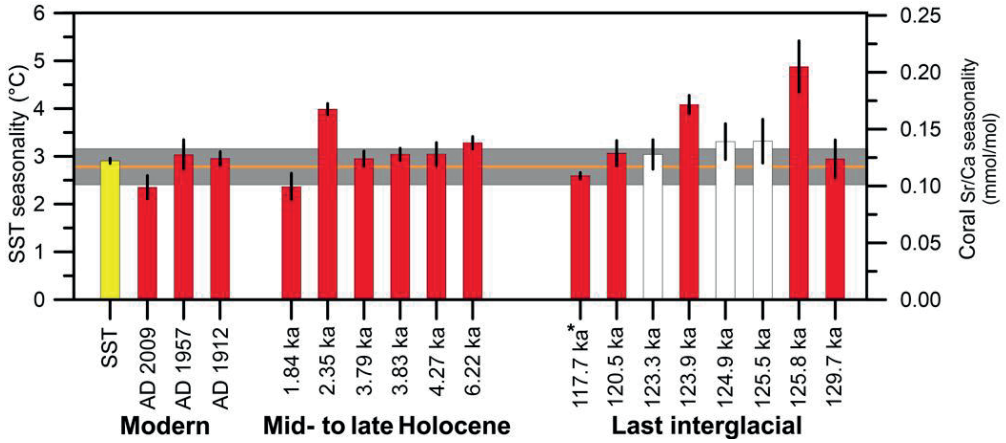

Figure 4.19: Reproduced from Brocas et al. [2016]. Bar chart showing the seasonal amplitude of SST at Bonaire as recorded by fossilized corals. The modern day average SST is shown in yellow, with one standard deviation shown in the shaded gray area. The measurement uncertainty is shown in the error bars for each coral.

Table 4.4: Relative changes relative to PI (Modern) in seasonal amplitude at Bonaire in the simulations (coral measurements).

Experiment	Model	Corals
	%Δ w.r.t. PI	
LIG 130	41	-3
LIG 125	66	83
LIG 120	16	3

simulation as well as in the corals, as shown in Figure 4.20-A.

Expressing the seasonal amplitudes changes in percent relative to PI eliminates a possible error bias, as simulated changes are compared to the simulated PI control simulation, and measured changes and compared against the measured modern-day control coral. These percentages are shown in Table 4.4.

Prior to the investigations conduced in this study, LIG tropical Atlantic SST variability had only been examined by a four year record of SST in the north eastern Carribbean [Winter et al., 2003], and a twenty year record from the end of the LIG at the same site as the present study, by Felis et al. [2015]. Based upon these two studies, SST seasonality

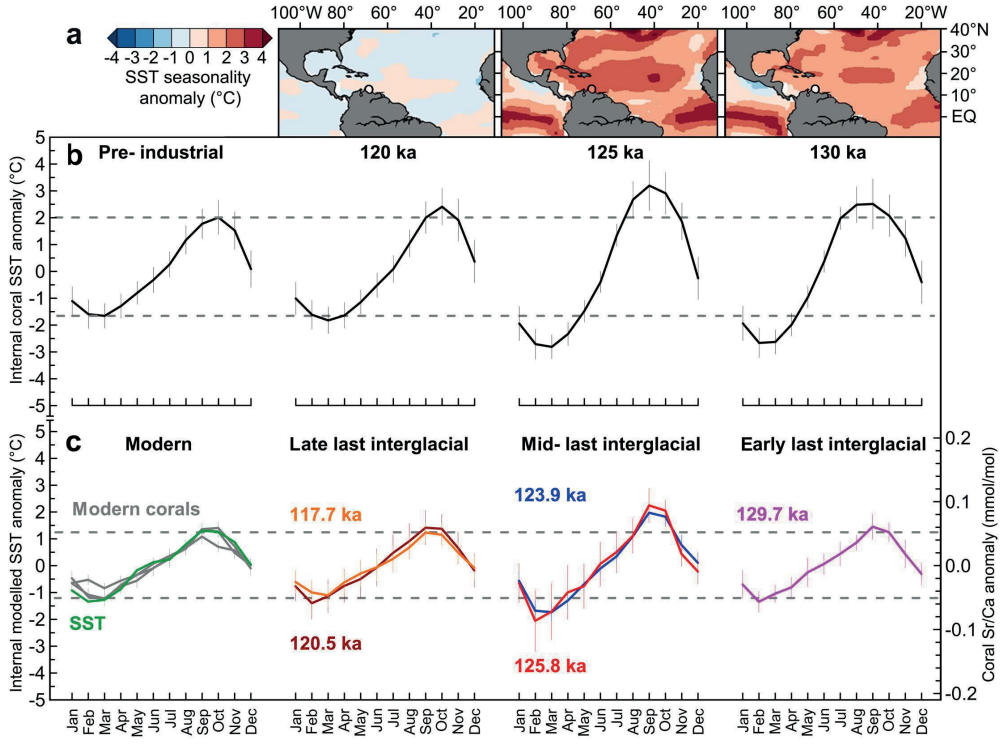

Figure 4.20: Reproduced from Brocas et al. [2016]. Panel A demonstrates the deviations of the seasonal amplitude from the PI time period, showing an agreement between both the late and mid LIG simulations. Panel B shows the monthly deviations from the annual mean temperature for each simulated time slice, while panel C shows the same monthly deviations as recorded by the fossilized coral records.

was respectively reported to be slightly higher (variations of 1.0 °C) and within the same range as modern day seasonal amplitudes. Here, these results are confirmed, as an increase of seasonality is only reconstructed for the mid LIG.

In the Northern Hemisphere, the annual cycle of insolation was significantly enhanced during the LIG, as shown in Figure 3.1 on page 36. This enhanced insolation is driven by an increase value in orbital precession. The significantly increased seasonality recorded by the coral proxies at 125.8 ka B.P., also simulated by COSMOS-WISO coincides with the peak of insolation at around 125.5 ka B.P. reported by Berger [1978]. The primary advantage offered by combining coral reconstructions with global simulations lies in the ability to detect the mechanism behind the increase of seasonality, which

is caused primarily by summer warming, contrary to conclusions reached by previous examinations of the area [Winter et al., 2003].

The LIG remains an important testing ground for hypothesis testing of the dynamics of warm climate states. By studying sub-annual climate variability utilizing coral records, Brocas et al. [2016] discovered that the peak LIG SST seasonality of the tropical North Atlantic was enhanced relative to PI amplitudes, and that the primary cause of this amplification is tied to the orbital forcing of the climate. In the last model-data comparison of this chapter, the simulations of the LIG realized by COSMOS-WISO are compared to long records of climate variability; ice cores extracted from both the Greenland and Antarctic Ice Sheets which enable for an examination of climate changes over glacial-interglacial cycles.

4.4 Comparing Isotopic Values in Ice Cores

The isotopic composition of an ice core is affected by climate and water cycle variability, due to change in the evaporation conditions, the air mass trajectory and distillation history, as well as local condensation conditions [Noone and Simmonds, 1998, Masson-Delmotte et al., 2006, Sodemann and Stohl, 2009]. Changes in the ice rheology may also have an impact. Vinther et al. [2009] found that elevation can influence the overall trend of the $\delta^{18}O$ signal. This altitude effect can be responsible for a depletion of $-0.6\,‰$ per 100 m. This is primarily due to cooling of an air mass as it is forced to rise over the ice sheet, and as the air mass cools, precipitation is formed and fractionation takes place. Furthermore, the origin of the ice plays an important role on the isotopic composition of the ice core. Huybrechts et al. [2007] showed that temperature biases resulting from changes in elevation may result in variations that are up to half as strong as the climatatic effects, suggesting that the origin of ice (i.e. the deposition site) and how ice flows from this location to the drilling site may cause some variations in the

measured signal. Unlike the calcite measurements discussed in Section 4.1, or the coral measurements in Section 4.3, COSMOS-WISO can be directly compared to the isotopic values in ice cores, as no transfer function must be applied to these archives.

A study by Masson-Delmotte et al. [2010] examined the LIG as recorded by various ice cores in the Antarctic. It was primarily found that all ice cores recorded the LIG in a similar fashion, with some inter-site differences caused by precipitation intermittency biasing. Masson-Delmotte et al. [2010] indicate that utilizing stable water isotope enabled GCMs could assist in identifying variations in moisture sources and air mass trajectories, which may ultimately be responsible for such inter-site differences.

As it has often been mentioned, model resolution may cause some problems in model/data comparison, and it is necessary to examine if ice records are subject to localized effects that would not be captured by the simulations. Some work has demonstrated that some local effects may cause signal noise at the ice core site [Münch et al., 2015] when examining decadal variations with various firn drilling sites over lateral distance of several meters, but it was determined that ice cores are generally reliable records over long time scales, thus providing an accurate recorder of the $\delta^{18}O_P$ and δD_P signatures during past climate states. This would suggest that minor shifts in the drilling site would likely not cause differeces in the ice core record.

This next study aims to examine the feasibility of COSMOS-WISO at the relatively coarse resolution of T31L19 (See Chapter 2 for more details about the model resolution) to compare against measurements of $\delta^{18}O$ in Antarctic ice cores, as well as examining the temporal stability of the $\delta^{18}O/T$ relationship used by glaciologists to reconstruct temperatures from ice core measurements.

4.4.1 Ice Cores Used

Figure 4.21 shows the names and locations of the ice cores used in this comparison. Some of these ice cores are used by Capron et al. [2014] to construct the North Atlantic data compilations. All of these ice cores have been published on the EDC age scale [Masson-Delmotte et al., 2010], and the $\delta^{18}O_{ice}$ comparison is made utilizing that chronology.

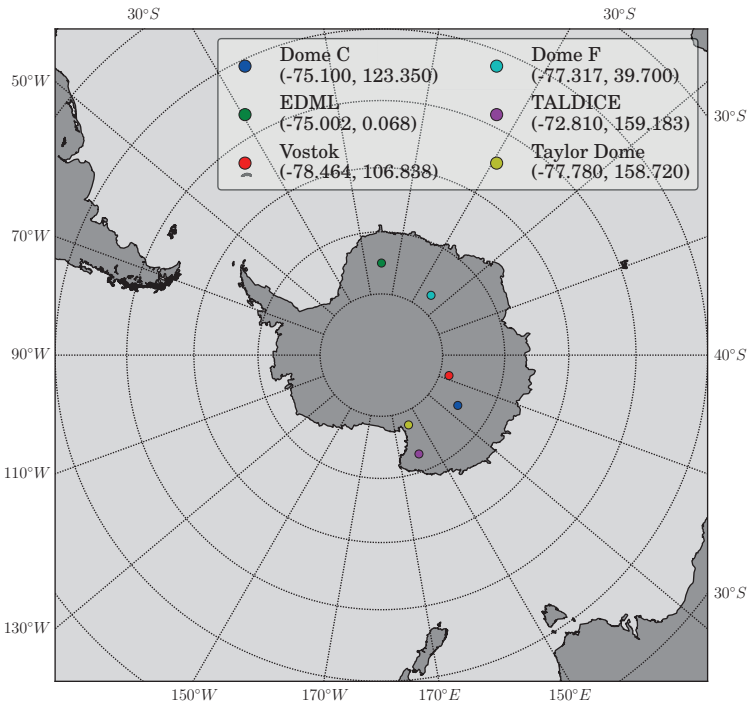

Figure 4.21: Locations of Antarctic ice cores which COSMOS-WISO is compared against.

The ice cores have been initially examined and published by:

Vostok Originally published by Lorius [1985], extended into the penultimate glacial maximum by Jouzel et al. [1993]

Dome F Watanabe et al. [2003]

Dome C Jouzel et al. [2007]

EDML EPICA community members [2004]

Taylor Dome (TD) Grootes et al. [2001]

TALDICE Stenni et al. [2001]

4.4.2 Quantifying Differences: Antarctic Ice Cores

Values of $\delta^{18}O_P$ from the transient experiment LIG-T are compared against $\delta^{18}O_{Ice}$ values at each of the core locations in Figure 4.22

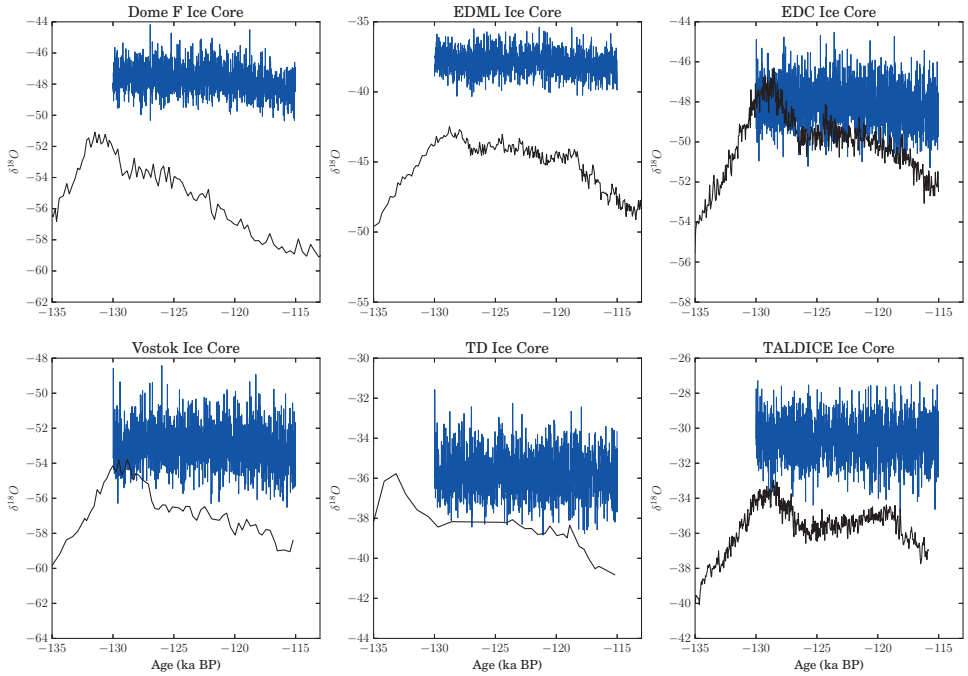

Figure 4.22: $\delta^{18}O$ simulated by COSMOS-WISO compared to the reconstructions gained from several Antarctic ice cores

An initial examination reveals that all of the ice core locations in the simulation are enriched relative to the measurements from the actual ice cores, with an offset between 2‰ to 8‰. This may in part be due to the coarse orography of the simulation. The elevation as measured at the core site (taken from Masson-Delmotte et al. [2010]) is compared to the elevation in the model orography in Figure 4.23.

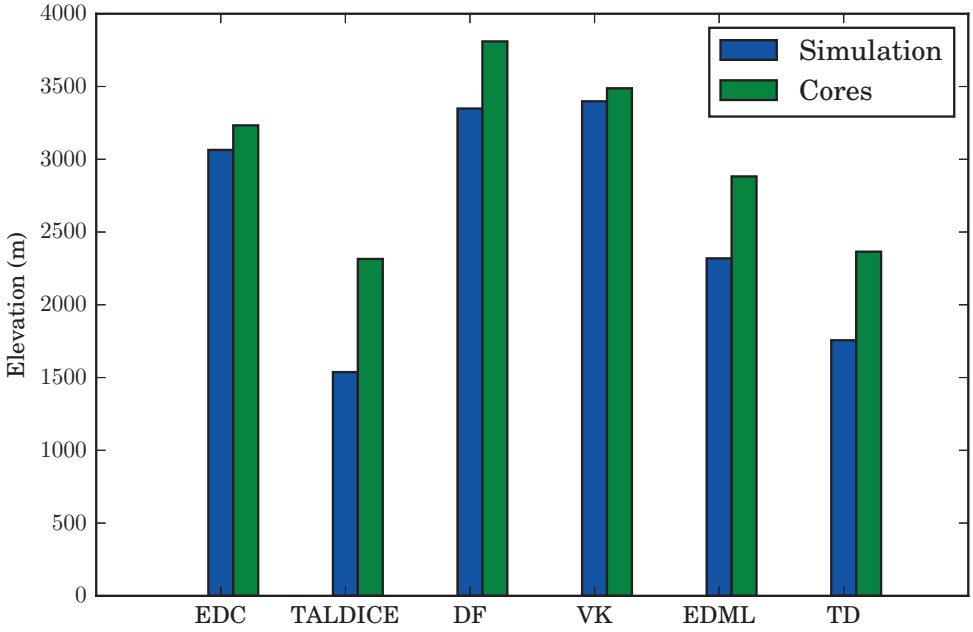

Figure 4.23: Simulated vs measured ice core elevations for 6 Antarctic Ice Cores.

Using the elevation correction of $-0.6\,‰$ per 100 m as found by Vinther et al. [2009], it is possible to partially rectify the offset caused by the coarse elevation. Upon applying this correction, the large offset seen in Figure 4.22 improves slightly, as can be seen in Figure 4.24

While the elevation correction assists in rectifying the offset between the simulation and measurements, the model is still too enriched for DF as well as EDML. This might indicate that the Atlantic sector of the Southern Ocean, where precipitation for these two ice cores originates, may be too enriched in the model. The other ice cores demonstrate simulated signatures that overlap with the measurements, particularly for the EDC and TALDICE cores. These two cores also display the highest temporal resolution, capturing the transient evolution of the LIG's rapid peak warming and extended plateau before the next glacial period begins. This transient evolution of the LIG is not very well represented in the simulation, and neither the rapid peak nor the slow depletion of $\delta^{18}O$ is see in the simulation.

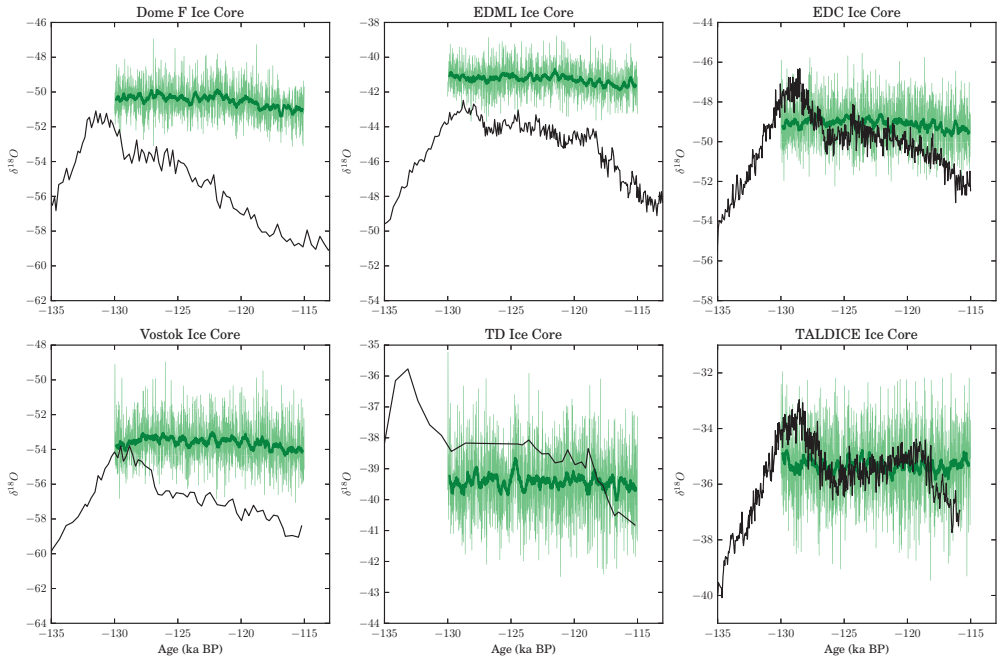

Figure 4.24: $\delta^{18}O$ simulated by COSMOS-WISO compared to the reconstructions gained from several Antarctic ice cores, incorporating a correction for coarse model elevation. A 30 point smoothing is shown by the thick green line.

When initially validating the atmospheric component of COSMOS-WISO against measurements for the Antarctic, Werner et al. [2011] found that even at very high resolutions (T159L31), ECHAM5 fails to reproduce the cold temperatures over the Antarctic continent. As a result, the isotopic values in ECHAM5-WISO are less depleted than in the observations. This warm bias is not unique to COSMOS-WISO, and is also found by other GCMs (e.g. Lee et al. [2007], Risi et al. [2010]). The underestimation of the cold extremes over Antarctica may be partially liked to poor representation of the polar atmospheric boundary layer in climate models, as discussed by Krinner et al. [1997].

Despite these offsets, it is of value to see if the COSMOS-WISO is able to reproduce the $\delta^{18}O$/T relationship over the Antarctic, and if this relationship remains stable for that region throughout the LIG's evolution. Modern observations indicate a $\delta^{18}O$/T relationship of 0.80 ± 0.01 ‰ $^{\circ}C^{-1}$ [Masson-Delmotte et al., 2008]. As was done in Section 3.5.4.3, the correlation coefficient R^2 as well as the slope of the regression line for

both arithmetic as well as precipitation weighted yearly mean temperature vs $\delta^{18}O_P$ are considered. The analysis is performed over a running window of 100 years, and the correlation coefficient R^2 as well as the slope of the regression line m is recorded, generating a timeseries of $\delta^{18}O/T$ correlations and slopes. The timeseries of the $\delta^{18}O/T$ regression slopes is shown in Figure 4.25.

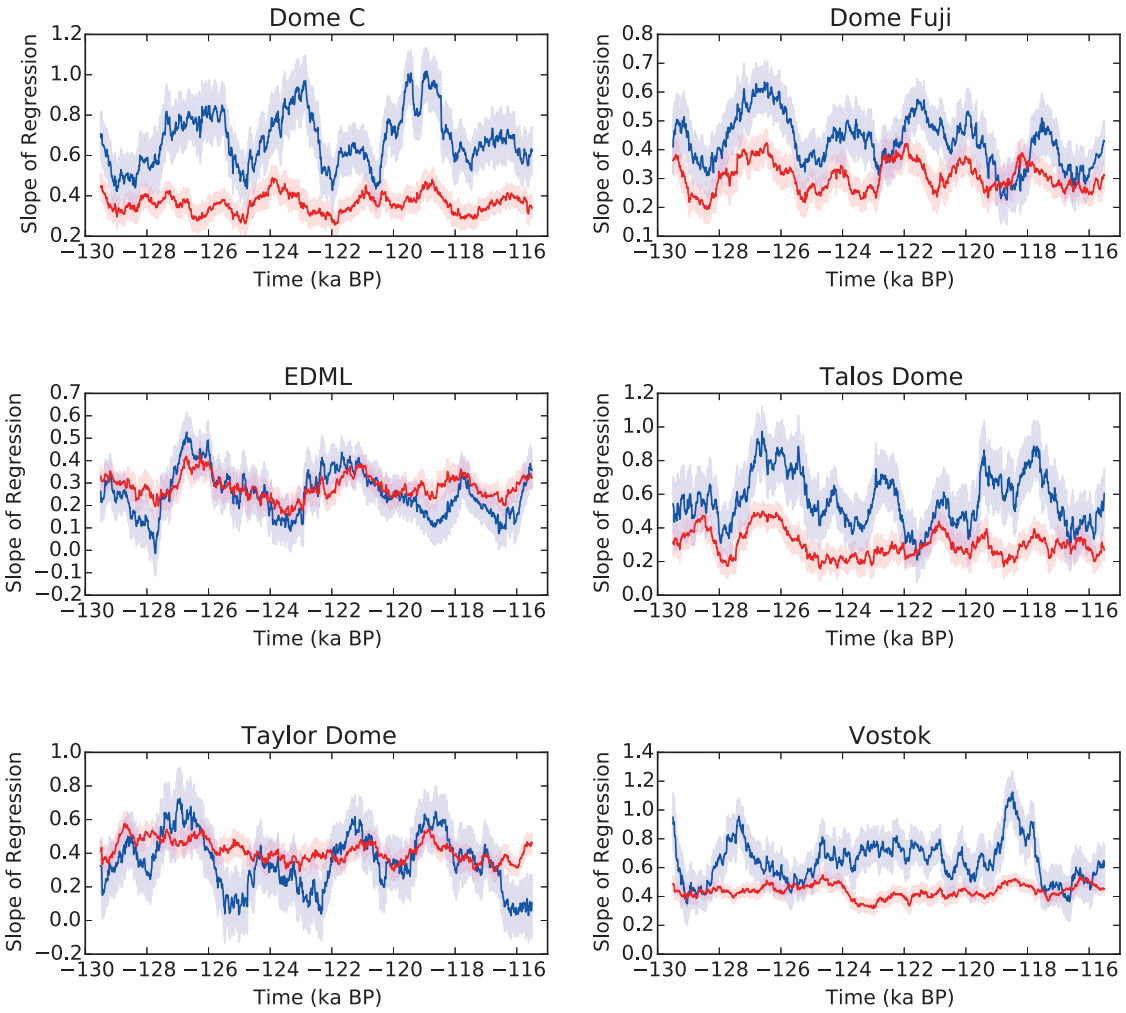

Figure 4.25: Slope of the linear regression line, showing the $\delta^{18}O/T$ relationship. Red lines indicate precipitation weighted temperatures have been used in constructing the relationship, whereas blue lines indicate that arithmetic means have been used.

While the relationship between yearly mean temperature and $\delta^{18}O$ is highly variable

throughout the LIG, this is not necessarily surprising, as it has already been established that the $\delta^{18}O$ signal has a precipitation intermittency bias (see Section 3.5.4.3). With the exception of the Dome Fuji and EDML ice cores, the $\delta^{18}O/T$ relationship remains stable throughout the LIG when precipitation weighting is applied. The values also are close to the value of $0.4\,‰\,^{\circ}C^{-1}$ which Werner et al. [2001] found for modern simulations using a T31L19 version of COSMOS-WISO. Werner et al. [2001] also found that increasing the resolution significantly improved the relationship, bringing it more in line with the observed values.

One aspect has not been examined here, namely that it is likely that the West Antarctic Ice Sheet (WAIS) was reduced during the LIG, as discussed later in Chapter 6. Future work could examine the changes of these results if an artificial reduction of the WAIS is incorporated in the simulation.

4.5 Conclusions and Next Steps

In this section, it has been demonstrated that COSMOS-WISO is able to reproduce both reconstructions for the North Atlantic, as well as for the Southern Ocean. Anomalous temperatures from both of these reconstructions point towards a weaker AMOC during the peak LIG, resulting in cooling in the North Atlantic, and relative warming in parts of the Southern Ocean. While COSMOS-WISO is unable to perfectly reproduce the climate reconstructions recorded by these proxies, this may very well lie in the fairly coarse model resolution, which is necessary to generate paleoclimate simulations, due to trade offs with computation time.

Furthermore, COSMOS-WISO is also able to reproduce high frequency changes as recorded by fossilized corals. Increases in the seasonal amplitude of tropical Atlantic SSTs are connected to changes in the insolation during the LIG. While the model overestimates the seasonal amplitude change during the early LIG, this may be due to

the fact that the simulation for LIG-130 was initialized from a warm climate state, and as such, any memory effects due to the preceding ice age are not taken into account.

COSMOS-WISO fails at reproducing the isotopic records of the LIG that are gained from Antarctic ice cores. While this is partially due to coarse model resolution, an elevation correction only assists in rectifying the offset between the simulation and the ice core records. The transient nature of the LIG is not well captured by the model, and this may be due to missing feedbacks that are not incorporated in the simulation. As was discussed in the Introduction (see Section 1.4), it is believed that the sea level was between 4 m to 9 m higher during the LIG than during the PI, and this indicates that the ice sheet geometry of both the Antarctic as well as the Greenland ice sheets must have been different than the present configuration. This critical feedback may be responsible for the offset in the model simulations of the Antarctic $\delta^{18}O$. While the stability of the ice sheets during the LIG is a topic reserved for Chapter 6, the next section shall examine how the climate would respond to the large amounts of freshwater that would be released during an ice sheet melt water pulse, in order to see to what extent the climate states may be influenced by large perturbations.

CHAPTER 5

Stability of the Last Interglacial Climate under Freshwater Perturbation

Climate states are by no means stable. If one examines records of the past climate, it immediately becomes clear that many of these records demonstrate a high level of variability, both from the oscilation between glacials and interglacials, as was already described in Section 1.2 and 1.4, but also on shorter time scales.

So-called rapid climate changes might be thought of as non-linear responses in the climate system, and these may occur on the order of decades to centuries, rather than the relatively slow changes of ice build up and collapse occurring between glacial and interglacial intervals. Both sudden meltwater pulses (Heinrich Events, reviewed by Naafs et al. [2013]) as well as ice sheet geometry changes [Zhang et al., 2014, Zhu et al., 2014] have been shown to cause abrupt reorganizations of the Atlantic Meridional Overturning Circulation (AMOC), which in turn reorganizes the heat distribution of the climate system. These changes to the AMOC are considered to be one of the primary

mechanisms for rapid climate change.

5.1 Proxy Indications of Rapid Climate Change during the LIG

While the mechanisms described above are generally constrained to glacial climates due to the requirement of large ice sheets for the rapid input of melt water and change in large orographic barriers; there have been recent indications that interglacials may be susceptible to rapid climate change as well [Nicholl et al., 2012]. Freshwater input into the North Atlantic could occur via melting of the Greenland Ice Sheet (GrIS), and such a melting event would be tied to a rise in sea level. Estimates of sea level change indicate that the GrIS was indeed reduced during the Last Interglacial (LIG) [Dutton and Lambeck, 2012, Dutton et al., 2015b]. One difficulty here lies in constraining the timing and magnitude of GrIS disintegration during the LIG, as Dutton and Lambeck [2012] indicate uncertainties in the sea level reconstructions. These are based largely upon examining fossil coral reef terraces, which lie above the modern sea level, and can be dated using U-series geochronometry. However, the sites which were examined to reconstruct LIG sea level changes were not all tectonically stable, and geologic uplift cannot be ruled out for all locations. Such a geophysical effect would conceivably lead to changes in the actual measured elevation relative to the paleo-elevation. Additionally the paleo-water depth at which the corals lived is associated with significant vertical uncertainties [Dutton et al., 2015b] of up to 2 m. Therefore, the magnitude of freshwater contribution that might originate from GrIS melting cannot be precisely constrained. Timing of GrIS is also an issue, as there are some challenges interpreting the potential alteration of U-Th isotopic signatures [Stirling and Andersen, 2009].

Such a disintegration of the GrIS – while uncertain – is one candidate for a large

freshwater input into the North Atlantic during the LIG, yet other options also exist. It has been suggested that post glacial lake drainage into the ocean may also be a sufficient mechanism to cause an AMOC collapse. A well-studied example of such an event is the Lake Agassiz outburst during the early Holocene [Clement and Peterson, 2008, Teller et al., 2002, Teller and Leverington, 2004, Li et al., 2009], and recent evidence indicates that such lake outbursts might be a common feature of many interglacial climates. Nicholl et al. [2012] have found distinctive layers of red detrital sediment in the Labrador Sea at Eirik Drift (Site U1305, $57°29'N, 48°32'W$), and Orphan Knoll (Site U1302, $50°10'N, 45°38'W$). This sediment layer is thought to be an indicator of an analogous lake outburst to the Lake Agassiz outburst flood around 8,400 years ago. Age models of these records suggest that the sediment was deposited 126 ka B.P., slightly after the peak of the LIG thought to be 128 ka B.P.. Nicholl et al. [2012] measured $\delta^{18}O$ of planktonic foraminifera[1], and found a distinct decrease in $\delta^{18}O$ of up to 1‰ in this red sediment layer. This is thought to suggest either the addition of fresh water to the surface water, or the mixing of isotopically ligher brines resulting from sea ice spreading linked to a freshening event. Interestingly enough, Nicholl et al. [2012] also find that there is no coarse Ice Rafted Debris (IRD) – an indicator of iceberg rafting – present at the site, suggesting that it was not deposited by iceberg discharge from a desintegrating ice sheet. Deposition from surface plumes of suspended sediment is also unlikely, due to the distance of both sites from the mouth of the Hudson Strait. A similar layer of carbonate-rich, red colored sediment was depsoited during the final outburst of glacial Lake Agassiz 8.4 ka B.P. [Kerwin, 1997, St-Onge and Lajeunesse, 2007, Lajeunesse and St-Onge, 2008]. The final discharge of Lake Agassiz has been associtaed with a cooling event 8.2 ka B.P., which has been shown to be associated with a perturbation of the AMOC [Hillaire-Marcel et al., 2007]. Nicholl et al. [2012] suggest that analogues of this event should also be found in other high-resolution climate records.

[1] specifically, from *G. bulloides*

5.1.1 Speleothem Record

The primary paleoclimate data archive used in this chapter is a speleothem collected from Corchia Cave, in Italy. The record itself is described, as well as how speleothem records in general can be used for paleoclimate interpretations.

Records of the isotopic composition of $\delta^{18}O$ and $\delta^{13}C$ in the calcium carbonate as well as the growth rates were extracted from a stalagmite sample collected from Antro del Corchia, a large cave system in the Alpi Apuane mountain range, Italy ($44.02°N, 10.29°E$) [Drysdale et al., 2005]. Stalagmite CC5 was collected approximately 500 m from the entrance of the cave, in a chamber with a mean annual temperature of 7.5 °C. The cave receives between 2500 $mm\,yr^{-1}$ to 3000 $mm\,yr^{-1}$ hydrological input from a recharge zone situated at approximately 1200 m to 1600 m above sea level.

Speleothems such as this one can provide insight into various key aspects of climate variability, namely temperature, precipitation variations, as well as vegetation responses to climate changes by a variety of measurable parameters. Variations in the isotopic composition of the calcite in stalagmites are excellent paleoarchives, as they are precipitated from meteoric water. Furthermore, stalagmites in caves are generally protected from erosion for long periods of time.

The $\delta^{18}O_c$ (speleothem signature) is controlled by (i) the calcite precipitation temperature and (ii) the seepage water signature, which reflect changes in the $\delta^{18}O_P$. A recent review of speleothems' utility as paleoclimate archives by McDermott [2004] suggests that the community consensus is generally on the latter factor being more important, namely the signature of seepage water rather than temperature within the cave.

Changes in the precipitation $\delta^{18}O$ are controlled by a variety of factors; such as shifts in the vapor source signature, changes in air-mass trajectories, condensation temperature, and overall rainfall amount. Air-mass trajectory changes would lead to possible different source regions producing the precipitation from which the speleothem

is generated. The temperature effect has a positive relationship with rainfall $\delta^{18}O$; as the air temperature increases, rainfall $\delta^{18}O$ increases. Observations at similar latitudes as the Corchia cave site in the Mediterranean have shown an isotope-air temperature gradient of between $0.2\,‰\,°C^{-1}$ to $0.3\,‰\,°C^{-1}$ [Mussi et al., 1998, Drysdale et al., 2004]. Thus, this relationship would cancel out the effects of the temperature dependence of oxygen isotope fractionation during calcite precipitation from seepage water, which Kim and O'Neil [1997] report to be $-0.22\,‰\,°C^{-1}$ at 5 °C. Finally, changes in the amount of precipitation produces lower $\delta^{18}O$ as the amount increases, and *vice versa*. This phenomena has been well-documented in tropical speleothems [Wang et al., 2001, Yuan et al., 2004], and at Corchia Cave, the speleothem $\delta^{18}O$ is also interpreted to be primarily controlled by the rainfall amount signal [Drysdale et al., 2004, 2005, 2007].

$\delta^{13}C$ can also be measured in speleothems, and changes in $\delta^{13}C$ reflect changes in the overlaying soil CO_2, which in turn are linked to climate driven changes in vegetation. $\delta^{13}C$ is most likely controlled by biogenic soil CO_2 productivity [Gascoyne, 1992, Genty et al., 2006], which is controlled by vegetation productivity, and limited by temperature changes. Therefore, an increase in $\delta^{13}C$ is associated with lower levels of productivity and cooler temperature, and *vice versa* [Couchoud et al., 2009].

Identifying Possible Rapid Excursions

While Drysdale et al. [2005] used the CC5 stalagmite record to examine the onset of the LIG, finding striking similarities to the Vostok Ice Core (VK) ice core's record of the T-II deglaciation, rapid excursions of the $\delta^{18}O$ record are also found within the LIG.

Before being able to identify a rapid depletion or enrichment in the $\delta^{18}O_C$ of the speleothem record, it is important to be able to determine a precise age for each particular measured point. Speleothems provide a unique advantage here, namely that they can be precisely dated using $^{230}Th/U$. However, as the spatial resolution (drill spacing) for determining geologic age is lower than the resolution used to determine climate

characteristics, an age/depth model must be developed. While the age model for the Corchia speleothem record as not be independently published (Russell Drysdale, *personal communication*), the techniques for constructing the age/depth model have been reviewed and compared to other speleothem dating techniques by Scholz et al. [2012].

To construct the age model used for the Corchia stalagmite record, all determined ages are randomized within their uncertainty ranges, and a Monte-Carlo iteration is used to perform a least squares fit for the sequence of line segments connecting two age measurements. The growth rate of the speleothem is allowed to vary randomly between age determinations (within a user-defined intensity), and all iterations are then compared to determine a median age model and its uncertainty. The resulting uncertainties from age/depth model used for the Corchia speleothem is shown in Figure 5.1.

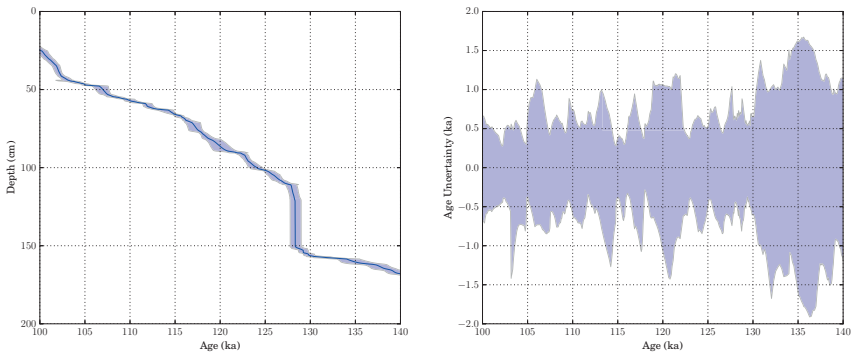

Figure 5.1: Age-depth relationship used to date the isotopic measurements from the Corchia Cave speleothem

The speleothem record is shown in Figure 5.2, with $\delta^{18}O$ points at ages of the median solution of the Monte-Carlo Age/Depth relationship. It can be seen that the record displays several rapid depletion excursions, a notable rapid depletion of $-0.64\,‰$ occurs between 125.06 ka B.P. to 125.03 ka B.P., taking place over 63 years[2].

[2]Given 95% (2σ) uncertainty in the age model, this event could have taken place over 1100 years

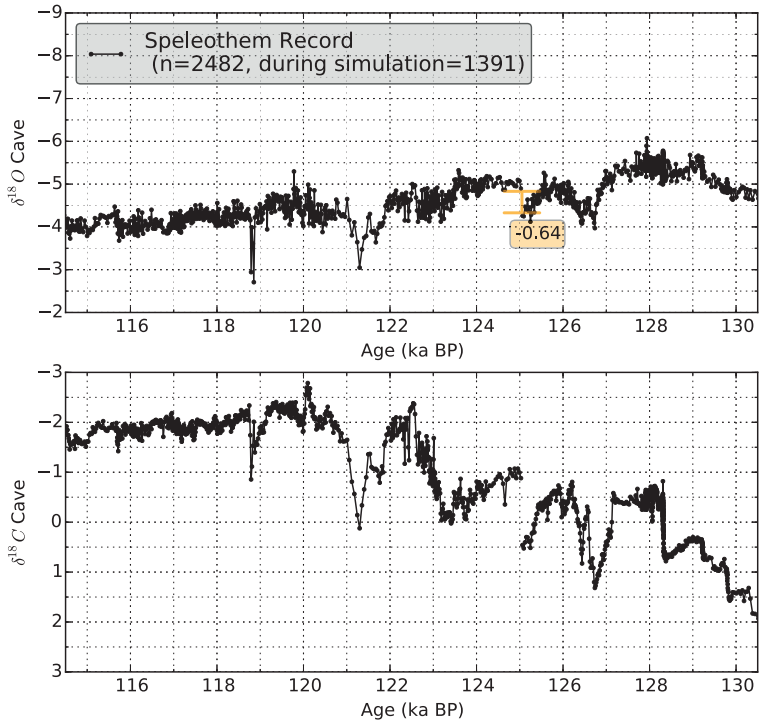

Figure 5.2: Speleothem record from Corchia Cave, with highlighted rapid $\delta^{18}O$ excursion at approximately 125 ka BP. The lower panel shows the $\delta^{13}C$ record.

Together with the record of $\delta^{13}C$ (lower panel of 5.2), which shows a similar excursion at 125 ka B.P., the speleothem demonstrates a very rapid climate response which may be indicating relative warming (due to the sudden depletion in $\delta^{13}C$) accompanied by a relative increase in precipitation (due to the rapid depletion of $\delta^{18}O$, as the Corchia cave site is thought to be controlled by the amount effect). Such a response may be indicative of a recovery following an AMOC collapse, and this signature has been found in other freshwater perturbation studies as well (e.g. Gong et al. [2013], finding cooling and drying during an AMOC collapse, followed by warming and increased precipitation), and in order to test if the physical and isotopic responses seen in the speleothem are the result of such a AMOC weakening, a hypothetical AMOC collapse is triggered in COSMOS-WISO, as described in the next section.

5.2 Experiment Design & Simulations Used

In order to compare against the speleothem record at Corchia Cave and examine if some of the sudden excursions in the $\delta^{18}O$ record are indeed the result of a rapid collapse of the AMOC – possibly triggered by GrIS melting or a post-glacial lake outburst event – several simulations are used. Beginning from a climate state at 125 ka B.P.[3], which is extracted from the transient simulation LIG-T, several additional simulations are performed. Both a strong (0.2 Sv, simulation LIG-125-HS)) as well as weak (0.05 Sv, simulation LIG-125-HW) freshwater perturbation is applied to the North Atlantic. The region of this freshwater perturbation is highlighted in Figure 5.3.

These simulations were run for a total of 500 model years, with greenhouse gas and orbital forcings set to the conditions at LIG-125, as described in Chapter 3. No additional spin-up time was utilized, as the simulations were branched from the transient simulation, which began in a stable state for 130 ka B.P.. As had been the case in the simulation LIG-130-H1, presented in Section 4, the freshwater perturbation was assigned an isotopic signature of $-30\,‰$, as has been done in similar studies by Hemming [2004] and Lewis et al. [2010].

5.3 Comparison to a Transient Simulation of the LIG

If indeed the excursions of $\delta^{18}O_C$ found in Corchia Cave are indicitive of rapid climate change events during the LIG, it is first necessary to exclude the possibility of such changes occurring within the natural variability of the system. To accomplish this, two seperate examinations are performed.

[3] this period is chosen as it has already been throughoughly examined in both Chapters 3 and 4

Figure 5.3: Example of total freshwater input for the simulation LIG-125-HS, showing freshwater input from net precipitation, river runoff, and the added freshwater perturbation in the central North Atlantic.

Comparison to Transient Simulation & Elevation Correction

First, the Corchia cave record is compared to the transient simulation LIG-T, which employs changing boundary conditions for both orbital configuration as well as greenhouse gas (GHG) concentrations. The simulation accelerated both forcing factors with a rate of 10, such that an average of 10 forcing years per 1 simulation year are used, following a method described by Lorenz and Lohmann [2004].

$\delta^{18}O_C$ is calculated for the cave site following the Kim and O'Neil [1997] calibration, which is also used by Werner et al. [2016] in studies comparing speleothems with COSMOS-WISO simulated $\delta^{18}O_C$ values for the Last Glacial Maximum (LGM). The

relevant equation is shown below:

$$\delta^{18}Oc_{(PDB)} = 0.97002 \times \delta^{18}Ow_{(SMOW)} - 29.98 \tag{5.1}$$

$$\delta^{18}Oc_{(SMOW)} = \delta^{18}Ow_{(SMOW)} + 18.03 \times \frac{1000}{T} - 32.42 + 0.27 \tag{5.2}$$

where T is the temperature (in Kelvin) during calcite formation. For the modelled speleothem record, the surface air temperature is used. It is furthermore assumed that the $\delta^{18}O$ values in drip water calculated in this manner are a reliable proxy for the annual mean $\delta^{18}O$ in the precipitation falling at the cave site.

As with the ice cores discussed in Section 4.4, the model orography is lower than elevation at the real cave site. This leads to an offset of the $\delta^{18}O$ values. Mussi et al. [1998] discovered an elevation/$\delta^{18}O$ relationship of 0.11 ‰ per 100 m. The offset between the measured precipitation recharge elevation of 1200 m to 1400 m found by Drysdale et al. [2005] and the model orography of 320 m leads to a correction of 1.1 ‰.

Utilizing this elevation correction, the simulated LIG is close to the isotopic values measured in the speleothem record. The results of this comparison can be seen in Figure 5.4. Both the simulation and the speleothem record show a slow enrichment of $\delta^{18}O_c$ as the LIG progresses.

It should however still be noted that the precipitation amounts in the model grid cell, where yearly averages are approximately 320 $\mathrm{mm\,yr^{-1}}$, drastically underestimate the precipitation at the cave site, ranging up to 2500 $\mathrm{mm\,yr^{-1}}$ to 3000 $\mathrm{mm\,yr^{-1}}$. This underestimation will play an important role when comparing the isotopic composition of the simulation and the isotopic values extracted from the speleothem, as later discussed in section 5.6.

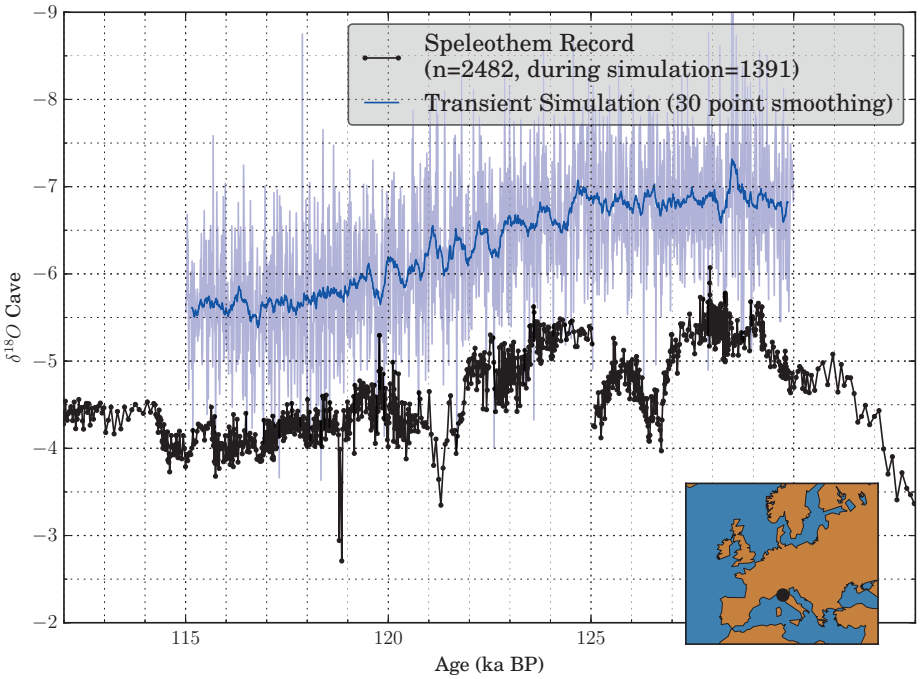

Figure 5.4: Comparison of the transient simulation LIG-T with the $\delta^{18}O_C$ record from Corchia Cave. The Y-Axis is inverted, with increasingly depleted values at the top of the axis. The location is highlighted in the inset. The offset between the simulation (blue curve) and the proxy record (black curve) is not artificial, the simulation is between 0.5‰ to 2.0‰ depleted. This offset is likely due to the coarse orography in the simulation. When the elevation correction of Mussi et al. [1998] is applied, the results between the simulated LIG and the measurements at Corchia Cave are closer together.

Eliminating Natural Variability

Secondly, in order to eliminate the possibility of natural variability causing large excursions in the $\delta^{18}O$ signal at the modelled location of the Corchia cave site, the variability of $\delta^{18}O_P$ in precipitation is examined in the stable, unperturbed experiment LIG-125, described in Chapter 3. The yearly averaged isotopic signal of precipitation is further smoothed with a 30 year running mean, in order to construct a climatological averaged. This interval is chosen based upon the World Meterological Association (WMO) definition of a climate mean state vs. shorter term variations that are more linked to synoptics and weather.

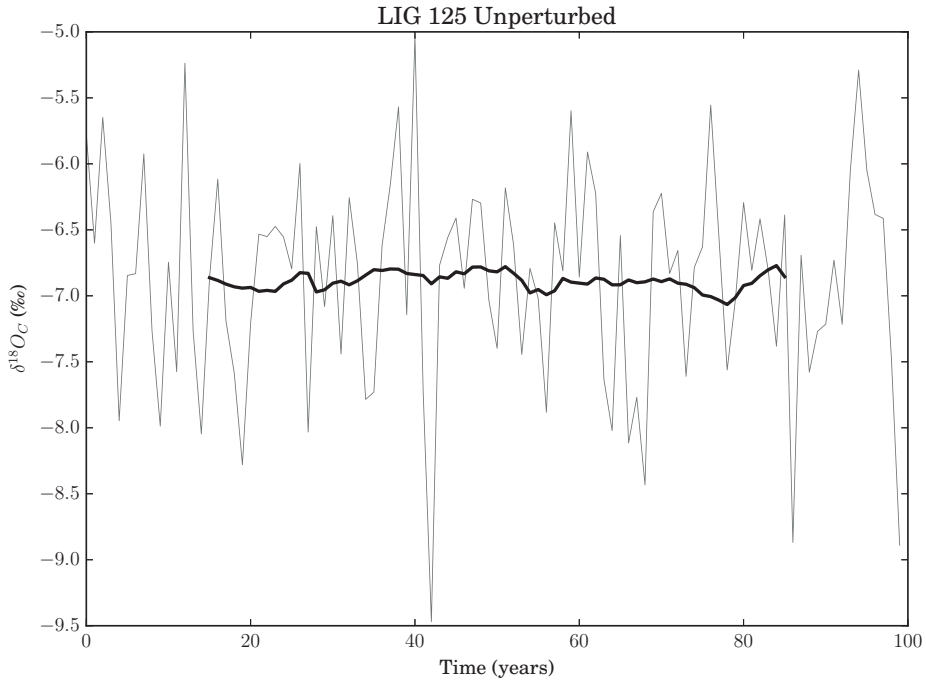

Figure 5.5: The natural variability of a 100 year simulation for Corchia Cave $\delta^{18}O_C$, calculated using the Kim and ONeill synthetic calcite equations.

The climatologically averaged timeseries of $\delta^{18}O_C$ (relative to PDB) can be seen in Figure 5.5. While the yearly values are quite variable, the climatological average is stable, with a standard deviation of 0.06‰.

Based upon these two examinations, first of the entire transient simulation, and next of the unperturbed climate state of LIG-125, it is unlikely that rapid excursions in $\delta^{18}O$ are caused solely by the forcings used for the transient and stable states. Rather, an additional forcing is likely required, and to examine to what extent an AMOC collapse might trigger $\delta^{18}O$ changes, freshwater perturbation experiments are used in the next step.

5.4 Model Response to Freshwater Perturbation

In the following sections, the simulated climate of the LIG is examined when perturbed with both constant and temporary freshwater perturbation. To begin, the experiments are shown with constant freshwater forcing of 0.2 Sv and 0.05 Sv. Thereafter, a transient forcing is examined, when the freshwater is applied and removed after 150 years, since a constant freshwater forcing is not feasible due to the sea level reconstructions and the limited amount of ice that can melt.

5.4.1 Constant Freshwater Forcing

The experiments LIG-125-HW and LIG-125-HS serve to examine the climate of the LIG when a permanent freshwater perturbation is applied. Both experiements use orbital and greenhouse gas forcing derived from the PMIP protocol, and additionally incorporate a freshwater pertubation with an isotopic signature of $-30\,‰$.

AMOC Response

After 500 years, the AMOC in both LIG-125-HW and LIG-125-HS has reduced considerably relative to the unperturbed LIG-125 strength of approximately 11 Sv. For LIG-125-HW, the AMOC weakens to a strength of approximately 8 Sv, based upon an index of the maximum overturning circulation strength simulated between 300 m to 2300 m, from a latitude of 30°N to 60°N. After the inital weakening, which occurs in the first 100 years of the simulation, the AMOC slightly recovers. The results are shown in Figure 5.6

The companion simulation LIG-125-HS shows considerably greater weakening of the AMOC. Here, the overturning breaks down to a strength of 4 Sv at the end of the 500 year simulation.

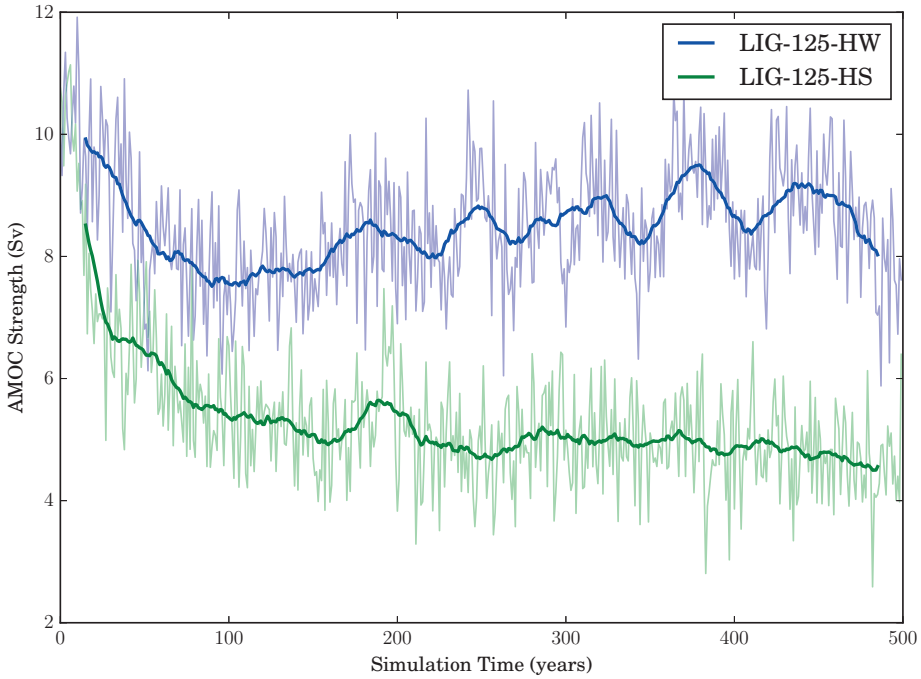

Figure 5.6: Evolution of the AMOC strength index for the maximum overturning circulation at a depth between 300 m to 2300 m and between 30° to 60°N.

Surface Temperature & Precipitation Response

Next, the temperature and precipitation amount responses of this AMOC weakening is examined (Figure 5.7). It can be seen that the relatively small reduction in AMOC in LIG-125-HW does not have a large influence on temperature and precipitation amounts over Europe and at the Corchia Cave site. Temperature decreases are small, ranging from $-0.1\,°C$ to $-0.5\,°C$ relative to the LIG-125 unperturbed state. Precipitation amounts over Europe do not decrease by more than $-2.5\,\mathrm{mm\,month^{-1}}$.

The response is more pronounced in LIG-125-HS. Here, temperature decreases are comparably stronger, with changes ranging from $-2.5\,°C$ to $-1.0\,°C$. Additionally, drying is seen over the entire European continent, with between $-2.5\,\mathrm{mm\,month^{-1}}$ to $-15\,\mathrm{mm\,month^{-1}}$. These relative changes correspond with both the speleothem $\delta^{18}O$ record, where a sudden enrichment excursion would be indicative of a drying event, and

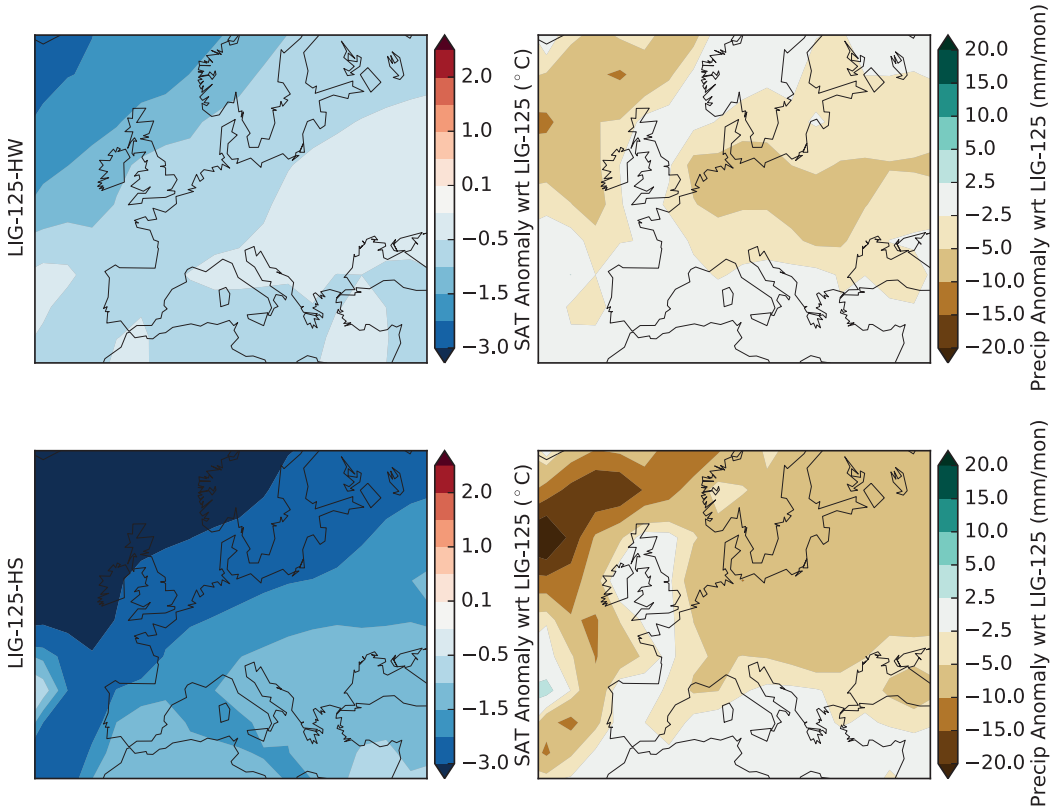

Figure 5.7: Mean of last 100 years of the simulations LIG-125-HW and LIG-125-HS for temperature and precipitation anomalies with respect to the unperturbed LIG-125 climate state.

the synchronous enrichment in carbon isotopes would be indicative of a cooling.

$\delta^{18}O$ Response

While these qualitative results could have been produced with a traditional General Circulation Model (GCM) which does not include stable water isotopes, the true advantage of COSMOS-WISO is once again apparent here, namely that it enables a direct quantitative comparison to the $\delta^{18}O_C$, where previously only relative temperature and precipitation changes, namely cooling and drying, would have been possible.

When examining changes to the isotopic composition of precipitation in the experiments with freshwater perturbation, COSMOS-WISO produces very little change in the isotopic signature during LIG-125-HW, with signatures less than $-0.1\,‰$ more depleted than in the control state. However, the strong perturbation causes a larger depletion, where values are between $-0.5\,‰$ to $-1.5\,‰$ more depleted in $\delta^{18}O_P$ relative to the control case, shown in Figure 5.8. Together with the strong cooling already shown in Figure 5.7, such a strong perturbation produces a shift in $\delta^{18}O_C$ as simulated at Corchia cave.

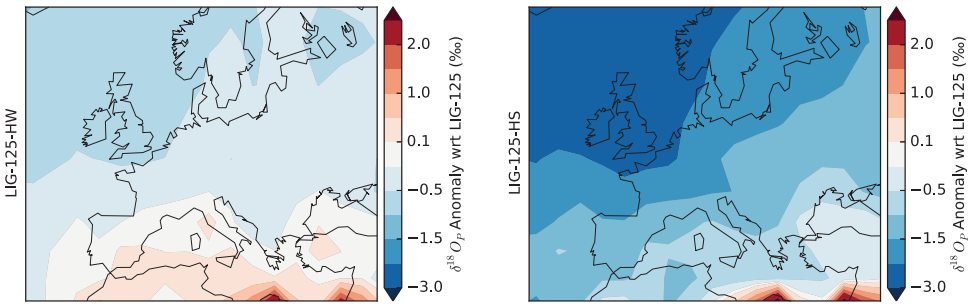

Figure 5.8: Mean of last 100 years of the simulations LIG-125-HW and LIG-125-HS for isotopic composition of precipitation anomalies with respect to the unperturbed LIG-125 climate state.

Examining the values directly at the simulated location of the cave, it is found that after 500 years of freshwater perturbation, only the simulation of a strong perturbation is able to produce $\delta^{18}O_C$ values that are considerably different from the unperturbed state for LIG-125. While LIG-125-HW produces a change of $\Delta\delta^{18}O_C = 0.06$, LIG-125-HS produces a larger change, $\Delta\delta^{18}O_C = 0.61$. These results are shown in Figure 5.9

The comparison with these isotopic values to the measurements from the speleothem, as well as reasons for why the simulation and record might differ, are presented after the temporally varying forcing is examined, since it is important to determine if the response seen here in these permanently perturbed experiments can still be seen if the

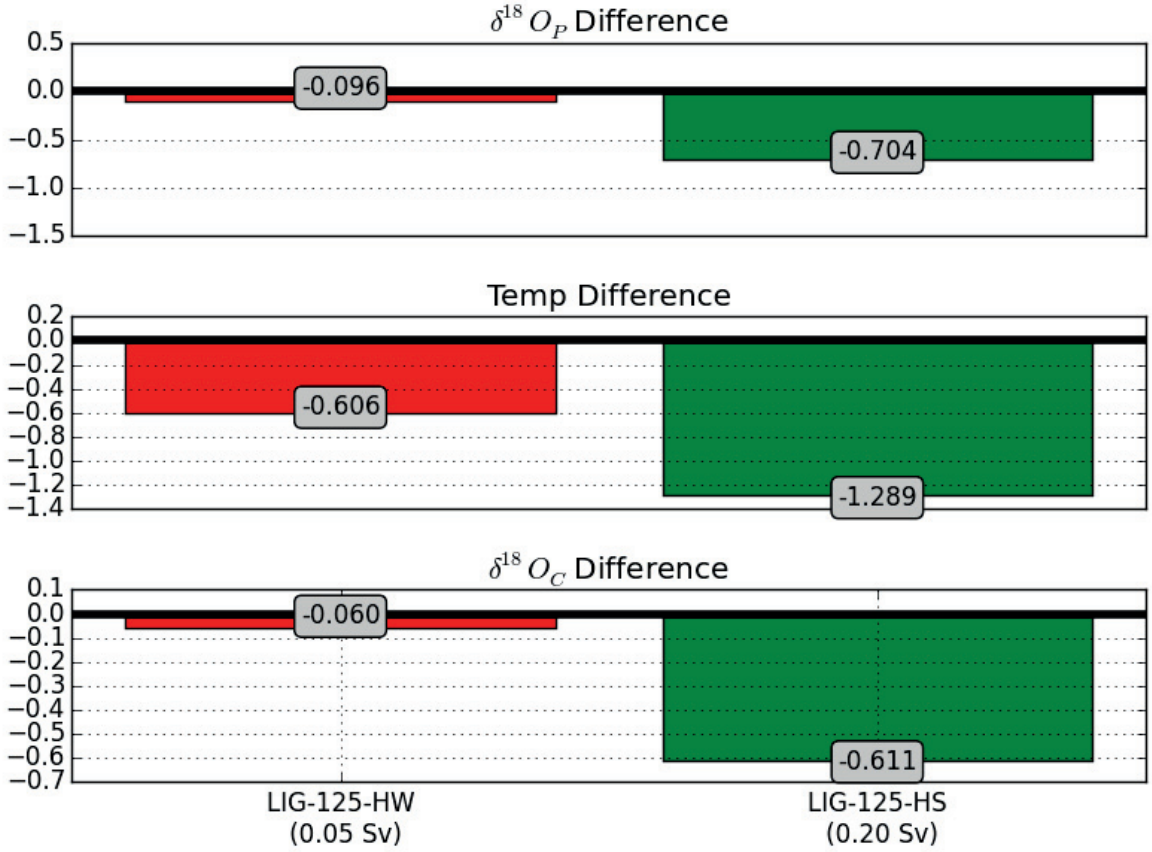

Figure 5.9: Mean of last 100 years of the simulations LIG-125-HW and LIG-125-HS for temperature, isotopic composition of precipitation, and $\delta^{18}O_C$ anomalies with respect to the unperturbed LIG-125 climate state, at the Corchia cave site.

freshwater is only temporarily applied.

5.4.2 Temporally Varying Freshwater Forcing

The most likely candidates to reproduce the $\delta^{18}O$ excursions seen in the Corchia Cave record are temporary freshwater injections based upon the strong response seen in LIG-125-HS, as the cooling and drying are strongest in this experiment. Therefore, a further experiment is performed (LIG-125-HSL), and the strong (0.2Sv) freshwater perturbation is applied for 150 years. Additionally, an experiment is performed with 50 years of perturbation, LIG-125-HSS. This amount of water is equivalent to approximately

2.58 m for LIG-125-HSL, and 0.86 m for LIG-125-HSS. This falls in line with what is possible from the GrIS contribution (up to 4 m) to the total LIG sea level rise of 6 m to 9 m reported by Dutton et al. [2015b].

AMOC Response

During these experiments, the AMOC briefly weakens, as can be seen in Figure 5.10. The overturning strength is shown as an index of the maximum between 30° to 60°N and at an ocean depth between 300 m to 2300 m.

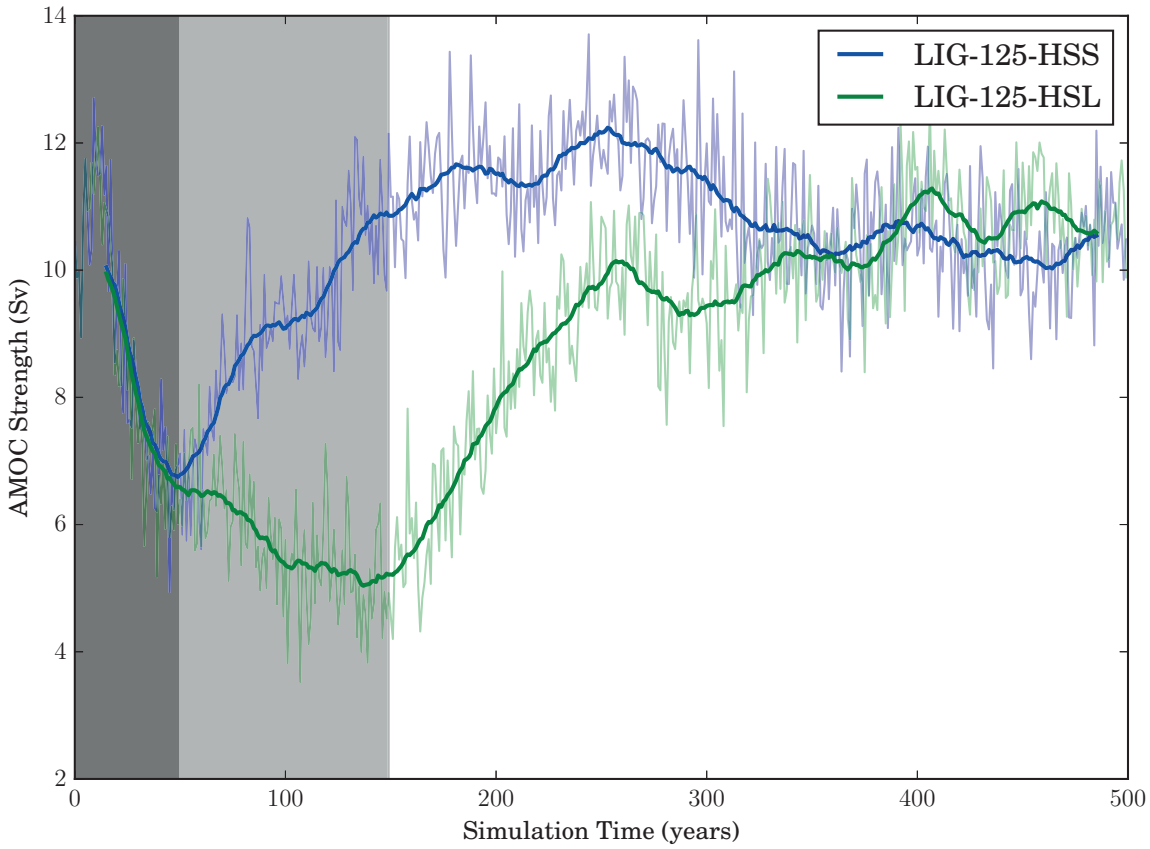

Figure 5.10: Transient response of the AMOC strength to 0.2Sv freshwater input of brief (50) and prolonged (150) years.

It can be seen that in both experiments, the maximum overturning strength reduces to 7 Sv in LIG-125-HSS by year 50 of the simulation. in LIG-125-HSL, the overturning

weakens further, reducing to a strength of 5 Sv. In both cases, the circulation recovers after the freshwater forcing is removed. Next, the physical response of the climate shall be examined at the minimum overturning strength for both simulations, in order to see if the cooling, drying, and isotopic depletion is seen, as this was the case in the permanently depressed simulations.

Physical Responses: Cooling and Drying

As was the case in LIG-125-HS, the Northern Hemisphere cools rapidly as the AMOC weakens, as a result of a decrease in the heat transported from the equatorial to the high latitudes in the Atlantic Ocean. The cooling response in the transient simulations are shown in Figure 5.11, for the time period at the peak of the AMOC decrease. Both simulations are approximately −0.5 °C to −2.5 °C cooler than in the stable simulation of LIG-125 without any freshwater forcing. The cooling is strongest over the northern parts of the North Atlantic, Northern Europe, and Scandinavia. At the site of Corchia Cave, the cooling of a 30 year climatological mean relative to LIG-125 is −2.2 °C after 50 years of freshwater perturbation. Simulation LIG-125-HSS begins to recover at this point, and the cooling decreases. At the end of the freshwater perturbation in LIG-125-HSL, the cooling is slightly stronger, with anomalous temperatures of −2.7 °C.

In LIG-125-HS, there was also considerable drying over Europe after 500 years of freshwater perturbation. During simulations LIG-125-HSS and LIG-125-HSL, a relative decrease in precipitation also occurs. For LIG-125-HSS, after 50 years of freshwater input there is −2.5 mm/month less precipitation than in the control state. After a further 100 years, the LIG-125-HSL simulation does not show an further decrease in precipitation, and is also shows approximately −2.5 mm/month less precipitation than LIG-125 (Shown in Figure 5.11).

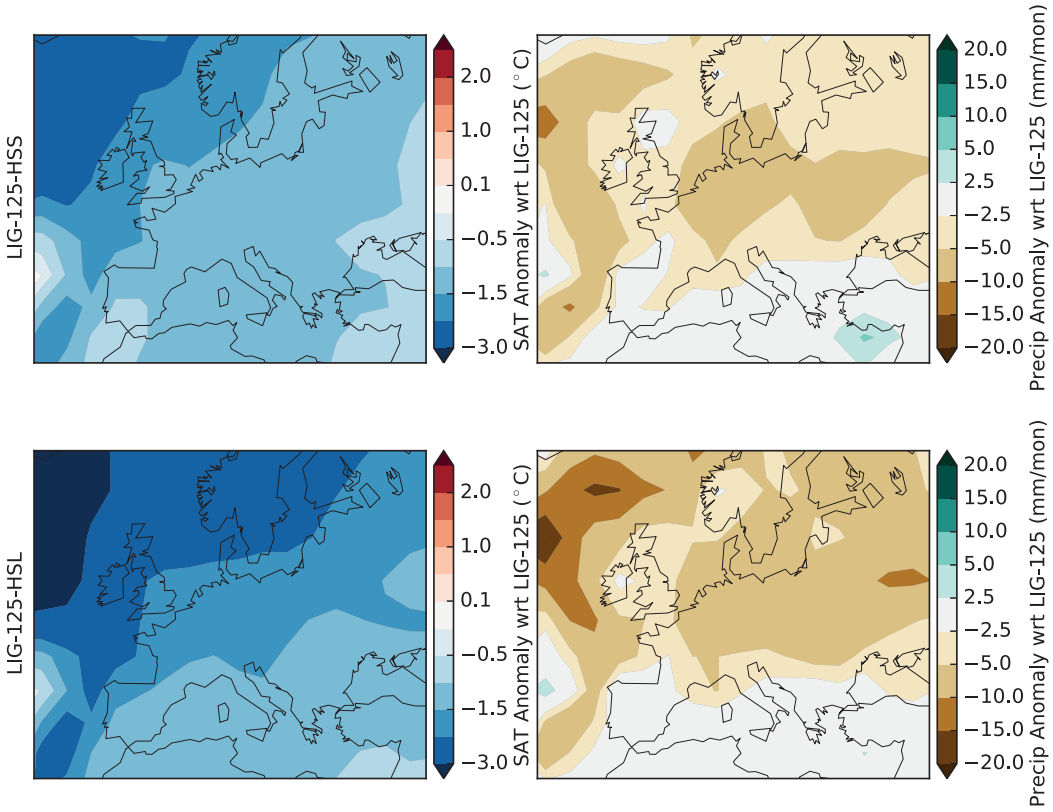

Figure 5.11: Transient response of temperature and precipitation to 50 and 150 years of 0.2Sv freshwater input. Cooling and drying can be seen in both simulations. The response is stronger in the simulation with the extended freshwater perturbation, as the heat transport from the equatorial latitudes to the high latitudes is further depressed.

Isotopic Responses

As in LIG-125-HS, the isotopic response in the temporally varying freshwater experiments is critical in determining if the climate model is able to reproduce the rapid excursions seen in the speleothem record quantitatively. The responses after 50 and 150 years are shown in Figure 5.12. The isotopic signature of precipitation decreases by between −0.25 ‰ to −0.4 ‰, becoming more depleted in the first 50 years, and the decrease continues in the longer simulation, with values down to −0.7 ‰ more depleted

than in the control state.

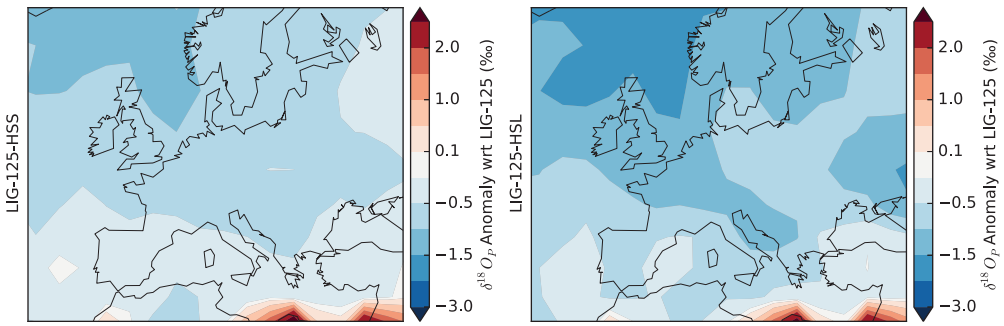

Figure 5.12: Transient response of stable water isotopic composition of precipitation to 50 and 150 years of 0.2Sv freshwater input. In both cases, the isotopic composition of precipitation becomes more depleted, and this response is slightly exaggerated in the simulation with a longer freshwater perturbation.

5.5 Comparing Simulations to the Speleothem Record

Finally, the transient simulations of temporary freshwater release are compared to the speleothem record, where a rapid depletion event occurs at approximately 125.0 ka B.P. to 124.5 ka B.P.. While the simulation also produces a rapid depletion, this is a result of the AMOC collapse and the associate effects, such as changes in the source region and cooling. In the speleothem record, the rapid depletion in $\delta^{18}O_c$ is instead interpreted as a recovery after an AMOC collapse. Thus, the isotopic response from the simulation and speleothem record show opposing results, as shown in Figure 5.13.

In order to understand why these responses are so different, it is important to examine the effects controlling $\delta^{18}O_C$ in both the simulation as well as in the speleothem record. As was mentioned earlier in section 5.1.1, $\delta^{18}O_C$ in the speleothem is controlled primarily by the “amount-effect”, as has been found and discussed in several studies

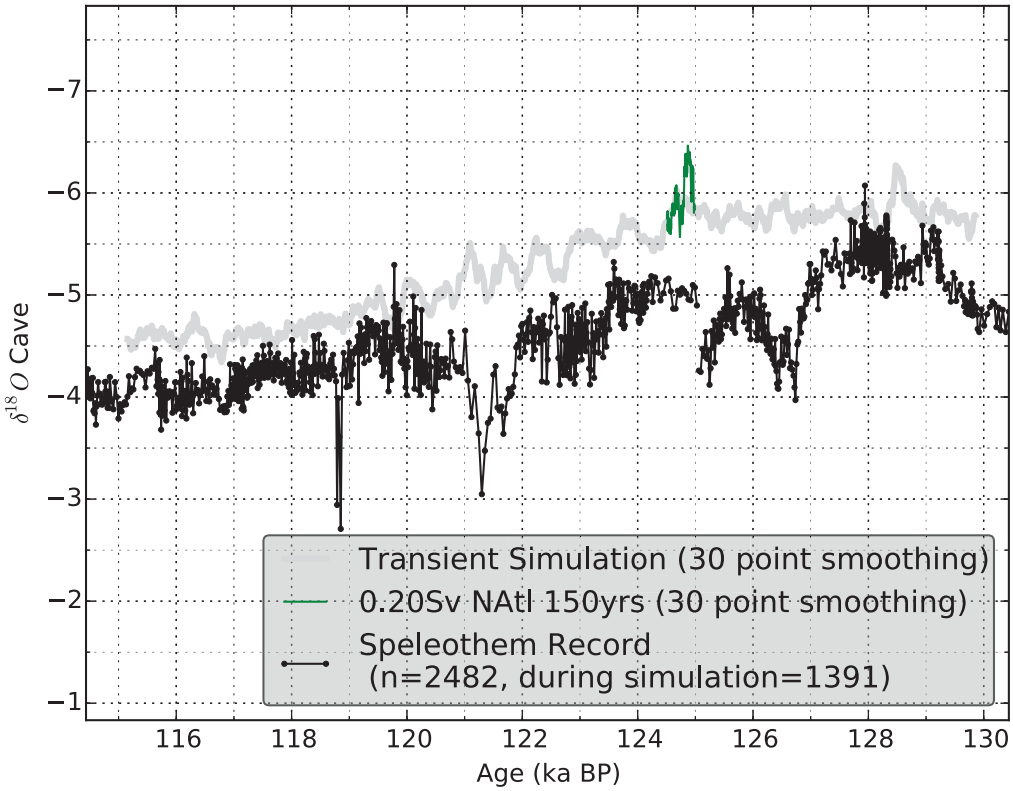

Figure 5.13: Comparison of the transient simulation from LIG-T, the temporary long freshwater perturbation, LIG-125-HSL, and the speleothem record. It can be seen that while the speleothem demonstrates an enrichment and sudden depletion as a result of an AMOC collapse, the simulation shows a sudden depletion. This is due to different effects acting on the isotopic signatures of the simulated system vs the real-world system.

of this particular site [Drysdale et al., 2004, 2005, 2007]. Modern-day observations of the "amount-effect" can be seen in Figure 5.14, where a linear/logarithmic relation between precipitation $\delta^{18}O$ signature and precipitation amount can be seen ($R^2 = 0.6$). The simulation does not produce this same amount effect, as the measurements with large amounts of precipitation are unable to be reproduced by the simulation. This is likely a result of the coarse model orography, as Drysdale et al. [2004] found an strong precipitation amount/altitude relationship of 200 mm per 100 m, suggesting that the precipitation at the cave site is likely due to orographic uplift of the air masses (i.e.,

Corchia is receiving so-called orographic relief rainfall).

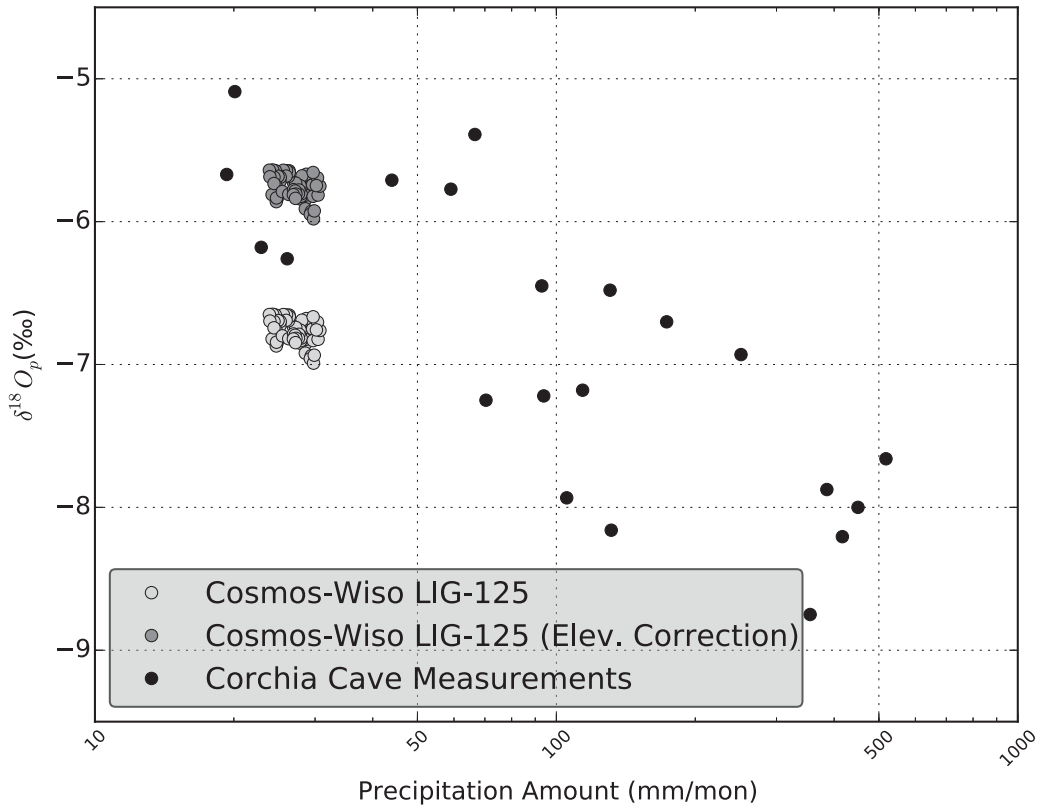

Figure 5.14: "Amount effect" of isotopic composition and precipitation amount from Corchia cave measurements, as well as in the unperturbed simulation LIG-125. It can be seen that the extremely wet and depleted isotopic values are not mirrored in the simulation

Instead, the simulated $\delta^{18}O_C$ reacts to changes in the source signature as well as changes in the temperature. The $\delta^{18}O_{sw}$ signature of the North Atlantic produces a distinctly separate regime of values during the freshwater perturbation, and the $\delta^{18}O_P$ signature of the rainfall (and, ultimately, in the simulated speleothem $\delta^{18}O_C$ calculated via the Kim and O'Neil [1997] equation) at Corchia cave is significantly more depleted during this time. $\delta^{18}O_P$ values averaging -7.3 ‰ are produced during the perturbation, compared to an average signature of -6.7 ‰ during the last 150 years of the simulation, when the AMOC has recovered.

5.6 Discussion

While COSMOS-WISO is able to match both the physical signals seen in the speleothem record qualitatively, namely cooling and drying during the AMOC decrease, the isotopic signature cannot be reproduced, as the "amount-effect", which controls the $\delta^{18}O_C$ in the speleothem, is not captured by the model at the Corchia cave location. However, COSMOS-WISO still provides some important insight that would not be seen from the speleothem record on its own.

The enrichment and following $-0.64\,‰$ depletion seen in the Corchia record, suggesting a drying followed by a return to wetter conditions as the AMOC re-invigorates, might be an underestimation of the magnitude of the isotopic changes occurring during such an AMOC collapse. The enrichment and following depletion could actually be larger than the $0.64\,‰$ deviation from the approximate $-5.0\,‰$ average $\delta^{18}O_C$ signature during 125 ka B.P.. As simulation suggests that the source $\delta^{18}O$ becomes more depleted, the actual real-world incoming rainfall from which the cave constructs the speleothem record might also become more depleted. Therefore, the amount of drying required to achieve the change in $\delta^{18}O_C$ to more enriched conditions is larger than what would be needed if the source signature would not change. Previous studies may have therefore underestimated the amount of precipitation decrease that takes place during such a rapid AMOC collapse. This also suggests that COSMOS-WISO is not sensitive enough to precipitation changes, and that model-data comparison studies such as this one critically depend on the model's ability to correctly capture all of the required features that may be controlling the signals seen in a proxy record. Nevertheless, the simulations used here were able to provide a new insight into the important influence of orography effects that cannot be accounted for without high resolution modeling[4]

There are further uncertainties that would influence these results. The "underesti-

[4]Unfortunately, resolving orography on the scale as would be required here would be too computationally expensive to feasibly produce paleoclimate simulations, as these require a long spin-up time.

mation" of the drying seen in the speleothem record is produced under the assumption that the freshwater perturbation had origins from the GrIS, where isotopic signatures can be estimated based upon studies from Heinrich events. The freshwater perturbation used (0.2 Sv for 150 years) implies a sea level increase of 2.5 m. Sea level estimates for the LIG lie between 5 m to 9 m [Dutton et al., 2015b], and while some of this sea level increase may stem from the GrIS, the exact timing of the sea level increase is unknown. LIG peak warming is earlier than the sudden excursion event studied here, suggesting that the GrIS may already have been reduced in size. Nicholl et al. [2012] suggest that a glacial lake may be responsible for the freshwater pertubation; however, further evidence of such a lake outburst has not yet been discovered. Additionally, while the study by Hemming [2004] provides an estimate for the isotopic signature of an ice sheet melt induced freshwater perturbation, the signature of a lake outburst would be much more difficult to estimate.

Another possibility is that the sudden isotopic excursion is triggered by a change in ocean circulation with Southern Ocean origins, and a West Antarctic Ice Sheet (WAIS) collapse during the LIG is likely [Sutter et al., 2016]. To test if the speleothem record is instead capturing signals which stem from a Southern ocean perturbation, an additional experiment is performed injecting freshwater with the same isotopic signature (−30 ‰) into the region around the Weddell Sea. The freshwater is applied for 500 years, and the AMOC evolution is shown in Figure 5.15. While there is no significant decrease during the first 200 years, the system is eventually effected by the freshwater input and weakens to a level of 8 Sv. When examining the spatial response to this freshwater forcing, it can be seen that the mean climatology becomes only slightly cooler (ΔT = 0.0 °C to −0.25 °C at speleothem location), as shown in Figure 5.16. Additionally, no drying takes place.

Furthermore, as the amount of freshwater required to produce this response is quite large (equivalent of 8 meter of sea level increase), it is unlikely that such an event would

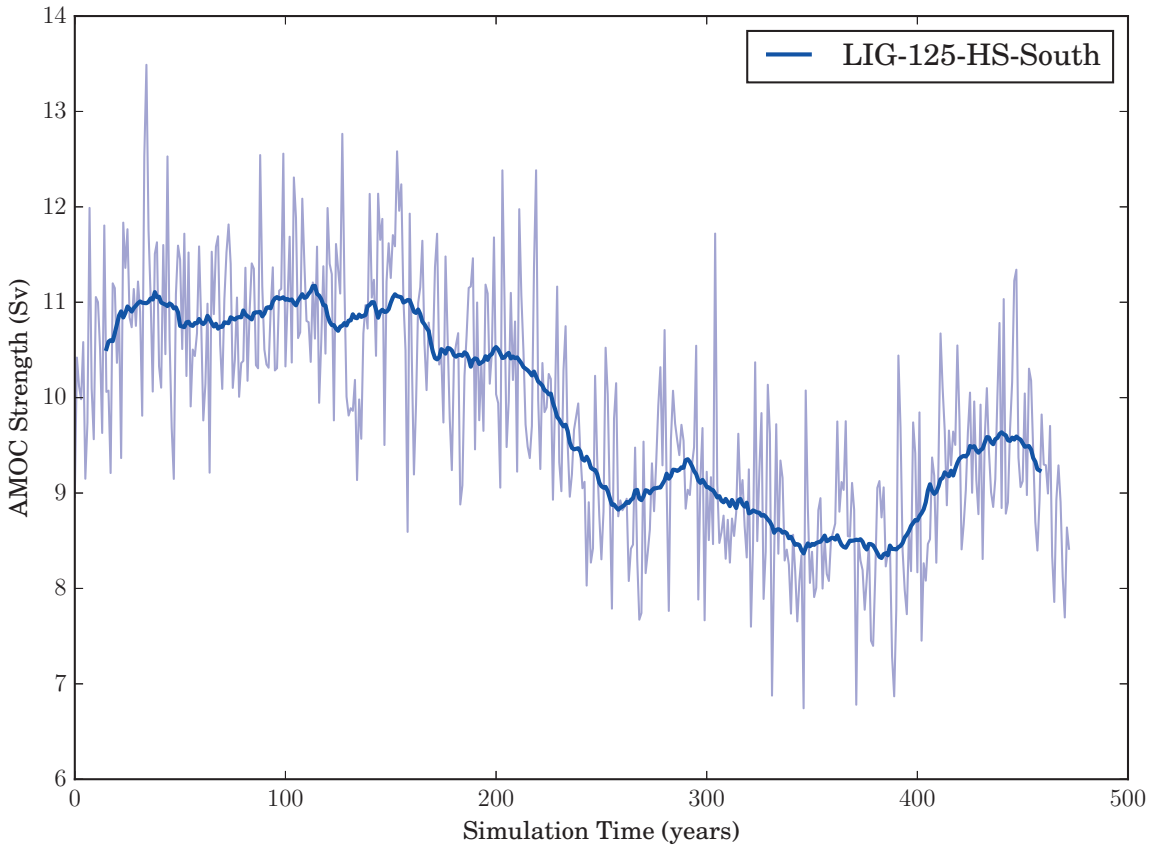

Figure 5.15: Timeseries of the AMOC strength evolution when subjected to constant Southern Ocean freshwater forcing. No significant weakening takes place until year 200, when the overturning circulation weakens to a level of approximately 8 Sv.

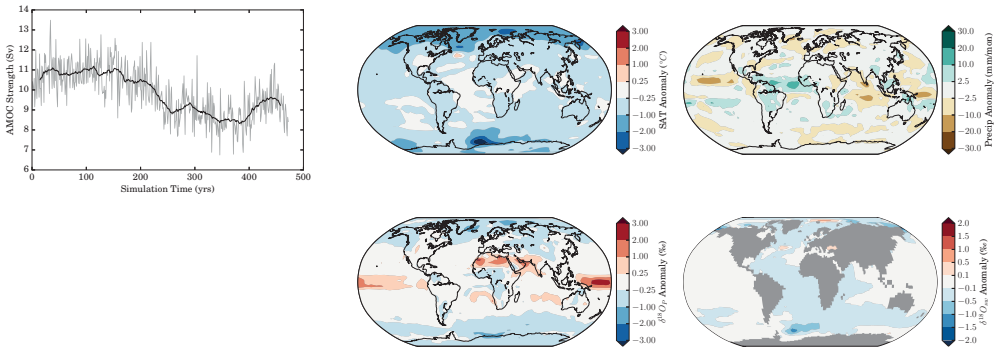

Figure 5.16: Spatial response of surface temperature, total precipitation, and isotopic signatures of rainfall as well as seawater, averaged for the last 50 years of the southern ocean perturbation experiment.

have happened in the real world climate system.

Collectively, it seems as if the freshwater perturbation experiments performed here do not yield an isotopic signature as is seen in the speleothem record. While Dutton et al. [2015a] provide an excellent review of sea level changes during the LIG, examining the original data from both Kopp et al. [2009] and Blanchon et al. [2009] demonstrates that the rate of change of sea level was uniform during 125 ka B.P., which would suggest that sudden meltwater bursts, as simulated here in the hypothetical scenarios, did not take place.

Finally, it is possible that COSMOS-WISO does not have sufficient sensitivity to freshwater perturbation, and therefore more freshwater than is really needed is used to generate the model response. This would lead to an overestimate of the required sea level change. It has already been found that different GCMs respond to freshwater pertubation with varying sensitivity under glacial conditions [Kageyama et al., 2013], and a similar multi-model approach would be required for the LIG to further constrain the amount of fresh water required to generate the isotopic excursions examined in the stable water isotopes.

5.7 Summary and Next Steps

In this chapter, a possible AMOC collapse during the peak LIG was examined. The motivation for performing such a study was found in speleothem records, where sudden enrichment in $\delta^{13}C$ indicated cooling, and simultaneous enrichment in $\delta^{18}O$ suggested a decrease in precipitation. These physical responses could be qualitatively reproduced by the model. However, the isotopic excursion in the speleothem could not be reproduced, as the record primarily responds to the amount effect, where enrichment in $\delta^{18}O$ takes place due to decreases precipitation. Instead, the simulation showed a depletion of the $\delta^{18}O$ signature, due to cooling and changes in the source region signature. While the

isotope record could not be reproduced, these changes in the source region would not have been uncovered without the aid of the stable water isotope enabled GCM. The hypothesis of rapid AMOC changes and consequent climate change remains interesting, and more data as well as a larger, coordinated simulation effort would be needed to conclusively prove or exclude the possibility rapid climate changes during the LIG.

In the next section, possible origins for freshwater perturbations are examined. Sea level estimates of the LIG suggest that both the GrIS as well as elements of the Antarctic ice sheet must have been different to the present day configuration in order to allow for the 5 m to 9 m sea level increase relative to Pre-Industrial (PI) found by Dutton et al. [2015b]. While Pfeiffer and Lohmann [2015] have examined how COSMOS responds to changes in the GrIS orography, another possible large scale ice sheet instability may have origins in a rapid disintegration of the WAIS, and temperature thresholds of such a collapse shall be examined.

CHAPTER 6

ICE SHEET/CLIMATE INTERACTIONS DURING THE LAST INTERGLACIAL (LIG) AND THE FUTURE

In these next two sections, the interactions between ice sheets and the broader climate system are examined. One case study is presented for the LIG, demonstrating possible instabilities of the Antarctic Ice Sheet, and a second study examines the interaction between future climate states and the Greenland Ice Sheet (GrIS)

6.1 The Ice Sheet Model RIMBAY

The studies described below utilize the Ice Sheet Model (ISM) RIMBAY extensively, and a brief introduction to this model is given in this section. Furthermore, RIMBAY's capabilities are briefly compared to other ISMs. A model description of RIMBAY has been published by Thoma et al. [2014].

Ice Dynamics

RIMBAY is a multi-approximation ice sheet/ice shelf model, originally based upon the higher order numerical ice flow model developed by Pattyn [2003]. RIMBAY includes numerical representations of all major features of the polar ice sheets (ice shelves, nunatuaks, fast-flowing glaciers, basal hydrology, etc.) A schematic of these processes are presented in Figure 6.1, which is adapted from Thoma et al. [2014].

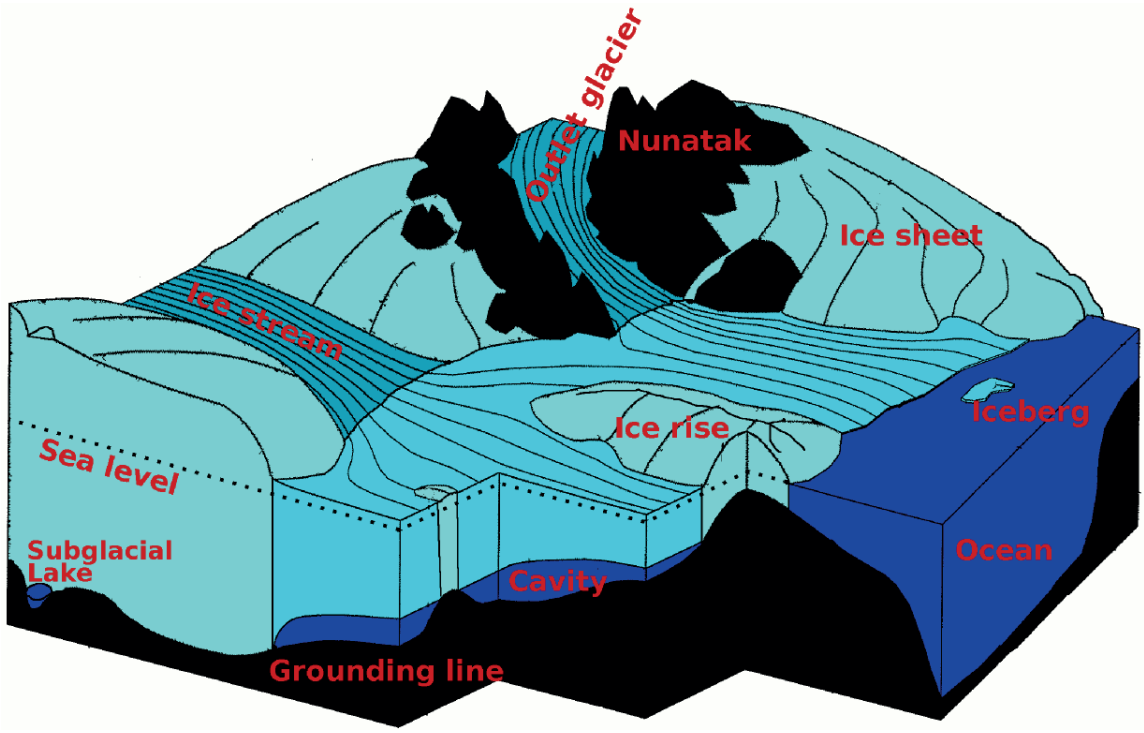

Figure 6.1: Schematic diagram illustrating several aspects which should be considered in ice sheet modeling (After Thoma et al. [2014]).

The complete ice dynamics can be described by the Navier-Stokes equation. As velocities in ice sheet/ice shelf modelling are rather small, acceleration can be ignored and the momentum equation can be written as:

$$\frac{\partial \tau_{xx}}{\partial x} + \frac{\partial \tau_{xy}}{\partial y} + \frac{\partial \tau_{xz}}{\partial z} - \frac{\partial p}{\partial x} = 0 \tag{6.1}$$

$$\frac{\partial \tau_{yx}}{\partial x} + \frac{\partial \tau_{yy}}{\partial y} + \frac{\partial \tau_{yz}}{\partial z} - \frac{\partial p}{\partial y} = 0 \tag{6.2}$$

$$\frac{\partial \tau_{zx}}{\partial x} + \frac{\partial \tau_{zy}}{\partial y} + \frac{\partial \tau_{zz}}{\partial z} - \frac{\partial p}{\partial z} = \rho g \tag{6.3}$$

Where τ = stress tensor

p = pressure

g = gravitational acceleration

ρ = (constant) density of the ice

Paterson and Budd [1982] demonstrated that the constitutive equation for polycrystalline ice links stress and strain rates such that:

$$\tau = 2\eta\dot{\varepsilon} \tag{6.4}$$

Here, $\dot{\varepsilon}$ is the effective strain rate, and η is defined as:

$$\eta := \frac{1}{2} A(\theta^*)^{\frac{1}{n}} \dot{\varepsilon}^{\frac{1-n}{n}}$$

Where $A(\theta^*)$ = flow rate factor, dependent on pressure corrected ice temperature

$n = 3$ (After Cuffey and Patterson 2010)

The model complexity has been reduced via the shallow-ice and shallow-shelf approximation of the Navier-Stokes equation, and higher terms are not solved due to the computation time requirements. The shallow-ice approximation solely solves the vertical stress terms of ice dynamics, shown in equations 6.5 and 6.6.

$$\tau_b = \beta^2 \cdot u \tag{6.5}$$

$$\vec{u}_z = -2(\rho g)^n |\nabla|^{n-1} \nabla_s \int_b^z A(\theta^*)(s-z)^n dz + \vec{u}_b \tag{6.6}$$

Where τ_b is the basal shear stress, β is the basal friction coefficient, and u the velocity. This intergral is evaluated from the bedrock at depth b underneath the ice surface at to the top of the ice sheet at height s.

The Shallow Ice Approximation (SIA) described above is valid for ice sheets with relatively small depth/width relationships, and applies for both the Greenland as well as the Antarctic ice sheets. Ice shelves must be treated differently, as the velocities are significantly higher, and here, the lateral velocities are assumed to be constant throughout the depth of the ice (i.e. $\frac{\partial u}{\partial z}, \frac{\partial v}{\partial z} = 0$).

6.2 Ocean Temperature Thresholds for LIG WAIS collapse

Proxy evidence suggets that global sea levels were between 7 m to 9 m higher than today during the LIG [Kopp et al., 2009, Dutton et al., 2015b], of which only about 3 m might originate from ocean thermal expansion [McKay et al., 2011]. Land-based glaciers may account for 0.5 m [Marzeion et al., 2012], and approximately 2 m from the GrIS [NEEM community members, 2013]. Therefore, the remaining 4 m must stem from a mass loss of the Antarctic Ice Sheet.

Observations and modeling studies of the present and future East Antarctic Ice Sheet have provided a mixed picture of possible responses, ranging from potential growth [Harig and Simons, 2015] to a partial colapse over the next several millennia [Bamber et al., 2009]. The West Antarctic Ice Sheet (WAIS) is largely made of ungrounded, marine ice, which floats on the ocean. As such, it is sensitive to instability changes caused by

warming of the ocean temperature [Joughin and Alley, 2011], as well as warming of the surface of the ice sheet [Mercer, 1978]. This instability, called Marine Ice Sheet Instability (MISI) [Schoof, 2007], could trigger a large scale collapse of the WAIS. Recent studies have suggested that such an instability is currently ongoing [Rignot et al., 2014], and sediment cores retrieved through boreholes on the marine sections of the WAIS suggest that an open marine environment existed during the late Pleistocence [Scherer et al., 1998]. Warming of the Southern ocean could have led to a partial or complete collapse of the WAIS, explaining the LIG sea level high stand, and thresholds for this collapse are investigated in the next study.[1]

6.2.1 Methods

The ISM RIMBAY was employed for this study, as described above. A 40 km×40 km grid size with 41 vertical layers was used, spanning the entire Antarctic Ice Sheet. RIMBAY was forced utilizing General Circulation Model (GCM) output from COSMOS. Transient forcing was generated by interpolating between the LIG and Pre-Industrial (PI) climate states utilizing a glacial index, where the index is derived from the Dome C deuterium depletion. Temperature changes at any given time during the simulation was given by:

$$T^{i,j}_{surf}(t) = L^{i,j}_{surf}(LIG) \cdot \frac{\delta t - \delta_{PD}}{1 - \delta_{PD}} + T^{i,j}_{surf}(PI) \cdot \frac{\delta t - \delta_{PD}}{1 - \delta_{PD}}$$

where $T^{i,j}$ denotes the temperature at grid cell i, j; $\delta(t)$ denotes the normalized deuterium value at time t, and δ_{PD} the normalized deuterium value for the present-day climate state.

The LIG climatology is extracted from the experiment LIG-125 (Shown in Chapter 3), and is denoted as experiment $E0$. A second experiment, E_g0, utilizes the climatology from COSMOS with a reduced GrIS orography, described by Pfeiffer and Lohmann [2015].

[1] The work presented in this section has been published by Sutter et al. [2016].

Additionally, both of these experiments are further perturbed by uniform ocean temperature anomalies ranging from 1 °C to 3 °C. (Experiments $E1$, $E2$, and $E3$, correspondingly E_g1, E_g2, and E_g3)

6.2.2 Results & Discussion

The Atlantic Meridional Overturning Circulation (AMOC) is weaker in both experiments $E0$ as well as in E_g0. While this leads to slight warming in the Southern Ocean via the bipolar seesaw, this warming is not sufficient to trigger any destabilization of the WAIS, as shown in the ice volume (depicted as sea level increase) time series in Figure 6.2-B. However, at warmer levels, the WAIS disintegrates, resulting in a relative sea level increase of between 2 m to 4.5 m. These results indicate that a collapse would occur between 2 °C to 3 °C, which is also a conceivable range of warming found in proxy data for the Southern Ocean[Capron et al., 2014]. Interestingly, WAIS collapse occurs non-linearly, initialized by a complete melt of the major ice shelves in the Ross and Weddell Seas (occurring within about 500 years), which is shown in Figure 6.3-A. Thereafter, due to a loss of buttressing and sustained melting close to the grounding line (the ice-sheet/ocean boundary between ice on the continent and floating ice), the ice sheet tributary glaciers drain the central Western Antarctic, and discharge increasing amounts of grounded ice into the ocean. The sea level increase is initially very rapid, with levels in excess of $1\,\mathrm{mm\,yr^{-1}}$ relative sea level rise averaged over 100 years, which is several times larger than present day estimates [Zammit-Mangion et al., 2015]. This high rate of sea level increase is sustained until 129 ka B.P., after which the ice loss slows down.

At this point, an open sea passage between the Weddell and Amundsen Seas has been established, and driven by large surface topography gradients, surface velocities of the remaining ice dome increase, leading to thinning and conversion of grounded ice into ice shelves. The grounding line retreats further, and the ice sheet approaches another

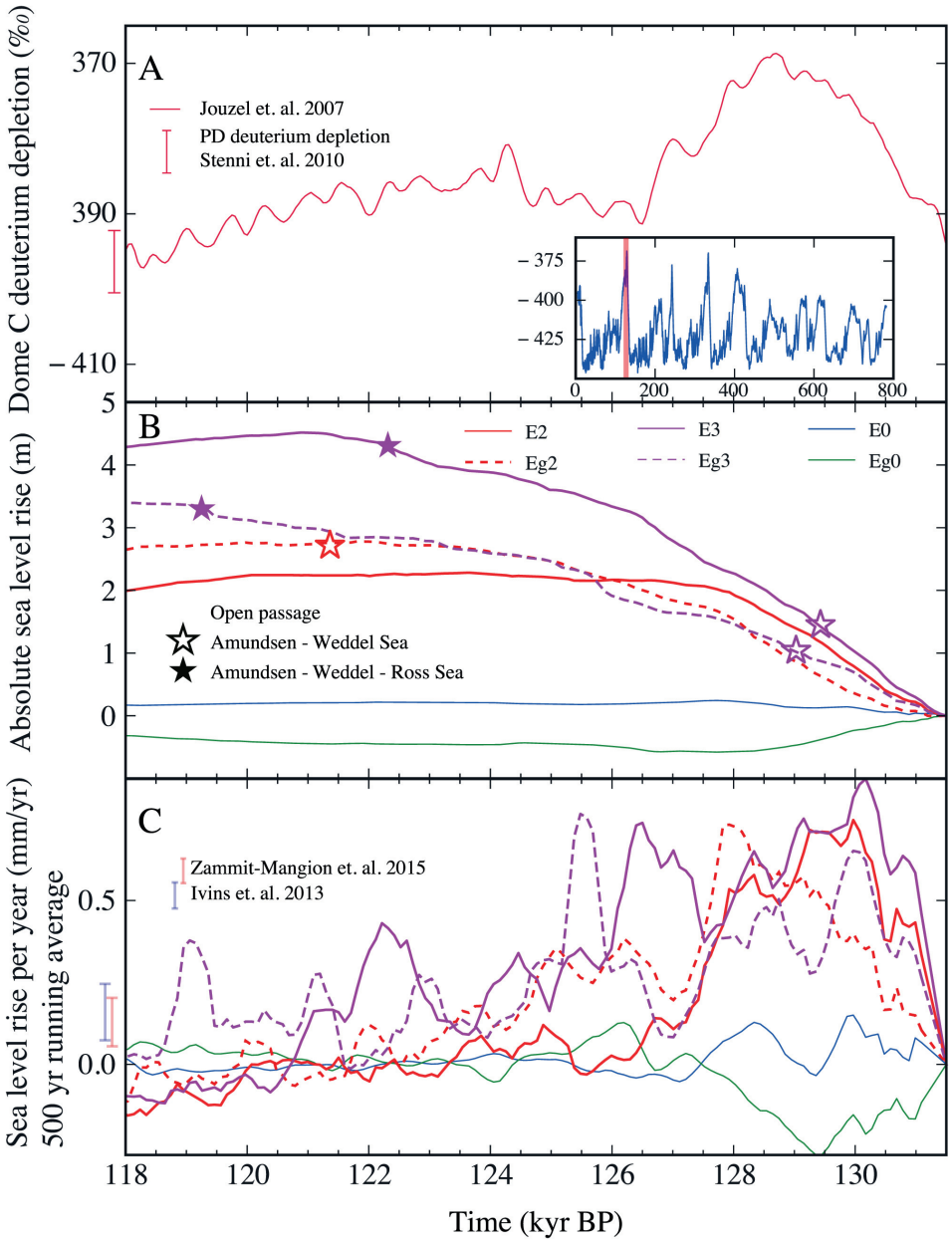

Figure 6.2: Reproduced from Sutter et al. [2016] (a) Deuterium depletion from Dome C ice core [Jouzel et al., 2007]; the inlay shows the complete record (with the highlighted section marking the LIG, time axis in kyr). The present-day mean deuterium depletion at the ice core site [Stenni et al., 2010] is depicted by the red bar next to the graph. Please note that the time axis runs from right (past) to left (present). (b) Simulated Antarctic contribution to sea level rise. Simulations with 2 and 3 °C Southern Ocean temperature anomalies are shown. The stars indicate the points in time at which partial (open) or complete (filled) WAIS collapse is reached. (c) The corresponding sea level rise rates in mm/yr (500 year running mean). The two bars next to the graph depict observed present-day Antarctic sea level contributions. Complete collapse is modeled in E3 and Eg3. Partial collapse is already reached at 2° ocean warming for scenario Eg2.

unstable configuration. Warm waters enter from the Amundsen Sea, melt newly formed shelf ice, and accelerate the ice loss a second time, with maximum sea level increases occurring again at around 126.5 ka B.P. to 125.5 ka B.P. (Figure 6.2-C).

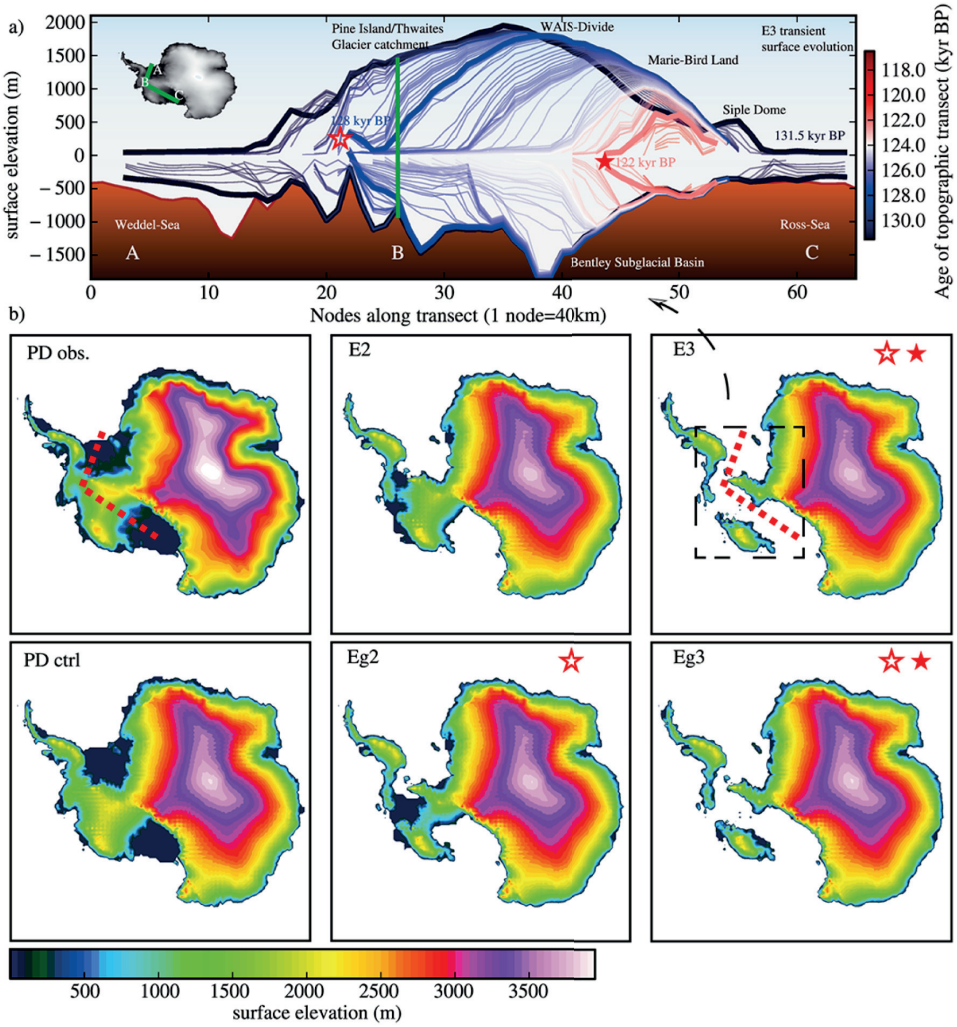

Figure 6.3: Reproduced from Sutter et al. [2016] (a) Transect across the WAIS showing the transient evolution of the surface topography during simulation E3. Each transect illustrates a snapshot during the LIG. Several semi-stable ground line positions are visible around inland ascending bedrock slopes Thick transect lines show times at which a partial of complete collapse of WAIS is reached, defined by the opening of ocean gateways between the Weddell and Amundsen Seas. (b) Surface topographies at the end of each simulation. Dark blue areas depict ice shelves, and the transect from panel a is shown as a red dashed line in E3.

These simulations show that during the LIG, strong subsurface Southern Ocean

warming is required to destabilize the West Antarctic Ice Sheet. The double peak in sea level rise observed in the simulations indicates a two-phase collapse of the WAIS due to its characteristic topography and bathymetric features. Melting at the base of Antarctic ice shelves is largely driven by warm deep water, which enters the shelf cavity along deep bathymetric channels [Schmidtko et al., 2014], a process which has only recently been simulated in high resolution ocean models [Hellmer et al., 2012]. While these processes are difficult to capture in current GCMs, these results indicate that such processes are essential if fully coupled ice sheet/climate dynamics are to be simulated in future studies.

The future evolution of the Antarctic Ice Sheet critically depends on both the amplitude and rate of ocean and surface warming. The GrIS, examined in the next study, is not as susceptible to ocean-induced melting, as the GrIS does not have large ice shelves. Despite this, the future of the GrIS ice sheet can critically influence the AMOC, as large scale melt water can hinder North Atlantic Deep Water (NADW) formation.

6.3 GrIS Meltwater Impacts on the AMOC in Future Climate Scenarios

The work presented in this section has been published by Gierz et al. [2015], and futher examinations regarding the rate of change of greenhouse gas (GHG) emissions were the subject previous work [Gierz, 2013].

The AMOC is one of the key drivers for heat transport within the climate system [Boccaletti et al., 2005]. It has been well established that this system of deep ocean circulation is sensitive to both freshwater perturbations and changes in ocean temperature [Rahmstorf, 2002]. Previous work has demonstrated that freshwater input to the North Atlantic by so-called Heinrich events had triggered abrupt climate changes due to a sudden collapse of the AMOC system [McManus et al., 2004]. Abrupt climate change of

this nature has occurred in the past, as shown by several paleoclimate studies [Naafs et al., 2013]. While previous research has demonstrated that an increase in atmospheric GHG concentrations and temperature alone can trigger an AMOC slowdown [Stocker et al., 1997], the additional disturbance caused by large scale melting of the GrIS could result in an even more dramatic slowdown. It has been speculated that melting of the GrIS could be one of the driving factors responsible for weakening of the circulation system in the future [Hu et al., 2011], and that some effects can already be seen today [Rahmstorf et al., 2015]. However, the extent of this weakening may still be unclear, and it appears to crucially depend on the strength of the freshwater flux [Hu et al., 2013].

Up until now, the scenarios as documented in the Intergovernmental Panel on Climate Change (IPCC) have examined many possible future climate projections [Moss et al., 2010], and there have been several investigations regarding the GrIS stability in the light of future climate warming. Robinson et al. [2012] found that the GrIS is multi-stable, but that a complete loss and an essentially ice-free state is possible with a surface warming of only 1.6 °C. The corresponding freshwater effects in the North Atlantic, and the possibility of a muted AMOC have also been investigated with prescribed freshwater perturbations representing GrIS melt; Jungclaus et al. [2006] and Driesschaert et al. [2007] both found that melt water inputs of 0.1 Sv can weaken the AMOC in studies using an Earth System Model of Intermediate Complexity (EMIC) coupled to an ice sheet model. General circulation models with prescribed freshwater perturbations have also been used; Mikolajewicz et al. [2012] studied multiple coarse resolution models and found that all models displayed a reduction of the AMOC when forced by 0.1 Sv of freshwater input of freshwater forcing distributed around Greenland. Weijer et al. [2012] found that model complexity may indeed play a role on the transient response of the AMOC to such a freshwater forcing, yet both strongly-eddying and coarse resolution ocean models produce a similar quantitative response on decadal time scales; however

work here has been limited to ocean-only models.

There has also been work performed using fully coupled climate-ice sheet models, such as the studies performed by Fichefet [2003], Ridley et al. [2005], Mikolajewicz et al. [2007], Charbit et al. [2008], and Vizcaíno et al. [2008]. However, each of these studies has had limitations, falling back upon coarser resolutions, inconsistent coupling, or idealized forcing scenarios. While these findings have provided a solid basis, there has yet to be a conclusive discussion regarding the connection between GrIS melting, AMOC weakening, and the resulting long term evolution of the climate system utilizing the current state-of-the-art forcing scenarios as presented in the IPCC. The study presented here attempts to fill this gap using a dynamic, high resolution ISM bi-directionally coupled to an Atmosphere-Ocean General Circulation Model (AO-GCM).

6.3.1 Model and Experimental Setup

The AO-GCM simulations in this study are examined with both fixed (designated as *ao* configuration) and dynamic (*aoi* configuration) ice sheets, simulating both Greenland and Antarctica. Both the earth system and the ice sheet models are run synchronously, exchanging information at the end of every simulated year. The AO-GCM and ISM are coupled bi-directionally and exchange information about the orography, surface temperature, precipitation, and ice melt. The methodology for this coupling is described by Barbi et al. [2014]. The *aoi* configuration and *ao* configuration both use identical forcings and boundary conditions. The AO-GCM used is COSMOS, which includes an atmospheric component ECHAM5, run at T31L19 resolution (3.75°×3.75°); and a dynamic ocean-sea ice model MPIOM, run on a GR30 grid (approximate average resolution 3.0°×1.8°, significantly higher at polar latitudes). A dynamic vegetation module is not included, and while vegetation feedbacks are naturally important, the land use changes projected by the IPCC are included in these forcing scenarios. COSMOS has been extensively used for

both present day and paleoclimate studies, such as experiments performed to investigate the Last Glacial Maximum [Zhang et al., 2013, Gong et al., 2013], the Holocene [Wei and Lohmann, 2012], the Pliocene [Stepanek and Lohmann, 2012]. The ISM RIMBAY [Thoma et al., 2014], was run on a 20 km resolution, and applied the shallow ice approximation to both the Greenland and Antarctic ice sheets.

Explicit consideration of a dynamic ice sheet in the model allows for the separation of factors, to determine the influence of melting of the GrIS on the ocean, the influence of changed ice sheet orography on the atmosphere, and cumulatively on the entire climate system. Four simulations following the IPCC Representative Concentration Pathway (RCP) scenarios are performed (RCP4.5-*aoi*, RCP4.5-*ao*, RCP6-*aoi*, and RCP6-*ao*). These simulations start from an initial concentration of 280 ppm CO_{2eq}, which corresponds to a pre-industrial climate state, simulate the prescribed historic period, and then follow the IPCC guidelines for RCP4.5 (583 ppm CO_{2eq}) and Representative Concentration Pathway 6 (RCP6) (808 ppm CO_{2eq}) as well as the extensions of these scenarios for time periods beyond the 21^{st} century. All forcings are prescribed in units of ppm CO_{2eq}; which transforms all possible forcings utilized in the IPCC experiments into equivalent amounts of GHG based on the resulting radiative forcing.

6.3.2 Ice Sheet Response

In response to the increase of GHG concentrations (Figure 6.4-a) and increasing atmospheric temperatures, the dynamic ice sheet begins to melt. For the extension of scenario RCP4.5, the globally averaged temperature increase for the last 30 years relative to the historic simulation is $\approx 4\,°C$ (calendar year 2370-2400), and for RCP6, it is $\approx 7\,°C$. These temperature increases are comparable with the RCP Extensions published by the IPCC, yet are slightly warmer than the multi-model ensemble presented, which shows a mean warming of 2.5 °C for Representative Concentration Pathway 4.5 (RCP4.5) and 4.2 °C for

RCP6 [Stocker et al., 2013]. This discrepancy is understandable, as the AO-GCM used in this study has a high climate sensitivity [Haywood et al., 2013]. Figures 6.4-b shows the total ice sheet mass decrease. By the end of extension scenario RCP4.5, the GrIS mass decreases from an initial state of $\approx 3.1 \times 10^6$ Gt to $\approx 3.0 \times 10^6$ Gt, corresponding to a loss of $\approx 3\%$ of its mass; resulting in ≈ 0.3 m of sea level rise. In scenario RCP6 , it loses $\approx 6\%$, with a final ice mass of $\approx 2.9 \times 10^6$ Gt, or ≈ 0.7 m of sea level rise. These values fit well compared to the published findings in the IPCC [Stocker et al., 2013], which suggest a long-term sea level increase of 0.11 m to 0.65 m due to runoff from the GrIS in models using intermediate radiative forcing. However, it should be noted that this sea level estimate does not include the thermal expansion of the ocean or isostatic adjustment of the Earth's mantle. For both scenarios, the slope of the total ice mass time-series and the mass balance time-series indicates that melting would likely continue if the simulation were extended, and it is possible that an irreversible melting has been triggered by crossing a threshold point, as suggested by Robinson et al. [2012], yet this determination would require further research. A comparison with other model studies is also possible, Vizcaino et al. [2015] performed a similar fully coupled study for RCP4.5, focusing primarily on the ice sheet response. While the ISM used in that work was different from the one used in this study, both the ice sheet volume change in sea level equivalent as well as the surface mass balance for the GrIS are comparable to these simulation results.

Spatially, the variability of the ice sheet's response to the atmospheric warming is diverse. Figure 6.4-e and 6.4-f show the amount of ice remaining as a percentage of the initial ice thickness for RCP4.5 and RCP6. Most of the ice melt occurs along the southern margin of Greenland, suggesting that a majority of the meltwater is introduced to the ocean in the Greenland Sea. The center of the ice sheet is less susceptible to ice melt, as much of central Greenland remains intact at the end of the simulation. These findings

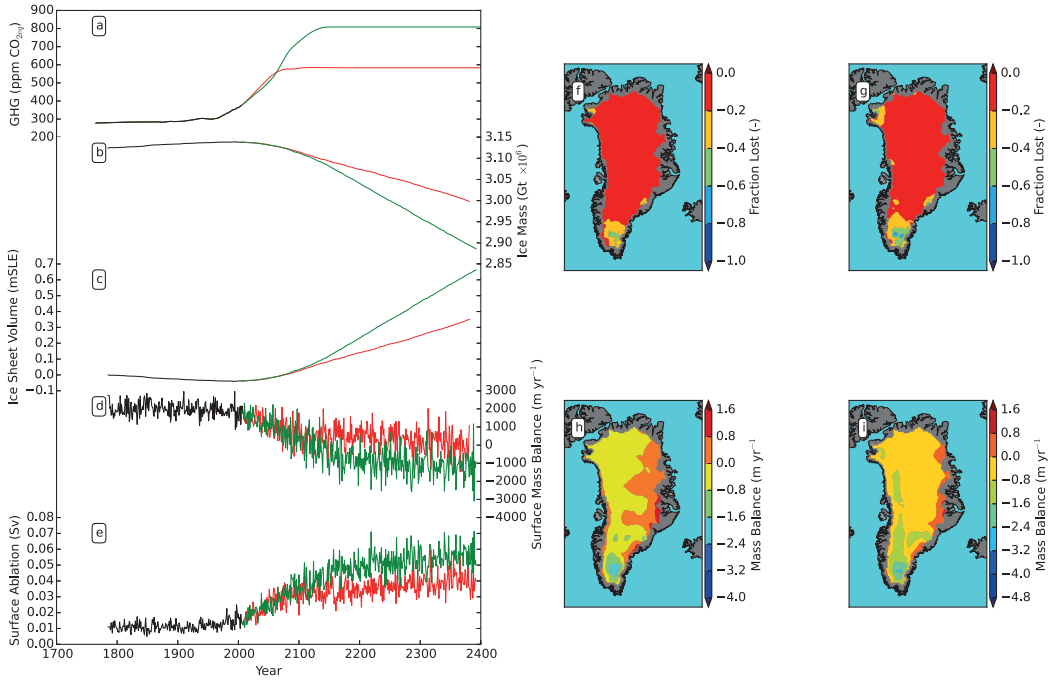

Figure 6.4: Time series and spatial response of the GrIS in the *aoi* simulations. (a) the radiative forcing used in the model scenarios in equivalent amounts of CO_2, (b) the ice sheet's total mass (c) equivalent amount of sea level rise in meters due to GrIS ablation (d) summed mass balance of the GrIS (e) amount of ablated ice in terms of freshwater discharge to the ocean (f) and (h) spatial response of the ice sheet in scenario RCP4.5 (g) and (i) response for RCP6. The upper panels (f) and (g) show the fraction of ice lost at the end of the simulation with -1 corresponding to a complete loss of ice thickness. The lower two panels (h) and (i) show the spatial distribution of mass balance of the ice sheet, as a sum of ablation, calving, and ice dynamics.

are supported by the spatial distributions of melting rates (Figures 6.4-g and 6.4-h).

6.3.3 Ice Sheet Feedbacks

As the GrIS melts, its surface elevation will decrease, causing changes to the wind fields; which in turn will change how much momentum is transferred to the ocean. It has been suggested that these changes to wind strength could induce changes in the local climate [Ridley et al., 2005], and it is important to see if there are any changes in the wind-induced surface ocean circulation. Based upon Figure 6.4, the primary

elevation changes in the ice sheet occur along its southern edge. This change is minimal at the AO-GCM resolution, as was also found by Vizcaino et al. [2015]. Examining the horizontal barotropic streamfunction of the ocean gives an indication of surface gyres, and it is discovered that the orographic changes caused by ice sheet melting have a minimal effect on surface ocean circulation. Since these changes are less than 10% of the absolute magnitude of the gyre strength, one can conclude that the primary influence of the ice sheet on the atmosphere-ocean system at this resolution is the surface ablation and meltwater. It should, however, be noted that ice sheet orgraphy effects have been suggested to play a critical role in the climate system, both on paleoclimatological time scales [Eisenman et al., 2009, Zhu et al., 2014], as well as in hypothetical sensitivity studies of the present day climate [Davini et al., 2015].

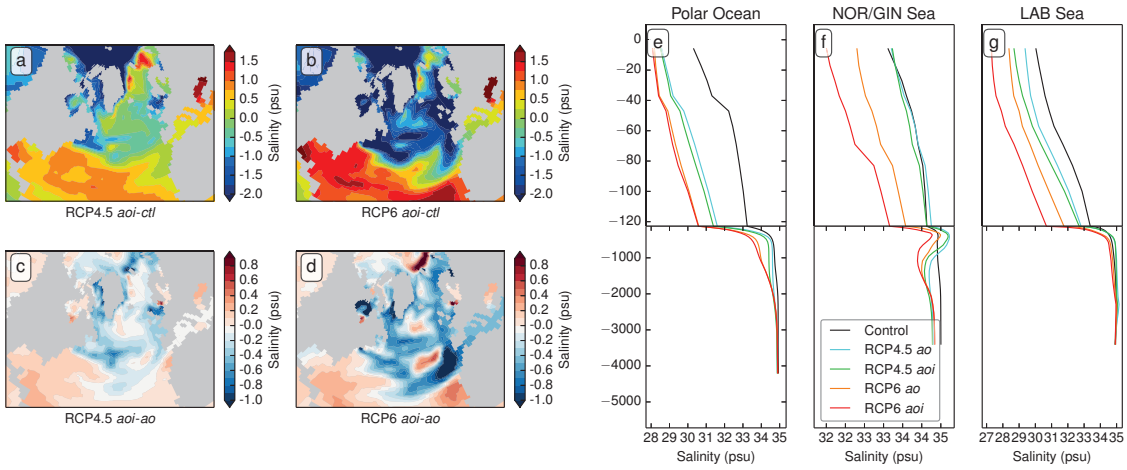

Figure 6.5: Salinity response of the North Atlantic. (a) and (b) changes in sea surface salinity between the end of scenarios RCP4.5 and RCP6 as 30 year averages in the *aoi* simulation relative to the control state, respectively. (c) and (d) show the anomaly between the *aoi* and *ao* simulations, together with hatching marking non-significant differences (95% level). Panels (e), (f), and (g) show the salinity profile of the Polar, GIN, and LAB seas, respectively, again as 30 year mean.

In the coupled *aoi* model configuration, the ice sheet meltwater discharges into the surface layers of the North Atlantic and the Nordic Seas. As a result, the sea surface

salinity is decreased by up to 2 pratical salinity units (psu) relative to the initial state (Figure 6.5-a and 6.5-b). Comparing the *aoi* and *ao* setups at the end of the simulations shows that including the dynamic ice sheet in the coupled climate simulation significantly increases the freshwater anomaly in the upper ocean layers of the North Atlantic, as *aoi* simulates an additional salinity decrease by up to 1 psu, doubling the signal relative to *ao* (Figures 6.5-c and 6.5-d). The magnitude of this anomaly implies that meltwater from the GrIS plays an important role in determining the salinity budget of the North Atlantic in a warming world, which is a signal that has not been dynamically included in other state-of-the-art coupled atmosphere-ocean general circulation climate models. Previously, such effects were studied via the prescription of continental ice sheet melting in the form of *ad hoc* freshwater perturbation, whose strength had to be estimated rather than dynamically calculated from a bi-directionally coupled ISM.

6.3.4 Ocean Response

Changes in the upper ocean's salinity also change the vertical density structure in the high latitudes. Vertical profiles of salinity at the end of the simulation period for the GIN, LAB, and Arctic Seas (ARC) basin are shown in Figure 6.5-e through 6.5-g. The NADW formation zones east of Greenland are particularly affected (Figure 6.5-f) by the changes in the salinity budget and the ice sheet's meltwater contribution. In the RCP6 simulation, the formation of a strong halocline prevents new NADW formation due to the increased surface buoyancy. These findings are in accordance with the polar halocline catastrophe theory initially proposed by Bryan [1986], who suggested that strong high latitude haloclines would severely impact vertical mixing within the ocean.

The changes in the North Atlantic's freshwater budget and accompanying halocline formation in the high latitudes effect the NADW formation rate, and therefore the AMOC strength. The circulation pattern, shown in its initial state in Figure 3-b, weakens rapidly

during the first 150 years of the simulation under the influence of increasing GHG concentrations. In the *aoi* experiments, this can be attributed not only to sea surface temperature increases and sea ice melting as is solely the case in the *ao* experiments, but also to the explicit consideration of meltwater discharge from the GrIS. The ice sheet meltwater causes an additional AMOC decrease by ≈2 Sv compared to the *ao* experiments. The difference of weakening of the NADW circulation cell can be seen in Figure 3-c, d, shown as an average anomaly of the last 30 years of the simulation. The primary cause for this difference is the strong high latitude halocline which develops, hindering vertical convection and causing the upper cell to weaken. In RCP4.5, the AMOC is able to recover again to a slightly depressed state, as the negative density perturbation caused by warming and freshening of the North Atlantic is not so severe. As seen in Figure 6.5-f, the salinity change is not so large in RCP4.5, which may explain its recovery to the the initial state. This suggests that the GIN seas likely play an important role in the AMOC strength, and that the meltwater introduced here has a severe impact.

Figure 6.6-a shows the temporal evolution of the maximum strength of the upper AMOC cell at a depth of 1020 meters between 20°N and 40°N. The initial decrease in the AMOC occurs in the first 150 years, which is related to the degree of atmospheric warming. After the GHG levels have stabilized in RCP4.5, the AMOC slowly begins to recover again. This is in contrast to the situation in RCP6, where the warming and resulting freshening is too severe to allow for a recovery. It is also noticeable that the AMOC remains consistently 2 Sv weaker in the *aoi* case compared to the *ao* case. This consistent weakening is caused by the introduction of meltwater into the critical deep convection zones in the GIN seas (Figure 6.5-f) via recirculation in the surface currents.

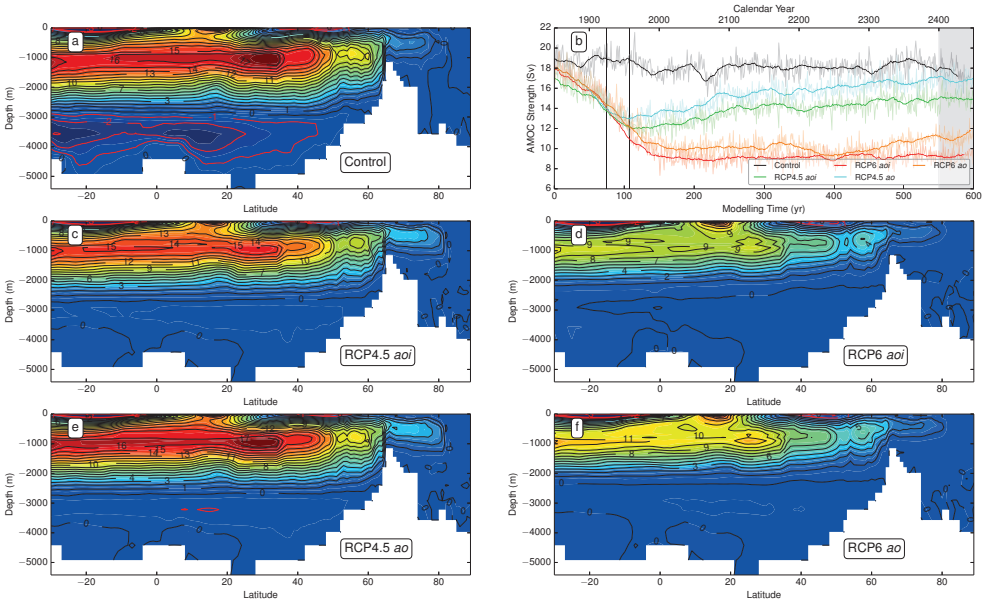

Figure 6.6: AMOC Response. The temporal evolution of the maximum AMOC strength in the upper cell is shown in (a). (b) shows the 30 year average of the AMOC in the control simulation in Sv. We can see a strong, upper circulation cell, transporting water from the high latitudes towards the south. (c) and (d) show the anomaly between the model configurations of this overturning structure at the end of simulations RCP4.5 and RCP6, respectively.

6.3.5 Discussion and Conclusion

The additional ≈ 2 Sv AMOC decrease simulated in both experiments RCP4.5 and RCP6 caused by including the ISM has major implications for future climate in a warming world. The anomalous reduction in *aoi* effectively decreases surface air temperature over the North Atlantic, Europe, and North America by $\approx 1-2^{\circ}$ C when compared to the *ao* configuration (Figures 6.7-c and 6.7-d), which corresponds to a significant temperature decrease of up to 40%. The temperature decrease is caused by a relative reduction of heat transport from the mid to high latitudes between the two model configurations. This implies that the models included in the previous IPCC reports may have overestimated the Northern Hemisphere warming.

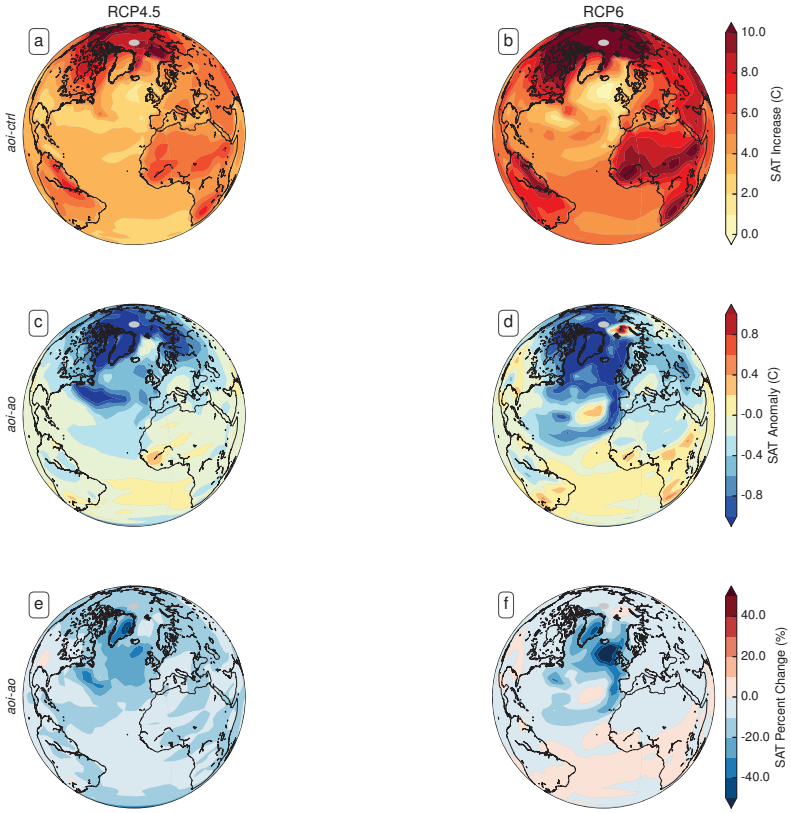

Figure 6.7: Resulting SAT differences. (a) and (b) show the surface air temperature increase for scenarios RCP4.5 and RCP6 using the *aoi* model, respectively. The differences between the model configurations are shown in (c) and (d). These differences are approximately 20-30% of the overall warming signal, suggesting that models without dynamic ice sheets may have partially overestimated climate warming in some regions. Hatching of insignificant regions is as in Figure 6.5.

Comparing these results to previous work, one finds that the estimates of other studies utilizing *ad hoc* freshwater perturbation compare reasonably well with the simulated meltwater input in this model, 0.04 Sv for RCP4.5 and 0.06 Sv for RCP6. Hu et al. [2013] use a range of ablation rates from the GrIS; varying from 0.027 Sv to 0.192 Sv for their experiments; also finding that the AMOC is highly sensitive to continental ice melt. However, both Jungclaus et al. [2006] and Driesschaert et al. [2007] find that only in very strong perturbation cases of 0.1 Sv is a noticeable AMOC change induced.

When examining systems with fully coupled ice sheets, Mikolajewicz et al. [2007] and Vizcaíno et al. [2008] found that a freshwater input of 0.02 to 0.03 Sv is sufficient to reduce the AMOC's ability to recover under idealized scenarios, a finding this study is able to support using a higher resolution ice sheet model and the most recent IPCC scenarios. It can therefore be stressed that freshwater perturbation experiments should be viewed critically and may underestimate the sensitivity of the AMOC. However, a multi-model experiment is necessary to avoid systematic biases in the simulation of the AMOC, as has been previously discussed by Weaver et al. [2012]. One such study that addresses multi-model analysis is work performed by Swingedouw et al. [2015], who found an appreciable increased weakening of the AMOC in response to hosing expirements compared to radiative forcing of extreme future projections (RCP 8.5) alone, yet that the sensitivity to freshwater input may be smaller than previously thought. The same multi-model approach is necessary for ice sheet models, which can display a variety of responses to identical forcings, as seen by Dolan et al. [2014]. Therefore, an ensemble style approach would be recommended in future studies.

In conclusion, this study demonstrated that including a dynamic ice sheet component into an AO-GCM forced by IPCC warming scenarios has immediate effects on the mass balance of the GrIS. The resulting melt water from the ice sheet discharges into the North Atlantic, intensifying the formation of high latitude haloclines. Furthermore, the reduction of the upper layer salinity inhibits NADW formation, reducing the AMOC by $\approx$ 2Sv, and the associated changes in heat transport cause relatively less warming over the Northern Hemisphere when compared to simulations utilizing fixed ice sheets. As melting land ice and the corresponding effects on ocean salinity and heat distributions is a very likely possibility in a warming future climate [Stocker et al., 2013], the inclusion of dynamic ice sheet components in climate models is of paramount importance to fully understand processes responsible for regulating and shaping future global climate.

CHAPTER 7

SYNTHESIS AND DISCUSSION

In this chapter, connections between the various studies are presented, in an attempt to provide some holisitc, integrated conclusions based upon the results of the studies presented in Chapters 3 through 6. Additionally, some indications for further work are made, along with some discussion of the limitations of these studies, and where improvements to the results presented in the previous chapters can be made.

7.1 Synthesis: Common Ideas

Several common ideas were seen in the studies presented. Two themes are briefly expanded upon. First, the role of the Atlantic Meridional Overturning Circulation (AMOC) as a system of ocean circulation that controls both the simulated as well as the proxy-measured climate is discussed. Secondly, the importance of the various effects controlling isotopic composition became apparent during several of the model-data comparisons.

7.1.1 The AMOC

It was shown in Chapter 4 that cooling in the North Atlantic, as measured by sea surface temperature proxies by Capron et al. [2014], is the result of an AMOC weakening, and that the extent of this cooling could range depending on the state of the circulation system. A complete AMOC shutdown, as seen in experiments LIG-130-H1 and the simulations performed by Stone et al. [2016] would produce a strong cooling of $-4\,^{\circ}\mathrm{C}$ to $-7\,^{\circ}\mathrm{C}$ over much of the North Atlantic. A slightly weaker AMOC, on the other hand, would produce only mild cooling of $-1.5\,^{\circ}\mathrm{C}$ to $-3\,^{\circ}\mathrm{C}$ in certain key regions, as was the case in experiment LIG-130. Using the isotope simulations of COSMOS-WISO, it was demonstrated that a larger weakening (as in LIG-130-H1) would produce isotope responses that are unrealistic, providing a possible further constraint to the climate state possibilities.

The AMOC also played an important role in Chapter 5, where the speleothem record from Corchia cave seemed to be recording an AMOC weakening, which resulted in cooling and drying over much of the European continent. However, the isotope response in $\delta^{18}O_C$ could not be captured by the model, as the simulation was unable to reproduce the extremely wet conditions at Corchia cave, a difficulty likely linked to orographic precipitation and coarse model resolution.

Additionally, the AMOC was shown to respond to freshwater input from ice sheet melting events in possible future climate scenarios presented in Chapter 6, where the mechanisms responsible for AMOC weakening due to freshwater changes are also presented. The warming in simulations including meltwater input from the Greenland Ice Sheet (GrIS) was significantly reduced relative to simulations that did not include this effect, suggesting that accounting for all of the feedbacks in climate scenarios of the future is of critical importance.

7.1.2 Effects Controlling Isotopic Composition

Various effects controlling isotopic composition also proved to be of key importance in understanding the simulated results of the Last Interglacial (LIG) climate state. Both the temperature as well as the "amount" effect influenced the isotopic composition of precipitation.

In Chapter 3, it was demonstrated that the isotopic composition of rainfall during the LIG had a strong seasonal dependence, with the signatures primarily controlled by summer signals, as more precipitation generally fell during these months. Furthermore, it was found that the temperature/$\delta^{18}O_P$ relationship were not temporally stable throughout the LIG.

Chapter 4 used the isotopic composition of foraminifera, $\delta^{18}O_C$, which is dependent not only on the $\delta^{18}O_{SW}$ composition of seawater, but also on the temperature. With the aid of the simulated $\delta^{18}O_C$, it could be shown that a freshwater perturbation during the early LIG at 130 ka B.P. was unlikely, as the resulting changes to temperature and seawater composition led to isotopic values which were inconsistent with proxy measurements.

When comparing the climate simulations of COSMOS-WISO with speleothems records, the "amount" effect played an important role on the isotopic composition within the stalagmite. COSMOS-WISO was unable to reproduce the records quantitatively, as the cave location shows a measured precipitation amount of up to 2500 mm yr^{-1} to 3000 mm yr^{-1}, whereas the model only showed approximately 300 mm yr^{-1}. Due to this large offset, a drying in the simulation, even if of the correct relative magnitude, would not have been able to show the same enrichment as was seen in the speleothem record. However, the comparison between the speleothem record and the climate simulation still allowed new insights, as it could be demonstrated that the source region composition of the seawater in the North Atlantic, and therefore the $\delta^{18}O$ in the cloud water vapor as well as of the

precipitation became depleted due to the depleted $-30\,‰$ signature of the meltwater.

7.2 Limitations & Improvements

7.2.1 Model Resolution

One of the key challenges in climate modeling is the necessity to parameterize certain processes due to limitations imposed by computational power. Some processes would necessitate extremely fine spatial resolution to truly resolve, and would thus be computationally very expensive. This problem is exacerbated by the long time periods that must be used in order to spin-up a model to paleoclimate conditions.

This difficulty appeared at several points in the previous studies presented here. In Chapter 4 capturing key ocean fronts was a problem in both the North Atlantic as well as the Southern Ocean, leading to offsets between the model and paleoclimate proxy data. The coarse model resolution also played a role during the comparison to ice cores, where the elevation accounted for some of the offset between the simulation and the measured values [1]

Model resolution also led to offsets between the simulated isotopic values and the measured values at Corchia cave, as discussed in Chapter 5. While the offset could partially be corrected for with measured gradients between elevation and isotopic composition of rainfall, further effects could not be compensated for. In particular, the rainfall at Corchia is likely to be caused by orographic uplift of air, leading to rain out as the air masses pass over the mountain range. As this orographic rain-out effect and the corresponding amount-effect of the isotopic composition cannot be easily corrected for, only the qualitative effects seen in the Corchia speleothem (cooling and drying) could be reproduced, and the isotopic composition could not be captured. However, the model-data

[1] Although, comparing to Antarctic ice cores is generally a problem for General Circulation Models (GCMs), as the extremely cold temperatures over the Antarctic continent are difficult to reproduce.

comparison still severed an important purpose, namely demonstrating that a freshwater perturbation would be accompanied by a change in the source region seawater signature, and therefore, the drying signature, which was seen as an enrichment in the $\delta^{18}O$, was not reproduced.

7.2.2 Dynamic Ice Coupling

While one of the two studies presented in Chapter 6 had utilized a fully coupled dynamic ice sheet [Gierz et al., 2015], such a model configuration is still very novel, and has not yet been used for paleoclimate simulations. However, the interactions between the climate and the cryosphere are certainly of relevance for paleoclimate scenarios, and future work should focus on enabling such a coupling to also be feasible for paleoclimate simulations.

A key advantage of such a coupled GCM-Ice Sheet Model (ISM) system would be the analysis of potential sea level changes throughout warm climate periods. One of the primary uncertainties of the LIG's climate surrounds timing and magnitude of sea level increases. A fully coupled climate-ice simulation would allow for an examination of sea level increases, answering questions about the timing and contribution of meltwater from both Greenland as well as Antarctica.

Furthermore, key climate feedbacks – such as meltwater induced AMOC changes – would be calculated dynamically by the simulation, rather than necessitating the estimation of timing and magnitude of freshwater perturbation as was done in Chapter 5.

One additional aspect would be of benefit to explore in the future. Even if uncoupled, a modification of the Antarctic ice sheet orography to conditions presented in Sutter et al. [2016] could give an indication of how important the orographic effects are on the climate as well as the isotopic record. Furthermore, it might be useful in future studies

to adapt sea surface temperatures around Antarctica to correspond with the 2 °C to 3 °C threshold, as a sensitivity study to examine if the model-data comparisons improve in this case.

7.2.3 Other Considerations

Some other considerations must also be mentioned. While the results presented partially mismatched between model and data may be explainable by model insufficiencies, the proxies themselves also have certain weaknesses and drawbacks. Difficulties in absolute dating making model-data comparisons more challenging, and temporal resolution can also be problematic. Of those proxies that offer a high temporal resolution, such as fossilized corals, the length of the records are often quite short. In the case of the comparison performed in section 4.3, record lengths ranged from just 3 years at the minimum to 37 years at the maximum.

Furthermore, the studies that are presented here always relied only on one model, COSMOS-WISO. It has been demonstrated by several model intercomparison projects [Bakker et al., 2014, Haywood et al., 2013, Bakker et al., 2013, Weaver et al., 2012, Crucifix et al., 2012] that simulations not only of the LIG, but also for the future climate require several different models in order to fully explore the range of possibilities. Examining the climate of the LIG has become a target for the next paleoclimate model intercomparison project, and results from that effort will hopefully assist in understanding and supporting the findings presented here.

In the final chapter, the questions posed in the introduction are addressed, and the findings from each study are summarized.

CHAPTER 8

CONCLUSIONS

In Chapter 1, several questions were posed, with overall aim of utilizing a stable water isotope equipped general circulation model to better understand the climate of the Last Interglacial. Having presented the primary findings of several studies undertaken with the aid of this model, an attempt is now made to answer some of these questions.

- **What are the general characteristics of the Last Interglacial (LIG) climate that are produced using a stable water isotope equipped climate model? In how far are the physical and isotopic representations of the climate consistent with one another?**

  These questions were primarily addressed in Chapter 3. It was found that the LIG's climate was varied over the progression of three examined time periods, with a relatively cooler than present global average temperature during the early LIG, progressing to a warmer-than-present climate during the mid LIG, and returning once more towards a climate state which was similar to the pre-industrial during the late LIG. Furthermore, a precipitation amount bias was uncovered, suggesting

that a significant seasonal weighting exists in the utility of $\delta^{18}O_P$ as a temperature proxy.

- **In which cases do stable water isotopes fail to accurately reproduce the physical climate?**

  One important finding in Section 3 was an inconsistency in the $\delta^{18}O/T$ relationships throughout the LIG. The classic paleothermometer described by Dansgaard [1964] suggests a spatial gradient of approximately $0.69\,‰\,°C^{-1}$. This gradient is often utilized as a first approximation to reconstruct temperature differences in past climate states from measured $\delta^{18}O$ differences.

  COSMOS-WISO slightly underestimates the value found by Dansgaard [1964]. When this spatial relationship is compared to the temporal gradient (as would be done to reconstruct a past temperature change from a measured $\delta^{18}O$ change), it was discovered that the $\delta^{18}O$/T relationship was globally hetereogenous. This implies that using the measured spatial $\delta^{18}O/T$ gradient would produce incorrect temperature changes. Furthermore, the $\delta^{18}O/T$ gradient only produced physically sensible values if the temperature changes were large enough. Temperature changes of $\Delta T_{LIG-PI} \geq 0.5°C$ produced negative relationships at some locations, which is indicative of a "recorder problem" as a negative relation is implausible from the fundamental physical principles of water isotope fractionation.

- **To what extent can this climate model reproduce signals that are acquired from paleoclimate archives? Are any paleoclimate archives particularly difficult to reproduce?**

  In Chapter 4, the simulations performed with COSMOS-WISO were compared against proxy reconstructions of temperature changes in both the North Atlantic and the Southern Oceans. It was found that COSMOS-WISO produced temperature

changes that were within the error range of the reconstructions.

In the North Atlantic, previous studies by Capron et al. [2014] and Stone et al. [2016] have attempted to constrain the climate of the North Atlantic. While the proxy reconstructions indicated a cooling in this area, several General Circulation Model (GCM) simulations are unable to reproduce this pattern. Simulations utilizing the HAD-CM climate model attempted to rectify this offset with the aid of a freshwater perturbation. When reproducing this experiment, it was discovered that COSMOS-WISO produces a similar physical response to the freshwater perturbation as is seen in HAD-CM simulation. Despite this, both the perturbed and unperturbed climate states produce sea surface temperatures that are within the error range of the proxy reconstructions. To further constrain the possibilities, a preliminary analysis comparing the $\delta^{18}O_C$ was performed[1]. It was discovered that the climate state including a freshwater perturbation produced calcite signals that did not match the measurements, thereby suggesting that the melt water pulse at the end of the preceding glacial period (MIS-6) occurred even earlier than 130 ka B.P..

The comparisons in the Southern Ocean did not include stable water isotope measurements, and served to independently validate the climate model against a second set of measurements. Both the simulations for the peak and late LIG as well as the proxy reconstructions of the same period revealed similar patterns. A warming of the Antarctic Circumpolar Current (ACC) during the peak LIG may be due to a bipolar seesaw effect and a reduced Atlantic Meridional Overturning Circulation (AMOC) strength during the peak LIG, with conditions in both the simulation and the reconstructions closer to Pre-Industrial (PI) conditions at 120 ka B.P..

[1]This analysis cannot be finalized until those sediment cores with available $\delta^{18}O_C$ measurements have been precisely dated; Emelie Capron (*personal communication)*

Another comparison was performed to examine if the high frequency variability of the LIG climate as produced by COSMOS-WISO. Fossilized corals are one of the few paleoclimate archives that are able to capture sub-annual variability. Section 4.3 examined seasonal sea surface temperature (SST) cycles during the LIG. It was found that COSMOS-WISO was able to reproduce the same amplitudes as discovered in the coral records.

Finally, a transient simulation of the LIG made with COSMOS-WISO was compared to ice core records. A primary offset between the ice core $\delta^{18}O$ and the simulated $\delta^{18}O$ was discovered due to coarse resolution, which can be partially rectified by utilizing a elevation correction, accounting for the difference between the height in the simulation and the elevation in the real world. Despite this correction, some features of the LIG as recorded by $\delta^{18}O$ in ice cores are not reproduced by the simulation. This may be due to the fact that COSMOS-WISO is unable to capture the extremely low temperatures over Antarctica, which is a problem in many GCMs. Furthermore, it could be that the West Antarctic Ice Sheet (WAIS) was considerably reduced during the peak LIG, and additional work should explore the climate and isotope responses of reducing the WAIS.

- **Is the climate of the LIG stable, or is it sensitive to rapid non-linear changes induced by small perturbations?**

  Chapter 5 examined freshwater perturbation experiments in the North Atlantic, with the aim of reproducing sudden excursions in the isotopic record of the LIG from a speleothem calcite archive. It was found that freshwater perturbations of 0.2 Sv with an isotopic signature of $-30\,‰$ led to a rapid excursion of $-0.61\,‰$ in $\delta^{18}O_C$ over the course of several decades. This rapid depletion is in good agreement with the speleothem record, where a sudden excursion of $-0.64\,‰$ took place.

  Together with the record of carbon isotopes from the speleothem, which indicated

a simultaneous rapid cooling and drying, it is possible to suggest that an AMOC collapse may have taken place during the LIG at approximately 125 ka B.P.. The triggering mechanism, namely a rapid freshening of the North Atlantic, calls for a fairly large amount of freshwater being released, an equivalent of 2.6 m sea level increase. This amount of freshwater is within the approximated range of the sea level contribution from the Greenland Ice Sheet (GrIS). While the occurrence of such an event in the real world cannot be conclusively proven without further proxy evidence, it is a good first indication that the climate of the LIG was susceptible to rapid non-linear changes, as has also been found for glacial climate states.

- **Are the ice sheets stable during the LIG?**

  Chapter 6 examined changes to the Antarctic Ice Sheet due to ocean warming during the LIG. While it was found that the GCM COSMOS-WISO was unable to produce a warming large enough to trigger a collapse of the WAIS. However, hypothetical warming experiments indicate that a WAIS disintegration would occur given warming between 2.0 °C to 3.0 °C. This collapse happens in multiple stages, starting with the opening of the Weddell and Amundsen seas, followed by the opening of the Ross sea. This behavior suggests a dynamic non-linear response of the Antarctic ice sheet to ocean warming.

- **Can any of the findings from these questions find application to future climate scenarios?**

  A further investigation in 6 showed the importance of including ice sheet feedbacks in future climate scenarios. By enabling the freshwater feedback from melting of the GrIS, it was shown that the AMOC is further weakened than already assumed in more traditional atmosphere-ocean models. This leads to an relative decrease in the amount of warming due to increased greenhouse gas (GHG) concentrations, and it could be that models without dynamic ice sheet components are simultaneously

overestimating AMOC strength in the future, as well as the overall amount of warming, which may be overestimated by as much as 30%.

In conclusion, the diverse examinations presented here have allowed for several new insights into the climate of the LIG. Utilizing a stable water isotope equipped model afforded the unique advantage of being able to directly compare against proxy records, rather than interpretations. The robustness of the classic isotope paleothermometer was examined, and it was found that seasonal biases must be taken into account due to the precipitation intermittency. Furthermore, with this method of comparison, it was possible to show further constraints on North Atlantic climate, which would not have been possible with a traditional GCM. Furthermore, rapid climate change events could be identified in a speleothem record, and directly reproduced with the GCM, with quantitatively similar excursions in the isotopic record. When attempting to identify possible triggering mechanisms to such rapid change excursions, thresholds for Antarctic ice sheet collapse were discovered.

Research interest in the LIG should by no means be considered to be at an end, and the climate period remains an important area of investigation to fully understand the controlling mechanisms of warm climate states in general. Only by continuing to explore the interconnected dynamics of the atmosphere, ocean, ice sheets, and biosphere will conclusive answers be found, which will hopefully enable further understanding of how Earth's climate changes without human influence, allowing for better disentanglement of future climate responses between natural variability and anthropogenthically induced modifications.

BIBLIOGRAPHY

A. Abelmann and R. Gersonde. Biosiliceous Particle-Flux in the Southern Ocean. *Marine Chemistry*, 35(1-4):503–536, Nov. 1991.

S. Aciego, B. Bourdon, J. Schwander, H. Baur, and A. Forieri. Toward a radiometric ice clock: uranium ages of the Dome C ice core. *Quaternary Science Reviews*, 30(19-20):2389–2397, Sept. 2011.

A. Arakawa and V. R. Lamb. Computational design of the basic dynamical processes of the UCLA general circulation model. *Methods in computational physics*, 1977.

L. K. Armand and A. Leventer. Palaeo Sea Ice Distribution and Reconstruction Derived from the Geological Record. In *Sea Ice: Second Edition*, pages 469–529. Wiley-Blackwell, Oxford, UK, Jan. 2010.

P. Bakker, E. J. Stone, S. Charbit, M. Groeger, U. Krebs-Kanzow, S. P. Ritz, V. Varma, V. Khon, D. J. Lunt, U. Mikolajewicz, M. Prange, H. Renssen, B. Schneider, and M. Schulz. Last interglacial temperature evolution - a model inter-comparison. *Climate of the Past*, 9(2):605–619, 2013.

P. Bakker, V. Masson-Delmotte, B. Martrat, S. Charbit, H. Renssen, M. Groeger, U. Krebs-Kanzow, G. Lohmann, D. J. Lunt, M. Pfeiffer, S. J. Phipps, M. Prange, S. P. Ritz, M. Schulz, B. Stenni, E. J. Stone, and V. Varma. Temperature trends during the Present and Last Interglacial periods - a multi-model-data comparison. *Quaternary Science Reviews*, 99:224–243, 2014.

J. L. Bamber, R. E. M. Riva, B. L. A. Vermeersen, and A. M. LeBrocq. Reassessment of the Potential Sea-Level Rise from a Collapse of the West Antarctic Ice Sheet. *Science*, 324(5929):901–903, 2009.

D. Barbi, G. Lohmann, K. Grosfeld, and M. Thoma. Ice sheet dynamics within an earth system model: downscaling, coupling and first results. *Geoscientific Model Development*, 7(5):2003–2013, September 2014.

S. Barker, P. Diz, M. J. Vautravers, J. Pike, G. Knorr, and I. R. Hall. Interhemispheric Atlantic seesaw

response during the last deglaciation. *Nature*, 2009.

E. J. Barron, W. W. Hay, and S. Thompson. The hydrologic cycle: A major variable during earth history. *Palaeogeography, Palaeoclimatology, Palaeoecology*, 75(3):157–174, Aug. 1989.

H. A. Bauch, E. S. Kandiano, and J. P. Helmke. Contrasting ocean changes between the subpolar and polar North Atlantic during the past 135 ka. *Geophysical Research Letters*, 39(11):n/a–n/a, June 2012.

L. Bazin, A. Landais, B. Lemieux-Dudon, H. T. M. Kele, D. Veres, F. Parrenin, P. Martinerie, C. Ritz, E. Capron, V. Lipenkov, M. F. Loutre, D. Raynaud, B. Vinther, A. Svensson, S. O. Rasmussen, M. Severi, T. Blunier, M. Leuenberger, H. Fischer, V. Masson-Delmotte, J. Chappellaz, and E. Wolff. An optimized multi-proxy, multi-site Antarctic ice and gas orbital chronology (AICC2012): 120-800 ka. *Climate of the Past*, 9(4):1715–1731, 2013.

A. Beckmann and R. Döscher. A method for improved representation of dense water spreading over topography in geopotential-coordinate models. *Journal of Physical Oceanography*, 27(4): 581–591, 1997.

M. Bender, T. Sowers, and L. Labeyrie. The Dole effect and its variations during the last 130,000 years as measured in the Vostok ice core. *Global Biogeochemical Cycles*, 1994.

M. L. Bender. Orbital tuning chronology for the Vostok climate record supported by trapped gas composition. *Earth and Planetary Science Letters*, 204(1-2):275–289, 2002.

A. Berger and M. F. Loutre. Insolation values for the climate of the last 10 million years. *Quaternary Science Reviews*, 10(4):297–317, Jan. 1991.

A. L. Berger. Long-term variations of caloric insolation resulting from the Earth's orbital elements. *Quaternary Research*, 1978.

P. Blanchon, A. Eisenhauer, J. Fietzke, and V. Liebetrau. Rapid sea-level rise and reef back-stepping at the close of the last interglacial highstand. *Nature*, 458(7240):881–U6, 2009.

G. Boccaletti, R. Ferrari, A. Adcroft, D. Ferreira, and J. Marshall. The vertical structure of ocean heat transport. *Geophysical Research Letters*, 32(10), 2005. ISSN 1944-8007.

W. M. Brocas, T. Felis, J. C. Obert, P. Gierz, G. Lohmann, D. Scholz, M. Kölling, and S. R. Scheffers. Last interglacial temperature seasonality reconstructed from tropical Atlantic corals. *Earth and Planetary Science Letters*, 449:418–429, 2016.

V. Brovkin, T. Raddatz, C. H. Reick, M. Claussen, and V. Gayler. Global biogeophysical interactions between forest and climate. *Geophysical Research Letters*, 36(7):L07405, Apr. 2009.

F. Bryan. High-latitude salinity effects and interhemispheric thermohaline circulations. *Nature*, 323(6086):301–304, Sept. 1986.

CAPE Last Interglacial Project members. Last Interglacial Arctic warmth confirms polar amplification of climate change. *Quaternary Science Reviews*, 25(13–14):1383–1400, 2006.

E. Capron, A. Govin, and E. J. Stone. Temporal and spatial structure of multi-millennial temperature changes at high latitudes during the Last Interglacial. *Quaternary Science Reviews*, 103: 116–133, 2014.

S. Charbit, D. Paillard, and G. Ramstein. Amount of co2 emissions irreversibly leading to the total melting of greenland. *Geophysical Research Letters*, 35(12):n/a–n/a, 2008. ISSN 1944-8007. L12503.

D. Chen, R. Gerdes, and G. Lohmann. A 1-D atmospheric energy balance model developed for ocean modelling. *Theoretical and Applied Climatology*, 51(1):25–38, 1995.

M. Claussen, L. Mysak, A. Weaver, M. Crucifix, and T. Fichefet. Earth system models of intermediate complexity: closing the gap in the spectrum of climate system models. *Climate Dynamics*, 2002.

A. C. Clement and L. C. Peterson. Mechanisms of abrupt climate change of the last glacial period. *Reviews of Geophysics*, 2008.

I. Couchoud, D. Genty, D. Hoffmann, R. Drysdale, and D. Blamart. Millennial-scale climate variability during the Last Interglacial recorded in a speleothem from south-western France. *Quaternary Science Reviews*, 28(27-28):3263–3274, Dec. 2009.

H. Craig and L. I. Gordon. *Deuterium and Oxygen 18 Variations in the Ocean and the Marine Atmosphere*. Consiglio nazionale delle richerche, Laboratorio de geologia nucleare, 1965.

T. J. Crowley. North Atlantic deep water cools the Southern Hemisphere. *Paleoceanography*, 1992.

M. Crucifix, S. Harrison, and C. Brierley. Recent and deep pasts in paleoclimate model intercomparison project. *Eos, Transactions American Geophysical Union*, 93(51):539, Dec. 2012.

K. M. Cuffey and S. J. Marshall. Substantial contribution to sea-level rise during the last interglacial from the Greenland ice sheet. *Nature*, 404(6778): 591–594, 2000.

W. Dansgaard. Stable isotopes in precipitation. *Tellus*, 16(4):436–468, 1964.

P. Davini, J. von Hardenberg, L. Filippi, and A. Provenzale. Impact of greenland orography on the atlantic meridional overturning circulation. *Geophysical Research Letters*, 42(3):871–879, 2015. ISSN 1944-8007. 2014GL062668.

P. Deines. Comment on "An explanation of the effect of seawater carbonate concentration on

foraminiferal oxygen isotopes," by R. E. Zeebe (1999). *Geochimica et Cosmochimica Acta*, 69(3): 787–787, 2005.

E. T. DeWeaver, E. C. Hunke, and M. M. Holland. On the reliability of simulated Arctic sea ice in global climate models. *Geophysical Research Letters*, 35 (4), 2008.

M. Dima and G. Lohmann. Conceptual model for millennial climate variability: A possible combined solar-thermohaline circulation origin for the ,à^{o}1,500-year cycle. *Climate Dynamics*, 32 (2-3):301–311, Jan. 2009.

A. M. Dolan, S. J. Hunter, D. J. Hill, A. M. Haywood, S. J. Koenig, B. L. Otto-Bliesner, A. Abe-Ouchi, F. Bragg, W.-L. Chan, M. A. Chandler, C. Contoux, A. Jost, Y. Kamae, G. Lohmann, D. J. Lunt, G. Ramstein, N. A. Rosenbloom, L. Sohl, C. Stepanek, H. Ueda, Q. Yan, and Z. Zhang. Using results from the pliomip ensemble to investigate the greenland ice sheet during the warm pliocene. *Climate of the Past Discussions*, 10(4): 3483–3535, 2014. doi: 10.5194/cpd-10-3483-2014.

W. Dreybrodt and D. Scholz. Climatic dependence of stable carbon and oxygen isotope signals recorded in speleothems: From soil water to speleothem calcite. *Geochimica et Cosmochimica Acta*, 75(3): 734–752, Feb. 2011.

E. Driesschaert, T. Fichefet, H. Goosse, P. Huybrechts, I. Janssens, A. Mouchet, G. Munhoven, V. Brovkin, and S. L. Weber. Modeling the influence of Greenland ice sheet melting on the Atlantic meridional overturning circulation during the next millennia. *Geophysical Research Letters*, 34(10):L10707, May 2007.

S. Drijfhout, G. J. van Oldenborgh, and A. Cimatoribus. Is a Decline of AMOC Causing the Warming Hole above the North Atlantic in Observed and Modeled Warming Patterns? *Journal of Climate*, 25(24):8373–8379, 2012.

R. N. Drysdale, G. Zanchetta, J. C. Hellstrom, A. E. Fallick, J.-x. Zhao, I. Isola, and G. Bruschi. Palaeoclimatic implications of the growth history and stable isotope (δ^{18}O and δ^{13}C) geochemistry of a Middle to Late Pleistocene stalagmite from central-western Italy. *Earth and Planetary Science Letters*, 227(3-4):215–229, Nov. 2004.

R. N. Drysdale, G. Zanchetta, J. C. Hellstrom, A. E. Fallick, and J.-x. Zhao. Stalagmite evidence for the onset of the Last Interglacial in southern Europe at 129 ± 1 ka. *Geophysical Research Letters*, 32(24):L24708, Dec. 2005.

R. N. Drysdale, G. Zanchetta, J. C. Hellstrom, A. E. Fallick, J. McDonald, and I. Cartwright. Stalagmite evidence for the precise timing of North Atlantic cold events during the early last glacial. *Geology*, 35(1):77–80, Jan. 2007.

R. N. Drysdale, J. C. Hellstrom, G. Zanchetta, A. E. Fallick, M. F. S. Goñi, I. Couchoud, J. McDonald, R. Maas, G. Lohmann, and I. Isola. Evidence

for Obliquity Forcing of Glacial Termination II. *Science*, 325(5947):1527–1531, Sept. 2009.

N. W. Dunbar, W. C. McIntosh, and R. P. Esser. Physical setting and tephrochronology of the summit caldera ice record at Mount Moulton, West Antarctica. *Geological Society of America Bulletin*, 120(7-8):796–812, 2008.

J.-C. Duplessy, C. Lalou, and A. C. Vinot. Differential Isotopic Fractionation in Benthic Foraminifera and Paleotemperatures Reassessed. *Science*, 168 (3928):250–251, Apr. 1970.

A. Dutton and K. Lambeck. Ice volume and sea level during the last interglacial. *Science*, 337(6091): 216–219, July 2012.

A. Dutton, A. E. Carlson, A. J. Long, G. A. Milne, P. U. Clark, R. DeConto, B. P. Horton, S. Rahmstorf, and M. E. Raymo. Sea-level rise due to polar ice-sheet mass loss during past warm periods. *Science*, 349(6244):–aaa4019, 2015a.

A. Dutton, J. M. Webster, D. Zwartz, K. Lambeck, and B. Wohlfarth. Tropical tales of polar ice: evidence of Last Interglacial polar ice sheet retreat recorded by fossil reefs of the granitic Seychelles islands. *Quaternary Science Reviews*, 107 IS -: 182–196, 2015b.

I. Eisenman, C. M. Bitz, and E. Tziperman. Rain driven by receding ice sheets as a cause of past climate change. *Paleoceanography*, 24(4), Dec. 2009.

EPICA community members. Eight glacial cycles from an Antarctic ice core. *Nature*, 429(6992): 623–628, June 2004.

O. Esper and R. Gersonde. Quaternary surface water temperature estimations: New diatom transfer functions for the Southern Ocean. *Palaeogeography, Palaeoclimatology, Palaeoecology*, 414: 1–19, Nov. 2014a.

O. Esper and R. Gersonde. New tools for the reconstruction of Pleistocene Antarctic sea ice. *Palaeogeography, Palaeoclimatology, Palaeoecology*, 399: 260–283, 2014b.

O. Esper, R. Gersonde, and N. Kadagies. Diatom distribution in southeastern Pacific surface sediments and their relationship to modern environmental variables. *Palaeogeography, Palaeoclimatology, Palaeoecology*, 287(1-4):1–27, 2010.

T. Felis, G. Lohmann, H. Kuhnert, S. J. Lorenz, D. Scholz, J. Pätzold, S. A. Al-Rousan, and S. M. Al-Moghrabi. Increased seasonality in Middle East temperatures during the last interglacial period. *Nature*, 429(6988):164–168, 2004.

T. Felis, C. Giry, D. Scholz, G. Lohmann, M. Pfeiffer, J. Pätzold, M. Kölling, and S. R. Scheffers. Tropical Atlantic temperature seasonality at the end of the last interglacial. *Nature Communications*, 6:6159, Jan. 2015.

T. Fichefet. Implications of changes in freshwater flux from the Greenland ice sheet for the climate

of the 21st century. *Geophysical Research Letters*, 30(17), 2003.

G. Fischer, R. Gersonde, and G. Wefer. Organic carbon, biogenic silica and diatom fluxes in the Northern Seasonal Ice Zone in the Polar Front Region in the Southern Ocean (Atlantic Sector): Interannual variation and changes in composition. *Deep Sea Research, Part II*, 49:1721–1745, 2002.

M. Gascoyne. Paleoclimate Determination From Cave Calcite Deposits. *Quaternary Science Reviews*, 11(6):609–632, 1992.

J. R. Gat. Oxygen and Hydrogen Isotopes in the Hydrologic Cycle. *Annual Review of Earth and Planetary Sciences*, 24(1):225–262, 1996.

P. R. Gent, J. Willebrand, T. J. McDougall, and J. C. McWilliams. Parameterizing Eddy-Induced Tracer Transports in Ocean Circulation Models. 25(4):463–474, Feb. 2010.

D. Genty, D. Blamart, B. Ghaleb, V. Plagnes, C. Causse, M. Bakalowicz, K. Zouari, N. Chkir, J. Hellstrom, and K. Wainer. Timing and dynamics of the last deglaciation from European and North African δ13C stalagmite profiles—comparison with Chinese and South Hemisphere stalagmites. *Quaternary Science Reviews*, 25(17-18):2118–2142, Sept. 2006.

P. Gierz. Ocean circulation stability under possible future climate scenarios: Lessons from a coupled atmosphere-ocean-cryosphere model, June 2013.

P. Gierz, G. Lohmann, and W. Wei. Response of Atlantic overturning to future warming in a coupled atmosphere-ocean-ice sheet model. *Geophysical Research Letters*, 42(16):6811–6818, Aug. 2015.

C. Giry, T. Felis, M. Koelling, and S. Scheffers. Geochemistry and skeletal structure of Diploria strigosa, implications for coral-based climate reconstruction. *Palaeogeography Palaeoclimatology Palaeoecology*, 298(3-4):378–387, 2010.

C. Giry, T. Felis, M. Koelling, D. Scholz, W. Wei, G. Lohmann, and S. Scheffers. Mid- to late Holocene changes in tropical Atlantic temperature seasonality and interannual to multidecadal variability documented in southern Caribbean corals. *Earth and Planetary Science Letters*, 331: 187–200, 2012.

H. Godwin. Half-Life of Radiocarbon. *Nature*, Vol: 195, Sept. 1962.

X. Gong, G. Knorr, G. Lohmann, and X. Zhang. Dependence of abrupt atlantic meridional ocean circulation changes on climate background states. *Geophysical Research Letters*, 40(14):3698–3704, 2013. ISSN 1944-8007.

H. Goosse, P. Y. Barriat, W. Lefebvre, M. F. Loutre, and V. Zunz. *Introduction to climate dynamics and climate modeling*. Cambridge University Press, 2010.

A. Govin, P. Braconnot, E. Capron, E. Cortijo, J. C. Duplessy, E. Jansen, L. Labeyrie, A. Landais,

O. Marti, E. Michel, E. Mosquet, B. Risebrobakken, D. Swingedouw, and C. Waelbroeck. Persistent influence of ice sheet melting on high northern latitude climate during the early Last Interglacial. *CP*, 8(2):483–507, Mar. 2012.

A. Govin, E. Capron, Tzedakis, P. C., S. Verheyden, B. Ghaleb, C. Hillaire-Marcel, G. St-Onge, J. S. Stoner, F. Bassinot, L. Bazin, T. Blunier, N. Combourieu-Nebout, A. El Ouahabi, D. Genty, R. Gersonde, P. Jimenez-Amat, A. Landais, B. Martrat, V. Masson-Delmotte, F. Parrenin, M. S. Seidenkrantz, D. Veres, C. Waelbroeck, and R. Zahn. Sequence of events from the onset to the demise of the Last Interglacial: Evaluating strengths and limitations of chronologies used in climatic archives. *Quaternary Science Reviews*, 129:1–36, 2015.

R. T. Gregory and H. P. Taylor. An oxygen isotope profile in a section of cretaceous oceanic crust, samail ophiolite, oman: Evidence for δ^{18}o buffering of the oceans by deep (> 5 km) seawater-hydrothermal circulation at mid-ocean ridges. *Journal of Geophysical Research: Solid Earth*, 86(B4):2737–2755, 1981.

P. M. Grootes, E. J. Steig, M. Stuiver, E. D. Waddington, D. L. Morse, and M.-J. Nadeau. The Taylor Dome Antarctic 18O Record and Globally Synchronous Changes in Climate. *Quaternary Research*, 56(3):289–298, Nov. 2001.

B. Haese, M. Werner, and G. Lohmann. Stable water isotopes in the coupled atmosphere-land surface model ECHAM5-JSBACH. *Geoscientific Model Development*, 6(5):1463–1480, 2013.

C. Harig and F. J. Simons. Accelerated West Antarctic ice mass loss continues to outpace East Antarctic gains. *Earth and Planetary Science Letters*, 415:134–141, 2015.

J. D. Hays, J. Imbrie, and N. J. Shackleton. Variations in the Earth's Orbit: Pacemaker of the Ice Ages. *Science*, 194(4270):1121–1132, Dec. 1976.

A. M. Haywood, D. J. Hill, A. M. Dolan, B. L. Otto-Bliesner, F. Bragg, W. L. Chan, M. A. Chandler, C. Contoux, H. J. Dowsett, A. Jost, Y. Kamae, G. Lohmann, D. J. Lunt, A. Abe-Ouchi, S. J. Pickering, G. Ramstein, N. A. Rosenbloom, U. Salzmann, L. Sohl, C. Stepanek, H. Ueda, Q. Yan, and Z. Zhang. Large-scale features of Pliocene climate: results from the Pliocene Model Intercomparison Project. *Climate of the Past*, 9(1):191–209, 2013.

H. H. Hellmer, F. Kauker, R. Timmermann, J. Determann, and J. Rae. Twenty-first-century warming of a large Antarctic ice-shelf cavity by a redirected coastal current. *Nature*, 485(7397):225–228, 2012.

S. R. Hemming. Heinrich events: Massive late Pleistocene detritus layers of the North Atlantic and their global climate imprint. *Reviews of Geophysics*, 42(1):RG1005, Mar. 2004.

M. Herold and G. Lohmann. Eemian tropical and subtropical African moisture transport: an iso-

tope modelling study. *Climate Dynamics*, 33(7-8): 1075–1088, 2009.

S. Hetzinger, M. Pfeiffer, and W. C. Dullo. Sr/Ca and δ18O in a fast-growing Diploria strigosa coral: Evaluation of a new climate archive for the tropical Atlantic. *Geochemistry*, 2006.

C. Hillaire-Marcel, A. de Vernal, and D. J. W. Piper. Lake Agassiz Final drainage event in the northwest North Atlantic. *Geophysical Research Letters*, 34(15), Aug. 2007.

J. Hoefs. *Stable Isotope Geochemistry*. Springer, Göttingen, 1997.

G. Hoffmann, M. Werner, and M. Heimann. Water isotope module of the ECHAM atmospheric general circulation model: A study on timescales from days to several years. *Journal of Geophysical Research-Atmospheres*, 103(D14):16871–16896, July 1998.

A. Hu, G. A. Meehl, W. Han, and J. Yin. Effect of the potential melting of the Greenland Ice Sheet on the Meridional Overturning Circulation and global climate in the future. *Deep Sea Research Part II: Topical Studies in Oceanography*, 58:1914–1926, 2011. ISSN 09670645.

A. Hu, G. A. Meehl, W. Han, J. Yin, B. Wu, and M. Kimoto. Influence of continental ice retreat on future global climate. *Journal of Climate*, 26: 3087–3111, 2013. ISSN 08948755.

K. A. Hughen, D. P. Schrag, S. B. Jacobsen, and W. Hantoro. El Nino during the last interglacial period recorded by a fossil coral from Indonesia. *Geophysical Research Letters*, 26(20):3129–3132, 1999.

G. Hut. Consultants' group meeting on stable isotope reference samples for geochemical and hydrological investigations. Apr. 1987.

W. H. Hutson. Agulhas Current During the Late Pleistocene - Analysis of Modern Faunal Analogs. *Science*, 207(4426):64–66, 1980.

P. Huybrechts, I. Janssens, C. Pocin, and T. Fichefet. The response of the Greenland ice sheet to climate changes in the 21st century by interactive coupling of an AOGCM with a thermomechanical ice-sheet model. *Annals of Glaciology, Vol 35*, 35: 409–415, 2002.

P. Huybrechts, O. Rybak, F. Pattyn, U. Ruth, and D. Steinhage. Ice thinning, upstream advection, and non-climatic biases for the upper 89% of the EDML ice core from a nested model of the Antarctic ice sheet. *Climate of the Past*, 3(4):577–589, 2007.

J. Imbrie and N. Kipp. A new micropaleontological method for quantitative Paleoclimatology: Application to a late Pleistocene core, Late Cenozoic Glacial Ages KK Turekian, 71–181. 1971.

Intergovernmental Panel on Climate Change. *Climate Change 2013 – The Physical Science Basis*.

Working Group I Contribution to the Fifth Assessment Report of the Intergovernmental Panel on Climate Change. Cambridge University Press, Mar. 2014.

I. Joughin and R. B. Alley. Stability of the West Antarctic ice sheet in a warming world. *Nature Geoscience*, 4(8):506–513, Aug. 2011.

J. Jouzel, N. I. Barkov, J. M. Barnola, M. Bender, J. Chappellaz, C. Genthon, V. M. Kotlyakov, V. Lipenkov, C. Lorius, J. R. Petit, D. Raynaud, G. Raisbeck, C. Ritz, T. Sowers, M. Stievenard, F. Yiou, and P. Yiou. Extending the Vostok ice-core record of palaeoclimate to the penultimate glacial period. *Nature*, 364(6436):407–412, July 1993.

J. Jouzel, V. Masson-Delmotte, O. Cattani, G. Dreyfus, S. Falourd, G. Hoffmann, B. Minster, J. Nouet, J. M. Barnola, J. Chappellaz, H. Fischer, J. C. Gallet, S. Johnsen, M. Leuenberger, L. Loulergue, D. Luethi, H. Oerter, F. Parrenin, G. Raisbeck, D. Raynaud, A. Schilt, J. Schwander, E. Selmo, R. Souchez, R. Spahni, B. Stauffer, J. P. Steffensen, B. Stenni, T. F. Stocker, J. L. Tison, M. Werner, and E. W. Wolff. Orbital and Millennial Antarctic Climate Variability over the Past 800,000 Years. *Science*, 317(5839):793–796, Aug. 2007.

S. Juggins. Quantitative reconstructions in palaeolimnology: new paradigm or sick science? *Quaternary Science Reviews*, 64:20–32, 2013.

J. H. Jungclaus, H. Haak, M. Latif, S. J. Marsland, and F. Röske. The Max-Planck-Institute global ocean/sea ice model with orthogonal curvilinear coordinates. 5(2):91–127, 2002.

J. H. Jungclaus, E. Roeckner, J. Marotzke, H. Haak, and M. Esch. Will Greenland melting halt the thermohaline circulation? *Geophysical Research Letters*, 33(17):L17708, 2006.

M. Kageyama, U. Merkel, B. L. Otto-Bliesner, M. Prange, A. Abe-Ouchi, G. Lohmann, R. Ohgaito, D. M. Roche, J. Singarayer, D. Swingedouw, and X Zhang. Climatic impacts of fresh water hosing under Last Glacial Maximum conditions: a multi-model study. *CP*, 9(2): 935–953, Apr. 2013.

F. Kaspar, N. Kuhl, U. Cubasch, and T. Litt. A model-data comparison of European temperatures in the Eemian interglacial. *Geophysical Research Letters*, 32(11):–5, 2005.

K. Kawamura, F. Parrenin, L. Lisiecki, R. Uemura, F. Vimeux, J. P. Severinghaus, M. A. Hutterli, T. Nakazawa, S. Aoki, J. Jouzel, M. E. Raymo, K. Matsumoto, H. Nakata, H. Motoyama, S. Fujita, K. Goto-Azuma, Y. Fujii, and O. Watanabe. Northern Hemisphere forcing of climatic cycles in Antarctica over the past 360,000 years. *Nature*, 448(7156):912–U4, 2007.

M. W. Kerwin. A regional stratigraphic isochron (ca. 8000 1 4 C yr BP) from final deglaciation of

Hudson Strait. *Oceanographic Literature Review*, 3(44):216, 1997.

S.-T. Kim and J. R. O'Neil. Equilibrium and nonequilibrium oxygen isotope effects in synthetic carbonates. *Geochimica et Cosmochimica Acta*, 61(16): 3461–3475, Aug. 1997.

S.-T. Kim, C. Hillaire-Marcel, and A. Mucci. Mechanisms of equilibrium and kinetic oxygen isotope effects in synthetic aragonite at 25°C. *Geochimica et Cosmochimica Acta*, 70(23):5790–5801, Dec. 2006.

R. Knutti, R. Furrer, C. Tebaldi, J. Cermak, and G. A. Meehl. Challenges in Combining Projections from Multiple Climate Models. *Journal of Climate*, 23 (10):2739–2758, 2010.

R. M. Koerner. Ice Core Evidence for Extensive Melting of the Greenland Ice Sheet in the Last Interglacial. *Science*, 244(4907):964–968, May 1989.

R. E. Kopp, F. J. Simons, J. X. Mitrovica, A. C. Maloof, and M. Oppenheimer. Probabilistic assessment of sea level during the last interglacial stage. *Nature*, 462(7275):863–867, Dec. 2009.

R. Kozdon, A. Eisenhauer, and M. Weinelt. Reassessing Mg/Ca temperature calibrations of Neogloboquadrina pachyderma (sinistral) using paired δ44/40Ca and Mg/Ca measurements. *Geochemistry*, 2009.

G. Krinner and M. Werner. Impact of precipitation seasonality changes on isotopic signals in polar ice cores: a multi-model analysis. *Earth and Planetary Science Letters*, 216(4):525–538, Dec. 2003.

G. Krinner, C. Genthon, Z. X. Li, and P. Le Van. Studies of the Antarctic climate with a stretched-grid general circulation model. *Journal of Geophysical Research-Atmospheres*, 102(D12):13731–13745, June 1997.

P. Lajeunesse and G. St-Onge. The subglacial origin of the lake Agassiz-Ojibway final outburst flood. *Nature Geoscience*, 1(3):184–188, Mar. 2008.

A. Landais, G. Dreyfus, E. Capron, J. Jouzel, V. Masson-Delmotte, D. M. Roche, F. Prie, N. Caillon, J. Chappellaz, M. Leuenberger, A. Lourantou, F. Parrenin, D. Raynaud, and G. Teste. Two-phase change in CO2, Antarctic temperature and global climate during Termination II. *Nature Geoscience*, 6(12):1062–1065, Dec. 2013.

J. Laskar, A. Fienga, M. Gastineau, and H. Manche. La2010: a new orbital solution for the long-term motion of the Earth,ãÜ. *A&A*, 532:A89, Aug. 2011.

J. E. Lee and I. Fung. "Amount effect" of water isotopes and quantitative analysis of post-condensation processes. *Hydrological Processes*, 22(1):1–8, Jan. 2008.

J. E. Lee, I. Fung, D. J. DePaolo, and C. C. Henning. Analysis of the global distribution of water

isotopes using the NCAR atmospheric general circulation model. *Journal of Geophysical Research-Atmospheres*, 112(D16):D16306, Aug. 2007.

S. C. Lewis, A. N. Legrande, M. Kelley, and G. A. Schmidt. Water vapour source impacts on oxygen isotope variability in tropical precipitation during Heinrich events. *Climate of the Past*, 6(3): 325–343, June 2010.

Y. X. Li, H. Renssen, A. P. Wiersma, and T. E. Törnqvist. Investigating the impact of Lake Agassiz drainage routes on the 8.2 ka cold event with a climate model. *Climate of the Past*, 5(3):471–480, Dec. 2009.

S.-J. Lin and R. B. Rood. Multidimensional Flux-Form Semi-Lagrangian Transport Schemes. *Monthly Weather Review*, 124(9):2046–2070, Sept. 1996.

G. Lohmann, R. Gerdes, and D. Chen. Stability of the thermohaline circulation in a simple coupled model. *Tellus, Series A: Dynamic Meteorology and Oceanography*, 48(3):465–476, May 1996.

S. J. Lorenz and G. Lohmann. Acceleration technique for Milankovitch type forcing in a coupled atmosphere-ocean circulation model: method and application for the Holocene. *Climate Dynamics*, 2004.

C. Lorius. A 150 000 year climatic record from Antarctic ice. *Nature*, 316(6029):591–596, Dec. 1985.

F. Lott. Alleviation of Stationary Biases in a GCM through a Mountain Drag Parameterization Scheme and a Simple Representation of Mountain Lift Forces. *Monthly Weather Review*, 127(5): 788–801, Feb. 1999.

L. Loulergue, A. Schilt, R. Spahni, V. Masson-Delmotte, T. Blunier, B. Lemieux, J. M. Barnola, D. Raynaud, T. F. Stocker, and J. Chappellaz. Orbital and millennial-scale features of atmospheric CH4 over the past 800,000 | [thinsp] | years. *Nature*, 453(7193):383–386, May 2008.

D. J. Lunt, A. Abe-Ouchi, P. Bakker, and A. Berger. A multi-model assessment of last interglacial temperatures. *Climate of the Past*, 2013.

D. Lüthi, M. Le Floch, B. Bereiter, T. Blunier, J. M. Barnola, U. Siegenthaler, D. Raynaud, J. Jouzel, H. Fischer, K. Kawamura, and T. F. Stocker. High-resolution carbon dioxide concentration record 650,000-800,000[thinsp]years before present. *Nature*, 453(7193):379–382, May 2008.

S. J. Marsland, H. Haak, J. H. Jungclaus, M. Latif, and F. Röske. The Max-Planck-Institute global ocean/sea ice model with orthogonal curvilinear coordinates. *Ocean modelling*, 2003.

B. Marzeion, A. H. Jarosch, and M. Hofer. Past and future sea-level change from the surface mass balance of glaciers. *Cryosphere*, 6(6):1295–1322, 2012.

V. Masson-Delmotte, G. Dreyfus, P. Braconnot, S. Johnsen, J. Jouzel, M. Kageyama, A. Landais,

M. F. Loutre, J. Nouet, F. Parrenin, D. Raynaud, B. Stenni, and E. Tuenter. Past temperature reconstructions from deep ice cores: relevance for future climate change. *Climate of the Past*, 2(2): 145–165, 2006.

V. Masson-Delmotte, S. Hou, A. Ekaykin, J. Jouzel, A. Aristarain, R. T. Bernardo, D. Bromwich, O. Cattani, M. Delmotte, S. Falourd, M. Frezzotti, H. Gallee, L. Genoni, E. Isaksson, A. Landais, M. M. Helsen, G. Hoffmann, J. Lopez, V. Morgan, H. Motoyama, D. Noone, H. Oerter, J. R. Petit, A. Royer, R. Uemura, G. A. Schmidt, E. Schlosser, J. C. Simoes, E. J. Steig, B. Stenni, M. Stievenard, M. R. van den Broeke, R. S. W. v. de Wal, W. J. v. de Berg, F. Vimeux, and J. W. C. White. A review of Antarctic surface snow isotopic composition: Observations, atmospheric circulation, and isotopic modeling. *Journal of Climate*, 21(13): 3359–3387, July 2008.

V. Masson-Delmotte, D. Buiron, and A. Ekaykin. A comparison of the present and last interglacial periods in six Antarctic ice cores. *Climate of the Past*, 2010.

V. Masson-Delmotte, P. Braconnot, G. Hoffman, J. Jouzel, M. Kageyama, A. Landais, Q. Lejeune, C. Risi, L. C. Sime, J. Sjolte, D. Swingedouw, and B. Vinther. Sensitivity of interglacial Greenland temperature and delta 18 O: ice core data, orbital and increased CO2 climate simulations. *CP*, 7(3): 1041–1059, 2011.

M. T. McCulloch, A. W. Tudhope, T. M. Esat, G. E. Mortimer, J. Chappell, B. Pillans, A. R. Chivas, and A. Omura. Coral record of equatorial sea-surface temperatures during the penultimate deglaciation at Huon Peninsula. *Science*, 283 (5399):202–204, 1999.

F. McDermott. Palaeo-climate reconstruction from stable isotope variations in speleothems: a review. *Quaternary Science Reviews*, 23(7-8):901–918, Apr. 2004.

N. P. McKay, J. T. Overpeck, and B. L. Otto-Bliesner. The role of ocean thermal expansion in Last Interglacial sea level rise. *Geophysical Research Letters*, 38, 2011.

J. F. McManus, R. Francois, J.-M. Gherardi, L. D. Keigwin, and S. Brown-Leger. Collapse and rapid resumption of Atlantic meridional circulation linked to deglacial climate changes. *Nature*, 428 (6985):834–837, Apr. 2004.

J. C. McWilliams. Parameterizing eddy-induced tracer transports in ocean circulation models. *J Phys Oceanogr*, 1995.

J. H. Mercer. West Antarctic Ice Sheet and Co2 Greenhouse Effect - Threat of Disaster. *Nature*, 271(5643):321–325, 1978.

U. Mikolajewicz, M. Vizcaino, J. Jungclaus, and G. Schurgers. Effect of ice sheet interactions in anthropogenic climate change simulations. *Geophysical Research Letters*, 2007.

U. Mikolajewicz, D. Swingedouw, C. B. Rodehacke, E. Behrens, M. Menary, S. M. Olsen, Y. Gao, J. Mignot, and A. Biastoch. Decadal fingerprints of freshwater discharge around Greenland in a multi-model ensemble. *Climate Dynamics*, 41 (3-4):695–720, Sept. 2012.

M. Milankovic. *Kanon der Erdbestrahlung und seine Anwendung auf das Eiszeitproblem*. Königlich Serbische Akademie, 1941.

R. H. Moss, J. A. Edmonds, K. A. Hibbard, M. R. Manning, S. K. Rose, D. P. van Vuuren, T. R. Carter, S. Emori, M. Kainuma, T. Kram, G. A. Meehl, J. F. B. Mitchell, N. Nakicenovic, K. Riahi, S. J. Smith, R. J. Stouffer, A. M. Thomson, J. P. Weyant, and T. J. Wilbanks. The next generation of scenarios for climate change research and assessment. *Nature*, 463(7282):747–756, Feb. 2010.

K. Muehlenbachs and R. Clayton. Oxygen isotope composition of the oceanic crust and its bearing on seawater. *Journal of Geophysical Research*, 81 (23):4365–4369, 1976.

T. Münch, S. Kipfstuhl, J. Freitag, and H. Meyer. Regional climate signal vs. local noise: a two-dimensional view of water isotopes in Antarctic firn at Kohnen station, Dronning Maud Land. *Clim Past Discuss*, 2015.

M. Mussi, G. Leone, and I. Nardi. *Isotopic geochemistry of natural waters from the Alpi Apuane-Garfagnana area, Northern Tuscany, Italy*. Miner. Petrogr. Acta, 1998.

B. D. A. Naafs, J. Hefter, and R. Stein. Millennial-scale ice rafting events and Hudson Strait Heinrich(-like) Events during the late Pliocene and Pleistocene: a review. *Quaternary Science Reviews*, 80:1–28, Nov. 2013.

NEEM community members. Eemian interglacial reconstructed from a Greenland folded ice core. *Nature*, 493(7433):489–494, 2013.

J. Nicholl, D. A. Hodell, and B. Naafs. A Laurentide outburst flooding event during the last interglacial period. *Nature*, 5(12):901–904, 2012.

D. Noone and I. Simmonds. Implications for the interpretation of ice-core isotope data from analysis of modelled Antarctic precipitation. *Annals of Glaciology, Vol 35*, 27:398–402, 1998.

D. Notz. Challenges in simulating sea ice in Earth System Models. *Wiley Interdisciplinary Reviews-Climate Change*, 3(6):509–526, 2012.

M. J. O 'Leary, P. J. Hearty, W. G. Thompson, M. E. Raymo, J. X. Mitrovica, and J. M. Webster. Ice sheet collapse following a prolonged period of stable sea level during the last interglacial. *Nature Geoscience*, 6(9):796–800, 2013.

J. C. Obert, D. Scholz, T. Felis, W. M. Brocas, K. P. Jochum, and M. O. Andreae. Th-230/U dating of Last Interglacial brain corals from Bonaire (southern Caribbean) using bulk and theca wall

material. *Geochimica Et Cosmochimica Acta*, 178: 20–40, 2016.

D. Olbers, V. Gouretsky, G. Seiss, and J. Schröter. Hydrographic Atlas of the Southern Ocean. *Alfred-Wegener-Institut, Bremerhaven*, 1992.

B. L. Otto-Bliesner, S. J. Marshall, J. T. Overpeck, G. H. Miller, A. Hu, and C. L. I. P. members. Simulating Arctic Climate Warmth and Icefield Retreat in the Last Interglaciation. 311(5768):1751–1753, Mar. 2006.

B. L. Otto-Bliesner, N. Rosenbloom, E. J. Stone, N. P. McKay, D. J. Lunt, E. C. Brady, and J. T. Overpeck. How warm was the last interglacial? New model–data comparisons. *Philosophical Transactions of the Royal Society of London A: Mathematical, Physical and Engineering Sciences*, 371 (2001):–20130097, Sept. 2013.

F. Parrenin, J. M. Barnola, J. Beer, T. Blunier, E. Castellano, J. Chappellaz, G. Dreyfus, H. Fischer, S. Fujita, J. Jouzel, K. Kawamura, B. Lemieux-Dudon, L. Loulergue, V. Masson-Delmotte, B. Narcisi, J. R. Petit, G. Raisbeck, D. Raynaud, U. Ruth, J. Schwander, M. Severi, R. Spahni, J. P. Steffensen, A. Svensson, R. Udisti, C. Waelbroeck, and E. Wolff. The EDC3 chronology for the EPICA dome C ice core. *Climate of the Past*, 3(3):485–497, 2007.

W. S. B. Paterson and W. F. Budd. Flow parameters for ice sheet modeling. *Cold Regions Science and Technology*, 6(2):175–177, 1982.

F. Pattyn. A new three-dimensional higher-order thermomechanical ice sheet model: Basic sensitivity, ice stream development, and ice flow across subglacial lakes. *Journal of Geophysical Research-Solid Earth*, 108(B8), 2003.

J. P. Peixoto and A. H. Oort. *Physics of Climate*. American Institute of Physics, 1992.

J. R. Petit, J. Jouzel, D. Raynaud, N. I. Barkov, J. M. Barnola, I. Basile, M. Bender, J. Chappellaz, M. Davis, G. Delaygue, M. Delmotte, V. M. Kotlyakov, M. Legrand, V. Y. Lipenkov, C. Lorius, L. PÉpin, C. Ritz, E. Saltzman, and M. Stievenard. Climate and atmospheric history of the past 420,000 years from the Vostok ice core, Antarctica. *Nature*, 399(6735):429–436, June 1999.

M. Pfeiffer and G. Lohmann. Greenland Ice Sheet influence on Last Interglacial climate: global sensitivity studies performed with an atmosphere–ocean general circulation model. *CPD*, 11(2):933–995, Mar. 2015.

R. T. Pierrehumbert. *Principles of Planetary Climate*. Cambridge University Press, New York, 2010.

F. G. Prahl and S. G. Wakeham. Calibration of Unsaturation Patterns in Long-Chain Ketone Compositions for Paleotemperature Assessment. *Nature*, 330(6146):367–369, 1987.

W. L. Prell. Stability of low-latitude sea-surface temperatures: an evaluation of the CLIMAP re-

construction with emphasis on the positive SST anomalies. Final report. 1985.

T. J. Raddatz, C. H. Reick, W. Knorr, J. Kattge, E. Roeckner, R. Schnur, K. G. Schnitzler, P. Wetzel, and J. Jungclaus. Will the tropical land biosphere dominate the climate–carbon cycle feedback during the twenty-first century? *Climate Dynamics*, 29(6):565–574, 2007.

S. Rahmstorf. Ocean circulation and climate during the past 120,000 years. *Nature*, 419(6903): 207–214, Sept. 2002.

S. Rahmstorf, J. E. Box, G. Feulner, M. E. Mann, A. Robinson, S. Rutherford, and E. J. Schaffernicht. Exceptional twentieth-century slowdown in Atlantic Ocean overturning circulation. *Nature Climate Change*, 5(5):475–480, 2015.

G. M. Raisbeck, F. Yiou, J. Jouzel, and T. F. Stocker. Direct north-south synchronization of abrupt climate change record in ice cores using Beryllium 10. *Climate of the Past*, 3(3):541–547, 2007.

S. O. Rasmussen, K. K. Andersen, A. M. Svensson, J. P. Steffensen, B. M. Vinther, H. B. Clausen, M. L. Siggaard-Andersen, S. J. Johnsen, L. B. Larsen, D. Dahl-Jensen, M. Bigler, R. Rothlisberger, H. Fischer, K. Goto-Azuma, M. E. Hansson, and U. Ruth. A new Greenland ice core chronology for the last glacial termination. *Journal of Geophysical Research-Atmospheres*, 111 (D6), 2006.

D. Raynaud, V. Lipenkov, B. Lemieux-Dudon, P. Duval, M.-F. Loutre, and N. Lhomme. The local insolation signature of air content in Antarctic ice. A new step toward an absolute dating of ice records. *Earth and Planetary Science Letters*, 261 (3-4):337–349, 2007.

R. W. Reynolds, N. A. Rayner, T. M. Smith, D. C. Stokes, and W. Q. Wang. An improved in situ and satellite SST analysis for climate. *Journal of Climate*, 15(13):1609–1625, July 2002.

R. W. Reynolds, T. M. Smith, C. Liu, D. B. Chelton, K. S. Casey, and M. G. Schlax. Daily High-Resolution-Blended Analyses for Sea Surface Temperature. *Journal of Climate*, 20(22):5473–5496, Nov. 2007.

J. K. Ridley, P. Huybrechts, J. M. Gregory, and J. A. Lowe. Elimination of the Greenland Ice Sheet in a High CO_2 Climate. *Journal of Climate*, 18(17): 3409–3427, 2005.

E. Rignot, J. Mouginot, M. Morlighem, H. Seroussi, and B. Scheuchl. Widespread, rapid grounding line retreat of Pine Island, Thwaites, Smith, and Kohler glaciers, West Antarctica, from 1992 to 2011. *Geophysical Research Letters*, 41(10):3502–3509, 2014.

C. Risi, S. Bony, F. Vimeux, and J. Jouzel. Water-stable isotopes in the LMDZ4 general circulation model: Model evaluation for present-day and past climates and applications to climatic interpretations of tropical isotopic records (vol 115,

D24123, 2010). *Journal of Geophysical Research-Atmospheres*, 115(D24), 2010.

A. Robinson, A. Ganopolski, and R. Calov. Multistability and critical thresholds of the Greenland ice sheet. 2(6):429–432, 2012.

E. Roeckner. The Atmospheric General Circulation Model ECHAM5: Part 1 : Model Description. 2003.

E. Roeckner, R. Brokopf, M. Esch, M. Giorgetta, S. Hagemann, L. Kornblueh, E. Manzini, U. Schlese, and U. Schulzweida. Sensitivity of Simulated Climate to Horizontal and Vertical Resolution in the ECHAM5 Atmosphere Model. *Journal of Climate*, 19(16):3771–3791, Aug. 2006.

K. Rozanski, L. Araguas-Araguas, and R. Gonfiantini. Relation Between Long-Term Trends of Oxygen-18 Isotope Composition of Precipitation and Climate. *Science*, 258(5084):981–5, Dec. 1992.

W. F. Ruddiman and M. E. Raymo. A methane-based time scale for Vostok ice. *Quaternary Science Reviews*, 22(2-4):141–155, Feb. 2003.

R. P. Scherer, A. Aldahan, S. Tulaczyk, G. Possnert, H. Engelhardt, and B. Kamb. Pleistocene collapse of the West Antarctic ice sheet. *Science*, 281 (5373):82–85, 1998.

S. Schmidtko, K. J. Heywood, A. F. Thompson, and S. Aoki. Multidecadal warming of Antarctic waters. *Science*, 346(6214):1227–1231, 2014.

D. Scholz, D. L. Hoffmann, J. Hellstrom, and C. Bronk Ramsey. A comparison of different methods for speleothem age modelling. *Quaternary Geochronology*, 14:94–104, Dec. 2012.

C. Schoof. Ice sheet grounding line dynamics: Steady states, stability, and hysteresis. *Journal of Geophysical Research-Earth Surface*, 112(F3), 2007.

H. Schrader and R. Gersonde. Diatoms and silicoflagellates. *In Zachariasse et al. Microplaeontological counting methods and techniques - an excercise on an eight metres section of the lower Pliocene of Capo Rossello. Sicily. Utrecht Micropal. Bull. 17:, pp. 129-176*, 1978.

N. J. Shackleton. Oxygen isotope analyses and Pleistocene temperatures re-assessed. *Nature*, 215 (5096):15–17, 1967.

N. J. Shackleton. Attainment of isotopic equilibrium between ocean water and the benthonic foraminifera genus Uvigerina: isotopic changes in the ocean during the last glacial. *Colloques Internationaux du CNRS*, 1974.

L. C. Sime, J. C. Tindall, E. W. Wolff, W. M. Connolley, and P. J. Valdes. Antarctic isotopic thermometer during a CO2 forced warming event. *Journal of Geophysical Research-Atmospheres*, 113(D24): D24119, Dec. 2008.

L. C. Sime, C. Risi, J. C. Tindall, J. Sjolte, E. W. Wolff, V. Masson-Delmotte, and E. Capron. Warm climate isotopic simulations: what do we learn

about interglacial signals in Greenland ice cores? *Quaternary Science Reviews*, 67:59–80, May 2013.

J. Sjolte, G. Hoffman, and S. J. Johnsen. Modelling the response of stable water isotopes in Greenland precipitation to orbital configurations of the previous interglacial. *Tellus B*, 66(0):1383, Sept. 2014.

T. M. Smith, R. W. Reynolds, T. C. Peterson, and J. Lawrimore. Improvements to NOAA's Historical Merged Land–Ocean Surface Temperature Analysis (1880–2006). *Journal of Climate*, 21(10): 2283–2296, May 2008.

H. Sodemann and A. Stohl. Asymmetries in the moisture origin of Antarctic precipitation. *Geophysical Research Letters*, 36(22), 2009.

R. Spahni, J. Chappellaz, T. F. Stocker, L. Loulergue, G. Hausammann, K. Kawamura, J. Flückiger, J. Schwander, D. Raynaud, V. Masson-Delmotte, and J. Jouzel. Atmospheric Methane and Nitrous Oxide of the Late Pleistocene from Antarctic Ice Cores. *Science*, 310(5752):1317–1321, Nov. 2005.

G. St-Onge and P. Lajeunesse. Flood-Induced Turbidites From Northern Hudson Bay And Western Hudson Strait: A Two-Pulse Record Of Lake Agassiz Final Outburst Flood? In *Submarine Mass Movements and Their Consequences*, pages 129–137. Springer Netherlands, Dordrecht, 2007.

B. Stenni, V. Masson-Delmotte, S. Johnsen, J. Jouzel, A. Longinelli, E. Monnin, R. Röthlisberger, and E. Selmo. An Oceanic Cold Reversal During the Last Deglaciation. *Science*, 293(5537):2074–2077, Sept. 2001.

B. Stenni, V. Masson-Delmotte, E. Selmo, H. Oerter, H. Meyer, R. Roethlisberger, J. Jouzel, O. Cattani, S. Falourd, H. Fischer, G. Hoffmann, P. Iacumin, S. J. Johnsen, B. Minster, and R. Udisti. The deuterium excess records of EPICA Dome C and Dronning Maud Land ice cores (East Antarctica). *Quaternary Science Reviews*, 29(1-2):146–159, Jan. 2010.

C. Stepanek and G. Lohmann. Modelling mid-Pliocene climate with COSMOS. *Geoscientific Model Development*, 5(5):1221–1243, Oct. 2012.

C. H. Stirling and M. B. Andersen. Uranium-series dating of fossil coral reefs: Extending the sea-level record beyond the last glacial cycle. *Earth and Planetary Science Letters*, 284(3-4):269–283, 2009.

C. H. Stirling, T. M. Esat, K. Lambeck, and M. T. McCulloch. Timing and duration of the Last Interglacial: Evidence for a restricted interval of widespread coral reef growth. *Earth and Planetary Science Letters*, 160(3-4):745–762, Aug. 1998.

T. Stocker, D. Qin, G.-K. Plattner, M. Tignor, S. Allen, J. Boschung, A. Nauels, Y. Xia, V. Bex, and P. Midgley, editors. *Climate Change 2013: The Physical Science Basis. Contribution of Working Group I to the Fifth Assessment Report of the In-*

tergovernmental Panel on Climate Change. Cambridge University Press, 2013.

T. F. Stocker and S. J. Johnsen. A minimum thermodynamic model for the bipolar seesaw. *Paleoceanography*, 18(4), 2003. ISSN 1944-9186. 1087.

T. F. Stocker, T. F. Stocker, A. Schmittner, and A. Schmittner. Influence of CO2 emission rates on the stability of the thermohaline circulation. *Nature*, 388(6645):862–865, Aug. 1997.

H. Stommel. Thermohaline convection with two stable regimes of flow. *Tellus*, 1961.

E. J. Stone, E. Capron, D. J. Lunt, A. J. Payne, J. S. Singarayer, P. J. Valdes, and E. W. Wolff. Impact of melt water on high latitude early Last Interglacial climate. *CPD*, 2016:1–22, Feb. 2016.

J. Sutter, P. Gierz, K. Grosfeld, M. Thoma, and G. Lohmann. Ocean temperature thresholds for Last Interglacial West Antarctic Ice Sheet collapse. *Geophysical Research Letters*, pages n/a–n/a, Jan. 2016.

A. Suzuki, M. K. Gagan, P. De Deckker, A. Omura, I. Yukino, and H. Kawahata. Last Interglacial coral record of enhanced insolation seasonality and seawater O enrichment in the Ryukyu Islands, northwest Pacific. *Geophysical Research Letters*, 28(19):3685–3688, Oct. 2001.

A. Svensson, K. K. Andersen, M. Bigler, H. B. Clausen, D. Dahl-Jensen, S. M. Davies, S. J. Johnsen, R. Muscheler, F. Parrenin, S. O. Rasmussen, R. Roethlisberger, I. Seierstad, J. P. Steffensen, and B. M. Vinther. A 60 000 year Greenland stratigraphic ice core chronology. *Climate of the Past*, 4(1):47–57, 2008.

D. Swingedouw, C. B. Rodehacke, S. M. Olsen, M. Menary, Y. Gao, U. Mikolajewicz, and J. Mignot. On the reduced sensitivity of the atlantic overturning to greenland ice sheet melting in projections: a multi-model assessment. *Climate Dynamics*, 44(11-12):3261–3279, 2015. ISSN 0930-7575.

J. T. Teller and D. W. Leverington. Glacial Lake Agassiz: A 5000 yr history of change and its relationship to the δ18O record of Greenland. *Bulletin of the Geological Society of America*, 116 (5-6):729–742, May 2004.

J. T. Teller, D. W. Leverington, and J. D. Mann. Freshwater outbursts to the oceans from glacial Lake Agassiz and their role in climate change during the last deglaciation. *Quaternary Science Reviews*, 21(8–9):879–887, 2002.

M. Thoma, K. Grosfeld, D. Barbi, J. Determann, S. Goeller, C. Mayer, and F. Pattyn. RIMBAY – a multi-approximation 3D ice-dynamics model for comprehensive applications: model description and examples. *Geoscientific Model Development*, 7(1):1–21, 2014.

J. C. Tindall and A. M. Haywood. Modeling oxygen isotopes in the Pliocene: Large-scale features

over the land and ocean. *Paleoceanography*, 30 (9):1183–1201, Sept. 2015.

A. W. Tudhope, C. P. Chilcott, M. T. McCulloch, E. R. Cook, J. Chappell, R. M. Ellam, D. W. Lea, J. M. Lough, and G. B. Shimmield. Variability in the El Niño-Southern Oscillation through a glacial-interglacial cycle. *Science*, 291(5508):1511–1517, Feb. 2001.

C. S. M. Turney and R. T. Jones. Does the Agulhas Current amplify global temperatures during super-interglacials? *Journal of Quaternary Science*, 25(6):839–843, Sept. 2010.

S. Valcke. The OASIS3 coupler: a European climate modelling community software. *GMD*, 6(2):373–388, Mar. 2013.

D. Veres, L. Bazin, A. Landais, H. T. M. Kele, B. Lemieux-Dudon, F. Parrenin, P. Martinerie, E. Blayo, T. Blunier, E. Capron, J. Chappellaz, S. O. Rasmussen, M. Severi, A. Svensson, B. Vinther, and E. W. Wolff. The Antarctic ice core chronology (AICC2012): an optimized multi-parameter and multi-site dating approach for the last 120 thousand years. *Climate of the Past*, 9 (4):1733–1748, 2013.

B. M. Vinther, S. L. Buchardt, H. B. Clausen, D. Dahl-Jensen, S. J. Johnsen, D. A. Fisher, R. M. Koerner, D. Raynaud, V. Lipenkov, K. K. Andersen, T. Blunier, S. O. Rasmussen, J. P. Steffensen, and A. M. Svensson. Holocene thinning of the Greenland ice sheet. *Nature*, 461(7262):385–388, 2009.

M. Vizcaíno, M. Gröger, E. Maier-Reimer, G. Schurgers, U. Mikolajewicz, and A. M. E. Winguth. Long-term ice sheet-climate interactions under anthropogenic greenhouse forcing simulated with a complex Earth System Model. 31(6):665–690, 2008.

M. Vizcaíno, W. H. Lipscomb, W. J. Sacks, and M. Van Den Broeke. Greenland Surface Mass Balance as Simulated by the Community Earth System Model. Part II: Twenty-First-Century Changes. *Journal of Climate*, 27(1):215–226, 2014.

M. Vizcaino, U. Mikolajewicz, F. Ziemen, C. B. Rodehacke, R. Greve, and M. R. van den Broeke. Coupled simulations of greenland ice sheet and climate change up to a.d. 2300. *Geophysical Research Letters*, 42(10):3927–3935, 2015. ISSN 1944-8007. 2014GL061142.

C. Wang, S. K. Lee, and D. B. Enfield. Atlantic Warm Pool acting as a link between Atlantic Multidecadal Oscillation and Atlantic tropical cyclone activity. *Geochemistry, Geophysics, Geosystems*, 9 (5):n/a–n/a, May 2008.

Y. J. Wang, H. Cheng, R. L. Edwards, Z. S. An, J. Y. Wu, C. C. Shen, and J. A. Dorale. A high-resolution absolute-dated Late Pleistocene monsoon record from Hulu Cave, China. *Science*, 294 (5550):2345–2348, 2001.

O. Watanabe, J. Jouzel, S. Johnsen, F. Parrenin, and H. Shoji. Homogeneous climate variability across East Antarctica over the past three glacial cycles. *Nature*, 2003.

A. J. Weaver, J. Sedláček, M. Eby, K. Alexander, E. Crespin, T. Fichefet, G. Philippon-Berthier, F. Joos, M. Kawamiya, M. Kawamiy, K. Matsumoto, M. Steinacher, K. Tachiiri, K. Tokos, M. Yoshimori, and K. Zickfeld. Stability of the Atlantic meridional overturning circulation: A model intercomparison. *Geophysical Research Letters*, 39(20):n/a–n/a, Oct. 2012.

W. Wei and G. Lohmann. Simulated atlantic multidecadal oscillation during the holocene. *Journal of Climate*, 25(25):6989–7002, 2012.

W. Weijer, M. E. Maltrud, M. W. Hecht, H. A. Dijkstra, and M. A. Kliphuis. Response of the Atlantic Ocean circulation to Greenland Ice Sheet melting in a strongly-eddying ocean model. *Geophysical Research Letters*, 39(9):n/a–n/a, May 2012.

M. Werner, M. Heimann, and G. Hoffmann. Isotopic composition and origin of polar precipitation in present and glacial climate simulations. *Tellus B*, 2001.

M. Werner, P. M. Langebroek, T. Carlsen, M. Herold, and G. Lohmann. Stable water isotopes in the ECHAM5 general circulation model: Toward high-resolution isotope modeling on a global scale. *Journal of Geophysical Research-Atmospheres*, 116(D15):D15109, Aug. 2011.

M. Werner, B. Haese, X. Xu, X. Zhang, M. Butzin, and G. Lohmann. Glacial–interglacial changes in $H_2^{18}O$, HDO and deuterium excess – results from the fully coupled ECHAM5/MPI-OM Earth system model. *GMD*, 9(2):647–670, Feb. 2016.

M. Wild, J. Grieser, and C. Schär. Combined surface solar brightening and increasing greenhouse effect support recent intensification of the global land-based hydrological cycle. *Geophysical Research Letters*, 35(17):L17706, Sept. 2008.

A. Winter, A. Paul, J. Nyberg, T. Oba, J. Lundberg, D. Schrag, and B. Taggart. Orbital control of low-latitude seasonality during the Eemian. *Geophysical Research Letters*, 30(4):1163, Feb. 2003.

M. Winton. Do Climate Models Underestimate the Sensitivity of Northern Hemisphere Sea Ice Cover? *Journal of Climate*, 24(15):3924–3934, Aug. 2011.

W. Xiao, T. Frederichs, R. Gersonde, G. Kuhn, O. Esper, and X. Zhang. Constraining the dating of late Quaternary marine sediment records from the Scotia Sea (Southern Ocean). *Quaternary Geochronology*, 31:97–118, Feb. 2016.

X. Xu, M. Werner, M. Butzin, and G. Lohmann. Water isotope variations in the global ocean model MPI-OM. *Geoscientific Model Development*, 5(3): 809–818, 2012.

D. Yuan, H. Cheng, R. L. Edwards, C. A. Dykoski, M. J. Kelly, M. Zhang, J. Qing, Y. Lin, Y. Wang,

J. Wu, J. A. Dorale, Z. An, and Y. Cai. Timing, Duration, and Transitions of the Last Interglacial Asian Monsoon. 304(5670):575–578, Apr. 2004.

A. Zammit-Mangion, J. Rougier, N. Schoen, F. Lindgren, and J. Bamber. Multivariate spatio-temporal modelling for assessing Antarctica's present-day contribution to sea-level rise. *Environmetrics*, 26(3):159–177, May 2015.

R. E. Zeebe. An explanation of the effect of seawater carbonate concentration on foraminiferal oxygen isotopes. *Geochimica et Cosmochimica Acta*, 63 (13-14):2001–2007, July 1999.

R. E. Zeebe. Reply to the comment by P. Deines on "An explanation of the effect. of seawater carbonate concentration on foraminiferal oxygen isotopes," by R. E. Zeebe 1999. *Geochimica et Cosmochimica Acta*, 69(3):789–790, 2005.

X. Zhang, G. Lohmann, G. Knorr, and X. Xu. Different ocean states and transient characteristics in last glacial maximum simulations and implications for deglaciation. *Climate of the Past*, 9(5): 2319–2333, 2013.

X. Zhang, G. Lohmann, G. Knorr, and C. Purcell. Abrupt glacial climate shifts controlled by ice sheet changes. *Nature*, 512(7514):290–294, Aug. 2014.

J. Zhu, Z. Liu, X. Zhang, I. Eisenman, and W. Liu. Linear weakening of the amoc in response to receding glacial ice sheets in ccsm3. *Geophysical Research Letters*, 41(17):6252–6258, 2014. ISSN 1944-8007. 2014GL060891.

U. Zielinski and R. Gersonde. Diatom distribution in Southern Ocean surface sediments (Atlantic sector): Implications for paleoenvironmental reconstructions. *Palaeogeography, Palaeoclimatology, Palaeoecology*, 129(3-4):213–250, Apr. 1997.